Université de Technologie de Belfort-Montbéliard
École doctorale SPIM « Sciences pour l'ingénieur et microtechniques »

THESE

Présentée à

L'Université de Technologie de Belfort-Montbéliard
en vue de l'obtention du titre de
Docteur

par

Giuseppe Marsala
Département Génie Électrique et Systèmes de Commande
de l'Université de Technologie de Belfort-Montbéliard

Modélisation et réalisation d'un émulateur de système de piles à combustibles
Développement des stratégies et des lois de commande
(Modelling and Implementation of an Emulator for Fuel Cell Systems Development of Control Strategies and Laws)

le 4 décembre 2008

Membres du jury :

M. Belkacem Ould Bouamama	Polytech'lille, Lille (Rapporteur)
M. Mohamed El Hachemi Benbouzid	Université de Brest
M. Massimo Vitelli	Seconda Università degli studi di Napoli (Italy)(Rapporteur)
M. Marcello Pucci	I.S.S.I.A.-C.N.R, Palermo (Italy)
M. Abdellatif Miraoui	UTBM, L2ES-SeT, Belfort
M. Maurizio Cirrincione	UTBM, L2ES-SeT, Belfort

"You can tell whether a man is clever by his answers.
You can tell whether a man is wise by his questions."
Naguib Mahfouz
(Egyptian novelist and screenplay writer 1988 Nobel Prize for Literature)

RÉSUMÉ

Titre: Modélisation et réalisation d'un émulateur de système de piles à combustibles - Développement des stratégies et des lois de commande

Giuseppe Marsala, Thèse de Doctorat, le 4 décembre 2008

Le sujet de thèse traite de la modélisation d'un système d'énergie avec piles à combustibles (PàC) de type PEMFC destiné à être intégré dans les véhicules électriques. Le but recherché par la réalisation de cet émulateur (objet matériel qui a le même comportement qu'un système réel) est de développer des lois de commande assurant un bon fonctionnement du système PàC.

Après une étude bibliographique sur les différentes modélisations de cœur de Pile à Combustible (PàC), le choix d'un convertisseur de type Buck a été retenu et mis en œuvre pour l'émulateur. L'originalité de ce travail réside dans la prise en compte de toutes les auxiliaires du système PàC. Les auxiliaires ont été introduites sous forme Hardware In the Loop (HIL). Pour cela l'environnement DSPACE a été utilisé. Plusieurs lois de commande et de contrôle ont été étudiées et mises en œuvre. L'émulateur a été conçu avec une large bande passante.

Le contrôle de la tension est réalisé avec la technique « State Variable Feedback », qui est capable de fixer correctement les pôles du système à boucle-fermé afin d'assurer la bande passante souhaité et le comportement à régime permanent.
Le cas particulier de la gestion de l'air a été largement développé et a permis de valider le principe d'émulation retenu. En effet, différentes stratégies de commande (static feedforward, PI) ont été étudiées et comparées en utilisant une nouvelle stratégie de commande basée sur les réseaux neuronaux. Cette dernière repose sur le principe d'inversion de la relation entre la vitesse de rotation du compresseur et le coefficient de « oxygen excess ratio », dont la régulation est d'importance capitale pour éviter l'appauvrissement en oxygène de la membrane.

Contexte : ce sujet est proposé dans le cadre partenariat avec Centre National de Recherche (CNR) d'Italie.

Mots Clés: Système Pile à Combustible, Pile à Combustible de type PEM (Proton Exchange Membrane), Buck Convertisseur, Emulateur, Véhicule Electrique (VE), Réseaux de neurones.

ABSTRACT

Title: Modelling and Implementation of an Emulator for Fuel Cell Systems- Development of Control Strategies Laws.

Giuseppe Marsala, PhD Thesis, 4 December 2008

This thesis deals with modelling of a PEM-Fuel Cell System (FCS) for power generation in an electrical vehicle. The goal of the research is the construction of an emulator of the PEM Fuel Cell stack, that of a device having the same behaviour as the real system, and the development of command strategies for the FCS.

After a bibliographical study of the models of a Fuel Cell stack, a buck converter structure has been chosen and then implemented to build the emulator. The novelty of this thesis is that all the auxiliary components of a FCS have been considered in a Hardware In the Loop (HIL) fashion by using a DSPACE development platform. .Several command strategies have been implemented and assessed by using the emulator, which has been designed with a high bandwidth.

The voltage control of the emulator has been accomplished by using the "State Variable Feedback ", which is a pole-placement technique for achieving the desired bandwidth and dynamical and steady-state performance.

The particular case of the control of the air-management system has been considered and used to asses the emulator. Actually several control strategies (static feedforward, PI) have been studied and their results compared also by using a novel neural network based command strategy. This neural network implements the inversion of the relationship between the compressor speed and the "oxygen excess ratio", whose regulation is a key issue for preventing the oxygen starvation of the membrane.

Context: this topic has been proposed in the framework of cooperation with the Italian National Research Council (CNR).

Key Words: Fuel Cell Systems (FCS), Proton Exchange Membrane Fuel Cell PEM-FC, Buck-Converter, Emulator, Electrical Vehicle (EV), Neural Networks.

To,

My Father

and

in loving memory of my Mother and my Grandmother

ACKNOWLEDGMENTS

I am very grateful to my advisors Maurizio Cirrincione, Full Professor at the UTBM; who patiently guided me during my research work and has been hugely supportive throughout the three years of the thesis,. Giansalvo Cirrincione, Associate Professor and HdR of the University of Picardie Jules Verne (Amiens); for his great help about the application of the GMR and his strong theoretical advice for any problem I have come across with , Marcello Pucci, Senior Researcher at the ISSIA-CNR (Palermo-Italy); for his invaluable technical inputs in several domains, his continual scientific support and for practical insights into the industrial aspects of the research, and Abdellatif Miraoui, Full Professor at the UTBM, for offering me precious suggestions, both scientific and moral, for providing me a highly stimulating research environment and for giving me the freedom in my research activity and filled me with enthusiasm.

I would also to thank Gianpaolo Vitale, Senior Researcher at the ISSIA-CNR (Palermo-Italy) for his impressive expertise in power electronics, which has been of great help in the development of the emulator, Calogero Serporta, Senior Researcher and Responsible of the ISSIA-CNR (Palermo-Italy), who has put all the ISSIA facilities at my disposal during my stay in Italy, Maria Carmela di Piazza, Researcher at the ISSIA-CNR (Palermo-Italy), for her kind technical advice during my stay in Palermo, Giuseppe Scordato and Antonio Sauro for their very precious practical help with the real implementation of the emulator. This thesis would not have been possible without their contributions.

I am also very grateful to Benjamin Blunier, Damien Paire, David Bouquain fo their help with my work and for their warmest welcome to the UTBM and support during my PhD period.

I wish to thank the professional staff of the GESC-SET-FClab for providing me with excellent support for the experimental phase of my work, making any difficult task more enjoyable and the Director of the SET, prof. Abderrafiâa Koukam, for his encouragement and having trusted me.

I would also express my gratitude for the cooperation between the UTBM and the CNR and their institutional support encouraging joint work in a very creative environment.

I would like to thank Maurizio for having been more a friend than a professor throughout these years. My warmest thanks also to my friends Murcel, Giovanni, Santo, Angelo, Mariarosa, Concetta Maria, Andrea, Alessio and Massimo for the unforgettable moments we have lived together.

Thank you to my whole family, who have been deprived of my company and attention for many months: they have never complained but gave me their help and understanding.

Particularly, I wish to pay tribute to my father for his support and tolerance: more important than anything else, without him this effort of mine could never have been accomplished.

Finally special thoughts go to my Mother and my Grandmother, who have always been near me, as it has always been.

TABLE OF CONTENTS

Introduction

0.1 The Context

Over the last few decades there has been a growing interest in Fuel Cell Systems (FCS) for power generation both for stationary and mobile applications. Particularly Proton Exchange Membrane Fuel Cells Systems (PEM-FCS) seem to be a good solution for distributed generation and ground vehicle applications, because of high power density, solid electrolyte, low corrosion, low-temperature operation. However, some issues are still of concern, in particular their cost, their size and weight, and the complexity of peripheral devices. A FCS is a complex system, where different physical phenomena occur: thermal, electrochemical, electrical and so on. As a matter of fact the fuel cell stack needs several auxiliary components in order to work properly, like the hydrogen supply system for the anode, the air management system for the cathode, the cooling system, the humidifier system. All of the components of these auxiliaries should be analysed, designed and optimised to improve the FCS performance, so that not only the FC stack can be improved but also that the strong nonlinear interactions between the different auxiliaries can be optimised.

On the other hand the present price of FC stacks, the cost of the hydrogen, and the fact that the life of a fuel cell stack is determined by the number of hours of use and off/on cycles limit their employment in experimentation. This is a problem for example when designing and verifying Power Conditioner Systems (PCS) at the output of the FC, which in general consists of DC-DC step-up converter with a bidirectional DC-DC converter (if a buffer energy source is present) and a DC-AC inverter. So far most PCSs are mainly tested with a constant DC source with a first-order delay. Moreover the size of the auxiliary equipment can have too great a size according to the size of the FC and this can result in too high associated costs and space. Finally, simply the testing of the PCS control system, or even the control systems of auxiliaries can be dangerous for the FCs and very expensive because of the potential damages. All the above issues call for the use of a low-cost device which can behave electrically like the real FCs, but whose testing is not risky. These systems are called in literature real-time simulators or emulators.

In this area the FClab-SET-UTBM, Belfort, France and the ISSIA-CNR, Palermo, Italy in the framework of their activity research about modelling and controlling Fuel Cell Systems are developing a complete PEM-FCS emulator, the scheme of which is represented in Fig.0.1. The target is to manage to realise an emulator for a complete FCS, both for the electrical part, which is the topic of this thesis, and for the thermodynamical and fluidodynamical parts. All the subsystems of the FCS (the humidifier, the air management, the cooling system, the hydrogen supply system and the output power management) are then emulated with proper thermal, fluid and electrical systems, and they are managed in the dSPACE environment.

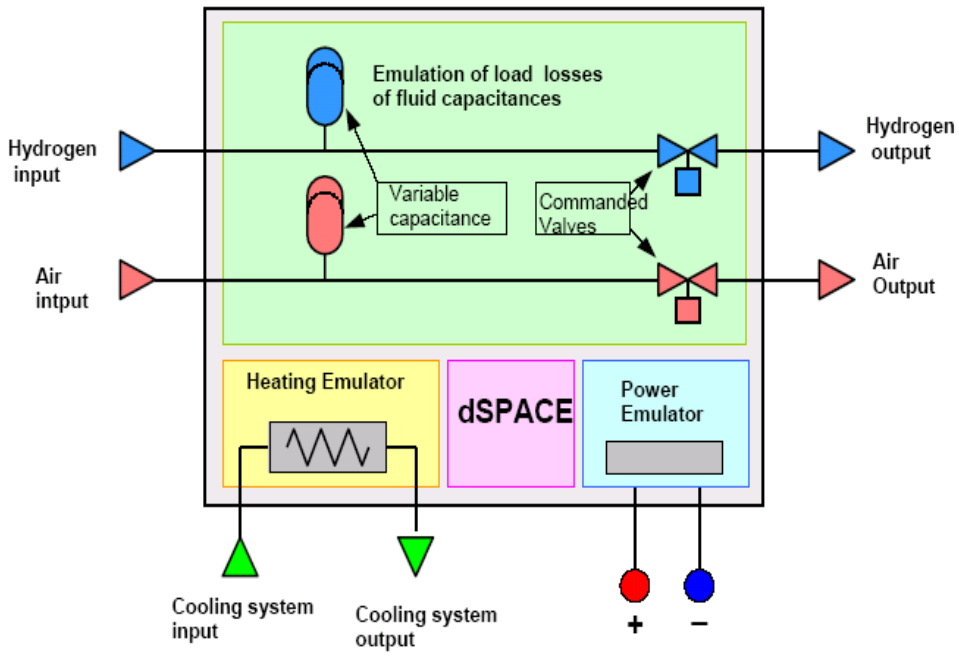

Fig.0.1. Emulator for the whole FCS.

0.2 The aims

This work wants to address the following issues:

1) *Why should a Fuel Cell Stack be emulated with a hardware system?* The question is an important issue. Actually the answer lied in the need of avoiding too dangerous and expensive use of real Fuel cells for experimentation or for pedagogical issues. Also the start-up time of actual FCS and the necessary auxiliary components (tanks, compressors, pressure regulators, etc) as well as their size and the need of suitable facilities require that an easy-to-use flexible low-cost device be developed to replace the real one. Moreover the life span of a Fuel Cell depends on the on/off cycles and therefore it is advisable to use it as least as possible. In the end the use of a real Fuel Cell Stack for experimentation of several control strategies could result in damaging of the stack itself. All these considerations lead up to the conclusion that for experimentation and testing of control strategies a hardware device that has the same external behaviour of the Fuel Cell Stack should be envisaged, so that the real Fuel Cell Stack can be used only at the last step, when all the experimentation has been carried out. Chapter 2 gives a survey of the current state of the art about FCS, after making some descriptions of the emulators used in Photo-Voltaic, from which FCS have taken inspiration.
2) *Why emulation and not only simulation?* The development of FCS for power generation is tightly connected with the Power Conditioner System (PCS), generally consisting of a DC-DC converter for adapting the FC voltage to the DC bus, as well as a bi-directional DC-DC converter connected to a storage system (ultracapacitors or batteries) or a DC-AC converter connected to a sinusoidal load.

The proper development of the PCS requires that its dynamics be considered in a real-world scenario also considering the nonlinear V-I characteristic of the FCS, which is not the case for a simulation programme developed on a PC. In this way an advanced test-bench is set-up for experimentation. Moreover, the FCs emulator can be connected to an already existing test set-up with other kind of DG (distributed Generation) units, exactly emulating the real FCs but without its need. It permits to have a real FCs practically reproduced at low cost in various parts of the world. Furthermore, an emulator can reproduce the behaviour of FCs with different characteristics or with different auxiliaries. Finally, it can also reproduce, applying the same logic, a completely different kind of source (Photovoltaic for example).

3) *What kind of hardware device should be used for emulation?* Although theoretically any DC-DC converter could be used, in general a Buck-converter is a good solution, since it avoids discontinuous conduction mode if properly designed, and is easy to control in voltage with a simple PI or other control techniques to have a higher bandwidth than that of the reference model, thus quickly minimizing the difference between the converter output voltage and the reference voltage. A boost or a buck-boost converter could be used, but their control is more complex. Whatever it may be, a key issue is that the emulator should have the portability as a desirable feature for laboratory equipment. Chapter 4 focuses on the design and construction of a Buck-converter for this purpose, dealing also with the control law to be used. A real prototype has been developed and then used for experimental validation.
4) *Do most FC emulators consider the whole FCS with its auxiliary components?* One of the key issues that must be realized is that the emulator should respond to variations of such variables as pressure of the anode and cathode, temperature, air mass rate, speed of the compressor, and so on. This means that the auxiliary systems are to be well modelled and interact with the emulator itself, so as to give a realistic response. Chapter 3 is entirely devoted to present an accurate model for the whole FCS and its implementation on a DSPACE board controlling both the emulator and the whole system. It is also shown how the voltage-current characteristic of a FCs, including its auxiliaries, is quite different from that of a simple stack.
5) *What kind of control strategy should be used in FCS?* The answer depends on the performance that is expected from the FCS. A FCS system is a multi-variable system and moreover it has many non-linearities. Few works have been developed in this domain and practically hardly any about the control of a FCS with an FC emulator. Chapter 5 presents a control of an important sub-system, the one for the air management, for regulating the excess oxygen ratio while considering the constraints imposed by the use of a centrifugal compressor. First a PI control is applied, and then a feed-forward neural control is added to improve the performance. In any case, also the PI design is

not an easy task, since it must consider even the stability issues of the centrifugal compressor, apart from the stability of the controller itself.

0.3 What is new

This thesis presents the analysis, design and experimental implementation of the emulator of the FC stack with particular attention to the air-management system. In particular:

1) all the auxiliaries of the system have been considered, each including its own control system, as in a real FCS, by implementing them in the dSPACE board;

2) the converter is a classical DC-DC buck converter with a free-wheeling diode and is designed to have a high bandwidth and to be practically always in conduction mode (discontinuous mode appears only at very low currents);

3) the voltage control is made by space-state controller, able to properly fix the closed loop poles of the system, thus ensuring the desired bandwidth of the control system;

4) it can be used in laboratory as a stand-alone low-cost system for design and experimental purposes.

The following parts of the thesis represent original achievements:

- development, construction and experimental verification of a buck-converter for emulating a PEM-FC (chapter 4);
- choice, tuning and design of the controllers used in the emulator (chapter 4);
- implementation of the model of the FCS on a DSPACE DS1004 board (section 5.2.5);
- development of the recall phase of the GMR for its application to the feed-forward control of the FCS (appendix A2)
- implementation and investigation of a novel neural control strategy for the FCS (section 5.3).

0.4 The Organization

Chapter 1 gives a brief survey of the Fuel Cell (FC) technology. After describing the fundamentals of Fuel Cells and their history, the principal types used in various domains are described with their limitations and

advantages, in particular their environmental benefits, particularly the reduced gas emissions, their efficiency, their applicability both to stationary power production and to portable devices.

Chapter 2 focuses on the necessity of using an emulator. After presenting a state of the art, also in comparison with Photo-Voltaic systems, which have inspired emulators of FCS, the chapter deals with the characteristics that an emulator should possess, that is high bandwidth and capability of having the same dynamical behaviour of the FC.

Chapter 3 presents the mathematical model of the whole FCS. Particularly it presents the model of the following sub-systems: the compressor, the cooling system, the humidifier, the supply and return manifold, the cathode, the anode.

Chapter 4 deals with the development and construction of the Buck-converter as well as its experimentation. After shortly describing the various types of possible candidates for emulation, the procedure to follow to design a buck-converter operating in continuous current mode is presented, as well as the criteria to consider for filter design. Then a state-variable feedback is described for controlling in voltage the buck-converter and the performance improvement with respect to a normal PI is shown as well as the stability analysis. In the end the prototype which has been constructed is verified experimentally both in its dynamical and steady state performance.

Chapter 5 presents a brief state of the art for the control of a FCS and then focuses on the control of the air management system. After detecting the input-output variables of interest and the corresponding state-space equations derived from the model of the FCS, a linearization is made and then used for developing a conventional PI controller. After assessing experimentally the performance of this control a neural feed-forward control is realised by using the GMR (General Mapping Regression) which is a neural network capable of naturally implementing the inverse of any relationship, in particular that of the nonlinear model of the FCS. Also in this case the experimental verification is made and the improvement with respect of the simple PI controller is shown.

Chapter 1

A Basic Overview of Fuel Cell Technology

Today, the hydrogen and the technologies that use this kind of fuel are considered very interesting in the industrial world and in the scientific society. This is driven by the requirement to reduce pollution levels and lead to a more sustainable environmental policy. In general the most important application of the hydrogen in the energy system is as reactant in the fuel cell. In this system, the chemical energy is converted into electrical energy by the reaction of the hydrogen with the oxygen. This conversion does not involve though the heat conversion as in traditional generators and is used in several applications, like in vehicular transportation. At present the most important motor industries are studying and developing prototypes of car with hydrogen tanks to feed them. As a matter of fact, the need of new technologies for the vehicular transportation derives from the problems of the actual fuels: their emissions of polluted substances and their low efficiency.

1.1 Fuel Cell Basics

The fuel cell is a system that takes the hydrogen as a fuel in the input and produces electricity as output (see Figure 1.1) and it can operate virtually continuously as long as the necessary flows are maintained [1]. The difference between fuel cell and batteries is the following: batteries are considered a energy "storage" device as they store their fuel internally. Thus, when the fuel of the battery is spent, the battery must be disposed of or recharged. In contrast, the fuel cells are a power "generating" device as they draw fuel from an external source and generate electricity as long as fuel is supplied. On the other hand combustion engines use the chemical energy stored in a tank and transform it into mechanical or electrical energy, thus working in a different way from fuel cells. The combustion of hydrogen is the following:

$$H_2 + \frac{1}{2}O_2 \leftrightarrow H_2O \qquad 1.1$$

At molecular scale, during the reaction there are collisions between the oxygen and hydrogen molecules and these are oxidized, producing water and heat. On atomic scale, the hydrogen-hydrogen bonds and oxygen–oxygen bonds are broken, forming hydrogen-oxygen bonds. This process is made by the transfer of electrons between the molecules. The final energy state is lower than the initial energy state of hydrogen and oxygen gases and this difference is converted as heat. Although the moving of electrons from a state of

energy to another produces a new electronic reconfiguration, the electrical energy cannot be directly generated because this reconfiguration occurs in a time interval very short (picoseconds).

Thus, to produce electrical energy, it is necessary to convert the heat generated into mechanical energy, but this process is complex and inefficient. The chemical reaction can directly produce electricity, if something is used to drive the electrons, when they move from the high-energy reactant state to the low-energy product state. The fuel cell is a solution of this problem, because the hydrogen and oxygen reactants are spatially separate and so the electron transfer occurs over a great length scale. Then, the electrons can be driven as an electrical current, when they move from the fuel side to the oxidant side.

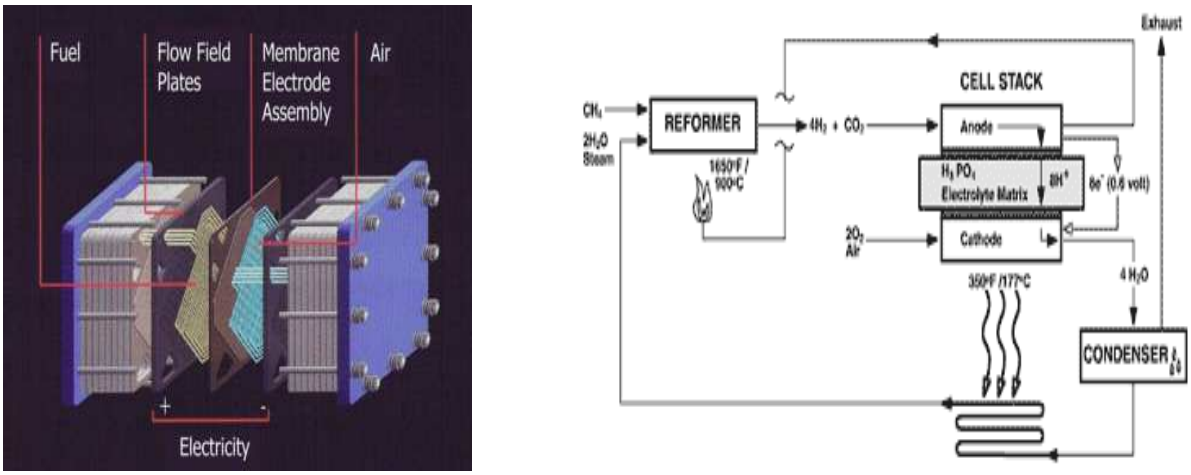

Fig. 1.1.Fuel Cell System.

1.1.1 A brief history of fuel cell

The discovery of the fuel cell operating principle is assigned to the English lawyer and physicist Sir William Grove (1811-1896). He made the first prototype of a fuel cell by using two electrodes of platinum, where each one is blocked into a glass cylinder that contained a fuel (Figure 1.2a). This was needed to allow the anodic and cathode reactions to take place and the hydrogen was used for the anode and the oxygen for the cathode. Both electrodes were dipped into a diluted phosphoric acid to make an electrical contact by an electrolyte. The output voltage was very small and Sir Grove increased it by series connecting several cells. The discovery of the English physicist remained only a scientific curiosity for a century. In 1937, another Englishman, Francis T. Bacon, started working on the fuel cell and he developed a 6 kW fuel cell at the end of 1950s. However, General Electric developed the first application of fuel cell for the Gemini space

program and it used the first polymer membrane. Pratt & Whitney company used this fuel cell model in the Apollo space program to produce electricity for life support and communications (Figure 1.3b).

Although the fuel cells have continued to be successful in space applications, they have not been used in earth applications until the 1990s. In 1989, the Perry Energy Systems developed a polymer electrolyte membrane (PEM) fuel cell to power a submarine and in 1993, the Ballard Power Systems developed a fuel cell to power buses. In the same year, the Energy Partners developed a fuel cell to power a passenger car and from then on car companies, supported by the USA Department of Energy, worked a lot on this activity and by the end of century all car industries built a fuel cell to power a vehicle. At the start of the XXI century a new energy revolution has started and there is an ever increasing interest of the scientific community in its development and growth.

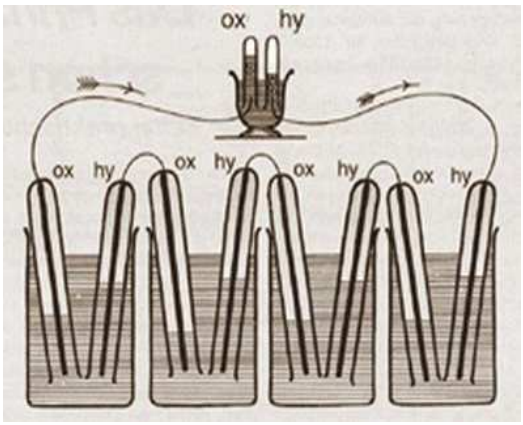

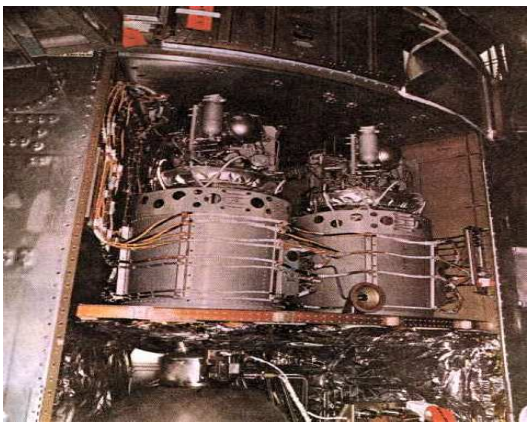

(a) **(b)**

Fig. 1.2. Fuel cell prototype developed by Sir Grove (a); **Fuel cells used in the APOLLO shuttle Program (b).**

1.1.2 How a fuel cell works

The fuel cell operating principle can be considered as the inverse process of the electrolysis of water. In this chemical reaction, the molecules of H_2O are decomposed into the molecules of hydrogen and oxygen by an extern source of energy like a continuous current. Basically a fuel cell is made up of an electrolyte between two electrodes, from which it is possible to extract current through chemical reactions. The electrolyte must have specific properties to allow the positive ions (protons) to be transferred against the contrasting action of the orbital motion of the electrons of the electrolyte. To understand how the reaction between the hydrogen and the oxygen can produce an electrical current, it is necessary to analyze the chemical reactions in the electrodes and for this purpose the fuel cell with an acid electrolyte will be used; proposed by the physicist Grove.

The anode chemical reaction is the following:

$$2H_2 \Rightarrow 4H^+ + 4e^- \qquad 1.2$$

This equation shows that two molecules of hydrogen cross the positive electrode (anode) and produce 4 positive ions H^+ and 4 electrons e^- with the help of a catalyst, which is a special material that facilities the reaction of oxygen and hydrogen. It is usually made of platinum mono-particles very thinly coated onto carbon paper or cloth. The catalyst is rough and porous so that the maximum surface area of the platinum can be exposed to the hydrogen or oxygen. Figure 1.3b shows that the protons by the electrolyte reach the other electrode, called cathode, while the free electrons feed an electrical load connected with an external circuit. In the cathode, the positive ions H^+ and the electrons e^- react with the oxygen to produce water and heat:

$$O_2 + 4H^+ + 4e^- \Rightarrow 2H_2O \qquad 1.3$$

The mass conservation principle of Lavoisier is satisfied by the following equation, which represents the global reaction of the fuel cell:

$$O_2 + 2H_2 \Rightarrow 2H_2O + heat \qquad 1.4$$

Then, two molecules of hydrogen are needed for each molecule of oxygen. In the output of a single fuel cell there is a voltage difference between 0 and 1 Volt, when it is not connected to a load. In order to have a greater value of voltage for supplying a load, it is necessary to connect in series several fuel cells, thus forming a stack.

The voltage difference value of the fuel cell depends on several factors [2]:

- Working condition of fuel cell (temperature and humidity).
- Electrolyte, in fact there are different kind of acid and polymeric electrolyte with several values of concentration of positive ions H^+ (see Chapter 3).
- Power of the load that is linked to the fuel cell

The current density supplied from a fuel cell is very little (0,5 A/cm^2 [3]), because the contact area between the gas , the electrolyte and the electrode is little and moreover the distance between the electrodes produce a big resistance of the circuit (100-150 mΩ/ cm^2 [3]). The contact area and the distance between the electrodes are reduced by using flat electrodes with a thin layer of electrolyte (figure 1.3b).

The structure of the electrode is porous to increase the contact area of the reactants and the speed of the reaction. The fuel cell, like every type of electronic device, has an internal electrical resistance that depends on the power loss caused from the exothermic chemical reaction. This power occurs in the form of heat.

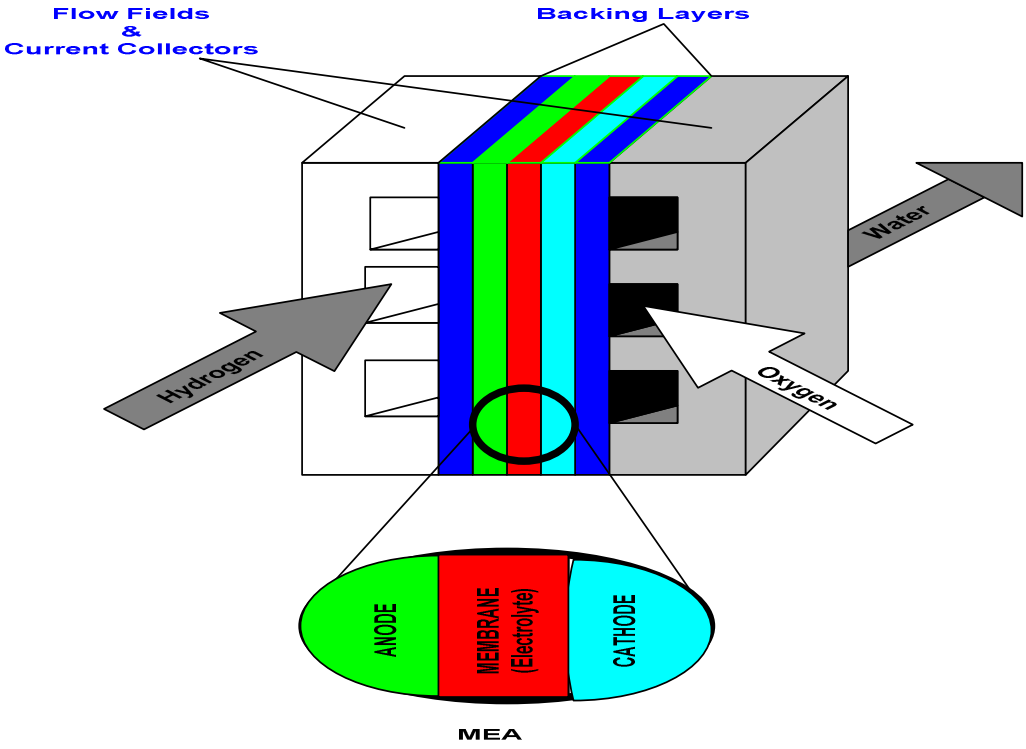

(a)

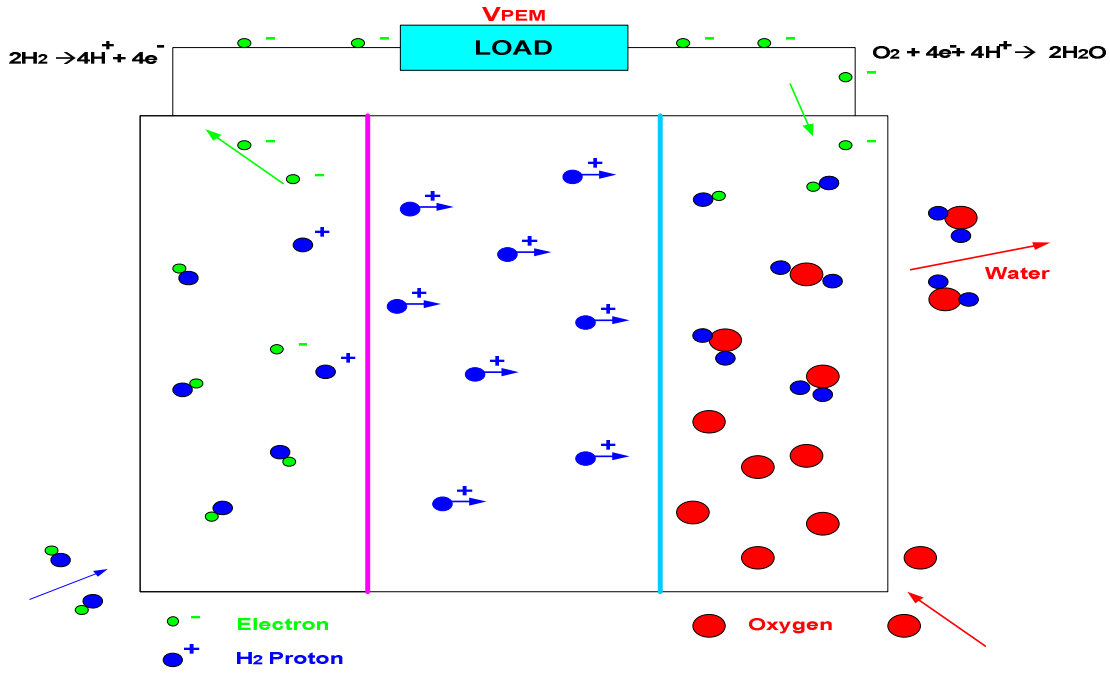

(b)

Fig. 1.3: (a) Fuel Cell Structure; (b)Fuel cell reaction.

1.2 Types of Fuel Cell

A variety of fuel cells are being developed in different stages. The choice of electrolyte dictates the operating temperature range of the fuel cell. The operating temperature and useful life of a fuel cell impose the physicochemical and thermomechanical properties of materials used in the cell components (electrodes, electrolyte, interconnect, current collector, etc.).

There are six major types of fuel cells, differentiated from one another by their electrolyte:

- Phosphoric acid fuel cell (PAFC)
- Polymer electrolyte membrane (PEMFC)
- Alkaline fuel cell (AFC)
- Molten carbonate fuel cell (MCFC)
- Solid-oxide fuel cell (SOFC)
- Direct methanol fuel cell (DMFC)

Although the six fuel cell types work with the same electrochemical principle, they all operate at different temperature regimes, with different materials and often with different fuel tolerance and performance characteristics, as shown in Table I.

1.2.1 Polymer electrolyte membrane (PEMFC)

The polymer exchange membrane fuel cell (PEMFC) is one of the most promising fuel cell technologies. This type of fuel cell will probably end up powering cars, buses and maybe even houses. The PEMFC uses one of the simplest reactions of any fuel cell. PEMFC are used in a wide variety of applications like in automotive, portable applications and in the situation where pure hydrogen can be used as a fuel. They offer the following advantages:

- High energy density 300-1000 mW/cm^3;
- The Solid electrolyte provides excellent resistance to gas crossover [2];
- No need of using an external thermal insulation because the range of operating temperature is between 30°C- 100°C;
- The low operating temperature allows rapid start-up;
- High current densities of over 2 A/ cm^2.

The low and narrow operating temperature range makes thermal management difficult, especially at very high current densities, and makes it difficult to use the rejected heat for cogeneration. In addition, PEMFC are quite sensitive to poisoning by trace levels of contaminants including CO, sulfur species and ammonia.

Nowadays the PEM fuel cells draw an increasing attention from the industrial world, because they can be produced in bulk and can be used in vehicular application. The estimation of the cost of this type of fuel cell is 100 €/kW, but if installation costs are included the price can rise up to 8000 €/kW.

The maximum temperature that allows an efficient electrical conduction of the electrolytic membrane is 100 °C. This low operating temperature and the use of particular electrodes and catalysts make the reaction sufficiently speed to ensure the correct working of the fuel cell. The first type of catalyst used in the PEM has been the platinum, but it is very expensive and nowadays, its quantity in PEM is very small, so its cost represents only a little percentage of the whole cost of the fuel cell.

The electrolyte polymeric membrane is an electronic insulator but is a good conductor of hydrogen ions. This membrane is made up of a mixture of a fluorine carbide and a sulfuric acid of the $H^+SO_3^-$ group and its moisturizing produces H^+ ions.

The several properties of the membrane depend on the type of process used to make it. The thickness of the membrane is between 50 and 175 µm and is made up of two overlapping papers of the material. The membrane is between the two electrodes, the anode and the cathode, that are constituted by good electrical conductor, the porous graphite. The surfaces of the electrodes are covered with a little quantity of platinum, to increase the speed reaction (catalyst). The three components before described, the anode , the cathode and the electrolyte, are joined together to do a single membrane, MEA (Membrane Electrode Assembly), shown in Figure 1.5, has a thickness of 1 mm.

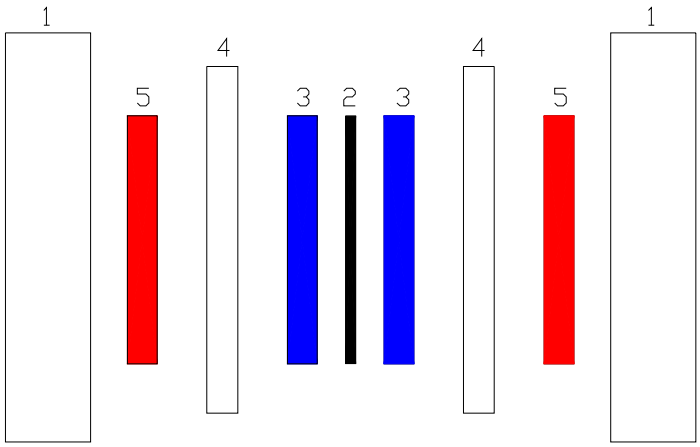

Fig. 1.4. Structure of the membrane MEA.

The elements shown in Figure 1.4 are the following and each part will be explained in the next paragraphs:

1 → bipolar dishes;

2 → proton exchange membrane;

3 → electrodes + membrane=MEA;

4 → gasket system;

5 → gas diffusers.

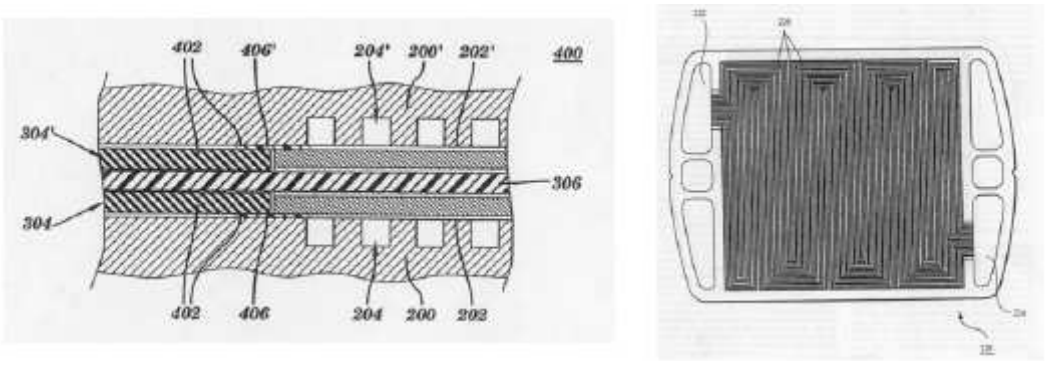

Fig.1.5. PEMFC Schematic([3]).

1.2.1.1 The bipolar dish.

The bipolar dish functions as an electrical collector between two neighbouring cells of a stack and a lot of manufactures realize the diffusion pipelines of the reactants into the dish, so as to integrate the several working phases.

The principal characteristics of a bipolar dish are the following:

- High electrical conductivity (>200 $\frac{S}{cm}$);
- High thermal conductivity (>50 $\frac{W}{m \cdot °C}$);
- Cheapness of the raw material and of the working process;
- Mechanical resistance;

- Resistance to the oxidant agents and to the corrosion;
- Impermeability to the reactants.

Either, the graphite or its polymeric compound, or iron metal alloys, or titanium alloys are the principal materials used to make the dishes. Each type of material has different advantages and disadvantages, but the carbon compounds are mostly used, because it is possible to obtain several different properties by changing of the fiber and the resin.

The dishes are made by using moulds and although this process requires a initial more expensive investment, it allows then to be produced on a large scale with a price of about 10 $/Kg or about 2 $/piece.

Some manufacturers, as “Plug Power” or “De Nora”, prefer metallic bipolar dishes, because of the cheapness and simplicity of its manufacturing.

Also, there is the possibility to make the dishes by a combining of several materials, like porous graphite, steel, or polycarbonate, which are joined together by using sealing conductors.

Cell	Charge carrier	Operating temperature	Catalyst	Electrolyte	Cell components	Fuel compatibility
Alkaline (AFC)	OH^-	60°-220°C	Platinum	Liquid KOH	Stainless based	H_2
Polymer membrane (PEMFC)	H^+	30°-100°C	Platinum	Polymer membrane	Carbon based	H_2 methanol
Direct methanol (DMFC)	H^+	20°-90°C	Platinum	Polymer membrane	Carbon based	methanol
Phosphoric acid (PAFC)	H^+	220°C	Platinum	Liquid H_3PO_4	Carbon based	H_2
Molten carbonate (MCFC)	$(C0_3)^{2-}$	650°C	Nickel	Molten carbonate	Stainless based	H_2 CH_4
Solid oxide	O^{2-}	600-1000°C	Perovskite (ceramic)	Ceramic	Ceramic based	H_2 CH_4 CO

TABLE I. Characteristics of different type of Fuel Cell.

1.2.1.2 The proton exchange membrane.

The proton exchange membrane (PEM) represents the electrolyte of the fuel cell. It allows the hydrogen ions to be carried from the anode to the cathode, but it stops the diffusion of the reactants. The characteristics of the proton exchange membrane are the following:

- High proton conductivity;
- High mechanical robustness;
- Stability of its performance during the time (> 10000 hours);
- High number of electrical charge carriers (> 3 $\frac{A}{cm^2}$);
- Cheapness of the raw material and of the manufacturing;

Nowadays, the PEM with polymeric membrane with the acid (per) fluorinated sulfuric is used, because it offers a good electrical charge transport.

The Nafion 117, produced by Du Pont, is mostly used and the Gore recently developed a membrane, called *Select*, that offers the same performances as the Nafion. The disadvantages of this type of membrane, called *fully fluorinated*, are its high price, its fast deterioration and the necessity to humidify it to allow the ionic conduction. The Ballard company is developing a new technology to produce a partial fluorinated membrane, which has a lower cost than the classic one. Other companies, like the Hoechst or the Foster-Miller, are developing new polymers made up of “Hydrocarbon-based”. The most important chemical industries that work in the fuel cell area, like the PRIMEA of the Gore company and the ELAT of the E-Tek company, are focussing on the production of a electrochemical package, called MEA.

1.2.1.3 Electrodes with porous diffusion

The diffuser electrode layer is physically inside the MEA structure and it is made up of a support of carbon paper or carbon cloth, which is impregnated of poly-tetrafluoroethylene (PTFE) and carbon. The PTFE has a double function, because it mixes the structure and gives hydrophobic characteristics to the electrode. The percentage weight of the PTFE ranges from 10% and 40% and, when the weight of the PTFE increases, the porosity of the electrode and the diffusion of the gaseous reactants of the catalyst decrease. The size of the pores is about 0.35 μm. The average life of a porous diffusion electrode is about 50-60000 hours.

1.2.1.4 Gasket system

The whole system, described so far, must be assembled to allow the structure to be hermetic, because a great deal of applications require a pressure of the reactants of about 2-3 atm. The gasket system must resist to a big surface pressure, which is necessary to ensure a good electrical connection between the cells. An approach for sealing the cell with flat gaskets is shown in figure 1.5 (Label 402), but there are many alternatives with gasket and plates having different shapes and grooves, respectively [3].

1.2.1.5 Gas diffusers

During the operation of the fuel cell, the reactants in the gaseous state react and produce molecules of water steam, which condense in proximity of the cathode surface. Some anomalous behaviour in the concentration of the gas is present inside the diffusing layer and this problem produces a reduction of the activity coefficient of the reaction, which is a factor used in thermodynamic to account for deviation from ideal behaviour in a mixture of chemical substances [4]. These gradients of pressure or partial concentration are caused by a wrong distribution of the gases, which is produced from losses of load inside the diffuser. This phenomenon can be limited by an increase of the pressure feed of the reagents until 3-4 atm, or an optimization of the fluid dynamic of the adduction channels of the reagents. A lot of industries, as the De Nora Company, have made a stack with a pressure cathode feed of 1.5 atm and this solution offers a good performance. The diffusers must evacuate the reaction water, the humidification water and sometimes a fraction of the cooling water.

1.2.2 Direct Methanol Fuel Cell (DMFC)

The cells with direct methanol do not use the pure hydrogen as fuel, but the methanol in liquid state, which contains hydrogen. The half reactions the following:

$$ANODE: CH_3OH + H_2O \rightarrow CO_2 + 6H^+ + 6e^- \quad (1.5)$$

$$CATHODE: (3/2)O_2 + 6H^+ + 6e^- \rightarrow 3H_2O \quad (1.6)$$

$$OVERALLREACTION: CH_3OH + (3/2)O_2 \rightarrow CO_2 + 2H_2O \quad (1.7)$$

During the methanol oxidation reaction carbon monoxide (CO) is formed, which strongly adsorb onto the platinum catalyst, reducing the surface area and thus the performance of the cell. The addition of another components, such as ruthenium or gold, to the catalyst tends to ameliorate this problem because these catalysts oxidize water to yield OH radicals: $H_2O \rightarrow OH\bullet + H^+ + e^-$. The OH species from the oxidized water molecule oxidizes CO to produce CO_2 which can then be released as a gas: CO+$OH\bullet \rightarrow CO_2 + H^+ + e^-$.

The disadvantages of the DMFC fuel cell are the following:

- Careful design of the stack to avoid the outflow of the methanol;
- Low output power (30-100 $\frac{mW}{cm^2}$);
- High activation losses in the anode and in the cathode. The activation loss occurs because the chemical process initially has not begun, thus activation energy necessary insure that the reaction tends toward the formation of water and electricity [5].
- The carbon dioxide is a by product as shown in equation 1.5.

Nowadays, a lot of industries are developing DMFC fuel cells to supply portable electronic devices, as personal computer (notebook). Indeed, the IBM and the Sanyo Electric have developed a prototype of DMFC battery to feed notebooks and it is likely to be commercialized in the next few years. This prototype has a weight of 2 Kg and it offers a supply for 8 hours by using a single cartridge, containing 130 cm^3 of pure methanol. This prototype includes a lithium battery supplied by the fuel cell, and gives energy to the notebook at the same time. A single fuel cell produces an output power of about 12 watt, while a hybrid system DMFC-polymeric battery produces a power of about 72 watt.

1.2.3 Alkaline Fuel Cell (AFC)

The alkaline fuel cell represents the oldest example of fuel cell and as of today it is still used in space shuttles and in submarines. The electrolyte is composed of a chemical aqueous solution of potassium hydroxide (KOH), contained inside a solid matrix (asbestos). The reduction reaction of the oxygen and the oxidation of the hydrogen occur inside the alkaline and involve hydroxylic ions (OH^-). These, which are produced by the cathode reduction of the water, go through the electrolyte and arrive at the anode, where react with the hydrogen to produce water.

In the following the reactions that occur are shown:

cathode $1/2O_2 + H_2O + 2e^- \rightarrow 2OH^-$ 1.8

anode $H_2 + 2OH^- \rightarrow 2H_2O + 2e^-$ 1.9

total reaction $H_2 + 1/2O_2 \rightarrow H_2O$ 1.10

The first prototype with a power of 5 KW was developed in 1955 by using the discoveries of Bacon in 1932. It was made up of an anode of nickel, a cathode of oxide of nickel and an electrolyte of a watery solution of KOH. It worked at a temperature of 200 °C and at a pressure of 5 MPa. Nowadays, the AFC fuel cells work with a maximum temperature of 100°C, using a low concentration of KOH (35%- 50%), because it is not necessary to work with a high value of temperature to increase the speed of the reaction. For this reason, the AFC fuel cell belongs to the class of fuel cells with a low working temperature (70°C).

The AFC fuel cell in respect to PAFC (see section 1.2.4) shows the following advantages [2]:

- The reduction reaction of the oxygen is faster than the oxidation one of the hydrogen, because the AFC is characterized by a better kinetics;
- Flexibility to use a wide range of electro-catalyst.
- A longer life, because the materials of the fuel cells are more robust to chemical attacks coming from the electrolyte.

The sensitivity of the electrolyte to CO_2 represent a disadvantage of the AFC, because it requires the use of highly pure H_2 as a fuel. As a consequence, the use of a reformer would require a highly effective CO and CO_2 removal system.

The production of carbonates represents the worst disadvantage of the AFC fuel cell. Indeed, the air and the hydrogen must be extremely pure and moreover they must be purified from the CO_2 and the CO, because the first compound can react with the electrolyte as shown below with production of carbonates:

$$CO_2 + 2OH^- \rightarrow CO_3^{2-} + H_2O \qquad 1.11$$

The production of carbonates overloads the pores of the electrolyte and then the performance of the fuel cell decreases. The carbon dioxide is removed from the air and the hydrogen by a system called "iron-sponge". Despite this disadvantage, the AFC fuel cell is characterized by a high efficiency.

This type of fuel cell was the first prototype developed, but it became obsolete very soon, because of its high sensitivity to CO_2.

1.2.4 Phosphoric Acid Fuel Cell (PAFC)

The phosphoric acid fuel cell has been the first fuel cell manufactured and used on a large scale. A lot of PAFC fuel cells with a nominal power of 200 kW, produced by Japanese companies, have been installed in USA and in Europe. This fuel cell uses extremely porous electrodes and catalysts with a high working temperature, to obtain an acceptable chemical speed reaction. The problem of refueling hydrogen is solved by using natural gases, as methanol and carbon dioxide, but the equipment to extract the hydrogen is very complex, expensive and cumbersome. Despite this problem, the PAFC fuel cell is extremely safe and few actions are enough for ordinary maintenance.

This fuel cell uses an electrolyte of phosphoric acid H_3PO_4, which is contained in a gelatinous matrix and is also place between two extremely porous electrodes.

The AFC fuel cell shows the following advantages [2]:

- PAFCs are much less sensitive to CO than PEFCs and AFCs: PAFCs tolerate about one percent of CO as a diluent;
- The operating temperature is still low enough to allow the use of common construction material;
- The waste heat from PAFC can be used in most commercial and industrial cogeneration applications.

The principal disadvantage of the PAFC fuel cell depends on the working temperature, because if its value is lower than 42°C then, the phosphoric acid solidifies.

The best working temperature range is between 180 °C and 210 °C, but if the temperature is greater than 210°C then the acid undergoes some alteration and it becomes unusable. The gelatinous matrix contains the acid, separates the electrodes, attenuates the mechanic vibrations and minimizes the gas leakage. Some quantity of electrolyte goes out from the fuel cell and evaporates during normal operation of the PAFC, which results in the need to supply it with the electrolyte.

The catalyst of the PAFC fuel cell is made up of the platinum and it produces carbon monoxide in the cathode and sulphuric acid in the anode. This acid is poisonous and corrosive and its quantity must be lower than 50 ppm, to make the fuel cell have a good performance.

1.2.5 Solid-Oxide Fuel Cell (SOFC)

The working temperature range of a solid oxide fuel cell is between 600 °C and 1000 °C and then it does not need to use expensive catalyst to reach a high reaction speed and also the natural gas can be used directly (because at a high value temperature, the hydrogen is produced in a natural way). Although the simplicity is the most important advantage of this fuel cell, it is very difficult to produce the ceramic materials used to make it and therefore, its manufacturing cost is very expensive. The SOFC fuel cell is manufactured in plate form and in tubular form: the cathode, the electrolyte and the anode are placed on the internal surface of the ceramic pipe. The gas crosses the internal side of the pipe, while the oxygen of the air crosses the external side.

The SOFC fuel cell is used to produce decentralized energy with power of about 100 kW. It is employed in stationary and mobile applications. The stationary plants are designed for the residential and the industrial area. The high temperature heat produced by the SOFC can be used in several industrial applications. For example, in the next future will be produced SOFC fuel cells for big electrical plants, where the heat produced can be utilized from turbines to generate electrical energy. These plants can reach an efficiency of about 70%.

In mobile applications, the SOFC is used to replace the traditional batteries of ground vehicles. This depends on the necessity to have more electrical energy for supplying the several devices of the car, even when the motor is turned off. In this application the fuel is the petrol, which, before entering into the fuel cell, is processed by a reforming and desulphurization treatment.

The SOFC fuel cell shows the following advantages [2]:

- It is the fuel cell with the longest continuous development period, starting in the late 1950s;
- The electrolyte is solid, then the cell can be cast into various shapes, such as tubular, planar or monolithic and also, it avoids electrolyte movement or flooding in the electrodes;
- The kinetics of the cell are relatively fast, and CO is a directly useable fuel;
- There is no requirement for CO_2 at the cathode;
- The materials used in SOFC are modest in cost.

The high temperature of the SOFC has its drawbacks:

- There are thermal expansion mismatches among materials;
- The high operating temperature places severe constrains on material selection and results in difficult fabrication processes;
- Corrosion of metal stack components.

These factors limit stack-level power density, thermal cycling and stack life.

1.2.6 Molten carbonate fuel cell (MCFC)

The principal characteristic of the fused carbonate fuel cell, is the necessity to supply it with combustion air with a specific quantity of carbon dioxide. The high working temperature allows the nickel to be used as a very cheap catalyst and as an electrode. In this type of fuel cell, like the SOFC, the fuel is the natural gas and the electrolyte is made up of a fusion of alkaline carbonates $(Li_2CO_{3,}K_2CO_3)$. The MCFC fuel cells are developed for fixed applications and because of their high working temperature (650 °C), they are used in industrial plants where a high temperature is necessary. Classic MCFC plants produce a power of about 300 kW but it is possible to obtain a greater value of about 10 MW. Moreover, MCFC fuel cells are used to produce motors for ships.

The relatively high operating temperature of the MCFC (650°C)results in several benefits: no expensive electro-catalyst, are needed as the nickel electrodes provide sufficient activity, and both CO and certain hydrocarbons are fuels for the MCFC. In addition, the high temperature waste heat allows the use of a bottoming cycle to further boost the system efficiency.

The main difficult for MCFC developers depends on the very corrosive and mobile electrolyte, which requires use of a nickel and high-grade stainless steel as the cell hardware. The higher temperatures promote material problems, impacting mechanical stability and stack life.

1.2.7 Others Type of Fuel Cell

Fuel cell with flow of blood

The aim of the project *BIO-MEDNANO* is to develop bio-catalytic fuel cells, which use the corporal fluids as fuel and the enzymes to convert the chemical energy in to electricity. These fuel cells can be used to supply several types of medical devices, as the cardiac stimulator, the insulin pump, joint prosthesis, robot for microsurgery and bio-sensor systems. In the next future, these fuel cell will have small size and will be installed under the skin to feed the medical devices. The use of these fuel cells will entail a better performance better than the traditional supply sources. Indeed, for example, the cardiac stimulator is supplied by a lithium battery, which is reactive and then, the process of miniaturization is complex and expensive [7].

1.3 Fuel Cell Advantages

1.3.1 Environmental benefits

Worldwide demand for energy is growing at an alarming rate. The European "World Energy Technology and Climate Policy Outlook" (METO) predicts an average growth rate of 1.8% per annum for the period 2000-2030 for primary energy worldwide. The increased demand is being met largely by reserves of fossil fuel that emit both greenhouse gasses and other pollutants. Those reserves are diminishing and they will become increasingly expensive. Currently, the level of CO_2 emissions for developing nations is 20% of that for the major industrial nations. As developing nations industrialised, this will increase substantially. By 2030, CO_2 emissions from developing could account for more than half the world CO_2 emissions [8].

Fuel cells represent a solution to this critical problem, since they do not produce the same air pollution emissions generated by burning gasoline as in cars or burning coal and other fossil fuels as in power plants. With fuel cells there is no combustion, so fewer gases are released into the environment. For example, almost no sulphur oxides (SO x) or nitrogen oxides (NO x) are emitted by fuel cells and therefore emissions do not imply any problem. The greenhouse gas carbon dioxide (CO_2) is a by product, but since noxious air

emissions are so low from the fuel cell system, certifications and permissions are seldom needed to install commercial fuel cells. Today 96% of hydrogen is generated from fossil fuel sources: 48% from natural gas, 30% from oil and 18% from coal [6]. in the next future, fuel cells could use the hydrogen produced by electrolysis powered by electricity generated from renewable sources and then the environmental benefits would be even greater (Figure 1.7).

Based on measured data, a fuel cell power plant may create less than one ounce (1 ounce=28,35 grams) of pollution per 1000 kilowatt-hours of electricity produced, compared to the 25 pounds (1 pound=453.59237 grams) of pollutants for conventional combustion generating systems.

In transportation, the fuel cells used as auxiliary power units (APUs) to power air conditioners accessories in over the road trucks could reduce emissions by up down to 45% from long haul vehicles. For example, according to DOE (Department of Energy of USA), the fuel cell APUs in class 8 trucks can save 670 million gallons of diesel fuel per year and 6.64 million tons of CO_2 per year [8].

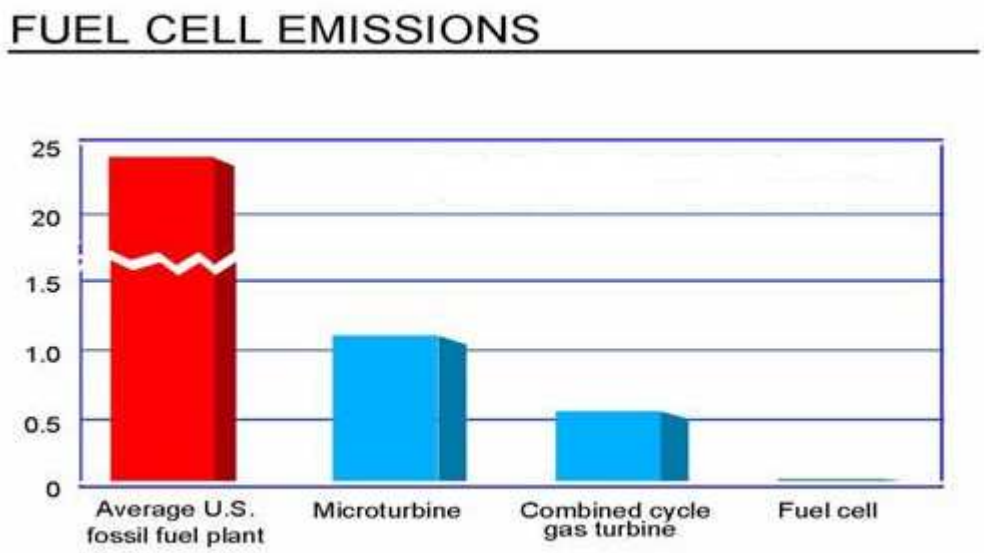

Fig. 1.6. Pounds of emissions per 1000kWh NOx, CO, SOx, Hydrocarbon, Particulates.

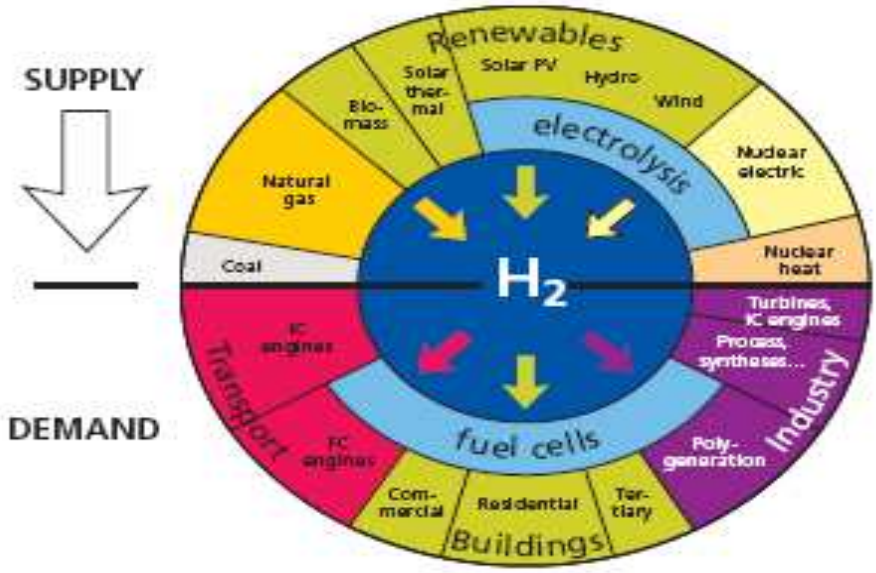

Fig. 1.7. Hydrogen. Primary energy sources, energy converters and applications.

1.3.2 High efficiency

Fuel cells are fundamentally more efficient than combustion systems because they produce energy electrochemically and do not to burn fuel. In fact, the efficiency $\eta_{FC} = \Delta G_o / \Delta H_o$ (ΔG_o = Giggs Energy and ΔH_o = Enthalpy) of a fuel cell can exceed the Carnot limit because the electrochemical process of the fuel cell does not involve conversion of thermal to mechanical energy. Moreover a fuel cell is near the point of use, its waste heat can be captured for beneficial purposes (cogeneration). In large-scale building, e.g., systems, these fuel cells cogeneration systems can reduce energy service cost by 20% to 40% compared to conventional energy service. Today, power generation systems achieve 40% to 50% fuel to electricity efficiency by utilizing hydrocarbon fuels. If fuel cells are fueled by pure hydrogen, they can provide more than 50% efficiency and even more efficient systems are under development. If a fuel cell is used in combination with a turbine, the electrical efficiency can exceed 60 % and, when the waste heat is used to use for heating and cooling, the fuel utilization can exceed 85%. Fuel cell passenger vehicles are three times as efficient as internal combustion engines, which now operate at 10 to 16 percent efficiency (Figure 1.8).

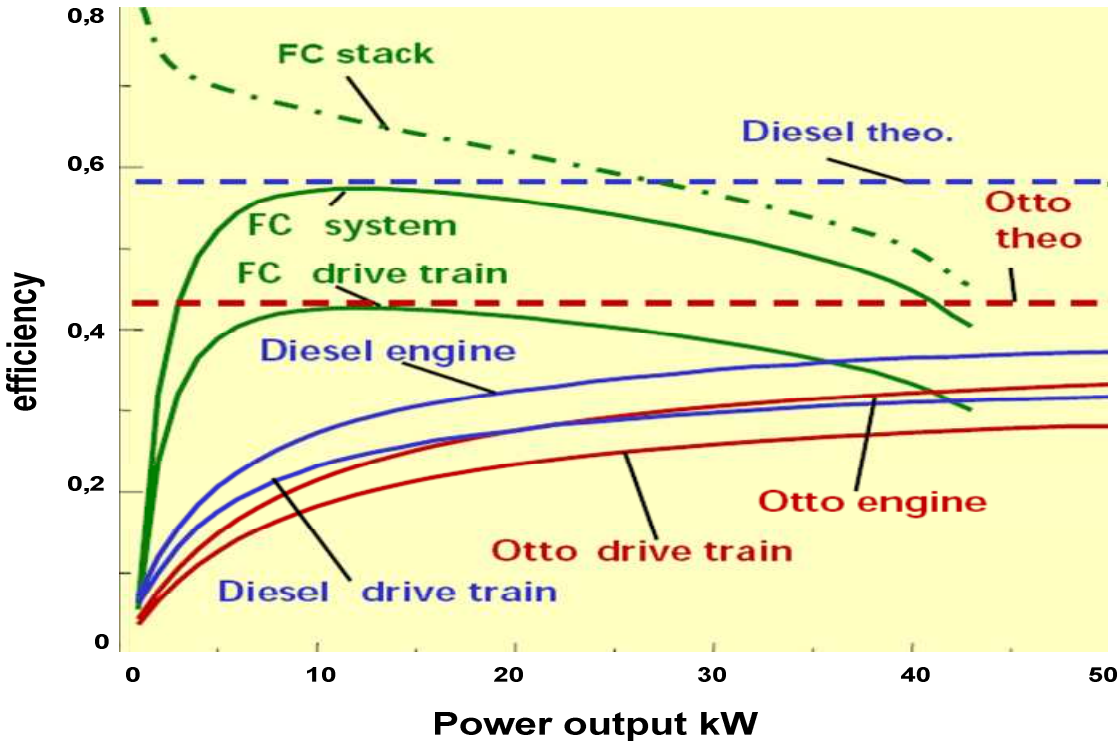

Fig. 1.8. Fuel cell efficiency vs internal combustion engines efficiency.

Neverthless, the results shown in Figure 1.8 are true if the energy needed to produce the hydrogen is considered negligible. For example, if the hydrogen is produced by the electrolyse process of water and if this process is supplied by the electrical distribution network, then the efficiency of the electolyse is equal to 75% and the maximal efficiency of the process to stock and to distribute the hydrogen is equal to 90% (the efficency of the manufacturing system is considered negligible). Therefore, the efficency of an electrical vehicle fuels by a cell of hydrogen is equal to 25%, if it is compared to the diesel engine. If the hydrogen is produced by a natural process, then the total efficency is equal to 28% [9].

1.3.3 Security

Fuel cells have a distinct advantage over other clean generators such as wind turbines and photovoltaics in that they can produce continuous power as long as they are supplied with a constant supply of hydrogen. The ability to produce continuous power makes fuel cell well suited for supporting critical loads for security applications.

Hydrogen can be produced from domestic sources, eliminating the need to import foreign oil, which would have an impact on national security. Passenger vehicles alone consume 6 million barrels of oil every single day, equivalent to 85 percent of oil imports. If just 20 percent of cars used fuel cells, the oil imports would be cut by 1.5 million barrels every day.

Since fuel cells do not have to be connected to the electric grid, they allow the country do without high voltage power generation units, which are sensitive targets for terrorist's attacks.

1.3.4 High Quality Power

The National Power Laboratory in USA estimates that a typical computer location experiences 289 power disturbances a year that are outside the voltage limits of the computer equipment. U.S. businesses lose $29 billion annually from computer failures due to power outages. The power output of fuel cell is clean and of high quality, because it is free from voltage disturbances like sags, spikes or transients. Thus, fuel cells may help prevent not only losses of power, but also losses of dollars. Fuel cells can be configured to provide grid-indipendent power or they can use the grid as a backup system.

1.3.5 Fuel Flexibility

A lot of fuel cells run on hydrogen and will continue to generate power as long as the fuel cell is supplied. For a fuel cell is not important where the hydrogen comes from, so a fuel cell that including a fuel reformer can generate hydrogen from several domestic resources including fossil fuels, natural gas and coal, alcohol fuels, (such as methanol or ethanol), from hydrogen compounds containing no carbon, such as ammonia or bore-hydride, or from biomass, methane, landfill gas[1] or anaerobic digester gas. In fact, a reformer is a technology that removes the hydrogen from these fuels and uses it to power the fuel cell. Therefore, a reformer can eliminate the hydrogen storage and distribution problems, which depend on the difficulty to

[1] Landfill gas is produced by organic waste decomposing under anaerobic conditions in a landfill

store the fuel at extremely low temperatures and high pressures [10]. Hydrogen can also be produced from electricity from conventional, nuclear or renewable sources such as solar or wind (figure 1.7).

1.3.6 Modularity

The modular nature of fuel cells allows more power to be obtained simply by adding more cells. The mass production of fuel cells may be significantly less expensive than traditional power plants. Instead of building big power plants, which must be designed well in advance, it may be cost-effective to gradually increase generation capacity by adding smaller fuel cells to the grid.

1.3.7 Simplicity and promise of low cost

Fuel cells are extremely simple. They are made in layers of repetitive components and they have no moving parts. For this reason, they can be mass produced with a cost comparable to that of existing energy conversion technologies or even lower. Since a fuel cell does not have any moving part, it may be expected to have a long life. Current technology may reach for fuel cells a lifetime acceptable for automotive applications (3000-5000 hours), but the durability must be improved by an order of magnitude for use in stationary power generator, where the requirement is greater than 40000-80000 hours.

1.3.8 Quietness

Fuel cells are very quiet, which may make them attractive for a variety of applications, such as portable power, backup power and military applications.

1.3.9 Lightweight and Battery alternative

Fuel cells may be made in a variety of sizes from microwatts to megawatts, which allow then to be used in a variety of applications, such as laptops, cellular phones, powering electronic, etc.

Fuel cells have a much longer operating life than batteries in a package of lighter or equal weight per unit of power output. A fuel cell does not require '*recharging*' and a liquid, solid or gaseous tank can be replaced easily. Fuel cells offer a much higher power density, packing more power in a smaller space. Many companies are working with the army to use the fuel cells in the equipment of soldiers, which includes several electronic devices, such as computers, personal radios, displays and thermal imaging, increase the effectiveness, lethality and survivability. Fuel cells can operate as much as 10 times longer than the conventional batteries used to power hand-held battlefield computer and are much lighter, they have no heat signature and are more cost-effective.

1.4 Fuel Cell Disadvantages

Fuel cells are not the perfect solution to the energy needs of the world. There are several problems that need solving before the widespread use of fuel cells occurs:

- *Too expensive*. The biggest obstacle of fuel cells is their cost. Although some fuel cell systems are in use today, very few are currently cost-effective. For stationary fuel cells, typical capital cost to install the system is greater than $ 5000/kW, while the target capital cost used by most energy generation developers is $1000-$1500 [11].
- *Early technology risks.* Fuel cells are still in a early stage of development and even the few commercially available models have limited operating experience. This new technology requires risk-taking in order to expose more consumers to the benefits of fuel cells.
- *Reliability and Durability.* Fuel cells must prove their adaptability for a variety of applications in order to be widely accepted as a clean distributed generator. Also, some fuel cell system components, like the cell stack which can require a costly replacement every one to five years depending on the model, must be developed to have a longer life span or to be easily and cheaply replaced.

1.5 Fuel Cell Applications

All fuel cells operate on the principle of combining oxygen and hydrogen to generate electricity, heat and water but they have many potential shapes and sizes for several applications (some of which are shown in Figure 1.9). The three main applications of fuel cells are: transportation, portable uses and stationary installations.

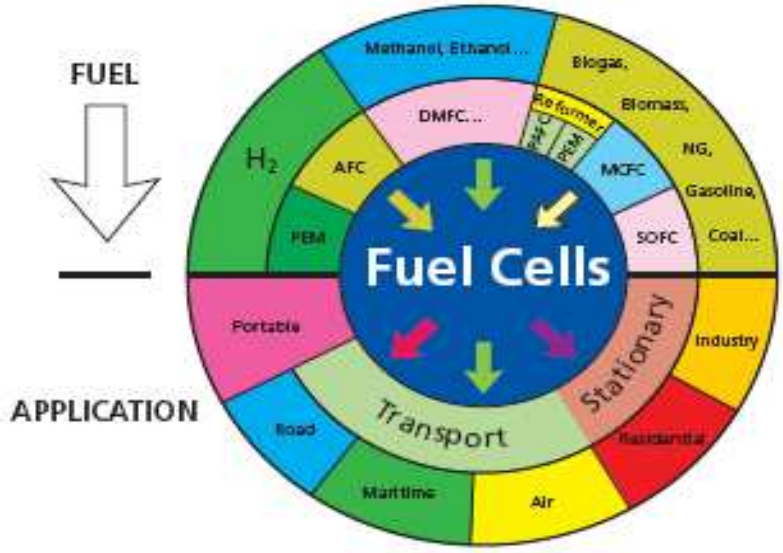

Fig. 1.9. Fuel cell technologies, possible fuel cells and applications.

1.5.1 Automotive Applications

- *Automobiles.* Many vehicle manufactures (DaimlerChryler, Ford, Nissan, Mazda, Hyunday, Fiat, Volkswagen) are researching and developing transportation fuel cells for future use in cars, trucks and buses. These fuel cells will need to be relatively small, light and durable. Fuel cells vehicles are much more efficient than conventionally powered vehicles because the electrochemical reaction is much more efficient than the burning process in a conventional internal-combustion engine. They also have advantages over battery-electric vehicles, because they do not need to be slowly recharged, but can be refueled very quickly at a filling station [13], [14], [15].

- *Scooters.* Although their small size, many scooters are a cause of pollution. Gas powered scooters, especially those with two stroke engines, produce emissions at a rate disproportionate to their small size. Fuel cells scooters running on hydrogen will eliminate emissions and in Asia and India, where many of the population use them, this is a great application for fuel cells [16].

- *Forklifts.* Fuel cells forklifts have potential lower total logistic cost because they require minimal refilling and less maintenance than electric forklifts, whose batteries must be periodically charged and refilled with water. Electric forklifts have numerous interruptions in current input and output, while fuel cells ensure constant performance, eliminating the reduction in voltage output that occurs when batteries discharge [17].
- *Trains.* An international consortium is developing the largest fuel cell vehicle, a 109 metric-ton, 1 MW locomotive for military and commercial railway applications [18].
- *Planes.* Fuel cells represent an attraction for aviation because they offer low emissions and make no noise. The army is especially interested in this application because of the noise, low thermal signature, and the capacity to reach high altitude. Companies like Boeing are developing a fuel cell plane [19].
- *Boats.* For each liter of fuel consumed, the average outboard produces 140 times the hydrocarbons produced by the average modern car. Fuel cell engines have higher energy efficiency than combustion engines and then offer better range and significantly reduced emissions. Iceland has decided to use fuel cells like auxiliary power in the boats of its large fishing fleet and, eventually, like primary power [20].
- *Buses.* More than 50 fuel cell buses have been developed in North and South America, Europe, Asia and Australia. Because the fuel cell system is so much quieter than a diesel engine, fuel cell buses significantly reduce noise pollution. Fuel cell are highly efficient, so even the hydrogen is produced from fossil fuel, fuel cell can reduce CO2 emissions [21].
- *Auxiliary power units.* Today heavy-trucks are equipped with a large number of electrical devices, from heaters and air conditioners to computers, televisions, stereos, refrigerators and microwaves. To power these devices while the truck is parked, drivers often must idle the engine. The Department of Energy (DOE) has estimated the annual fuel and maintenance costs of a idling heavy-truck at over $1800 and that using fuel cell APUs in class 8 trucks would save 670 million gallons of diesel fuel per year and 4.64 million tons of CO2 per year.

1.5.2 Stationary fuel cells

More than 2500 fuel cell systems have been installed all over the world in hospitals, nursing homes, hotels, office buildings, schools and either there are connected to the electric grid to give supplement power and backup assurance for critical areas or they are installed as a grid- independent generator in areas that are inaccessible by power lines. Today, a fuel cell power generation system has 40% fuel to electricity efficiency by using hydrocarbon fuels. The fuel cells reduce the air pollution and the noise pollution because they operate silently and offer a low emission of CO2. For this reason, the fuel cell can be built near the point of use and also, its heat can be captured for beneficial purposes (cogeneration).

- *Telecommunications.* With the use of computers, Internet and communication networks are increasing and there is the necessity to have a more reliable power than that provide by the current electric grid with this respect fuel cell, have shown to be almost 100% reliable. Fuel cells can replace batteries to provide power for 1KW to 5KW telecom sites without noise or emissions and thus are durable and can provide power in sites that are hard to access or are subject to bad weather conditions. Such systems would be useful for providing primary or backup power for telecommunication switch nodes, cell towers and other electronic systems.

- *Landfills and Wastewater treatment plants.* Two of the more interesting stationary fuel applications involve a major credit card center and at large solid waste landfills and sewage treatment plants. The credit card center uses a fuel cell as its primary electricity supply due to its extremely high reliability of providing uninterrupted power. The landfill/sewage treatment plants utilize the methane gas generated by the decomposition of wastes/sewage as their primary fuel source to generate electricity which is sold to communities. Even the building shown in figure 1.10 in New York City's Time Square is powered by fuel cells [12].

Fig. 1.10. Building in New York's Time Square (photo courtesy of Fuel Cell 2000).

1.5.3 Portable Power

Fuel cells can provide power where no electric grid is available and also they are quiet, so using one instead of a loud, polluting generator at a campsite would not only save emissions, but also does not it disturb nature, or camping neighbours. Portable fuel cells are also being used in emergency backup power situations and military applications. They are much lighter than batteries and this is very important for soldiers that must carry heavy equipment in the field. In the next future, laptop computers, cellular phones, video recorders and hearing aids could be powered by portable fuel cells [22]. Figure 1.11 shows some applications of fuel cell systems.

1.5.4 Conclusions

The world's ever-growing demand for power has created a need for new efficient and sustainable sources of energy and electricity. In recent years, fuel cells have become a highly-promising potential source of power for military, commercial and industrial uses. The benefits of fuel cells are undeniable. The quiet, clean and reliable nature of their operation and efficiency with which energy is produced make fuel cells prime candidates to replace fossil fuels. The high cost when compared to other energy sources, the need for time to warm-up and pressure for efficient operation, the lifetime of the cell and the potential for the poisoning of the sensitive catalysts are all issues standing in the way of integration of fuel cell technology into the energy systems of the nations. Technological advances are limiting these problems also. For example, improved, less expensive conducting materials allow new fuel cells to work at higher temperatures and generate more power per volume. Fuel cell vehicle experts think that the future of fuel cells in vehicles is not far off.

(a)

(b)

(c)

(d)

(e)

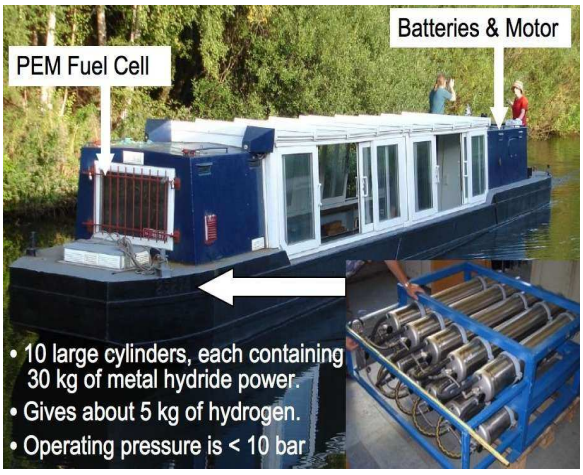

(f)

Fig.1.11. Fuel Cell Applications: (a) Fuel Cell Bus of Chicago; (b) Residential-scale Fuel Cell; (c) Fuel Cell Ford's car; (d) Fuel Cell Train; (e) Fuel cell boeing; (f) Fuel Cell Boat (photos courtesy of Fuel Cell 2000).

Chapter 2

The Emulator System

2.1 Introduction

An emulator is a device which represents or duplicates a working environment either in whole or in part or hybrid hardware-software platforms capable of copying the behaviour of physical systems, such that they can be used in replacement of the real equipment.

In this it differs from simulation, which is a modelling in a software environment. Sometimes an emulator is also called “simulation system”, which is an ambiguous definition, though.

In any case simulation and emulation have been used successfully for years to improve system design and management and it helps to maximize the process performance before a process is implemented.

It is generally agreed that the first real emulator was made in 1930’s with the RAF attempting to crudely building a cockpit, where they waggled levers which more or less corresponding to the joystick and other principal controls. Two or three muscular lads bounced the “aircraft” around in crude response to this waggling and, although based upon simple muscle power, the dynamic simulator was born [23]. Incidentally, the manufacturer of these early trainers went on become a world leader in the development of more sophisticated simulators.

The main reasons for using a simulator are safety, cheapness, and assessment because the working conditions may be dangerous, the cost to develop a whole real system may be very expensive and things which can be tried on a simulator are sometimes impossible to realize in real life.

2.2 Reasons for simulating a renewable energy system

It has been widely recognized that a laboratory analysis of renewable energy, as fuel cells and photovoltaic cells, is a very difficult challenge. The main reasons that justify this problem are the expensive cost of a complete system set-up, the excessive space required from the auxiliary equipment, the handling of all system, the start-up time and the constraints of safety and environmental conditions. For these reasons, the overall cost for a complete system is prohibitive for many educational institutions and for small companies interested in research about renewable energies. Simulators are needed by research and development activities to provide the flexibility and a convenient cost effective tool for assisting the test phase of various subsystems. The emulators, when they are hybrid hardware-software platforms capable of copying the behaviour of physical systems, such that they can be used in replacement of the real equipment.

The possibility to set up a complete experimental *emulator for a PV system* represents a very important goal. This is due firstly to the need of reproducing the environmental conditions as the PV cells electrical characteristics vary with solar irradiance and temperature (such as cloudy and nightly conditions) for a variety of solar panels and sizes. A high power photovoltaic module is very expensive thus demanding a high capital investment and actual solar insolation is continuously variable thus causing difficulties in development and experiments of laboratory photovoltaic converter system. For example, in Scandinavia the insolation level is very low between September and February. It is thus difficult to test photovoltaic equipment using natural light conditions for most of the year. If incandescent lamps are used to emulate the solar insolation, there are problems with enormous power requirement and heat generation. Approximately 10 kW of electric power is required to get an insolation level of 1 kW/m^2 for a 50 W solar panel. For a 2 kW solar array, the power requirement would be about 400 kW [24]. Novel discharge lamps are much more efficient. However, the spectrum does not correspond well to the sun. Another problem with solar emulators is achieving a uniform insolation distribution. By developing a photovoltaic emulator with the same output characteristics curves as those of photovoltaic modules, the results must be validated through experimentation with various loads. Also, the emulator does not require any heavy cabling work for connecting outdoor panels to the indoor equipment under test. Then, a PV emulator offers the advantages of flexibility in reproducing different weather conditions and in the modularity that allows increasing the emulator voltage and current capabilities in a manner analogous to the way in which the number of modules of a PV generating system is increased.

Fuel Cell emulators are expected to play a key role in the development of FC power electronics, because they represent an inexpensive alternative to mimicking the static and dynamic characteristics of fuel cells. In fact, the testing of an actual fuel cell for design and control of power electronic converters, optimization, diagnosis, and parameter estimation is not always easy.

The FC emulator can be used for the following motivation:

- Several tests can be accomplished with the emulator, prior to use the real stack, allowing for cost reduction and energy optimization. In fact, the emulator represents only a cost fraction of the real FC stack.
- Due to high price and operational complexity of the FC stack, researchers have difficulty on the development of a proper Power Conditioner System (PCS), which consists of a dc-dc boost converter, and a bi-directional dc-dc converter or a dc-ac inverter, according to the type of load it must feed. With this problem, until now, even though many PCS have been developed and reported, they are mainly tested with a constant dc source, not the real FC stack. Therefore, considering the nonlinear V-I characteristics of the FC, the actual performance and dynamics of the PCS cannot be examined. The FC emulator represents a solution that allows a Fuel Cell Generation system to be developed without using an actual FC stack and it is highly desired especially for the first stage of development.
- It is possible to develop synergetic technologies at the same time.

- It is possible to develop the system without using hydrogen, which has some safety concerns and still a high cost for low-volume use. As a consequence all risks of damage are decreased, along with the limited use of the FC stack and the reduction of hydrogen consumption.
- It is possible to make a scenario study and evaluate what should be expected from the FC stack in this market.
- Additional equipment is required (tanks, pumps, pressure regulator, etc) to run a FC stack. The size of the auxiliary equipment is related to the size of the FC stack and the associated costs and space can be excessive.
- It is possible to expand the emulator to other FC models and stack configurations by only changing the mathematical model (computer software).
- The emulator can be expanded to other FC sizes and arrangements, by only changing single parts.
- It is possible to know the requirement of hydrogen supply, environmental conditions and secondary effects on the micro-grid.

Among all kinds of renewable energies, wind energy is presenting the fastest development. As a consequence many researchers have focussed their interest on this field. To improve research activities related to the control of electrical generators for wind turbines, a controlled test environment is required that does not rely on the wind. Therefore, before deploying any Wind Turbine (WT) system, it is necessary to evaluate the steady state and dynamic behaviour of the wind turbine system and investigate the design of the power electronics and the controller in a laboratory environment to avoid problems at installation. A small *wind turbine emulator* (WTE), should be able to deal with over-speed situations so that the mechanical and electrical components of the turbine can keep operating safety. Also, it is always desirable to extract the maximum power from the wind turbine system. It is also recommended to supply the associated power electronics circuitry of the wind turbine from the wind turbine itself. A wind turbine emulator allows satisfying these requirements, because it incorporates over-speed control, isolated supply for the system power electronics and electronics for maximum power extraction.

2.3 Previous Work

Several works on modelling and simulation of the electrical behaviour of renewable energy systems have been presented in scientific and technical literature. The emulators of batteries, PV cells and arrays, fuel cells and wind turbine that have been studied until now, are briefly described in this section. Particular attention will be devoted to photovoltaic arrays emulators, since their design and implementation is strictly connected with those developed for FC system.

2.3.1 Battery Emulators

Typically the current drawn from a battery is constant. Recently, researchers started developing battery power management techniques that exploit non-ideal features of batteries in order to maximize their effective lifetime. To validate these power management techniques, researchers can use real batteries or battery emulators. If non-rechargeable batteries are used, then they must be replaced and disposed of after each experiment, making this approach expensive and unfriendly to the environment. Rechargeable batteries produce less waste, but may not be reproducible because the discharge and recharge of the battery and the battery age will affect the total charge level each time. In [25], Chou et al., have built a battery emulator using a programmable power supply that mimics the battery characteristics. The power circuit is made up of a 10 bit

data acquisition card (DAC) and an adjustable linear regulator which operates between 1 V and 4.5 V. The DAC offers the interface between the microcontroller and the linear adjustable regulator. The emulator contains measurement circuits for reading current, temperature and voltage. The digital platform consists of a PIC microcontroller and the battery emulator. The PIC is responsible for controlling the power circuitry and configuration, while the battery emulator can run locally on the PIC or externally on a workstation. The board uses the PIC16F877 microcontroller, an RS232 serial port, an Ethernet port and an optional USB port to communicate with a host computer. The PIC16F877 microcontroller has eight (analog to digital) ADC channels and a UART for serial communication. The PIC software runs a command interpreter, which analyzes instrumental commands and responds to query or configuration commands, including software calibration of the ADCs. The block diagram of the emulator is shown in Figure 2.1. The feedback information read from the measurement circuits is sent to the microcontroller which computes the battery emulator voltage which is sent to the linear regulator. The microcontroller has a limited memory and is implemented a simplified model that resembles a Mealy machine with 256 charge states. For elaborate simulation based on the chemical reactions inside the battery, the emulator can be controlled externally from a computer through the RS-232 port or the Ethernet port.

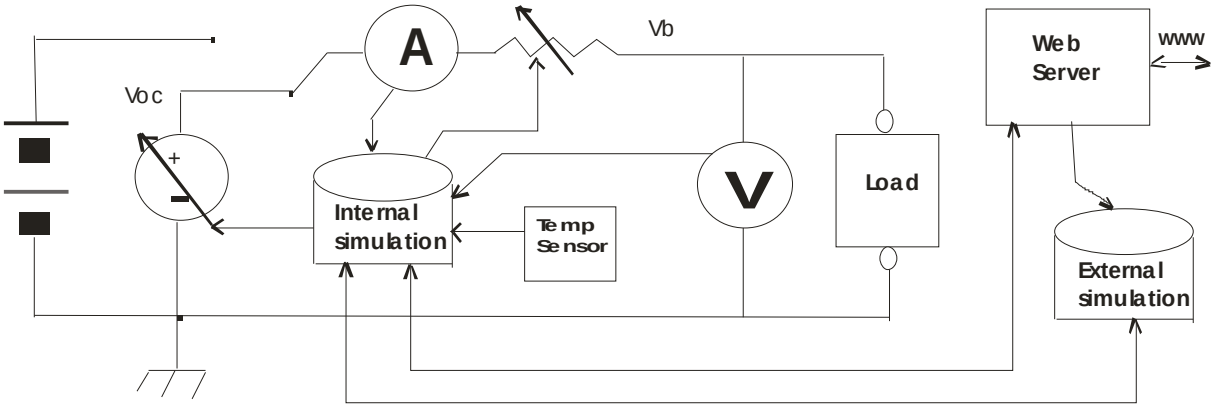

Fig. 2.1. Block Diagram of the Battery Emulator.

2.3.2 Solar Array Emulators

The photovoltaic emulator developed by Zeng et al., emulates the output characteristics of photovoltaic modules and as such it can be used in replacement of actual photovoltaic modules [26]. The emulator mainly consists of a bridge rectifier, a dc chopper and a control system based on the microprocessor 80C196KC as shown in Figure 2.2. The power conversion circuit is shown in Figure 2.3 and it is made up of a three phase bridge rectifier and a DC chopper. The input of the DC chopper is the output of the three phase bridge rectifier, which converts the AC source input to unregulated DC voltage. The DC chopper is designed as a typical step-down or buck chopper and an IGBT is used as a switching component. The control system controls the duty cycle of the pulse width modulation (PWM), so that the output of the DC chopper will follow the photovoltaic module I-V curve. The control system consists of an interface board, a microprocessor, a PWM generator and an operation board. The photovoltaic module I-V data tables are stored in the memory of the microprocessor, which calculates the reference voltage and sends it to the PWM generator. This generator adjusts the duty cycle of the PWM so that the feedback voltage will follow the reference voltage. The instantaneous current and voltage is sent to the PWM generator, while the average value of the current is sent to the 80C196KC CPU board. The interface board is designed to transform, to isolate and to filter the output current and voltage signals of the chopper from the current transducer. The operation board represents an user-interface that allows defining simulation parameters, like the number of modules and the solar insolation. This emulator offers the flexibility and the convenience required from electrical engineers for testing several conditions in the laboratory without using actual solar cells or working outdoors for testing various solar conditions.

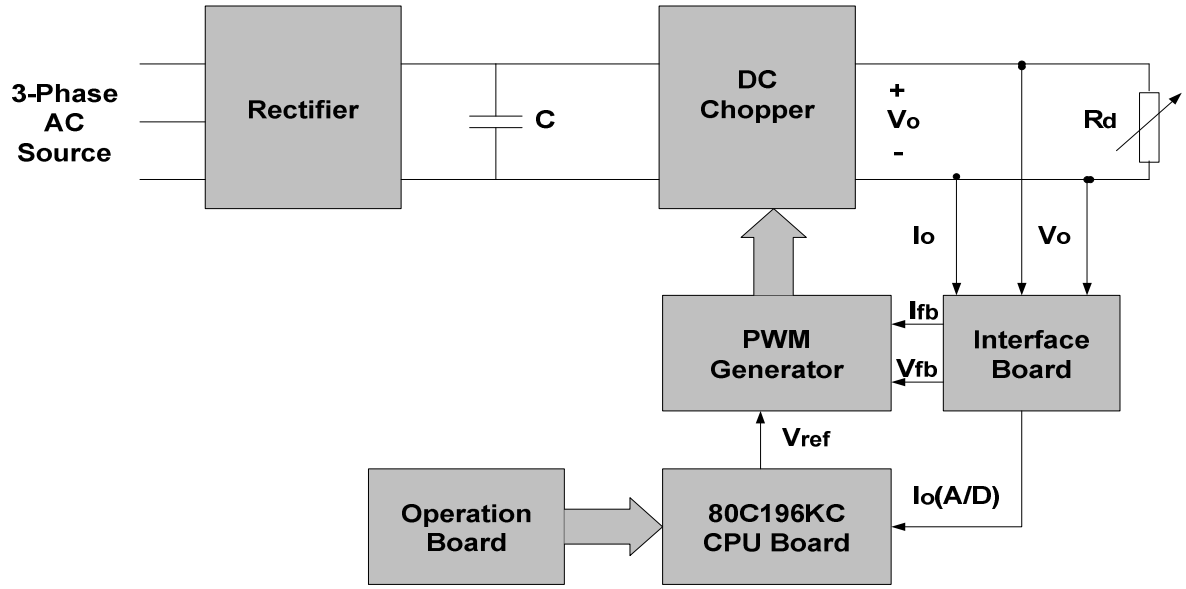

Fig. 2.2. Block Diagram of the Photovoltaic Emulator.

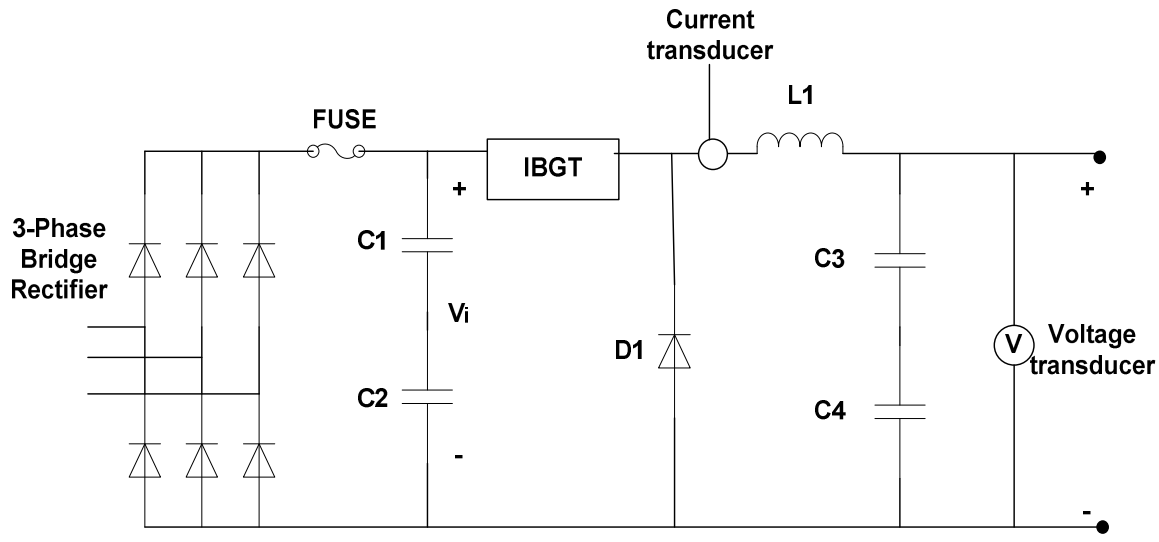

Fig. 2.3. Power Circuit of the Photovoltaic Emulator

The photovoltaic array emulator developed by Khouzam et al., is performed by a computer controlled DC power supply and a control software for generating real-time current voltage (I-V) output characteristics curves of space solar power system (SSPS)[27]. The overall power supply system is shown in Figure 2.4. The principal parts of the emulator are the Pre-Regulator, the switched mode regulator, the computer interface and the computer program. The pre-regulator supplies the switch mode regulator with a constant voltage source with an adequate current for the load. The function of the switched mode regulator (Figure 2.5) is to convert a DC voltage unregulated into a controlled regulated DC output. The regulation is achieved by using pulse width modulation (PWM) at a fixed frequency and a switching device. This device is made up of an ultra fast, high frequency insulated gate bipolar transistor (IGBT), with a switching frequency of 50 KHz. A computer reference voltage is computed by the voltage and current feedback from the power supply. The reference voltage is compared with the output voltage of the switched mode regulator and the difference of these signals is used to obtain a control voltage, which allows the pulse-width modulation for the switching device to be generated. An LC filter is used to obtain a continuous load current and to reduce harmonic amplitudes. The computer interface (Figure 2.6) provides the isolation amplifiers to cross reference analogue feedback signals from the power supply to the computer reference. Also, it provides scaling down the electrical signals into the correct range so that they can be used by the computer interface card. The control algorithm must ensure that the actual power supply output voltage be equal to the theoretical array output for the simulated PV array. The output current is measured by the interfacing card and it is used by the control software to calculate the theoretical array voltage for the connected load. This theoretical voltage is compared with the actual output voltage of the power supply and if the difference between these two signals is less than a tolerance threshold, then the correct operating point is reached. If this condition is not verified, the duty cycle of the switching component is iteratively varied until the theoretical output voltage equals the power supply output voltage.
This emulator offers advantages to simulate several types and sizes of arrays under any illumination and temperature condition in real-time with real loads.

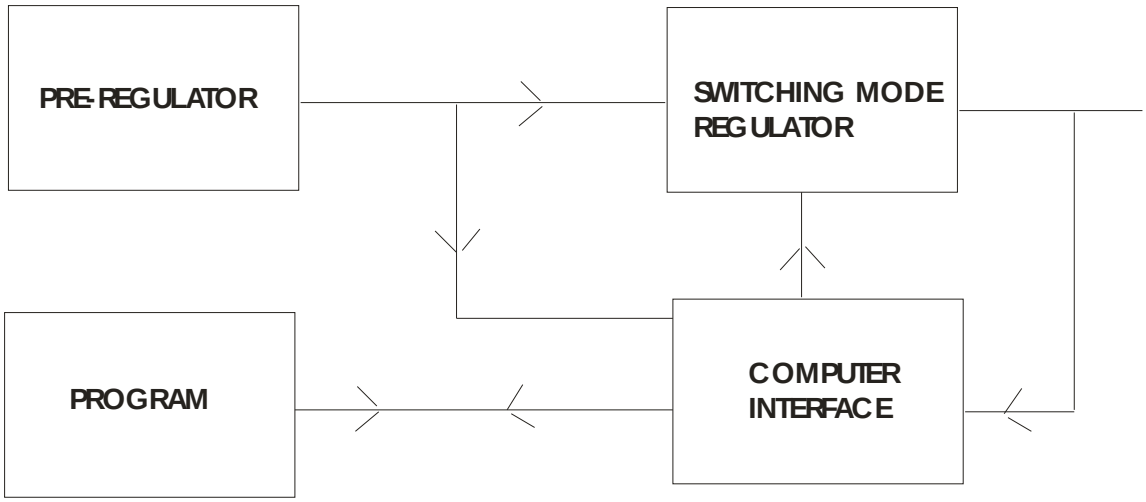

Fig. 2.4. Overall System Topology.

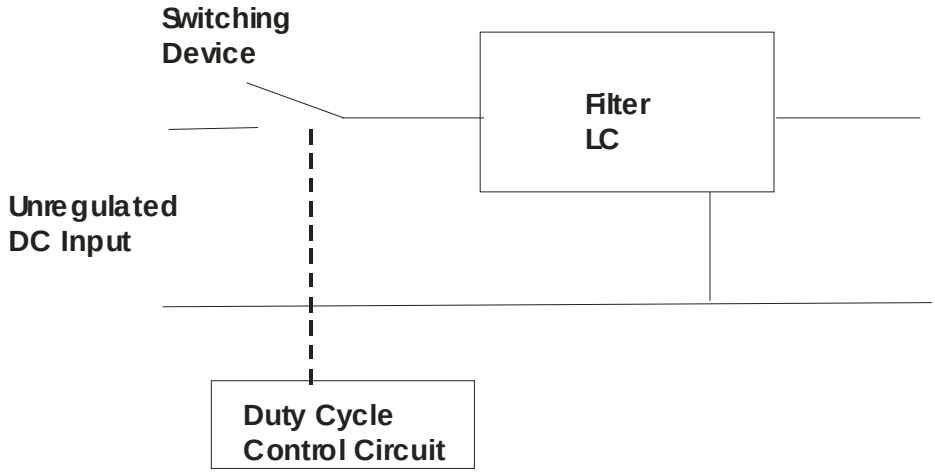

Fig. 2.5. Switched mode regulator.

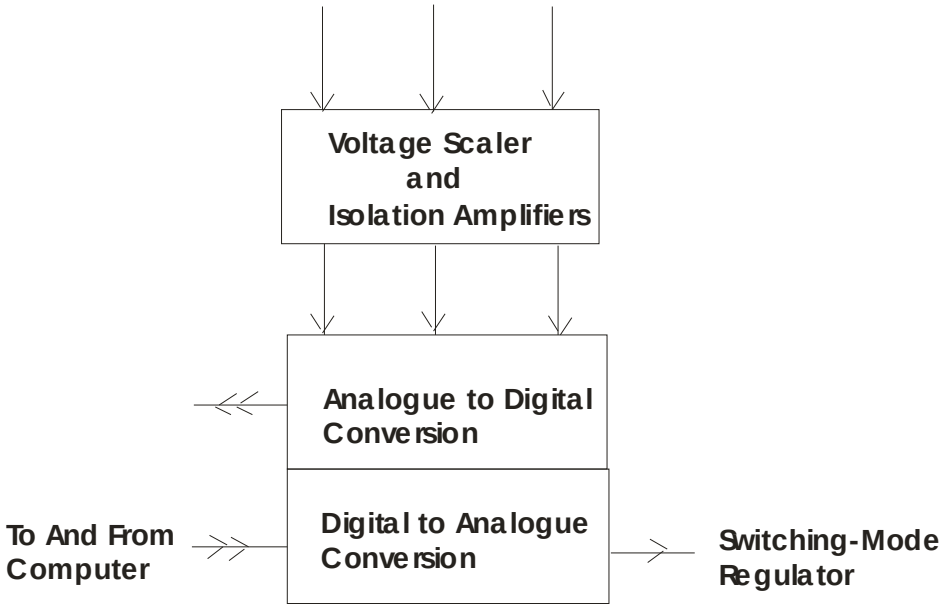

Fig. 2.6. Computer Interface.

The simple solar emulator proposed by Thean et al. uses the embedded Microcontroller to control the duty cycle of a DC/DC converter [28]. The Microcontroller can also communicate with a PC via RS232, so there are two control modes for the emulator system: the local control by the Microcontroller which can be programmed and the remote control by a PC through the RS232, which can plot the characteristic curves of the solar array. The basic diagram for the emulator is shown in Figure 2.7.

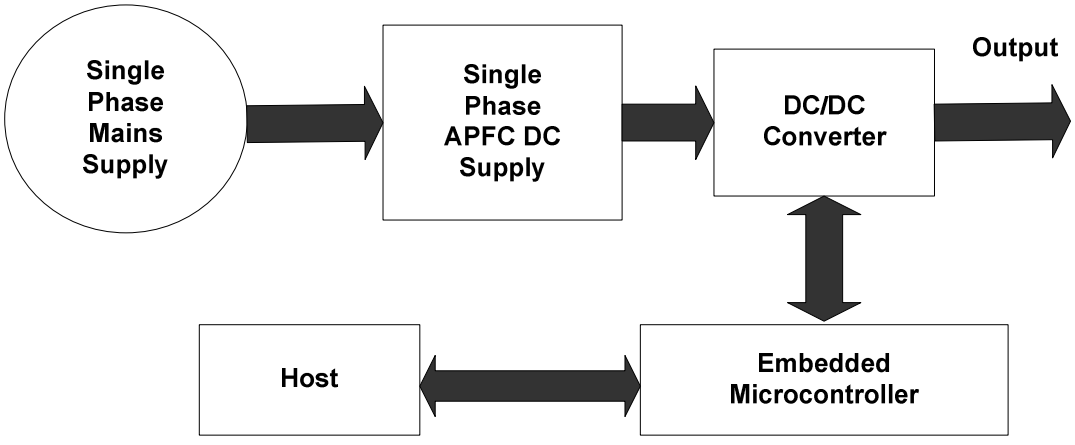

Fig. 2.7. Block diagram of programmable solar panel emulator.

The Microcontroller used is the PIC16F877 which has 13-bit program counter, capable of addressing an 8k program memory space and 33 I/O lines grouped into 5 ports used as analogue and digital I/O. The DC/DC power supply used in this project has been designed for high power low voltage applications which can output a voltage from 0-10 VDC and up to 100A. The PCW Compiler of Costumer Computer Service Inc. is used to develop the control software of PIC16F877 and the VC++ 6.0 is used to develop the host application software that communicates with the Microcontroller. Though the software can simulate any solar panel voltage, current and power characteristics, the dc power supply is the only limiting part which needs to be custom-built for specific power conditions. The system can either control the solar panel emulator individually or communicate with a host that can do simulation by RS232, so it can be a portable and effective system to simulate the solar panel. The block diagram of the control system is shown in Figure 2.8.

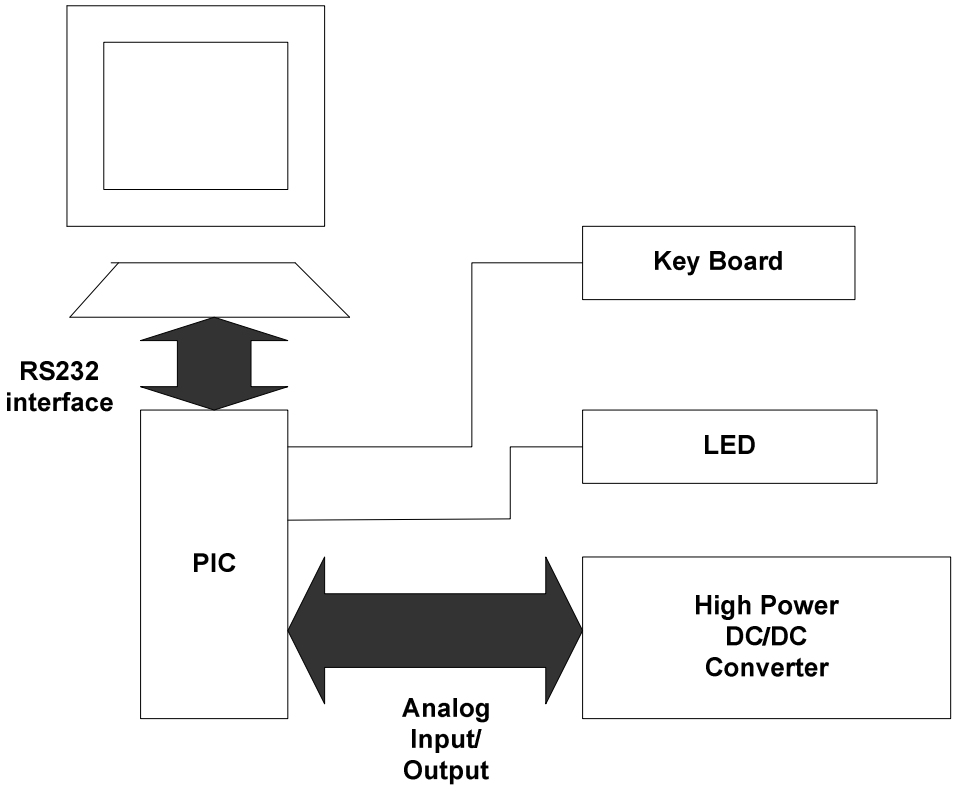

Fig. 2.8. The Microcontroller based control system of programmable solar panel emulator.

The solar array emulator developed by Smith et al., [29] adopts a different approach with respect to the previous solar emulators, because it uses pre-calculated I-V characteristics for specified temperatures and insolations. These are loaded into an EPROM which is used as a look up table. It uses a power supply module with a maximum power of 400 W to simulate two PV arrays, each of 5 series-connected panels connected in parallel, because, when the two arrays work in open circuit, the output voltage results in being between 36-40 V; while, when working in short circuit, the current output is about 10 A . This solution allows inverters larger than 400 W to be tested because other modules can be added either in series or in parallel. To achieve fast dynamic performance of the emulator a combination of a class A regulator and static switches (Figure 2.9) is used. The class A regulator is required to produce an output voltage to the test inverter as given by the I-V characteristics contained within the EPROM. The static switches A, B, C are automatically selected to keep the regulator within its working range when the operating point sweeps through the I-V characteristics. The emulator can work as a current regulator or as a voltage regulator. In the first mode, the input of the EPROM is the measured voltage and its output is the desired value for the load current. The current regulator compares the desired current with the actual current and adjusts the mosfet so that their difference can be minimized. When the emulator works as a voltage regulator the EPROM gives the desired voltage and the difference between this value and a proportion of the actual output voltage is used to set the input voltage to a current source amplifier. This uses the difference between the applied voltage and the voltage across a sensing resistor R_s to set the load current. This load current is passed through a current transducer, the output of which is the input of the EPROM. The voltage regulator was modelled using the Pspice circuit simulation package. The circuit was built and the simulated and the measured results were compared for validation. A look-up table can be used with Pspice but this has a limited number of points. To overcome this problem the Matlab Powerlib toolbox was used because it can use a 3 dimensional look-up table to represent the I-V characteristics.

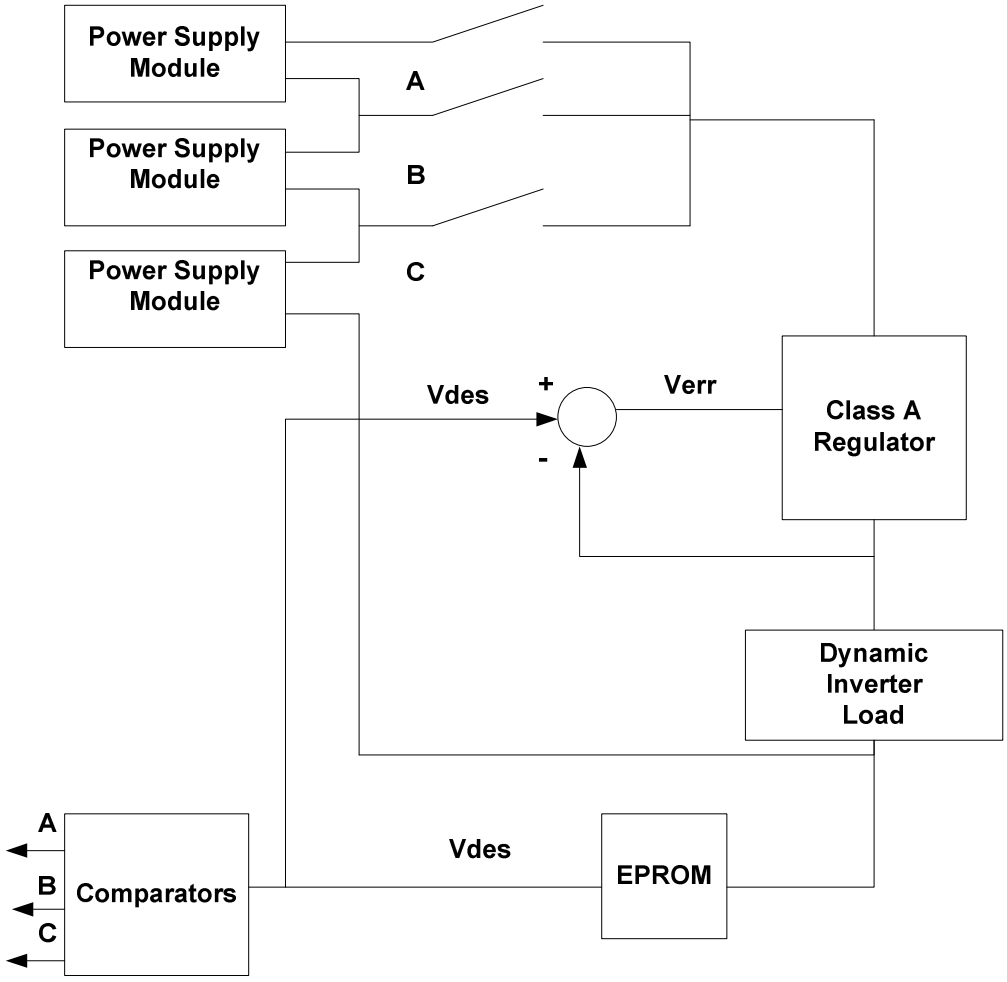

Fig. 2.9. Smith's PV Emulator Concept.

Elgar Electronics Corporation has developed a solar array emulator that reproduces various solar array outputs, based on the wide variety of input conditions, including orbital rotation, spin, axis alignment, eclipse events, beginning of life and end of life operation [30]. It provides complete programmable control of all the parameters that shape the solar cell I-V output curve. The solar array emulator is made up of the Elgar's Fast Profiling Current Source (FPCS) modules that can be connected in series or parallel depending on the application power requirements. Each FCPS module has an embedded Motorola microprocessor, which provides the computational power necessary to calculate the output transfer function, to communicate via a fibre optic data link to the system computer and to continuously monitoring the state of the power sections. The solar array emulator has a Windows NT graphical user interface and hardware control software. It can be controlled remotely and integrated into a customer's test system via a standard Ethernet.

The solar array emulator from Agilent Technologies is a DC power source that simulates the output characteristics of a solar array [31]. It is primarily a current source with very low output capacitance and is capable of simulating the I-V curve of different arrays under different conditions (temperature, age, etc).The I-V curve is programmable by the IEEE-488.2 bus and the emulator can operate in three different modes: emulator mode, table mode and fixed mode. In the emulator mode, an internal algorithm is used to approximate a solar array I-V curve and the open circuit voltage, the short circuit current and the current and voltage at peak power point on the curve are needed to shape a curve. In the table mode, the I-V curve is set by a user-defined table of points. As many as 30 tables may be stored in each of the emulators: built-in volatile and non-volatile memory using an IEEE-488.2 command. The fixed mode is the default mode when the unit is powered and this unit has the rectangular I-V characteristics of a standard power supply, when an output capacitor is added in this mode.

The solar array emulator developed by Spectra-Nova Technologies Inc., emulates the power generation of a solar array in diverse operating conditions [32]. This capability combined with their fast transient response, makes it possible to power a photovoltaic application device in exactly same way as a solar array. The software has a large data base storing the actual characteristics of the solar modules (crystalline and thin films) made up of the major manufactures around the world. They can be used in series/parallel combinations to generate a desired configuration of an array. The user can vary external conditions such as light intensities, temperature and tilting of the solar panel.

2.3.3 Fuel Cell Emulators

[33], [34] study and simulate the transient behaviour of a solid oxide fuel cell; electrochemical and thermodynamic equations are used to model the process in the fuel cell. The fuel cell model is simulated by a computer program, which uses parameter values for input gas flows, fuel cell temperature etc. and outputs the terminal fuel cell voltage and current. In [35] a model based on a closed-form calculation of solid oxide fuel cell (SOFC) voltage for a given current, fuel and air compositions, and temperature has been implemented in a spreadsheet format. In [36] a mathematical model is used to describe a proton exchange membrane (PEM) fuel cell and can be used to measure the stack performance. In all these simulation models, electrochemical and thermal equations are used to determine the polarization losses and calculate the terminal voltage. The modelling of the fuel cell is developed by using computer programs, but no actual hardware model is built.

The most common test-bench used by electrical engineers in place of a fuel cell is a DC power supply in series with a resistor representing the fuel cell internal resistance as shown in Figure 2.10. This method makes a linear

approximation of the output V-I curve of the fuel cell and at high currents the loss in the resistor is comparable with the power output. The variation of the output voltage (V_o) and the power loss with current is shown in figure 2.11. The power loss in the resistor is very high and is almost equal to the rated output of the fuel cell. This approach models only steady state characteristic by the resistor and it can not replicate the transient behaviour of a fuel cell.

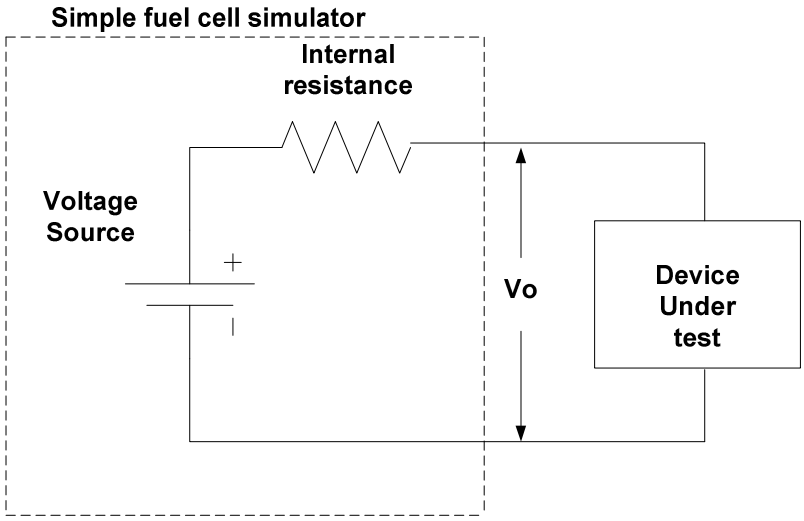

Fig. 2.10. A Simple Fuel Cell Emulator.

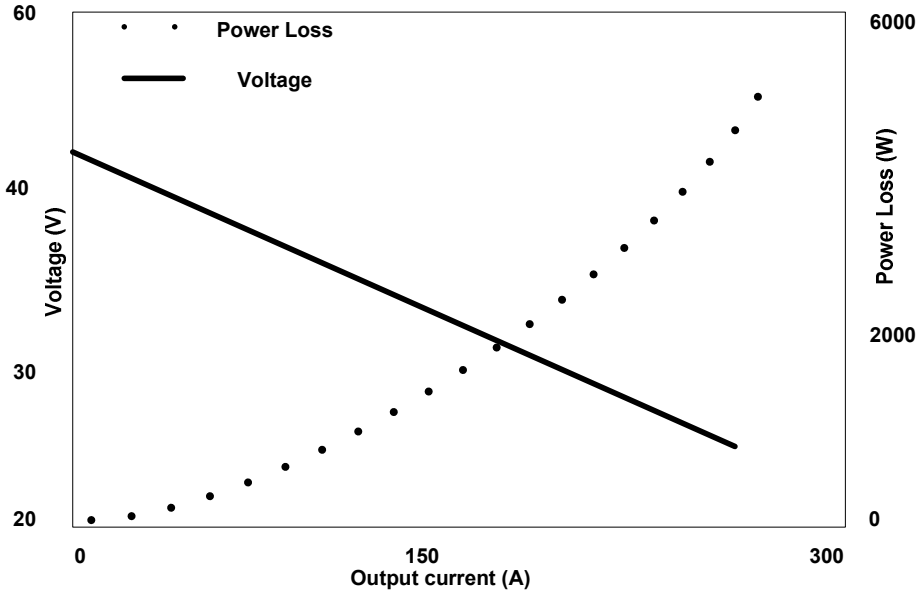

Fig. 2.11. Output Voltage and Power Loss vs Output Current.

In [37] it is proposed a low-cost and easy-to-use fuel cell emulator using a programmable DC power supply controlled by the LabVIEW graphical user interface. This emulator reproduces the dynamic electrical characteristics of a commercial 5 kW Solid Oxide Fuel Cell (SOFC) stack under several operating conditions. The proposed emulator uses a cubic polynomial curve-fitting technique to interpolate between data points for voltage and current of the fuel cell obtained from experiments and to analyze the fuel cell characteristics. This technique allows a unique relationship between voltage and current to be defined over the fuel cell operating range and then the V-I curve can be modelled by a voltage source connected in series with a non-linear internal impedance. The fuel cell emulator consists of a Magna-Power Electronics programmable DC power supply (10 kW, 0 to 55V DC) and a SBC 488A RS232 control interface (Figure 2.12). The LabVIEW program running on the computer commands the system based on the feedback signals that it receives from the device under test connected to the programmable DC power supply. The SBC 488A forms the interface between the controller and the power supply and is connected by a RS232 serial cable. The data acquisition card and signal-conditioning module form the communication path between the emulator controller and the device under test. Experimental results show that the proposed emulator closely follows the response time of the SOFC fuel cell under several load conditions, but this steady state model does not consider all circumstances, because the fuel cell has dependencies on fuel rate, temperature, pressure, etc.

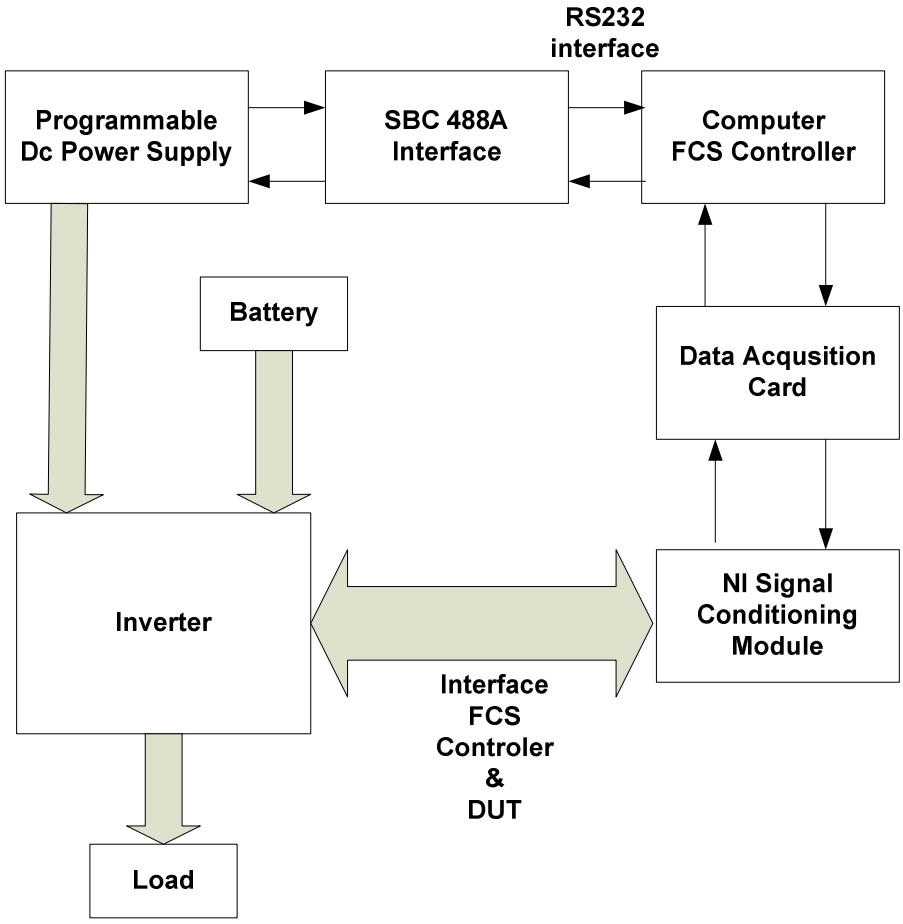

Fig. 2.12. Schematic of the fuel cell emulator used as test bench.

[38] and [39] is describe an emulator of a 3 kW proton exchange membrane fuel cell (PEM-FC), that was designed and manufactured as electrical characteristic of fuel cell generation system and it uses a simple buck converter (Figure 2.13). This converter is integrated with an advanced control algorithm to achieve the highly nonlinear V-I characteristic, but the entire complexity of the system is into the software, not hardware, so that the emulator can be implemented with low cost. The proposed control system is implemented by using the digital signal processor (DSP), TMS320C31, which has a function of floating-point arithmetic. The emulator has input voltage AC 220V (DC 311V) and output voltage DC 39~60V to obtain DC output for the characteristic of the fuel cell. In fact, a typical PEM-FC has output voltage in the range 39~60V (if connected in series) when it operates in ohmic region, while when it operates in the activation region the output voltage of the emulator is assumed constant. To model the V-I characteristic of the PEM_FC, at first, the output current is continually sensed trough the AD converter of the DSP and it is used at first to select the operating region of the PEM-FC

and then to calculate the voltage reference. This value is output by the by D/A converter and it is compared with a saw-tooth wave and to command the switching of the buck converter.

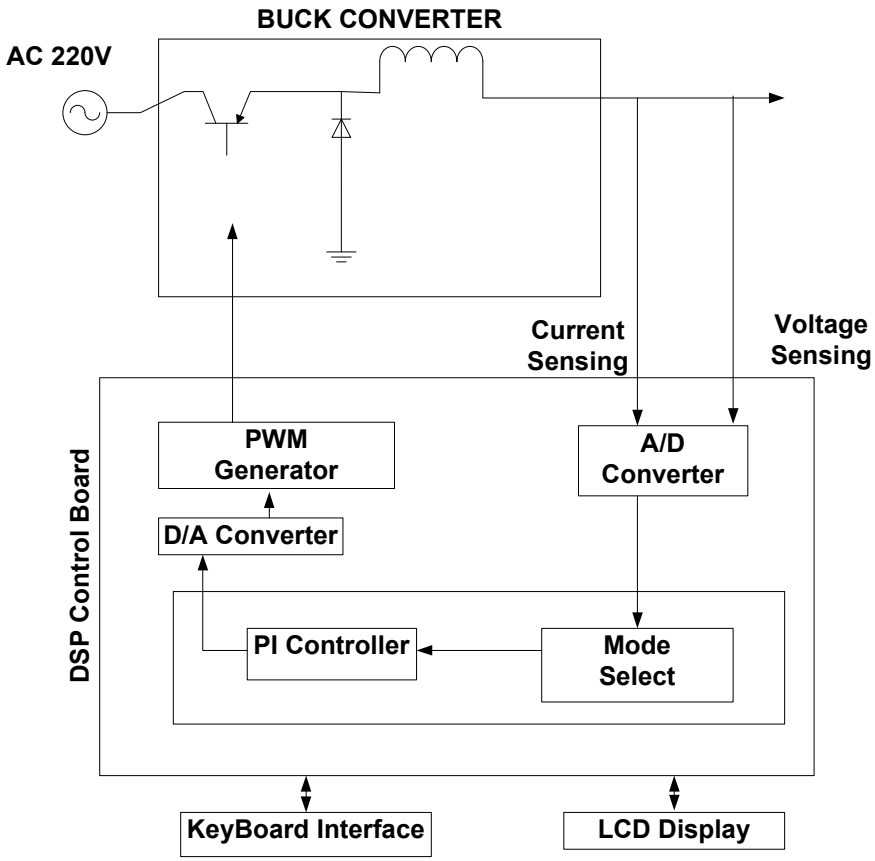

Fig. 2.13. Fuel cell Emulator proposed by T. W. Lee at al.

The FC emulator proposed by A. Gebregergis [40] is based on a dynamic lumped SOFC model, which accounts for the effects of activation, concentration and ohmic losses. The fuel cell emulator is designed to include the steady state and the transient response. Figure 2.14 shows a block diagram of the fuel cell system, which contains an FC emulator, power converters (DC/DC and/or DC/AC) and a load. The SOFC model is implemented in a Matlab/Simulink environment, which is eventually loaded into a dSPACE and/or DSP real-time controllers. The output voltage from the dSPACE controller drives a linear power amplifier connected to a DC-DC converter or a load. Figure 2.15 shows the overall experimental test set-up of the fuel cell emulator (dSPACE and measurements), the power converter and the load. The dSPACE controller is used to generate the PWM

switching control of the DC-DC power converter or a DC/AC inverter if it is needed. A 5 kW LCV5050 linear power supply amplifier with a slew rate of 30V per microsecond is used to interface the FC model to the power converter or the load. The SOFC emulator was connected to a variable resistive load to obtain the static response with different values of flow rates and cell temperatures. The results compared with experimental data, confirm that the FC emulator is good enough to replace the actual fuel cell during the steady state, although the choice of the parameters used can enhance the results of the emulator. The dynamic response of the FC emulator is obtained for a step change of the flow rate and cell voltage.

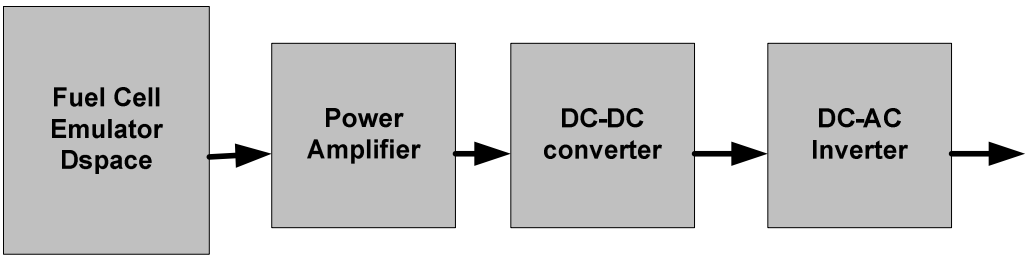

Fig. 2.14. Block diagram of a fuel cell system and power converter.

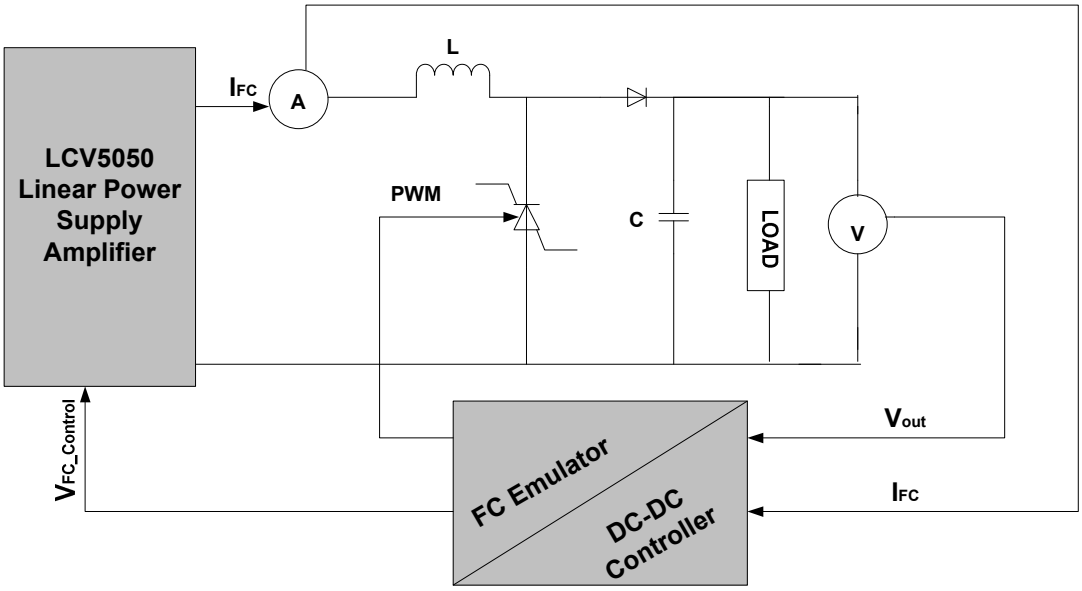

Fig. 2.15. The FC emulator and power converter circuit diagram by A. Gebregergis.

In [41] it is proposed an FC emulator that introduces the concept of replacing the computer model of the FC with an actual small single FC. A single FC costs a small fraction of a FC stack and can reproduce the behaviour of an expensive powerful FC stack by using scale-up operations. Figure 2.16 shows a block diagram of the proposed FC emulator, which uses a 150 mW single DMFC as the reference system. The electrical dynamic behaviour is achieved by controlling a fast dynamic switching power supply system (SMPS) that uses a reference signal that corresponds to the FC electrical output characteristics. The FC emulator contains four main parts: a single FC connected to an electronic load, a SMPS with DSP control, a Control Area Network (CAN) bus interface and a PC for monitoring and analysis. The DSP-controlled electronic load connected to the single FC behaves like a current source that extracts power out of the single FC. The reference signal generated by the single FC is used from the SMPS to emulate the behaviour of a FC stack to drive the actual application. The computer in the system may be used to monitor the system, to run a computer based model or to perform dynamic tests on the single FC. Figure 2.17 shows a functional diagram of the FC emulator operating principle. In this diagram there are two parts: the single FC connected to a current source on the left side of the dashed line and a voltage source on the right side of the dashed line. The current source represents the electronic load connected to the single FC, while the voltage source corresponds to the SMPS. The output current (i_o) corresponds to a portion of the current of the single FC and it is obtained by using the scale rule function α, that allows the effect of a bigger electrode effective area to be emulated. The voltage cell (V_{cell}) is amplified N times to emulate N single FC connected in series. To perform the operating system, the output current of the SMPS is measured by the DSP and it is transmitted by the CAN bus. The DSP controlled electronic load receives the current information and extracts a proportional current from the single FC by using the scale rule function α. The output voltage of the single FC changes dynamically according its output current, is measured by the DSP that controls the electronic load and is transmitted to the SMPS through the CAN bus. The SMPS receives this information and amplifies the single FC voltage with a gain of N. In this mode of operation the computer is used to monitor the exchange of parameters through the CAN bus, but the system can operate without computer to minimize the complexity of the system. The FC emulator can also run using a computer-based model and in this operation mode the single FC module can be eliminated.

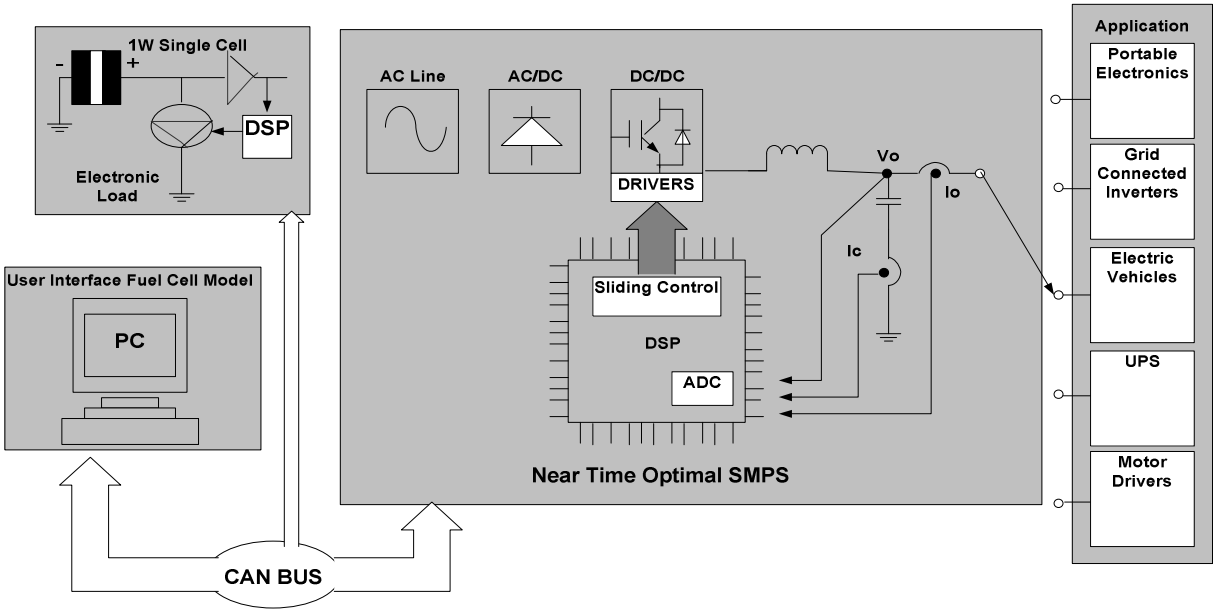

Fig. 2.16. FC emulator block diagram proposed by Ordonez.

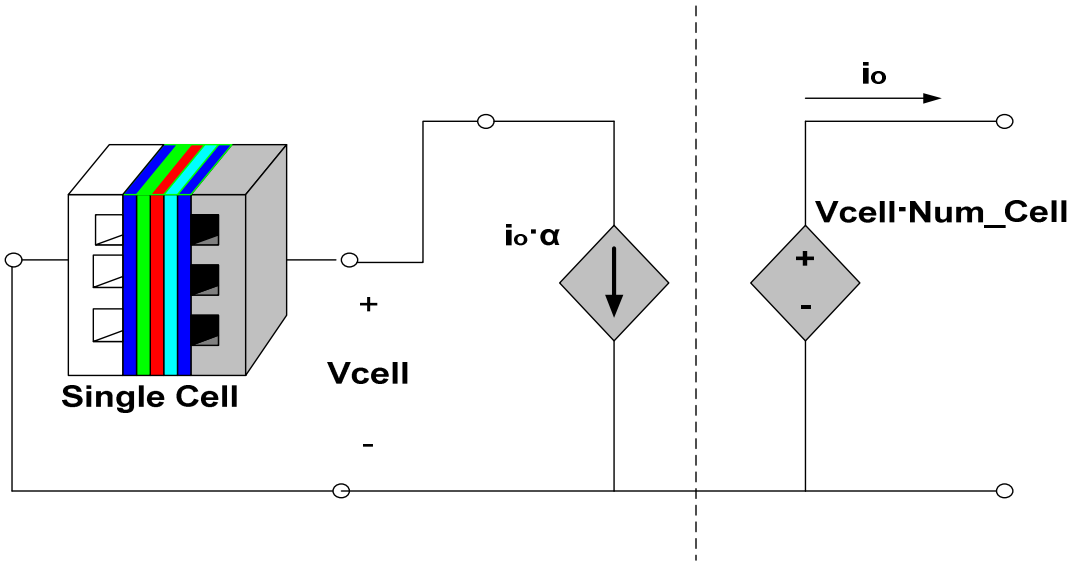

Fig. 2.17. Functional diagram of the FC emulator operating principle proposed by Ordonez.

2.3.4 Conclusions

This chapter has presented the current state of the art of emulators for fuel cells. In general, they either make a linear model of only the stack of the fuel cell or, even if they consider non linear models, they fail to take into consideration all the auxiliary sub-systems. This limitation makes it difficult to use these emulators for rapid prototyping of different control laws.

This thesis presents instead the analysis, design and experimental implementation of the emulator of the whole PEM-FCS where 1) All the auxiliaries of the system have been considered, each including its own control system, as in a real FCS, 2) The converter is a classic DC-DC buck converter with a free-wheeling diode and is designed to have a high bandwidth and to be practically always in conduction mode (discontinuous mode appears only at very low currents), 3) The voltage control is made by space-state controller, able to properly fix the closed loop poles of the system, thus ensuring the desired bandwidth of the control system 4) It can be used in laboratory as a stand-alone low-cost system for design and experimental purposes.

Chapter 3

Fuel Cell System (FCS) Model

3.1 Generality in the PEM Fuel Cell (PEM-FC)

Figure 3.1 shows the fuel cell system (FCS) PEM-FC modelled in this thesis:

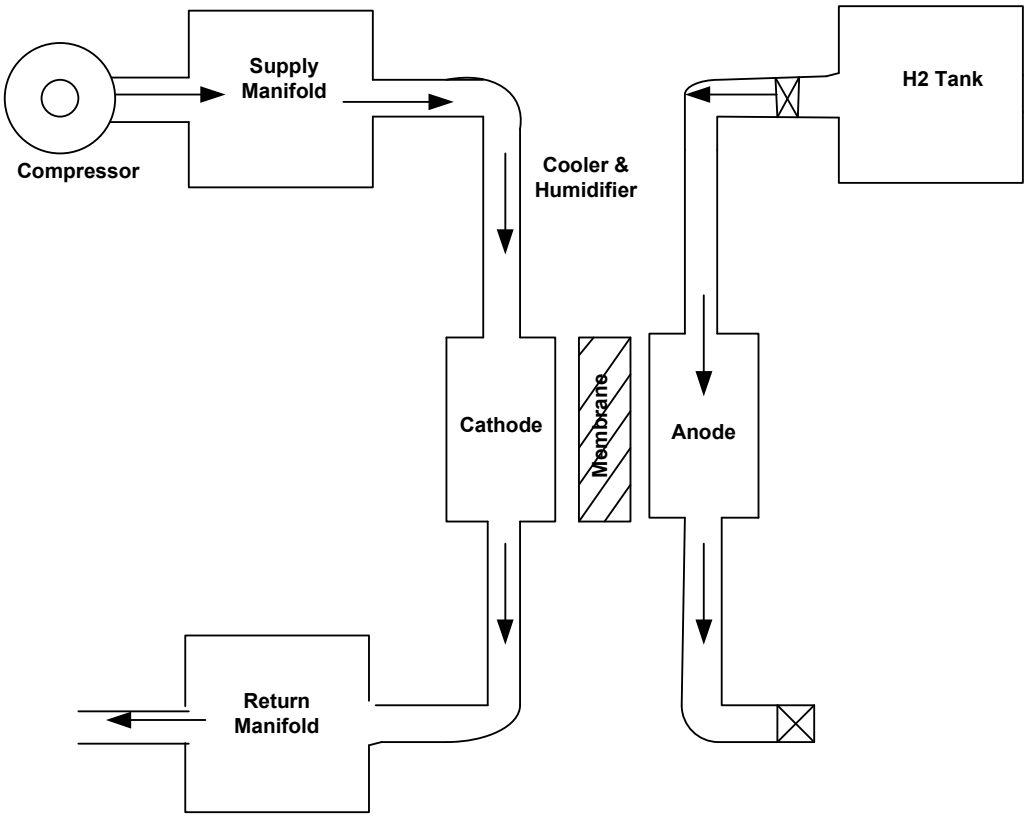

Fig. 3.1. Structure of a fuel cell PEM system.

This figure shows the following supply subsystems of a Fuel Cell System [66] [88 (based on 66)] (FCS):

1. compressor model;
2. radiator model;
3. humidifier model;
4. supply manifold model;
5. return manifold model;
6. cathode model;
7. anode model.

The model of the compressor, the radiator, the humidifier, the supply manifold and the return manifold are the auxiliary devices of a fuel cell system. The core of the PEM-FC is made up of the following subsystems:

- stack voltage model;
- anode flow model;
- cathode flow model;
- membrane hydration model.

The figure 3.2 shows the fuel cell stack block diagram with all input/output signals and all subsystems. Furthermore, a thermal model must be implemented to consider the temperature changes.

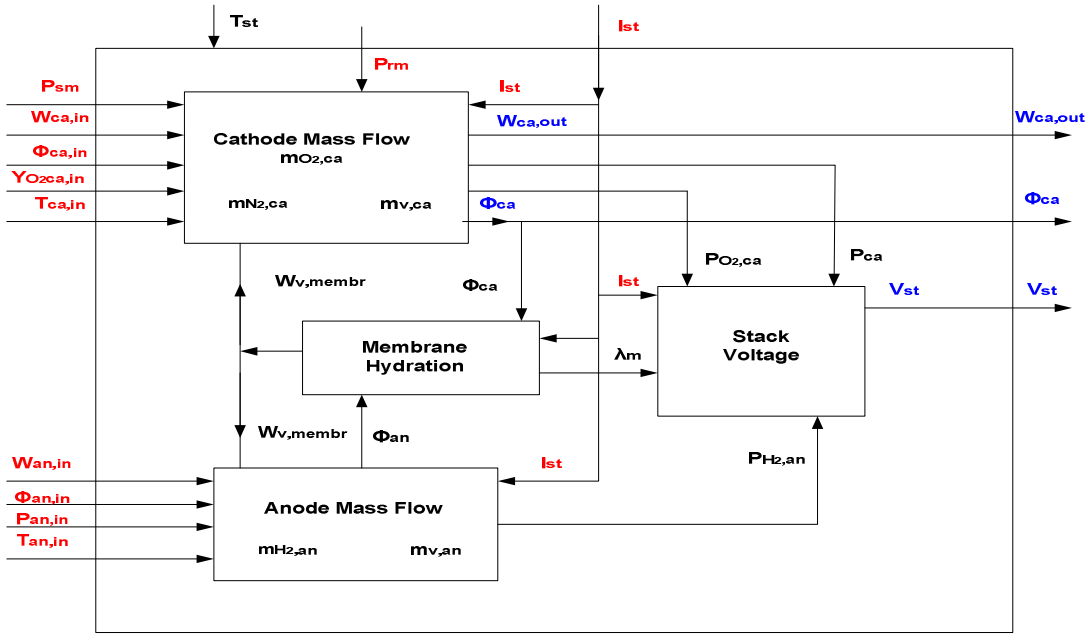

Fig. 3.2. Fuel cell stack block diagram.

In figure 3.2, the external inputs of the fuel cell stack are shown with a red colour and they are represented by the following variables:

- I_{st} the stack current (A);
- p_{sm} measured pressure in the supply manifold (Pa);
- p_{rm} measured pressure in the return manifold (Pa);
- $W_{ca,in}$ mass flow rate in the input of the cathode (Kg/s);
- $\phi_{ca,in}$ mass flow humidity in the input of the cathode;
- $y_{O_2,ca,in}$ oxygen mole fraction in the input mass flow of the cathode;
- $T_{ca,in}$ mass flow temperature in the cathode input (K);
- $W_{an,in}$ mass flow rate in the input of the anode (Kg/s);
- $\phi_{an,in}$ mass flow humidity in the input of the anode;
- $p_{an,in}$ mass flow measured pressure in the anode input (Pa);
- $T_{an,in}$ mass flow temperature in the input of the anode (K).

The blue color in figure 3.2 is used to show others important inputs/outputs of the stack, they are the following:

- $W_{ca,out}$ mass flow rate in the output of the cathode (Kg/s);
- $\phi_{ca,out}$ mass flow humidity in the output of the cathode;
- V_{st} stack voltage (V).

The black color shows the inputs/outputs used to implement the equations of several part of the stack (see in the next sections). They are the following:

- p_{ca} cathode total pressure (Pa);
- p_{O_2ca} oxygen partial pressure in the cathode (Pa);
- p_{H_2an} hydrogen partial pressure in the anode (Pa);
- ϕ_{an} relative mass flow humidity inside the anode;
- λ_m water content in the membrane;
- $W_{v,membr}$ total stack mass flow rate across the polymeric membrane (Kg/s).

In the model two important hypotheses are made:

- the electrochemical reactions at the polymeric membranes occurs instantly.
- the stack temperature is assumed to be constant and homogeneous into the stack, because its time constant is greater than time constants of the other dynamic phenomenon of the stack. Therefore, the stack temperature is assumed to be equal to 80°C.

This hypothesis, astonishing has it may appear, can be motivated more fully by the relevant time constant for an automotive propulsion-sized PEM fuel cells stack system listed as follows[66][89]:

- Electrochemistry O(10-19sec)
- Membrane Water Content O(unknown)
- Hydrogen & Air manifolds O(0.1 sec)
- Flow Control & Supercharge Device O(1 sec)
- Vehicle Inertia Dynamics O(10 sec)
- Cell & Stack Temperature O(100sec)

With such slow responses the cell and stack temperature can be considered as controlled by another distinct controller. With this respect the temperature can be looked-up as a constant in comparison with the other above faster sub-systems.

To calculate the stack voltage it is necessary to use the following parameters:

- the partial pressures of the reactants that are introduced into the fuel cell;
- the stack temperature;
- the membrane humidity.

The humidity and pressure changes of the reactants are calculated in the anode and cathode model. The following figure shows the principal mass flows, that characterize the behaviour of the fuel cell.

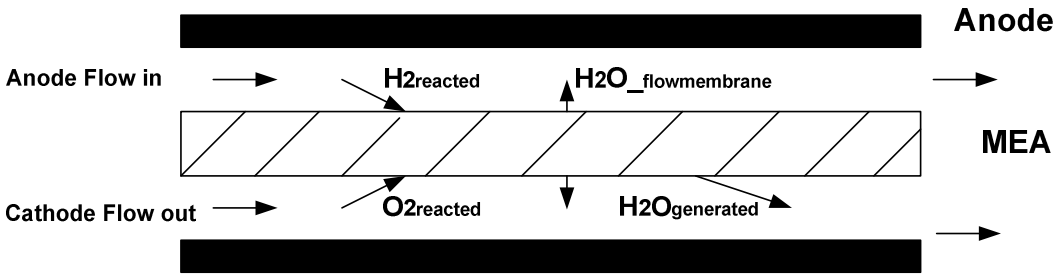

Fig. 3.3. Stack mass flow

The membrane hydration model allows the water produced during the working of the fuel cell to be quantified.

3.2 Stack Voltage Model

The stack voltage model uses the following inputs:

- The mean value of the water content in the membrane λ_m, which is used in the membrane hydration model. λ_m, can assume values in the range [0,14], which corresponds to the range [0,1] of relative humidity;
- The stack temperature T_{st} (K), which is considered an external constant input;
- The electrical current (A) demanded from the load of the fuel cell system;
- The oxygen partial pressure of the cathode (bar);
- The hydrogen partial pressure of the anode (bar);
- The global pressure of the cathode (bar).

To calculate the stack voltage produced by the fuel cells, the energetic balance between the chemical energy of the reactants and the electrical energy produced by the fuel cell is used. This energy can be calculated by the change in the Gibbs free energy Δ_g, which is the difference between the Gibbs free energy of the product and the Gibbs free energy of the reactants. The Gibbs free energy is used to represent the available energy to make the external work. For the hydrogen/oxygen fuel cell, the basic chemical reaction is:

$$H_2 + \frac{1}{2}O_2 \rightarrow H_2O$$

the change in Gibbs free energy Δ_g is:

$$\Delta_g = g_{producte} - g_{reac\tan s} = g_{H_2O} - g_{H_2} - g_{O_2} \qquad 3.1$$

The change in Gibbs free energy depends on the temperature and the pressure:

$$\Delta_g = \Delta_{g0} - RT \ln \frac{p_{H_2} p_{O_2}^{\frac{1}{2}}}{p_{H_2O}} \qquad 3.2$$

where:

- Δ_{g0} is the change in Gibbs energy at the standard pressure of 1 bar;
- T is the stack temperature (K);
- R is the universal gas constant
- p_{H_2} is the hydrogen partial pressure (bar)
- p_{O_2} is the oxygen partial pressure (bar)
- p_{H_2O} is the vapour partial pressure (bar)

The energy is produced by the reaction, because the value of the Δ_{g0} is negative. If the fuel cell is a reversible process, then the whole Gibbs free energy is entirely converted into electrical energy, which represents the energy used to move the electrical charges through the external circuit. In reality, the real fuel cell system is an irreversible process, where there are several phenomena of energetic losses. For each mole of hydrogen, two moles of electrons flow trough the external circuit and the electrical work made is:

$$L = -2FE \qquad 3.3$$

where:

- F is the Faraday constant, which represents the electric charge of one mole of electrons (96.485 C);
- E is the voltage of the fuel cell.

If the system were reversible:

$$\Delta_g = -2EF \qquad 3.4$$

$$\Delta_{g0} - RT \ln \frac{p_{H_2} p_{O_2}^{\frac{1}{2}}}{p_{H_2O}} = -2EF \qquad 3.5$$

Thus, using the equation 3.5, the reversible voltage of fuel cell is obtained:

$$E = -\frac{\Delta g}{2F} = -\frac{\Delta g_0}{2F} + \frac{RT}{2F}\ln\frac{p_{H_2}\, p_{O_2}^{\frac{1}{2}}}{p_{H_2O}} \qquad \textit{Nernst's equation} \qquad 3.6$$

The real fuel cell process is not a reversible process, because a part of the chemical energy is converted in heat and then the voltage difference of fuel cell is less then the value given by equation 3.6. The voltage E in the equation 3.6 is called the reversible open circuit voltage or "Nernst" voltage of a hydrogen fuel cell.

The term $-\frac{\Delta g_0}{2F}$ changes in accordance with the temperature:

$$-\frac{\Delta_{g0}}{2F} = 1.229 + (T - T_0)(\frac{\Delta S^0}{2F}) \qquad 3.7$$

where:

- T_0 is the standard temperature (298,15 K);
- ΔS^0 is the entropy change $(J/K \cdot mol)$.

The entropy changes of the reaction can be considered constant and can be set to the standard value, because the changes of the specific heat are minimal in respect to the stack temperature. This yields:

$$-\frac{\Delta_{g0}}{2F} = 1.229 - \frac{298.15\Delta S^0}{2F} + \left(\frac{\Delta S^0}{2F}\right)T_{fc} \qquad 3.8$$

Using the standard value of the entropy changes and the value of the constant F in the equation 3.8 , the Nernst voltage equation assumes the following form:

$$E = 1.229 - 0.85\cdot 10^{-3}(T - 298{,}15) + 4{,}3085\cdot 10^{-5}T\left[\ln\left(p_{H_2}\right) + \frac{1}{2}\ln\left(p_{O_2}\right)\right] \qquad 3.9$$

The voltage value calculated by the equation 3.9 is expressed in Volt if the pressures are expressed in atm and the temperature in K.

The fuel cell losses in the real fuel cell can be classified in the following three categories:

- activation loss;
- ohmic loss;
- concentration loss.

3.2.1 Activation Loss

The activation losses (called activation over voltages) depends on the necessity to move electrons, on the collisions between the reactants molecules and on the formation of chemical bonds in the anode and in the cathode. The activation over voltages occurs at both fuel cell electrodes (anode and cathode), but the reaction of hydrogen oxidation at the anode is faster than the reaction of oxygen reduction at the cathode. The following equation expresses the relationship between the activation overvoltage v_{act} and the current density of the fuel cell i:

$$v_{act} = A\ln\left(\frac{i}{i_0}\right) \qquad \textit{Tafel's equation} \qquad 3.10$$

where A is a constant, i_0 is the exchange current density: they are computed by an empiric methodology. The constant A assume big values when the reaction is slow and then the activation loss depends strongly on the cathode condition, because the reaction in this electrode is slower than the anode reaction. The constant i_0 represents the least value of the current density for which the activation overvoltage is different to zero. Therefore the Tafel's equation is valid when i> i_0 .

The Tafel's equation was deduced by an experimental method, but it has also a theoretical justification. In fact, it can be shown that, in a fuel cell where for each mole of hydrogen are produced two moles of electrons, the constant A is:

$$A = \frac{RT}{2\alpha F} \qquad 3.11$$

where :

- α is the transfer constant of charge, that is the part of electrical energy used to change the speed reaction. Its value depends on the type of the chemical reaction and the type of material of electrodes; its change in the range [0,1];
- T is the fuel cell temperature (K). The formula 3.11 shows that when the stack temperature increases, then the constant A and the activation overvoltage increases.

The reduction of the activation overvoltage can be obtained by changing the value of i_0, which can vary in a large range. Also, the value of i_0 depends on the type of material of electrodes. The global reaction of a fuel cell is:

$$O_2 + 4H^+ + 4e^- \Rightarrow 2H_2O \qquad 3.12$$

if the current density is equal to zero, the reaction 3.12 does not exist because otherwise there should be a production of free electrons. In reality, this reaction always exists in the both directions (direct and inverse) and then there is the following chemical equilibrium:

$$O_2 + 4H^+ + 4e^- \Leftrightarrow 2H_2O\,. \qquad 3.13$$

Then there is an electron flow from and to the electrolyte and this current represents the term i_0. If the value of this current density is greater, then the surface area of the electrode has a greater chemical activity and this increase the probability to have a current flow in a specific direction.

It is possible to facilitate the electron mobility by a link with an external load. The value of i_0 is very important to control the performance of the fuel cell and then this current must achieve the maximum possible value. If only the voltage drop caused by activation losses is considered, then the fuel cell voltage is:

$$v_{fc} = E - A\ln\left(\frac{i}{i_0}\right) \qquad 3.14$$

where E represents the voltage difference between the fuel cell electrodes, gives by the Nernst's equation. The following figure shows the voltage drop caused by activation losses, where the red line represents the fuel cell voltage without losses.

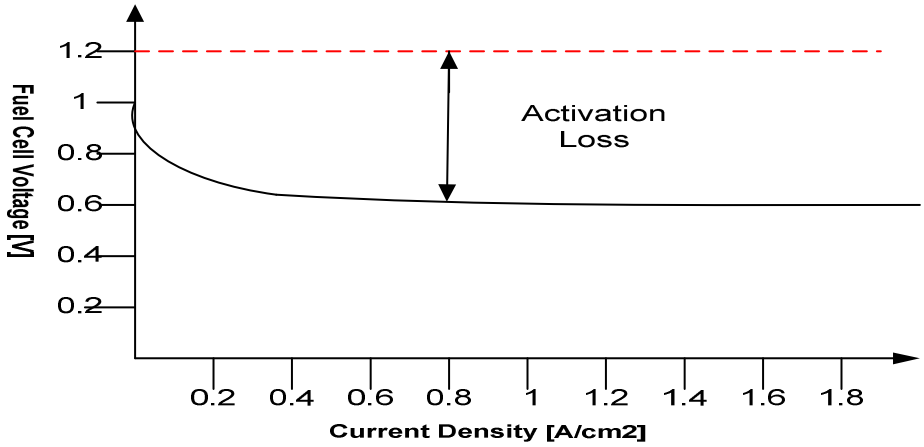

Fig. 3.4. Characteristic of PEM cell considering only the activation loss.

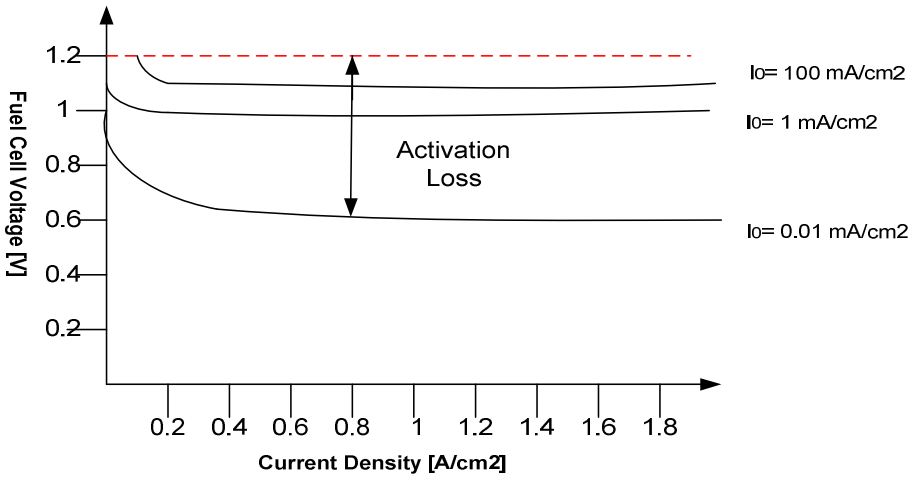

Fig. 3.5 Activation loss for several values of exchange current density i_0.

Figure 3.5 shows the fuel cell voltage as a function of the current density when there is only the activation loss and for different values of the exchange current density i_0. The activation loss near the cathode is greater than the activation loss near the anode, because the chemical reaction in the cathode is slower than the reaction in the anode. Nevertheless, in some types of fuel cell, for example for the fuel cell with forward methanol, the anodic overvoltage is not negligible and it is necessary to consider another term of the potential difference given from equation 3.10. The activation voltage is:

$$v_{act} = A_{an} \ln\left(\frac{i}{i_{0an}}\right) + A_{cat} \ln\left(\frac{i}{i_{0cat}}\right) \qquad 3.15$$

where:

A_{an} and A_{cat} are the anode and cathode constants, respectively;

i_{0an} (A/cm^2) and i_{0cat} (A/cm^2) are the exchange current density in the anode and in the cathode, respectively

or $v_{act} = A \ln\left(\frac{i}{b}\right)$ 3.16

where $A = A_{an} + A_{cat}$ and $b = i_{0an}^{\frac{A_{an}}{A}} + i_{0cat}^{\frac{A_{cat}}{A}}$.

To improve the implementation of the stack model, the equation 3.16 is approximated by the following equation:

$$v_{act} = v_0 + v_a\left(1 - e^{-c_1 i}\right) \qquad 3.17$$

where:

- v_0 is the voltage drop when the current density is equal to zero;
- v_a and c_1 are two constants that are determined by using regressive methods to solve the equation 3.16 and the experimental data.

The term v_0 is a function of the stack temperature, the cathode pressure and the saturation pressure:

$$v_0 = 0{,}279 - 8{,}5 \cdot 10^{-4}\left(T_{fc} - 298{,}15\right) + 4{,}308 \cdot 10^{-5} \cdot T_{fc}\left[\ln\left(\frac{p_{ca} - p_{sat}}{1{,}01325}\right) + \frac{1}{2}\ln\left(\frac{0{,}1173\left(p_{ca} - p_{sat}\right)}{1{,}01325}\right)\right]$$

where v_a is: 3.18

$$v_a = \left(1{,}618 10^{-5} T_{fc} + 1{,}618 10^{-2}\right) \cdot \left(\frac{p_{O_2}}{0{,}1173} + p_{sat}\right)^2 + \left(-1{,}8^{-4} T_{fc} - 0{,}166\right) \cdot \left(\frac{p_{O_2}}{0{,}1173} + p_{sat}\right)^2 + \left(-5{,}8 \cdot 10^{-4} \cdot T_{fc} + 0{,}5736\right)$$

and c_1 is equal to 10. [43] 3.19

It is necessary to increase the value of i_0 to reduce the activation loss, especially near the cathode, and to reach this objective several ways can be followed:

- to increase the fuel cell temperature (by reaching the temperature of 800°C, it is possible to have $i_0 = 10\frac{mA}{cm^2}$;
- to use different catalyst (Table II shows several values of i_0 like a function of the type of metal);
- to increase the roughness of the electrodes to increase the real contact surface with the reactants;
- to increase the concentration of the reactants by replacing, for example, atmospheric air with pure oxygen;
- to increase the pressure of the reactants.

Type of metal	Exchange current density(A/cm^2)
LEAD	$2.5 \cdot 10^{-13}$
ZINC	$3 \cdot 10^{-11}$
SILVER	$3 \cdot 10^{-7}$
NIKEL	$6 \cdot 10^{-6}$
PLATINUM	$5 \cdot 10^{-4}$
PALLADIUM	$4 \cdot 10^{-3}$

TABLE II. Exchange current density versus kind of electrode metal.

3.2.2 Ohmic Loss

The ohmic loss depends on the resistance of the polymer membrane to the transfer of protons and the resistance of the electrode and the collector plate to the transfer of electrons. The voltage drop that corresponds to the ohmic loss is proportional to the current density:

$$v_{ohm} = i \cdot R_{ohm} \qquad 3.20$$

where

- i is the current density, which has units $\frac{A}{cm^2}$;
- R_{ohm} is the internal electrical resistance, which has units $\Omega \cdot cm^2$.

This resistance depends mainly on the electrolyte, but the link resistance should be considered when several fuel cells are linked together. The value of the output voltage of the fuel cell, when there is only the ohmic loss, is given by:

$$v_{fc} = E - i \cdot R_{ohm} \qquad 3.21$$

where E represents the output fuel cell voltage when its is open.

The resistance depends strongly on the membrane humidity and the cell temperature and several studies shows that the ohmic resistance is a function of the membrane conductivity σ_m (S/m):

$$R_{ohm} = \frac{t_m}{\sigma_m} \qquad 3.22$$

where t_m is the thickness of the membrane and the membrane conductivity σ_m is a function of the membrane water content λ and the fuel cell temperature. The variation of the membrane conductivity with different membrane humidity and temperature is:

$$\sigma_m = b_1 \exp\left(b_2 \left(\frac{1}{303} - \frac{1}{T_{fc}} \right) \right) \qquad 3.23$$

where b_2 is a constant calculated by an empirical way, while the parameter b_1 is:

$$b_1 = \left(b_{11}\lambda - b_{12} \right) \qquad 3.24$$

and also b_{11} e b_{12} are calculated by an empirical way.

Then the ohmic voltage drop is:

$$v_{ohm} = \frac{i \cdot t_m}{b_1 \exp\left(b_2\left(\frac{1}{303} - \frac{1}{T_{fc}}\right)\right)} \qquad 3.25$$

The ohmic losses must be considered in all types of fuel cells and in particular in the SOFC fuel cells (solid oxide fuel cell).

The following figure shows the voltage trend when the current density produced changes and when only the ohmic losses are considered.

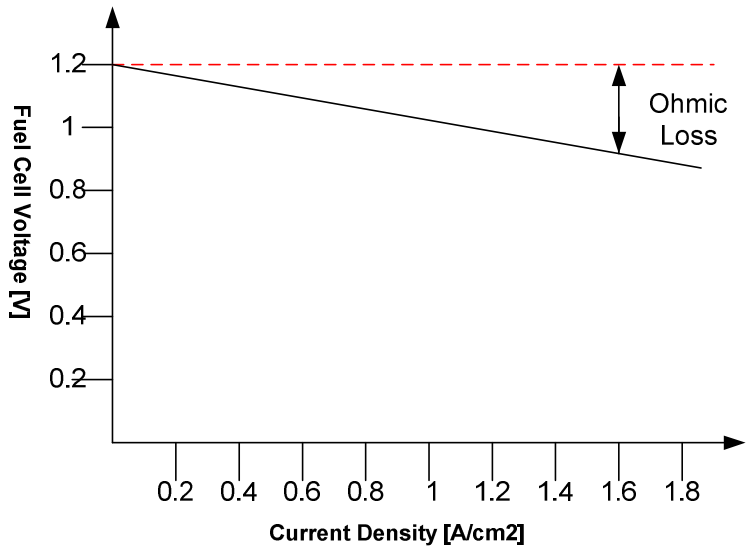

Figure 3.6. Characteristic of a PEM fuel cell when only the ohmic losses are considered.

The red colour represents the ideal trend of the voltage without losses. The ways to reduce the ohmic losses are the following:

- to use electrodes with big conductivity;
- to use appropriate materials for the bipolar dishes;
- to use an electrolyte membrane with small thickness.

The last methodology is not applicable because the membrane must have the same thickness of the mechanic support where the electrodes are lodged. In general the membrane thickness must give the mechanic robustness for the whole fuel cell and it must guarantee that there are not contacts between the two electrodes.

3.2.3 Concentration Loss

Concentration loss results from the drop in concentration of the reactants, oxygen and hydrogen, which changes during the reaction. In fact, during the operation of the fuel cell there is a light reduction of oxygen concentration near the electrode where the reaction of reduction happens (cathode). This reduction of oxygen concentration causes a reduction of the partial pressure of the oxygen and then a reduction of the electromotive force with the terminals open, in relationship of the following formula:

$$E = -\frac{\Delta g_0}{2F} + \frac{RT}{2F}\ln\frac{p_{H_2}\cdot p_{O_2}}{p_{H_2O}} \qquad 3.26$$

For these losses there are speed voltage drops when there are big values of density current.

The reduction of the oxygen concentration depends on the electrical current produced and on other factors that depend on the air circulation near the cathode.

Likewise there is a reduction of the hydrogen concentration near the electrode region where the reaction of oxidation occurs (anode). This reduction of hydrogen concentration depends on the same phenomena already examined for the reduction of the oxygen concentration. The final result is always a reduction of the partial pressure of the hydrogen and then a reduction of the electromotive force with the terminals open in relationship of the following formula:

$$E = -\frac{\Delta g}{2F} = -\frac{\Delta g_0}{2F} + \frac{RT}{2F}\ln\frac{p_{H_2}\cdot p_{O_2}}{p_{H_2O}} \qquad 3.27$$

The reduction of the voltage between the terminals of the fuel cell, when there is a reduction of the hydrogen partial pressure, is given from the following formula:

$$\Delta V = \frac{RT}{2F}\ln\left(\frac{p_2}{p_1}\right) \qquad 3.28$$

where:

- p_1 is the value of the hydrogen partial pressure when the current density produced is equal to zero;
- p_2 is the value of the hydrogen partial pressure when the current density produced is equal to the generic value i.

The current density i can have only values in the range $[0, i_1]$. The value i_1 is the maximum current density that can be produced by the fuel cell under study and therefore it is the value of the current when the hydrogen partial pressure is equal to zero. This value of current defines the maximum speed reaction of the fuel cell.

By assuming a linear relationship between the hydrogen partial pressure and the current density produced (under the hypothesis that there is a system of air recirculation near the anode able to satisfy the reduction of the oxygen partial pressure) then the generic value of the pressure p_2 is:

$p_2 = p_1\left(1-\frac{i}{i_1}\right)$ and replacing this formula into the 3.28 :

$$\Delta V = \frac{RT}{2F}\ln\left(1-\frac{i}{i_1}\right) \qquad 3.29$$

Since the term into the parenthesis is less then one, then the voltage change is negative and represents a voltage drop.

The difference voltage between the output terminals of the fuel cell, considering only the concentration loss is:

$$v_{fc} = E - \frac{RT}{2F}\ln\left(1-\frac{i}{i_1}\right) = E - B\ln\left(1-\frac{i}{i_1}\right) \qquad 3.30$$

The temperature effects and the discard products effects are not considered in this relationship.

An empirical relationship simpler than the previous one, that allows the concentration voltage drop to be computed, is the following:

$$v_{con} = i\left(c_2\frac{i}{i_{\max}}\right)^{c_3} \qquad 3.31$$

where c_2 , c_3 and i are constants that depend on the temperature and the partial pressures of the reagents and can be calculated by an empirical way. The parameter i_{max} is the maximum value of the current density.

The way to calculate the value of the parameter c_3 is explained in [42].

The parameter c_2 is calculated by the following equations that depend on the term $\frac{p_{O_2}}{0.1173} + p_{sat}$:

$$\begin{cases} \left(7{,}16 \cdot 10^{-4} T_{fc} - 0{,}622\right) \cdot \left(\frac{p_{O_2}}{0.1173} + p_{sat}\right) + \left(-1{,}45 \cdot 10^{-3} T_{fc} + 1{,}68\right) \; se \; \frac{p_{O_2}}{0.1173} + p_{sat} < 2atm \\ \left(8{,}66 \cdot 10^{-5} T_{fc} - 0{,}068\right) \cdot \left(\frac{p_{O_2}}{0.1173} + p_{sat}\right) + \left(-1{,}6 \cdot 10^{-4} T_{fc} + 0{,}54\right) \; se \; \frac{p_{O_2}}{0.1173} + p_{sat} > 2atm \end{cases}$$

3.32

The saturation pressure is calculated by the following relationships:

$$\begin{aligned} &6{,}853 \cdot 10^{-7} \cdot T_{st}^4 - 7{,}432 \cdot 10^{-4} \cdot T_{st}^3 + 0{,}304 \cdot T_{st}^2 - 55{,}613 \cdot T_{st} + 3{,}831 \cdot 10^3 = p_{sat} \; if \; T_{st} < 333{,}15K \\ &1{,}508 \cdot 10^{-6} \cdot T_{st}^4 - 0{,}0018 \cdot T_{st}^3 + 0{,}857 \cdot T_{st}^2 - 1{,}796 \cdot 10^2 \cdot T_{st} + 1{,}428 \cdot 10^4 = p_{sat} \; if \; 333{,}15K < T_{st} < 433{,}15K \\ &1{,}338 \cdot 10^{-6} \cdot T_{st}^4 - 0{,}0015 \cdot T_{st}^3 + 0{,}654 \cdot T_{st}^2 - 1{,}191 \cdot 10^2 \cdot T_{st} + 7{,}506 \cdot 10^3 = p_{sat} \; if \; 433{,}15K < T_{st} < 533{,}15K \\ &1{,}648 \cdot 10^{-6} \cdot T_{st}^4 - 0{,}0020 \cdot T_{st}^3 + 1{,}017 \cdot T_{st}^2 - 2{,}241 \cdot 10^2 \cdot T_{st} + 1{,}878 \cdot 10^4 = p_{sat} \; if \; 533{,}15K < T_{st} \end{aligned}$$

3.33

The parameters of the relationship 3.33 are calculated by the interpolating polynomial of fourth degree of the table of the thermodynamics properties of the water vapour [42].

The following figure shows the waveform of the voltage when the current density changes and when only the concentration loss is considered.

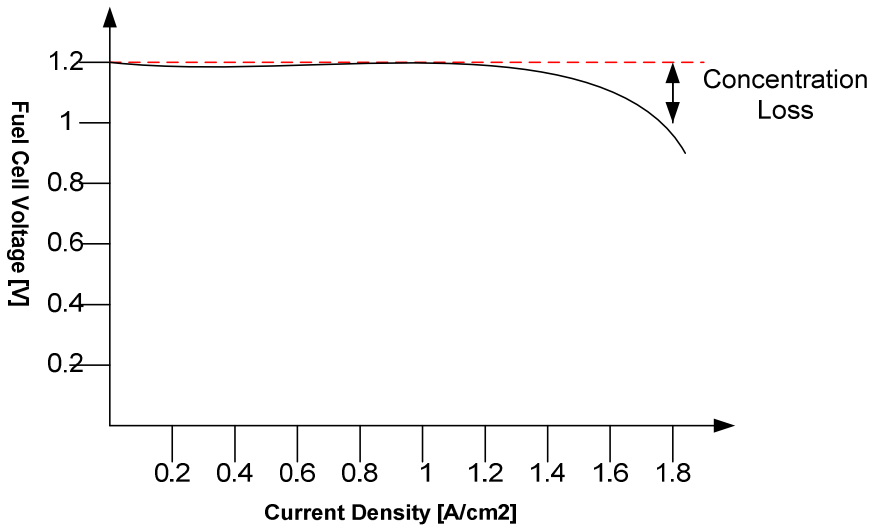

Fig. 3.7 Characteristics of a PEM fuel cell only considering the concentration losses.

The red colour represents the ideal waveform of the voltage without losses.

Figure 3.7 shows that the voltage drop due to the concentration losses is remarkable when the current density produced is greater then the threshold (about $0{,}8\frac{A}{cm^2}$), because the partial pressures of reactants decreases substantially.

The concentration losses achieve a remarkable value when the hydrogen originates from renewable sources, then the increase of the quantity of hydrogen could be insufficient to satisfy the request of the control system of the flow rate of the reactants. The loss of concentration in the cathode could have the same problem, when the recirculation air system is not efficient. When the oxygen present in the air is consumed, the quantity of nitrogen is very elevated and then, when the current requests from the load is big, the system of restocking of the oxygen could have problems.

In the PEM-FC the elimination of the water produced could cause other concentration losses, because in reality the water vapour is carried with the air that contains oxygen.

3.2.4 Fuel cell dynamic effects

Near the interface electrode/electrolyte there is a layer of charge, called the “charge double layer” [1], where electrical charge and then energy are stored. This layer has the same behaviour as an electrical capacitor. The electrical voltage generated by this capacitor corresponds to the combination of activation and concentration voltage considered previously. The presence of this electrical charge produces a non-instantaneous change of the activation and concentration voltage, when the current suddenly changes. Moreover the ohmic voltage drop responds instantaneously to a change in the current. To model the dynamic behaviour of the fuel cell, it is used the equivalent circuit shown in figure 1.8. In this circuit R_{ohm} is the ohmic resistance of the fuel cell, R_{conc} is the concentration resistance R_{act} is the activation resistance and C is the electrical capacitance that represents the “charge double layer” phenomenon. These parameters are used in the following equation:

$$R_{act} = \frac{\left[v_0 + v_a(1 - e^{-c_1 i})\right]}{i} \qquad 3.34$$

$$R_{conc} = (c_2 \frac{i}{i_{\max}})^{c_3} \qquad 3.35$$

$$C = \varepsilon \frac{A}{d} \qquad 3.36$$

Where ε is the dielectric constant of the membrane, A is the surface of the electrode and d is the distance between the two contiguous dishes.

The dynamic fuel cell behaviour can be described by the following equations:

$$C\frac{dv_C}{dt}+\frac{v_C-v_0}{R_{act}+R_{conc}}=i \qquad 3.37$$

$$v_{fc}=E-v_c-iR_{ohm} \qquad 3.38$$

The time constant of the fuel cell RC is not well established in the literature, but the author in [44] considered the time constant of 10^{-19} s, which indicates extremely fast dynamics. However, the charge double layer phenomenon is faster than other dynamics that are considered in the mathematical model of the fuel cell.

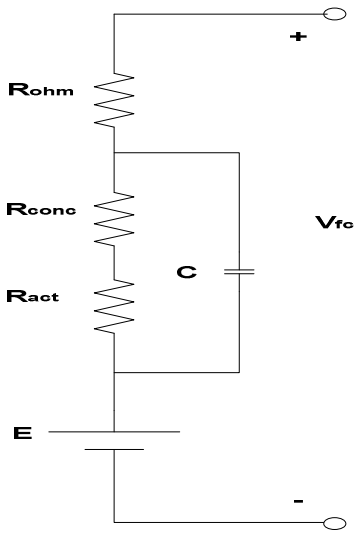

Fig. 3.8. Dynamic fuel cell equivalent circuits.

3.3 Cathode Flow Model

The cathode mass flow model represents the flow behaviour inside the cathode of the fuel cell stack. The model is developed by using the mass conservation principle and thermodynamic and psychometric characteristics of air [45]. The mass balance of oxygen, nitrogen and water, in the cathode volume, is shown in figure 3.9. The states of the model are oxygen mass $m_{O_2,ca}$, nitrogen mass $m_{N_2,ca}$ and the water mass $m_{w,ca}$.

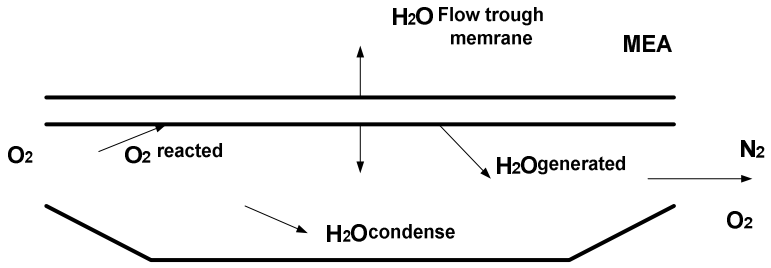

Fig. 3.9. Cathode mass flow.

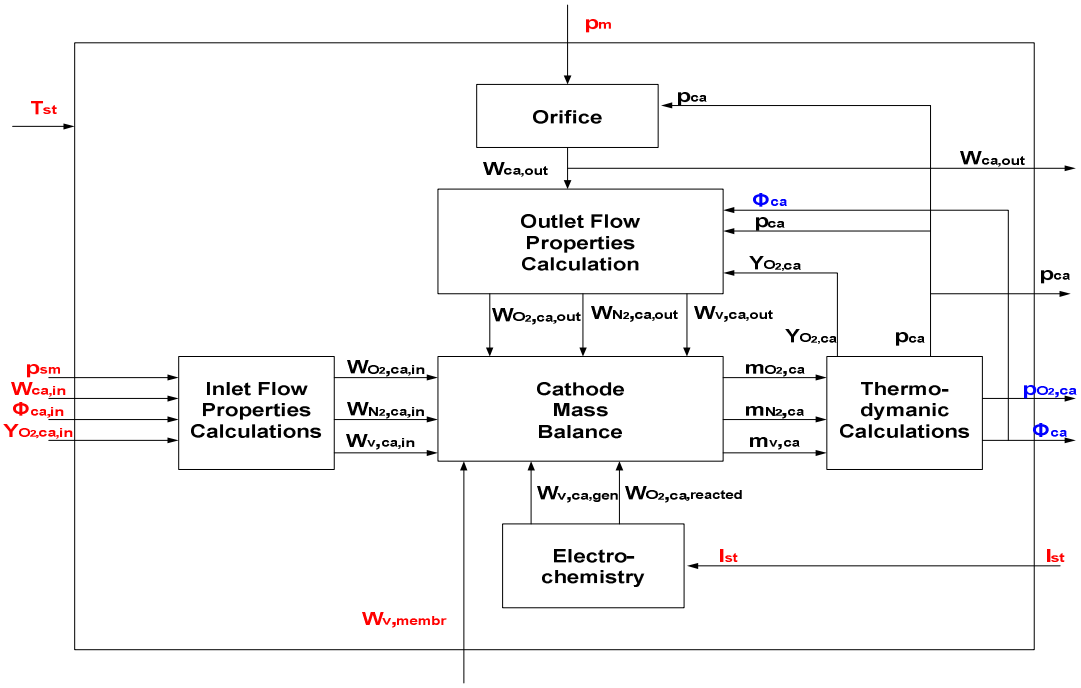

Fig. 3.10. Block Diagram of the Cathode flow model.

$$u = \begin{bmatrix} p_{rm} \\ W_{ca,in} \\ I_{st} \end{bmatrix} \qquad x = \begin{bmatrix} m_{O2} \\ m_{N2} \\ m_v \end{bmatrix}$$

The block diagram shown in Figure 3.10 represents the cathode flow model.

Red colour is used to show the external inputs of the cathode model:

- I_{st} stack current (A);
- p_{sm} supply manifold total pressure (Pa);
- p_{rm} return manifold total pressure (Pa);
- $W_{ca,in}$ input mass flow rate (kg/s);
- $\phi_{ca,in}$ input humidity;
- $y_{O_2,ca,in}$ input oxygen mole fraction;
- $T_{ca,in}$ inlet flow temperature (K).

Blue colour shows very important variables of the cathode flow model:

- $p_{O_2,ca}$ oxygen partial pressure (Pa);
- $\phi_{ca,out}$ output humidity.

Black colour shows the variables used to implement the equations of the others model :

- $W_{N_2,ca,in}$ mass flow rate of nitrogen gas entering the cathode (kg/s);
- $W_{O_2,ca,in}$ mass flow rate of oxygen gas entering the cathode (kg/s);
- $W_{v,ca,in}$ mass flow rate of vapour entering the cathode (kg/s);
- $W_{v,memb}$ mass flow rate of water transfer across the membrane (kg/s);
- $W_{v,ca,gen}$ rate of vapour generated in the fuel cell reaction (kg/s);
- $W_{O_2,ca,reacted}$ rate of oxygen reacted (kg/s);
- $m_{O_2,ca}$ oxygen mass (kg);
- $m_{N_2,ca}$ nitrogen mass (kg);
- $m_{v,ca}$ water mass (kg);
- $W_{N_2,ca,out}$ mass flow rate of nitrogen gas leaving the cathode (kg/s);
- $W_{O_2,ca,out}$ mass flow rate of oxygen gas leaving the cathode (kg/s);
- $W_{v,ca,out}$ mass flow rate of vapour leaving the cathode (kg/s);
- $W_{ca,out}$ total output mass flow rate (kg/s);
- p_{ca} total pressure in the cathode (Pa);

- $y_{O_2,ca}$ oxygen mole fraction in the cathode.
- u is the input variable
- x is the state variable

Figure 3.10 are shown six subsystems, which implement the mathematical equations used to modelled the cathode behaviour:

1) Mass continuity equations;
2) Electrochemistry equations;
3) Thermodynamic equations;
4) Computation of the input mass flow rate;
5) Computation of the output mass flow rate;
6) Computation of the total output mass flow rate.

The stack temperature can be calculated using a model of stack heat transfer, but it is assumed constant in this study.

Several assumptions are made:

- all gases are assumed as ideal gases ;
- the stack temperature is controlled by the cooling system so that its temperature is maintained constant at 80°C;
- the temperature in the cathode is assumed to be equal to the stack temperature ($T_{ca} = T_{st}$);
- the output variables of the cathode, like the humidity, the total pressure and the oxygen molar fraction, are assumed to be the same as the variables inside the cathode flow channel ($p_{ca}, \phi_{ca}, y_{O_2,ca}$);
- the flow channel and the cathode layer are lumped into one volume V_{ca} and spatial variations are ignored.
- The presence of water vapour and water liquid in the electrode, which is a porous material, has been neglected.
- No output variables are instrumented for measurement.

Moreover, when the relative humidity of the cathode gas exceeds 100%, the vapour condenses into a liquid form. This liquid water does not leave the stack and will evapourate into the cathode gas if the gas humidity drops below 100% or it will accumulate in the cathode.

3.3.1 Mass continuity Equations

The mass continuity is used to balance the mass oxygen, nitrogen and water inside the cathode volume, and yields the following equations:

a) $$d\frac{m_{O_{2,ca}}}{dt} = W_{O_{2,ca,in}} - W_{O_{2,ca,out}} - W_{O_{2,react}} \quad 3.39$$

b) $$d\frac{m_{N_{2,ca}}}{dt} = W_{N_{2,ca,in}} - W_{N_{2,ca,out}} \quad 3.40$$

c) $$d\frac{m_{w,ca}}{dt} = W_{v,ca,in} - W_{v,ca,out} + W_{v,ca,gen} + W_{v,membr} - W_{l,ca,out} \quad 3.41$$

where $W_{l,ca,out}$ is the rate of liquid water leaving the cathode.

$W_{v,menbrana}$ is the mass flow rate of water transfer across the membrane. The flow rate of liquid water leaving the cathode is zero $W_{l,ca,out}$ =0.

3.3.2 Electrochemistry Equations

Electrochemistry principles are used to calculate the rate of oxygen consumption and water production in the fuel cell reaction. The flow rate is a function of the stack current:

$$W_{O_2,react} = M_{O_2} \cdot n\frac{I_{st}}{4F}; \quad 3.42$$

$$W_{v,ca,gen} = M_v \cdot n\frac{I_{st}}{2F} \quad 3.43$$

where:

- M_{0_2} oxygen molar mass (Kg/mol);
- M_v vapour molar mass (Kg/mol);
- n is the number of cells in the stack ;
- F is the Faraday number.

3.3.3 Thermodynamic Equations

The water inside the cathode volume can be in two forms, vapour and liquid, depending on the saturation state of the cathode gas.

The maximum mass of vapour that the gas can hold $m_{v,\max,ca}$ is calculated from the vapour saturation pressure:

$$m_{v,\max,ca} = \frac{p_{sat} \cdot V_{ca}}{R_v \cdot T_{st}} \qquad 3.44$$

Where R_v is the gas constant of vapour.

If the mass of water computed in equation 3.39 is more than that of the saturated state, the extra vapour is assumed to condense into a liquid form instantaneously. Thus, the mass of vapour and liquid water is calculated by:

If $m_{w,ca} \le m_{v,\max,ca} \rightarrow m_{v,ca} = m_{w,ca}$ 3.45

If $m_{w,ca} > m_{v,\max,ca} \rightarrow m_{v,ca} = m_{v,\max,ca}$ 3.46

$$m_{l,ca} = m_{w,ca} - m_{v,\max,ca}\,. \qquad 3.47$$

3.3.4 Computation of the input mass flow rate.

Using the masses of oxygen, nitrogen, and vapour and the stack temperature, the pressure and the relative humidity of the gas inside the cathode channel can be calculated:

$$p_{O_{2,ca}} = \frac{m_{O_{2,ca}} \cdot R_{O_2} \cdot T_{ST}}{V_{ca}}; \qquad 3.48$$

$$p_{N_{2,ca}} = \frac{m_{N_{2,ca}} \cdot R_{N_2} \cdot T_{ST}}{V_{ca}}; \qquad 3.49$$

$$p_{v,ca} = \frac{m_{v,ca} \cdot R_{v_2} \cdot T_{ST}}{V_{ca}}\,. \qquad 3.50$$

The unit of measurement of the pressure is the Pascal in the previous equations and the Bar in the Nernst formula. The measurement compatibility can be obtained by dividing for 10^{-5} the equations 3.48, 3.49 and 3.50.

The partial pressure of dry air $p_{a,ca,in}$ is the sum of oxygen and nitrogen partial pressure:

$$p_{a,ca,in} = p_{O_{2,ca}} + p_{N_{2,ca}} \quad 3.51$$

Also, the input oxygen mole fraction $y_{O_2,ca,in}$ can be used to compute $p_{a,ca,in}$:

$$p_{a,ca,in} = \frac{p_{O2,ca,in}}{y_{O_2,ca,in}} \quad 3.52$$

The humid air is the mixture of dry air and vapour, then the dry air partial pressure is the difference between the air total pressure $p_{ca,in}$ and the vapour partial pressure:

$$p_{a,ca,in} = p_{ca,in} - p_{v,ca,in} \quad 3.53$$

The vapour partial pressure at the input of the cathode channel is obtained by the relative humidity of the input mass flow:

$$p_{v,ca,in} = \phi_{ca,in} \cdot p_{sat}\left(T_{ca,in}\right) \quad 3.54$$

where:

- $p_{sat}\left(T_{st}\right)$ is the vapour saturation pressure, a function of stack temperature;
- $\phi_{ca,in}$ is the humidity of the input mass flow.

The mass flow rate of dry air and vapour entering the cathode is:

$$W_{a,ca,in} = \frac{1}{1+\omega_{ca,in}} W_{ca,in}; \quad 3.55$$

$$W_{v,ca,in} = W_{ca,in} - W_{a,ca,in}; \quad 3.56$$

Where $\omega_{ca,in}$ is the humidity ratio and is defined as the ratio of the mass of water vapour to the mass of dry air:

$$\omega_{ca,in} = \frac{M_v}{M_{a,ca,in}} \cdot \frac{p_{v,ca,in}}{p_{a,ca,in}} \quad 3.57$$

where:

- $M_{a,ca,in}$ is dry air molar mass;
- M_v is the vapour molar mass.

The air molar mass is calculated by:

$$M_{a,ca,in} = y_{O_{2,ca,in}} \cdot M_{O_2} + \left(1 - y_{O_{2,ca,in}}\right) \cdot M_{N_2} \quad 3.58$$

where :

- $y_{O_{2,ca,in}}$ is the oxygen molar fraction;
- M_{O_2} is the molar mass of oxygen;
- M_{N_2} is the molar mass of nitrogen.

The oxygen mass flow rate can be calculated by:

$$W_{O_{2,ca,in}} = X_{O_{2,ca,in}} W_{a,ca,in} \ . \quad 3.59$$

where $X_{O_{2,ca,in}}$ is the oxygen concentration into one Kg of dry air.

The nitrogen mass flow rate can be calculated by:

$$W_{N_{2,ca,in}} = \left(1 - X_{O_{2,ca,in}}\right) \cdot W_{a,ca,in} \quad 3.60$$

$$X_{O_{2,ca,in}} = \frac{m_{O_2}}{m_{airdry}} = \frac{y_{0_{2,ca,in}} M_{0_2}}{y_{0_{2,ca,in}} M_{0_2} + \left(1 - y_{0_{2,ca,in}}\right) M_{N_2}} \quad 3.61$$

The mass flow rate entering the cathode $W_{ca,in}$ is the sum of the mass flow rate of water injected from external side $W_{v,inj}$ and the mass flow rate entering the air cooler system W_{cl}, which is also, the mass flow rate in the output of the supply manifold $W_{sm,out}$:

$$W_{ca,in} = W_{cl} + W_{v,inj} = W_{sm,out} + W_{v,inj} \quad 3.62$$

The gas total pressure entering the cathode, $p_{ca,in}$, is computed by the following equation:

$$p_{ca,in} = p_{a,cl} + \phi_{des} \cdot p_{sat}\left(T_{cl}\right) \quad 3.63$$

where:

- $p_{a,cl}$ is the air pressure inside the air cooler system;
- ϕ_{des} is the value of the desired relative humidity ;
- $p_{sat}(T_{cl})$ is the saturation pressure of the water inside the air cooler system.

The knowledge of the mass flow rate in the output of the cathode, of oxygen mass flow rate, of nitrogen mass flow rate and of vapour mass flow rate allows the output variables of the cathode to be computed, by using the same methodology adopted to obtain the input variables of the cathode.

3.3.5 Computation of the output mass flow rate.

Using the masses of oxygen, nitrogen, and vapour and the stack temperature, the pressure and the relative humidity of the gas inside the cathode channel can be calculated by:

$$p_{O_{2t},ca,out} = p_{O_2,ca}\,; \tag{3.64}$$

$$p_{N_{2,},ca,out} = p_{N_2,ca}\,; \tag{3.65}$$

$$p_{v,ca,out} = p_{v,ca}\,. \tag{3.66}$$

The partial pressure of dry air $p_{a,ca,out}$ is:

$$p_{a,ca,out} = p_{O_{2,ca,out}} + p_{N_{2,ca,out}} \tag{3.67}$$

Since humid air is the mixture of dry air and vapour, then the dry air partial pressure is the difference between the air total pressure and the vapour partial pressure:

$$p_{a,ca,out} = p_{ca,out} - p_{v,ca,out} \tag{3.68}$$

The mass flow rate of the dry air in the output of the cathode and the mass flow rate of the vapour are obtained by the following relationships:

$$W_{a,ca,out} = \frac{1}{1+\omega_{ca,out}} W_{ca,out}\,; \tag{3.69}$$

$$W_{v,ca,out} = W_{ca,out} - W_{a,ca,out}\,; \tag{3.70}$$

where

- $W_{ca,out}$ is the mass flow rate in the output of the cathode channel;
- $\omega_{ca,out}$ is the gas humidity in the output of the cathode channel.

The absolute humidity $\omega_{ca,out}$ of the gas flowing out of the cathode is given by:

$$\omega_{ca,out} = \frac{M_v}{M_{a,ca,out}} \cdot \frac{p_{v,ca,out}}{p_{a,ca,out}} \quad 3.71$$

where:

- M_v is the molar mass of the vapour;
- $M_{a,ca,out}$ is the molar mass of the dry air in the output of the cathode channel.

The molar mass of the dry air in the output of the cathode channel is:

$$M_{a,ca,out} = y_{O_{2,ca,out}} \cdot M_{O_2} + \left(1 - y_{O_{2,ca,out}}\right) \cdot M_{N_2} \quad 3.72$$

where:

- $y_{O_{2,ca,out}}$ is the oxygen molar fraction in the output of the cathode cannel;
- M_{O_2} is the oxygen molar mass in the input of the cathode channel;
- M_{N_2} is the nitrogen molar mass in the input of the cathode channel.

The oxygen molar fraction in the output of the cathode channel is:

$$y_{O_2,ca,out} = \frac{p_{O2,ca,out}}{p_{a,ca,out}}. \quad 3.73$$

The oxygen mass flow rate in the output of the cathode channel is

$$W_{O_{2,ca,out}} = X_{O_{2,ca,out}} W_{a,ca,out} \quad 3.74$$

Where $X_{O_{2,ca,out}}$ is the oxygen concentration into one Kg of dry air.

The nitrogen mass flow rate is:

$$W_{N_{2,ca,out}} = \left(1 - X_{O_{2,ca,out}}\right) \cdot W_{a,ca,out}\ . \quad 3.75$$

where $X_{O_{2,ca,out}}$ is obtained by the following equation:

$$X_{O_{2,ca,out}} = \frac{m_{O_2}}{m_{airdry}} = \frac{y_{0_{2,ca,out}} M_{0_2}}{y_{0_{2,ca,out}} M_{0_2} + \left(1 - y_{0_{2,ca,out}}\right) M_{N_2}} \quad 3.76$$

3.3.6 The orifice equation

The total flow rate in the output of the cathode channel is:

$$W_{ca,out} = k_{ca}(p_{ca} - p_{rm}) \qquad 3.77$$

where:

- p_{ca} is the total pressure of the cathode;
- p_{rm} is the return manifold pressure;
- k_{ca} is the orifice constant.

3.4 Anode Flow Model

For the system considered, hydrogen is compressed and stored in a hydrogen tank. The high pressure storage allows the anode inlet flow rate to be assumed to be instantaneously adjusted by a valve to maintain the minimum pressure difference between the cathode and the anode. In other words, the anode channel flow resistance is smaller than the cathode flow resistance.

The following assumptions are used:

- all gases are assumed as ideal gases ;
- the stack temperature is controller by the cooling system such that its temperature is maintained constant at 80°C;
- the temperature in the anode is assumed to be equal to the stack temperature ($T_{an} = T_{st}$);
- the output variables of the cathode, like the humidity, the total pressure and the oxygen molar fraction are assumed to be the same as the variables inside the anode flow channel (p_{ca} , ϕ_{ca} , $y_{O_2,ca}$), ;
- the flow channel and the anode layer are lumped into one volume V_{ca} and the spatial variations are ignored.
- The presence of water vapour and water liquid in the electrode, which is a porous material, has been neglected.

Figure 3.11 shows the mass flows trough the anode and figure 3.12 shows the anode block diagram.

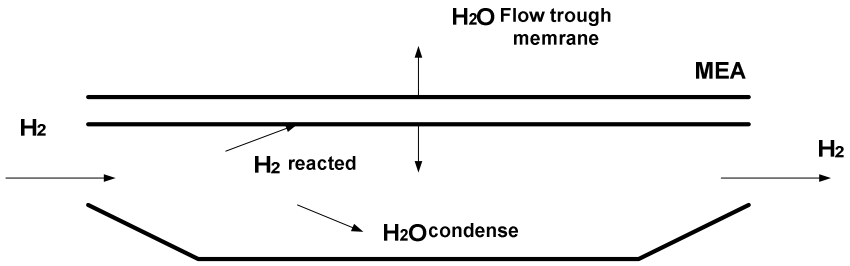

Fig. 3.11. Anode mass flow.

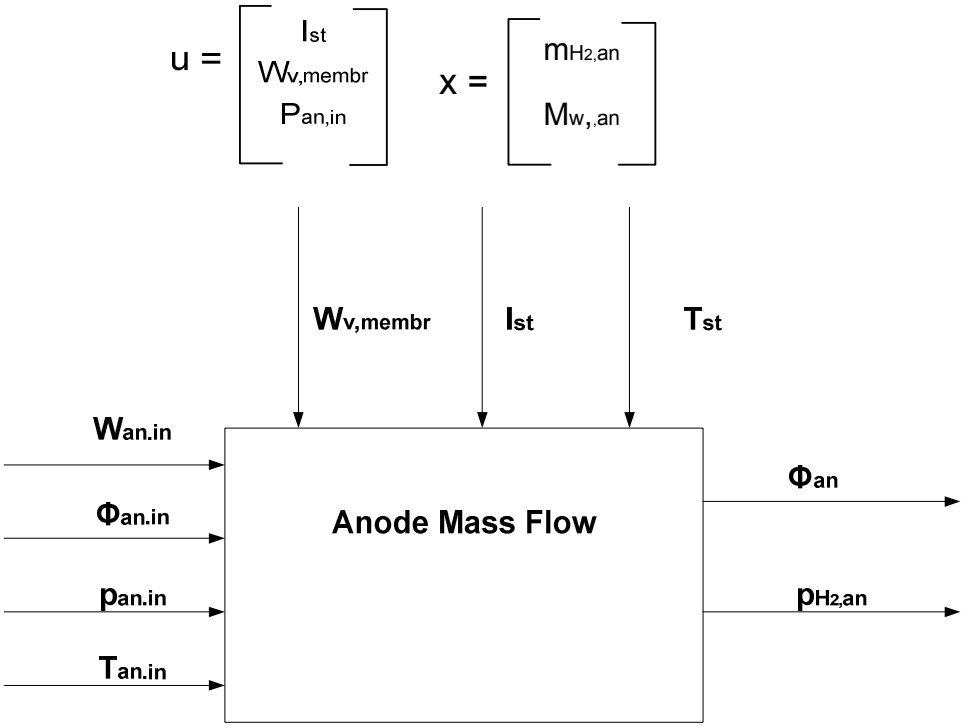

Fig. 3.12. Anode block diagram.

In the anode model the following variables are used:

- I_{st} stack current (A);
- $T_{an,in}$ inlet flow temperature (K);
- p_{sm} supply manifold pressure (Pa);
- $W_{v,menbrana}$ vapour flow rate across the membrane (kg/s);

- $W_{l,an,out}$ rate of liquid water leaving the anode (kg/s);
- p_{H_2an} hydrogen partial pressure;
- $\phi_{an,out}$ inlet flow humidity;
- $W_{v,an,in}$ mass flow rate of vapour entering the anode (kg/s);
- $W_{v,memb}$ mass flow rate of water transfer across the membrane (kg/s);
- $W_{v,an,out}$ mass flow rate of vapour leaving the anode (kg/s).
- $W_{H_2,reacted}$ rate of hydrogen reacted (kg/s);
- $m_{H_2,an}$ hydrogen mass (kg);
- $m_{v,ca}$ water mass (kg);
- $W_{H_2,an,out}$ mass flow rate of hydrogen gas leaving the anode (kg/s);
- $W_{H_2,an,in}$ mass flow rate of hydrogen gas entering the anode (kg/s);
- p_{an} total pressure in the anode channel.
- x is the state variable
- u is the input variable

In the anode model the following equations are implemented:

1. Mass continuity equations;
2. Electrochemistry equations;
3. Thermodynamic equations;
4. Computation of the input mass flow rate;
5. Computation of the output mass flow rate;
6. Computation of the total output mass flow rate;

3.4.1 Mass continuity Equations

The hydrogen and the water mass balance inside the anode allows computing the hydrogen partial pressure and the humidity of the anode flow mass.

The mass continuity principle as in the case of the cathode yield:

a) $$d\frac{m_{H_{2,an}}}{dt} = W_{H_{2,an,in}} - W_{H_{2,an,out}} - W_{H_{2,reacted}} \quad 3.78$$

b) $$d\frac{m_{w,an}}{dt} = W_{v,an,in} - W_{v,an,out} + W_{v,menbrane} - W_{l,an,out} \quad 3.79$$

The mass flow rate of water transfer across the membrane $W_{v,menbrana}$ is computed by using the membrane hydration model.

The rate of liquid water leaving the anode $W_{l,an,out}$ is set to zero, because it is assumed that the liquid water is stored in the anode and there is no passage available for it to leave the stack.

3.4.2 Electrochemistry Equations

The rate of hydrogen consumed in the reaction is a function of the stack current:

$$W_{H_2,reacted} = M_{H_2} \cdot n\frac{I_{st}}{2F} \quad 3.80$$

where:

- M_{H_2} is the hydrogen molar mass (Kg/mol);
- n is the number of cells;
- F is the Faraday number (C/mol).

3.4.3 Thermodynamic Equations

The maximum vapour mass $m_{v,\max,an}$ is calculated from:

$$m_{v,\max,an} = \frac{p_{sat} \cdot V_{an}}{R_v \cdot T_{st}} \qquad 3.81$$

where:

- p_{sat} is the vapour saturation pressure (Pa);
- V_{an} is the anodic volume (m^3);
- R_v is the vapour constant(J/Kg K);
- T_{st} is the stack temperature (K).

If the mass of water calculated in equation (3.79) is more than the maximum that the anode gas can hold, then the liquid $m_{w,an}$ forming inside the anode volume is:

se $m_{w,an} \leq m_{v,\max,an}$ then $m_{v,an} = m_{w,an}$; 3.82

se $m_{w,an} > m_{v,\max,an}$ then $m_{v,an} = m_{v,\max,an}$; 3.83

while the water condensed is:

$$m_{l,an} = m_{w,an} - m_{v,\max,an} . \qquad 3.84$$

3.4.4 Computation of the input mass flow rate

The inlet hydrogen mass flow $W_{H_{2,an}}$ and vapour mass flow $W_{v,an}$ are calculated using the anode inlet gas mass flow rate $W_{an,in}$ and the humidity $\phi_{an,in}$.

The hydrogen partial pressure of the mass flow entering in the anodic channel is computed from the following formula:

$$p_{H_{2,an,in}} = p_{an} - p_{v,an,in} \qquad 3.85$$

The vapour pressure is a function of the humidity:

$$p_{v,an,in} = \phi_{an,in} \cdot p_{sat}(T_{st}) \qquad 3.86$$

where:

- $p_{sat}(T_{st})$ is the vapour saturation pressure, which depends on the stack temperature;
- $\phi_{an,in}$ is the humidity of the mass flow entering the anode.

The mass flow rates of hydrogen and vapour entering the anode are:

$$W_{H_2,an,in} = \frac{1}{1+\omega_{an,in}} W_{an,in}; \qquad 3.87$$

$$W_{v,an,in} = W_{an,in} - W_{H_2,an,in}; \qquad 3.88$$

where $\omega_{an,in}$ is the absolute humidity of the gas entering in the anode and is:

$$\omega_{an,in} = \frac{M_v}{M_{H_2}} \cdot \frac{p_{v,an,in}}{p_{an,in}} \qquad 3.89$$

where:

- M_v is the molar mass of vapour (Kg/mol);
- M_{H_2} is the molar mass of hydrogen (Kg/mol).

3.4.5 Computation of the output mass flow rate

The anode exit flow rate $W_{an,out}$ represents the purge of anode gas to remove both liquid water and other gases accumulated in the anode (if reformed hydrogen is used).

It is assumed that the purge is zero in the model considered in this thesis. However, if the purge rate is known, the outlet hydrogen and vapour mass flow rate is calculated by the following equations:

$$\omega_{an,out} = \frac{M_v}{M_{H_2,an}} \cdot \frac{p_{v,an,out}}{p_{H_2,an,out}} \; ; \qquad 3.90$$

$$W_{H_2,an,out} = \frac{1}{1+\omega_{an,out}} W_{an,out} \; ; \qquad 3.91$$

$$W_{v,an,out} = W_{an,out} - W_{H_2,an,out} \; . \qquad 3.92$$

The relative humidity of the mass flow in the output of the anode is computer by the following formula:

$$\phi_{an,out} = \frac{p_{v,an,out}}{p_{sat}(T_{st})} \; . \qquad 3.93$$

It is assumed that the liquid water is stored in the anode and there is no passage available for it to leave the stack. Thus, the rate of liquid water leaving the anode $W_{l,an,out}$ is set to zero.

The mass of the hydrogen and vapour calculated is used to determine their partial pressures by the following equations:

$$p_{H_{2,an}} = \frac{m_{H_{2,an}} \cdot R_{H_2} \cdot T_{st}}{V_{an}} \; ; \qquad 3.94$$

$$p_{v,an} = \frac{m_{v,an} \cdot R_v \cdot T_{st}}{V_{an}} \qquad 3.95$$

3.4.6 The equation of the input orifice

The mass flow rate entering the anode is obtained by using the following equation:

$$W_{an,in} = K_1 (K_2 p_{sm} - p_{an}) \qquad 3.96$$

where:

- K_1 e K_2 are constant values: $K_1 = 2{,}1 \cdot 10^{-6} \frac{kg}{s \cdot kPa}$ e $K_2 = 0{,}94$; [1]
- p_{sm} is the pressure of the gas in the supply manifold (kPa);

- p_{an} is the output pressure of the gas in the anode (kPa).

The explication of the above formula is found in [66]: In the system considered in this study, hydrogen is supplied by a high-pressure tank and the flow rate is controlled by a valve. The inlet hydrogen flow is assumed to have 100% relative humidity. Due to the high-pressured storage, the hydrogen flow rate can be adjusted rapidly. The goal of the hydrogen flow control is to minimize the pressure difference across the membrane, i.e. the difference between the anode and cathode pressure. A P controller can be used based on the pressure difference, so that the anode pressure can quickly follow the cathode pressure variations. This P controller drives, by the valve the flow rate of hydrogen. The actual cathode pressure cannot be measured and it is approximately given the value of the supplied manifold pressure and reduce by the factor 0.94 account for the pressure drop. The anode pressure is practically equal to the supply manifold pressure because the supply manifold volume is small.

3.5 Membrane Hydration Model

The membrane hydration model allows the water content in the membrane and the rate of mass flow of water across the membrane.

The inputs of the model are the following:

- $\varphi_{ca,out}$ is the relative humidity of the flow mass in the output of the cathode;
- $\varphi_{an,out}$ is the relative humidity of the flow mass in the output of the anode;
- I_{st} is the stack current (A);
- T_{st} is the stack temperature (K).

The membrane water content and the rate of mass flow across the membrane are functions of the stack current and the relative humidity of the flow inside the anode and the cathode flow channels.

The relative humidity of the cathode and anode flow is the output of cathode flow model and anode flow model.

The water transport across the membrane is achieved through two different phenomena:

a) Water molecules are dragged across the membrane from anode to cathode by the hydrogen proton. This phenomenon is called electro-osmotic drag. The amount of water transported is represented by the electro-osmotic drag coefficient n_d , which is defined as the number of water molecules carried by each proton:

$$N_{osmo} = n_d \frac{i}{F} \qquad 3.97$$

where:

- N_{osmo} is the net water flow from anode to cathode of one cell caused by electro-osmotic drag $\left(mol/\sec\cdot cm^2\right)$;
- i is the stack current density $\left(A/cm^2\right)$;
- F is the Faraday number (C/mol).

b) The system considered is spatially distributed and there is a gradient of water concentration across the membrane that is caused by the difference in humidity in anode and cathode flows. The water concentration gradient, causes the *back-diffusion* of water from cathode to anode:

$$N_{dif} = D_w \frac{dc_v}{dy} \qquad 3.98$$

where:

- N_{dif} is the net water flow from cathode to anode of one cell caused by back-diffusion $\left(mol/\sec\cdot cm^2\right)$;
- c_v is the water concentration $\left(mol/cm^3\right)$;
- y is the distance in the direction normal to the membrane (cm);
- D_w is the diffusion coefficient of water in the membrane $\left(cm^2/\sec\right)$.

There is also a nitrogen flux caused by the gradient of the partial pressures (cathode-anode) which is however neglected.

Combining the two water transports and approximating the water concentration gradient in the membrane to be linear over the membrane thickness, the water flow across the membrane can be written as (assuming positive values in the direction from anode to cathode):

$$N_{v,membr} = n_d \frac{i}{F} - D_w \frac{c_{v,ca} - c_{v,an}}{t_m} \qquad 3.99$$

where:

- $c_{v,ca}$ is the water concentration in the cathode ;
- $c_{v,an}$ is the water concentration in the anode;
- t_m (cm) is the thickness of the membrane.

For a particular membrane, the electro-osmotic drag coefficient n_d and the diffusion coefficient D_w vary with water content in the membrane, which depends on the water content in the gas next to the membrane.
The equation 3.99 gives the flow rate of water per unit area $(mol/(\sec \cdot cm^2))$ in one fuel cell and then, the total stack mass flow rate across the membrane $W_{v,membr}$ can be calculated from:

$$W = N \cdot M_v \cdot A_{fc} \cdot n \qquad 3.100$$

where:

- M_v is the vapour molar mass;
- A_{fc} (cm^2) is the fuel cell active area;
- n is the number of fuel cell in the stack.

The average between the water contents in the anode flow and the cathode flow can be used to represent the membrane water content. However, using the water content in the anode flow presents a more conservative approach [46], because the membrane water content tends to be lower on the anode side. This is because at high current density, water transport from anode to cathode by electro-osmotic drag exceeds the water back-diffusion from cathode to anode. The membrane water content and the electro-osmotic and diffusion coefficients can be calculated using the activities of the gas in the anode and the cathode:

$$a_{an} = \frac{y_{v,an} \cdot p_{an}}{p_{sat,an}} = \frac{p_{v,an}}{p_{sat,an}} \qquad 3.101$$

$$a_{cat} = \frac{y_{v,cat} \cdot p_{ca}}{p_{sat,ca}} = \frac{p_{v,ca}}{p_{sat,ca}} \qquad 3.102$$

where:

- $y_{v,an}$, $y_{v,ca}$ are the mole fraction of vapour in the anode and in the cathode, respectively;
- p_{an}, p_{ca} are the total flow pressure in the anode and in the cathode, respectively;
- $p_{v,an}$, $p_{v,ca}$ are the vapour partial pressure in the anode and in the cathode, respectively;
- $p_{sat,an}$, $p_{sat,ca}$ are the vapour saturation pressure in the anode and in the cathode, respectively.

The water content in the membrane λ_i, defined as the ratio of water molecules to the number of charge sites, is calculated from water activities a_i ([47], [48]):

$$\lambda_{an} = \begin{cases} 0.043 + 17.81 a_{an} - 39.85 a_{an}^2 + 36.0 a_{an}^3 & \text{se } 0 \le a_{an} \le 1 \\ 14 + 1.4(a_{an} - 1) & 0 < a_{an} \le 3 \end{cases} \quad 3.103$$

and the water content in the membrane on the cathode side λ_{ca} is equal to:

$$\lambda_{ca} = \begin{cases} 0.043 + 17.81 a_{ca} - 39.85 a_{ca}^2 + 36.0 a_{ca}^3 & \text{se } 0 \le a_{ca} \le 1 \\ 14 + 1.4(a_{ca} - 1) & 0 < a_{ca} \le 3 \end{cases} \quad 3.104$$

The membrane average water content λ_m is:

$$\lambda_m = \begin{cases} 0.043 + 17.81 a_m - 39.85 a_m^2 + 36.0 a_m^3 & \text{se } 0 \le a_m \le 1 \\ 14 + 1.4(a_m - 1) & 0 < a_m \le 3 \end{cases} \quad 3.105$$

where a_m is the average water activity between the anode and cathode water activity:

$$a_m = \frac{a_{an} + a_{ca}}{2} \quad 3.106$$

The value of λ_m is used to represent the water content in the membrane and therefore the electro-osmotic drag coefficient n_d and the water diffusion coefficient D_w are calculated from the membrane water content [47]:

$$n_d = 0.0029 \lambda_m^2 + 0.05 \lambda_m^2 - 3.4 \cdot 10^{-19}$$

$$D_w = D_\lambda \exp\left[2416 \left(\frac{1}{303} - \frac{1}{T_{fc}} \right) \right] \quad 3.107$$

$$D_w = D_\lambda \exp\left[2416 \left(\frac{1}{303} - \frac{1}{T_{fc}} \right) \right] \quad 3.108$$

where:

- T_{fc} is the temperature of the fuel cell in Kelvin T_{st};
- D_λ is a coefficient that depends on λ_m and it assumes the following values:

$$D_\lambda = \begin{cases} 10^{-6} & \lambda_m < 2 \\ 10^{-6}\left[1 + 2(\lambda_m - 2)\right] & 2 \le \lambda_m \le 3 \\ 10^{-6}\left[3 - 1.67(\lambda_m - 3)\right] & 3 < \lambda_m < 4.5 \\ 1.25 \cdot 10^{-6} & \lambda_m > 4.5 \end{cases}$$

The water concentration at the membrane surfaces on anode and cathode sides, used in equation 3.97, is a function of the membrane water content:

$$c_{v,an} = \frac{\rho_{m,dry}}{M_{m,dry}} \lambda_{an}; \qquad 3.109$$

$$c_{v,ca} = \frac{\rho_{m,dry}}{M_{m,dry}} \lambda_{ca}; \qquad 3.110$$

where:

- $\rho_{m,dry}$ is the membrane dry density (kg/cm^3);
- $M_{m,dry}$ is the membrane dry equivalent weight (Kg/mol).

3.6 Auxiliary Components

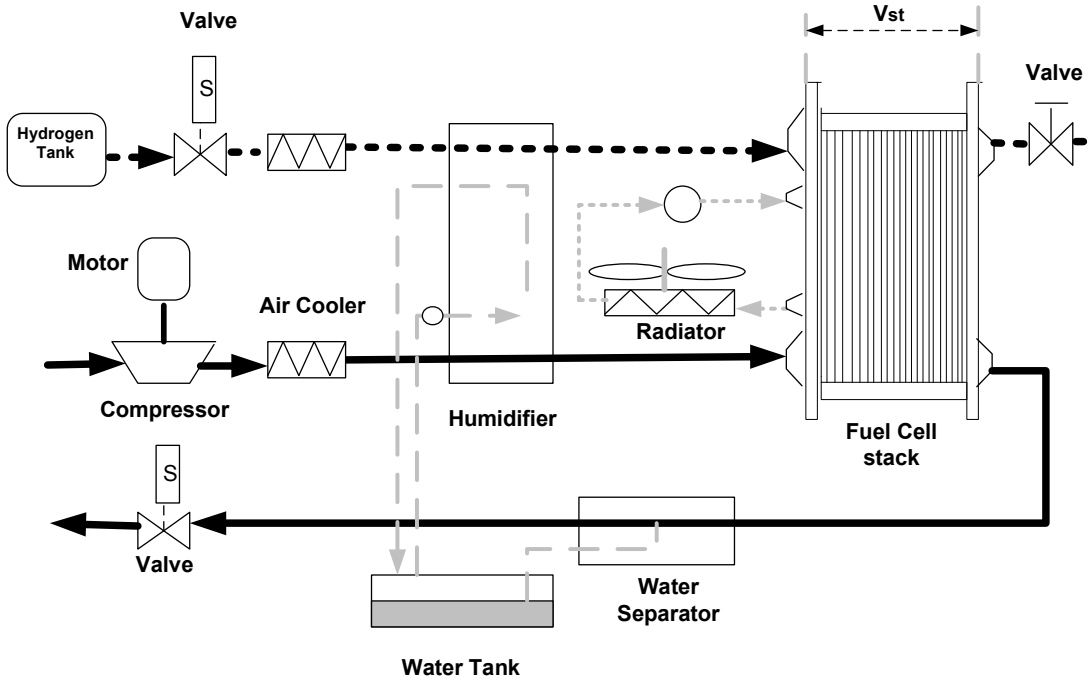

Fig. 3.13. FC system with control subsystems. A fuel cell systems includes four subsystems that manage the air, hydrogen humidity and stack temperature.

To be able to work properly, a fuel cell stack needs several auxiliary components, which should be analysed, designed and optimised to improve the FCS performance. All this allows not only the FC stack output to be improved but also the strong nonlinear interactions between the different auxiliaries to be managed.

The fundamental auxiliary components of the FC stack are:

- Compressor;
- Supply manifold;
- Return manifold;
- Humidifier;
- Air cooler.

3.6.1 Compressor Model

The inputs of the compressor model are the following:

- inlet air pressure $p_{cp,in}$ = p_{atm} (Pa) (atmospheric pressure);
- temperature of input air flow $T_{cp,in}$ = T_{atm} (K) (atmospheric temperature);
- downstream pressure $p_{cp,out}$, which is the supply manifold pressure p_{sm} (Pa);
- relative humidity of atmospheric air φ_{atm};
- voltage command to the compressor motor v_{cm}.

The implementation of the equations of the compressor model involves the following variables:

- T_{cp} temperature of output air flow (K);
- φ_{cp} relative humidity of output air flow;
- W_{cp} compressor air mass flow rate (kg/s);
- ω_{cp} compressor speed (rpm).

The temperature of output air flow and the power of the compressor are computed by using the equations of the thermodynamic balance. The compressor speed ω_{cp} is the only dynamic state variable. Also, the injected air is the atmospheric air and then, its pressure and temperature are $p_{atm} = 1$ atm e $T_{atm} = 298$ K, respectively. The motor command is one of the inputs of the fuel cell system and the downstream pressure is determined by the supply manifold model (see after). The compressor air mass flow rate W_{cp} (kg/sec) is determined through a compressor flow map (implemented by a look-up table [49]), from the pressure ratio across the compressor and the speed of the compressor.

3.6.1.1 Jensen & Kristensen method

To consider variations in the inlet condition of the compressor, which are the inlet flow pressure and temperature, the "corrected" values of mass flow rate and compressor speed are used in the compressor map. The corrected values [50] are the corrected compressor speed (rpm) $N_{cr} = N_{cp} / \theta$ and the corrected mass flow $W_{cr} = W_{cp}\sqrt{\theta} / \delta$, where $\theta = T_{cp,in} / 288$ (K) is the corrected temperature and $\delta = p_{cp,in} / 1$ (atm) is the corrected pressure.

Using the Jensen & Kristensen method, the dimensionless fundamental parameter Ψ is:

$$\Psi = C_p T_{cp,in}\left[\left(\frac{p_{cp,out}}{p_{cp,in}}\right)^{\frac{\gamma-1}{\gamma}} - 1\right] / \left(\frac{U_c^2}{2}\right) \qquad 3.111$$

where:

- C_p is the specific heat of the gas a constant pressure ($\frac{J}{Kg \cdot K}$);
- γ is the ratio of the specific heats of the gas a constant pressure and a constant volume, respectively;
- U_c is the compressor blade tip speed (m/s).

The compressor blade tip speed is given the following equation:
The tangential speed at the tip of the compressor blades is given by:

$$U_c = \frac{\pi}{60} d_c N_{cr} \qquad 3.112$$

where d_c is the compressor diameter (m);

The normalized compressor flow rate Φ is defined by:

$$\Phi = \frac{\dot{W}_{cor}}{\rho_a \frac{\pi}{4} d_c^2 U_c} \qquad 3.113$$

where ρ_a is the air density ($\frac{kg}{m^3}$).

The normalized compressor flow rate Φ is then correlated with the parameter Ψ by the equation:

$$\Phi = \Phi_{\max}\left[1-\exp\left(\beta\left(\frac{\Psi}{\Psi_{\max}-1}\right)\right)\right] \quad 3.114$$

where β, $\Psi_{\max}$ e $\Phi_{\max}$ are polynomial functions of the Mach number M:

$$\Phi_{\max} = a_4M^4 + a_3M^3 + a_2M^2 + a_1M + a_0; \quad 3.115$$

$$\beta = b_2M^2 + b_1M + b_0; \quad 3.116$$

$$\Psi_{\max} = c_5M^5 + c_4M^4 + c_3M^3 + c_2M^2 + c_1M + c_0. \quad 3.117$$

The regression coefficients a_i, b_i e c_i are obtained by curve fitting of the compressor data. The inlet Mach number M is defined by:

$$M = \frac{U_c}{\sqrt{\gamma R_a T_{cp,in}}} \quad 3.118$$

where R_a is the air gas constant.

A look-up table of the compressor efficiency η_{cp} is used to find the efficiency of the compressor from the mass flow rate and pressure ratio across the compressor. The maximum efficiency of the compressor is 80%.

The second thermodynamic law for the gases is given by the following equation ([51], [52]):

$$L_i + Q_c = \Delta_i + \Delta E_c \quad 3.119$$

where Q_c is the heat transfer, Δ_i is the enthalpy change of the gas and ΔE_c is the kinetic change of the gas. In an adiabatic system, like the compressor, there is no heat transfer and then the term Q_c in the equation 3.117 is equal to zero. Also, here is considered a compressor with negligible kinetic change ΔE_c. For these assumptions the equation 3.119 can be rewrritten:

$$L_i = \Delta_i \quad 3.120$$

and for an ideal gas $\Delta_i = C_p(T_1 - T_2)$. Therefore, $L_{isoentr} = C_p\left(T_{cp,isentr} - T_{cp,in}\right)$ represents the isentropic work of the compressor and $L_i = C_p\left(T_{cp,out} - T_{cp,in}\right)$ represents the compressor work.

The temperature of the air leaving the compressor $T_{cp,out}$ is computed by using the isentropic efficiency η_{ise}:

$$\eta_{ise} = \frac{L_{ise}}{L_i} = \frac{C_p\left(T_{cp,outise} - T_{cp,in}\right)}{C_p\left(T_{cp,out} - T_{cp,in}\right)} = \frac{T_{cp,in}}{T_{cp,out} - T_{cp,in}}\left[\frac{T_{cp,outise}}{T_{cp,in}} - 1\right] \quad 3.121$$

The compressor is regulated from a polytropic process, which is described by the following equations:

$$pv^k = C \rightarrow p_1 v_1^{\ k} = p_2 v_2^{\ k} \qquad 3.122$$

For an ideal gas $pv = R_a T \rightarrow \frac{T_2}{T_1} = \left(\frac{p_2}{p_1}\right)^{\frac{k-1}{k}} \rightarrow \frac{T_{cp,out}}{T_{cp,in}} = \left(\frac{p_{cp,out}}{p_{cp,in}}\right)^{\frac{k-1}{k}}$ 3.123

$$\eta_{cpise} = \frac{T_{cp,in}}{T_{cp,out} - T_{cp,in}}\left[\left(\frac{p_{cp,out}}{p_{cp,in}}\right)^{\frac{k-1}{k}} - 1\right] \qquad 3.124$$

$$T_{cp,out} = T_{cp,in} + \frac{T_{cp,in}}{\eta_{cpise}}\left[\left(\frac{p_{cp,out}}{p_{cp,in}}\right)^{\frac{k-1}{k}} - 1\right] \qquad 3.125$$

The compressor needs a power $P_{cp} = C_p \Delta T W_{cp}$ that is computed by means of the difference of temperatures $\Delta T = T_{cp,out} - T_{cp,in}$ and the equation 3.125:

$$P_{cp} = C_p \Delta T W_{cp} = C_p \frac{T_{cp,in}}{\eta_{cpise}}\left[\left(\frac{p_{cp,out}}{p_{cp,in}}\right)^{\frac{k-1}{k}} - 1\right] W_{cp} \qquad 3.126$$

The equation 3.126 is used to compute the torque required to drive the compressor $\tau_{cp} = P_{cp} / \omega_{cp}$ (N-m) :

$$\tau_{cp} = \frac{C_p T_{atm}}{\omega_{cp} \eta_{cp}}\left[\left(\frac{p_{cp,out}}{p_{atm}}\right)^{\frac{\gamma-1}{\gamma}} - 1\right] W_{cp} \qquad 3.127$$

A lumped rotational parameter model with inertia is used to represent the dynamic behaviour of the compressor speed:

$$d\frac{\omega_{cp}}{dt} = \frac{1}{J_{cp}}\left(\tau_{cm} - \tau_{cp}\right) \qquad 3.128$$

where:

- J_{cp} is the combined inertia of the compressor and the motor ($Kg \cdot m^2$) ;
- τ_{cm} is the compressor motor torque input (N-m).

The compressor motor torque is calculated using a DC electrical motor equations.

The armature current of the DC motor and the electromagnetic torque driving the compressor are given by the following equations:

$$\frac{di_a}{dt} = \frac{1}{L_a}\left(v_{cm} - R_a i_a - k_v \omega_{cp}\right) \qquad 3.129$$

$$\tau_{cm} = \eta_{cm} k_t \left(\phi \cdot i_a\right)$$

Where v_{cm} is the armature voltage, i_a is the armature current, Ra and L_a are respectively the resistance and the inductance of the armature, k_v is the characteristic constants of the electrical motor, η_{cm} is the motor mechanical efficiency and ϕ is the flux. This model can be considered a simplified model for a DC brushless motor.

Note that a model of a DC motor is used here for sake of simplicity, but it should be remarked that, because of the high rotating speed required by the centrifugal compressor, an AC drive (particularly a brushless AC drive) should be employed.

3.6.2 Lumped Model of Manifold Dynamics

The manifold model represents the lumped volume associated with pipes and connections between each device. The supply manifold volume includes the volume of the pipes between the compressor and the fuel cell including the volume of the cooler and the humidifier. The return manifold represents the pipeline at the fuel cell stack exhaust.

The mass conservation principle is used to develop the manifold model:

$$d\frac{m}{dt} = W_{in} - W_{out} \qquad 3.130$$

where:

- m is the mass of the gas accumulated in the manifold volume (Kg);
- W_{in} is the mass flow rate into of the manifold (Kg/sec);
- W_{out} is the mass flow rate out of the manifold (Kg/sec).

If the air temperature T (K) is assumed constant in the manifold and equal to the inlet flow temperature $T = T_{in}$, then the manifold dynamics follow an isothermal relation:

$$d\frac{p}{dt} = \frac{R_a T}{V}\left(W_{in} - W_{out}\right) \qquad 3.131$$

where:

- P is the manifold pressure (Pa);
- R_a is the gas constant of air ($J / Kg \cdot K$);
- V is the manifold volume (m^3).

The equation 3.129 can be proved by using the ideal gas law:

$$pV = nR_aT \qquad 3.132$$

or $pV = mR^*T$ 3.133

where:

- V is the volume of gas (m^3) ;
- R^* is the ratio between the constant of gas R_a and the molar mass of gas (Kg/mol);
- m is the mass of gas (Kg).

If the volume V is constant and the process is isothermal, then the derivative of the equation 3.131 is:

$$\frac{dp}{dt}V = \frac{dm}{dt}R^*T \rightarrow \frac{dp}{dt} = \frac{R^*T}{V}\frac{dm}{dt} = \frac{R^*T}{V}\left(W_{in} - W_{out}\right) \qquad 3.134$$

If the air temperature changes in the manifold, the pressure dynamic equation, which is derived from the energy conservation, the ideal gas law and the air thermodynamic properties is:

$$\frac{dp}{dt} = \frac{\gamma R_a}{V}\left(W_{in}\,T_{in} - W_{out}T\right) \qquad 3.135$$

where:

- γ is the ratio of the specific heats of the gas a constant pressure and a constant volume, respectively;
- T_{in} is the temperature of input air flow (K);
- T is the temperature in the manifold (K).

The equation 3.133 is proved by considering that the gas is ideal, its volume is constant and the process is polytropic. From the ideal gas law:

$$m = \frac{pV}{R^*T}. \qquad 3.136$$

The derivative of equation 3.136 with respect to time (the mass m is a function of the temperature and the pressure) is the following:

$$\frac{dm}{dt} = \frac{dp}{dt}\frac{\partial f}{\partial p} + \frac{dT}{dt}\frac{\partial f}{\partial T} = \frac{dp}{dt}\frac{V}{R^*T} - \frac{1}{T^2}\frac{pV}{R^*}\frac{dT}{dt}. \qquad 3.137$$

The value of the temperature T at the end of a polytropic process depends on its initial value T_1 by the following relationship:

$$T = T_1\left(\frac{p}{p_1}\right)^{\frac{\gamma-1}{\gamma}} \qquad 3.138$$

The derivative of the equation 3.138 with respect to time is:

$$\frac{dT}{dt} = T_1\frac{\gamma-1}{\gamma}\left(\frac{p}{p_1}\right)^{-\frac{1}{\gamma}}\frac{dp}{dt} \qquad 3.139$$

and by using the equation 3.139 in the 3.137:

$$\frac{dm}{dt} = \frac{dp}{dt}\frac{V}{R^*T} - \frac{1}{T^2}\frac{pV}{R^*}T_1\frac{\gamma-1}{\gamma}\left(\frac{p}{p_1}\right)^{-\frac{1}{\gamma}}\frac{dp}{dt} = \frac{dp}{dt}\frac{V}{R^*}\left(\frac{1}{T} - \frac{p}{T}T_1\frac{\gamma-1}{\gamma}\left(\frac{p}{p_1}\right)^{-\frac{1}{\gamma}}\right) =$$

$$= \frac{dp}{dt}\frac{V}{R^*T} - \frac{V}{R^*T}\frac{\gamma-1}{\gamma}\frac{dp}{dt} = \frac{dp}{dt}\frac{V}{R^*T}\left(1-\frac{\gamma-1}{\gamma}\right) = \frac{dp}{dt}\frac{V}{\gamma R^*T} \qquad 3.140$$

The derivative of pressure with respect to time is obtained by the equation 3.140:

$$\frac{dp}{dt} = \frac{\gamma R^*T}{V}\frac{dm}{dt} = \frac{\gamma R^*T}{V}\left(W_{in} - W_{out}\right) = \frac{\gamma R^*}{V}\left(T_{in}W_{in} - T_{out}W_{out}\right) \qquad 3.141$$

The nozzle flow equation, derived in [53], is used to compute the outlet flow of the manifold. The flow rate passing through a nozzle is a function of the upstream pressure p_1, the upstream temperature T_1 and the downstream pressure p_2 of the nozzle. The flow characteristic is divided into two regions by the critical pressure ratio:

$$\left(\frac{p_2}{p_1}\right)_{cri} = \left(\frac{2}{\gamma+1}\right)^{\frac{\gamma}{\gamma-1}} \qquad 3.142$$

For sub-critical flow where the pressure drop is less than the critical pressure ratio:

$$\left(\frac{p_2}{p_1}\right)_{cri} > \left(\frac{2}{\gamma+1}\right)^{\frac{\gamma}{\gamma-1}} \qquad 3.143$$

the mass flow rate is calculated from:

$$W = \frac{C_D A_T p_1}{\sqrt{\overline{R}T_1}} \left(\frac{p_2}{p_1}\right)^{\frac{1}{\gamma}} \left\{ \frac{2\gamma}{\gamma - 1} \left[1 - \left(\frac{p_2}{p_1}\right)^{\frac{\gamma-1}{\gamma}} \right] \right\}^{\frac{1}{2}} \qquad 3.144$$

For critical flow, the mass flow rate is given by:

$$W_{choked} = \frac{C_D A_T p_1}{\sqrt{\overline{R}T_1}} \sqrt{\gamma} \left(\frac{2}{\gamma+1}\right)^{\frac{\gamma+1}{2(\gamma-1)}} \text{ for } \left(\frac{p_2}{p_1}\right)_{cri} \le \left(\frac{2}{\gamma+1}\right)^{\frac{\gamma}{\gamma-1}} \qquad 3.145$$

where:

- C_D is the discharge coefficient of the nozzle;
- A_T is the opening area of the nozzle (m^2);
- $\overline{R}$ is the universal constant of gas ($J / Kg \cdot K$).

If the pressure difference between the manifold and the downstream volume is small and always falls into the subcritical flow region, the flow rate can be calculated by a linearized form of the subcritical nozzle flow equation:

$$W = k(p_1 - p_2) \qquad 3.146$$

where k is the nozzle constant.

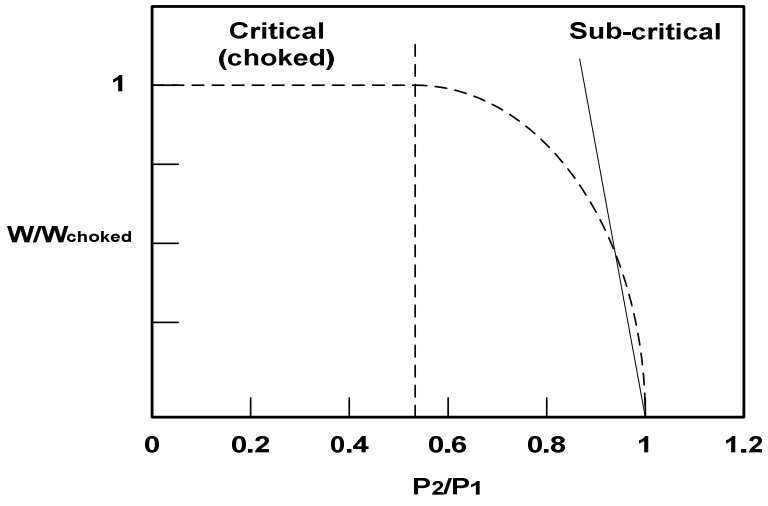

Fig. 3.14. Dashed line: relative mass flow rate as a function of nozzle pressure ratio; solid line: linearized mass flow rate at low pressure difference.

The plot of the linearized equation for various manifold pressures is shown in figure 3.14 as a solid line, compared to the plot of equation 3.142 shown as a dashed line.

3.6.2.1 Supply Manifold Model

The inputs of the model are:

- The total pressure of the cathode channel p_{ca} (Pa);
- The temperature of the input air flow is equal to the temperature of the output air flow of the compressor T_{cp} (K);
- the mass flow rate of the compressor W_{cp} (kg/s);
- the relative humidity of the output mass flow of the compressor φ_{ca} .

The equations of the supply manifold model allow to compute the following variables:

- T_{sm} is supply manifold pressure (K);
- p_{sm} is the supply manifold pressure (Pa);
- $W_{sm,out}$ is the output mass flow rate of the supply manifold (kg/s);
- φ_{sm} is the relative humidity of the output mass flow of the supply manifold.

Because the pressure difference between the supply manifold p_{sm} and the cathode p_{ca} is relatively small, then it is possible to write the following equation:

$$W_{sm,out} = k_{sm,out}\left(p_{sm} - p_{ca}\right) \qquad 3.147$$

where $k_{sm,out}$ is the supply manifold outlet flow constant.

Because the temperature of the air leaving the compressor is high, it is expected that the air temperature changes inside the supply manifold:

$$\frac{dm_{sm}}{dt} = W_{cp} - W_{sm,out} \qquad 3.148$$

$$\frac{dp_{sm}}{dt} = \frac{\gamma R_a}{V_{sm}}\left(W_{cp}\, T_{cp,out} - W_{sm,out}\, T_{sm}\right) \qquad 3.149$$

where:

- m_{sm} is the mass of gas into the supply manifold volume (Kg) ;
- V_{sm} is the supply manifold volume (m^3);
- T_{sm} is the supply manifold pressure (K).

The temperature T_{sm} is calculated from m_{sm} and p_{sm} by using the ideal gas law. The relative humidity φ_{sm} of the supply manifold output mass flow is computed by the following equation:

$$\varphi_{sm} = \frac{\varphi_{cp} \cdot p_{sat}(T_{cpout})}{p_{sat}(T_{sm})} \qquad 3.150$$

3.6.2.2 Return Manifold Model

The inputs of the model are:

- the output mass flow rate of the cathode channel $W_{ca,out} = W_{ca}$ (kg/s);
- the mass flow rate of the compressor W_{cp} (kg/s);
- the atmospheric pressure p_{atm} (Pa).

The equations of the supply manifold model allow to compute the following variables:

- T_{rm} is the temperature of the output mass flow of the return manifold (K);
- p_{rm} is the return manifold pressure (Pa);
- $W_{rm,out}$ is the output mass flow rate of the return manifold (kg/s);
- m_{rm} is the return manifold mass (kg).

The temperature of the air leaving the stack is relatively low and therefore, the changes of air temperature in the return manifold are negligible and the return manifold pressure is computed by:

$$\frac{dp_{rm}}{dt} = \frac{R_a T_{rm}}{V_{rm}} \left(W_{ca,out} - W_{rm,out} \right) \qquad 3.151$$

where V_{rm} is the return manifold volume (m^3).

The input mass flow rate of the return manifold is the same of the output mass flow rate of the cathode $W_{ca,out}$ (see the cathode model). The mass into the return manifold m_{rm} is obtained by the following equation:

$$\frac{dm_{rm}}{dt} = W_{ca,out} - W_{rm,out} \qquad 3.152$$

The outlet mass flow is a function of the manifold pressure p_{rm} and the pressure downstream from the manifold, which is assumed to be fixed at p_{atm}. Since the pressure drop between the return manifold and the atmospheric is relatively large, the equation of the return manifold exit flow are:

$$W_{rm,out} = \frac{C_{D,rm} A_{T,rm} p_{rm}}{\sqrt{\overline{R}T_{rm}}} \left(\frac{p_{atm}}{p_{rm}}\right)^{\frac{1}{\gamma}} \left\{\frac{2\gamma}{\gamma-1}\left[1-\left(\frac{p_{atm}}{p_{rm}}\right)^{\frac{\gamma-1}{\gamma}}\right]\right\}^{\frac{1}{2}} \qquad 3.153$$

for $\left(\frac{p_{atm}}{p_{rm}}\right) > \left(\frac{2}{\gamma+1}\right)^{\frac{\gamma}{\gamma-1}}$

and:

$$W_{rm,out} = \frac{C_{D,rm} A_{T,rm} p_{rm}}{\sqrt{\overline{R}T_{rm}}} \sqrt{\gamma}\left(\frac{2}{\gamma+1}\right)^{\frac{\gamma+1}{2(\gamma-1)}}; \qquad 3.154$$

for $\left(\frac{p_{atm}}{p_{rm}}\right) \le \left(\frac{2}{\gamma+1}\right)^{\frac{\gamma}{\gamma-1}}$

where $A_{T,rm}$ is the throttle opening area and it can be set constant or can be used as an extra control variable to regulate the return manifold pressure and thus the cathode pressure [54].

The pressure calculated in the supply manifold model is used in the compressor model to determine the pressure ratio across the compressor. The return manifold pressure calculated in the return manifold model is used to determine the flow rate exiting the fuel cell cathode.

3.6.3 Air Cooler Model

The inputs of the air cooler model are:

- the relative humidity of the supply manifold output mass flow φ_{sm};
- the supply manifold temperature T_{sm} (K);
- the supply manifold pressure p_{sm} (Pa).

The air cooler model allows computing the relative humidity of the output mass flow of the air cooler system. The temperature of the air in the supply manifold is typically high due to the high temperature of air leaving the compressor. To prevent any damage to the fuel cell membrane, the air needs to be cooled down to the stack operating temperature.

In this model it is assumed that:

- an ideal air cooler maintains the temperature of the air entering the stack at T_{cl} = 80°C;
- there is no pressure drop across the cooler $p_{cl} = p_{sm}$.

Because temperature change affects gas humidity, the humidity of the gas exiting the cooler is calculated by:

$$\phi_{cl} = \frac{p_{v,cl}}{p_{sat}(T_{cl})} = \frac{p_{cl}\, p_{v,atm}}{p_{atm}\, p_{sat}(T_{cl})} = \frac{p_{cl}\phi_{atm}\, p_{sat}(T_{atm})}{p_{atm}\, p_{sat}(T_{cl})} = \frac{p_{sm}\phi_{atm}\, p_{sat}(T_{atm})}{p_{atm}\, p_{sat}(T_{cl})} \qquad 3.155$$

where:

- ϕ_{atm} = 0.5 is the nominal ambient air relative humidity;
- $p_{sat}(T_{atm})$ is the vapour saturation pressure that is a function of temperature T_{atm} (Pa);
- $p_{sat}(T_{cl})$ is the saturation pressure inside the air cooler and it is a function of the air cooler temperature T_{cl} (Pa);
- $p_{v,atm}$ is the partial pressure of the vapour of the ambient air (Pa).

The saturation pressure is a function of the vapour temperature:

$$\begin{aligned}
&6{,}853\cdot 10^{-7}\cdot T^4 - 7{,}432\cdot 10^{-4}\cdot T^3 + 0{,}304\cdot T^2 - 55{,}613\cdot T + 3{,}831\cdot 10^3 = p_{sat} \;\; if \;\; T < 333{,}15K \\
&1{,}508\cdot 10^{-6}\cdot T^4 - 0{,}0018\cdot T^3 + 0{,}857\cdot T^2 - 1{,}796\cdot 10^2\cdot T + 1{,}428\cdot 10^4 = p_{sat} \;\; if \;\; 333{,}15K < T < 433{,}15K \\
&1{,}338\cdot 10^{-6}\cdot T^4 - 0{,}0015\cdot T^3 + 0{,}654\cdot T^2 - 1{,}191\cdot 10^2\cdot T + 7{,}506\cdot 10^3 = p_{sat} \;\; if \;\; 433{,}15K < T < 533{,}15K \\
&1{,}648\cdot 10^{-6}\cdot T^4 - 0{,}0020\cdot T_t^3 + 1{,}017\cdot T^2 - 2{,}241\cdot 10^2\cdot T + 1{,}878\cdot 10^4 = p_{sat} \;\; if \; 533{,}15K < T
\end{aligned} \qquad 3.156$$

Therefore, if the temperature of the input air flow and the temperature of the air cooler are known, then the saturation pressure of the ambient air $p_{sat}(T_{atm})$ and the saturation pressure of the air cooler $p_{sat}(T_{cl})$ can be computed by using equations 3.156. Also, the temperature T_{cl} is assumed constant.

3.6.4 Humidifier Model

The output air flow of the air cooler system is humidified before entering in the stack by using injection water into the air stream in the humidifier. Here, the humidifier system is modelled by a static model, because it is assumed that the system does not use moving components to humidify the air stream. Also, the volume of the humidifier is small and it can be considered as a part of a supply manifold volume. The humidifier model is needed to compute the changes of the air humidity that are caused from the water injections. It is assumed that the temperature of the mass flow in the humidifier T_{hum} is constant and it is equal to the temperature of the gas in the output of the air cooler T_{cl}. Also, it is assumed that the injected water is in the form of vapour.

The inputs of the humidifier model are the following:

- the mass flow rate W_{cl} ($W_{cl} = W_{sm,out}$) (kg/s);
- the air cooler pressure p_{cl} (Pa);
- the air cooler temperature T_{cl} (K);
- the relative humidity of the output mass flow of the air cooler model ϕ_{cl};
- the desired value of the relative humidity of the output mass flow of the air cooler φ_d.

The humidifier model allows to evaluate the following variables:

- $W_{a,cl}$, the mass flow rate of dry air from the cooler (kg/s);
- $p_{a,cl}$, the partial pressure of dry air in the air cooler (Pa);
- $p_{v,cl}$, the partial pressure of the vapour in the air cooler (Pa) ;
- $W_{v,cl}$, the mass flow rate of vapour from the cooler (kg/s) ;
- $\phi_{hum,out}$, the relative humidity of the output mass flow of the air cooler;
- $W_{v,inj}$, the vapour mass flow rate injected to obtain the desired value of the relative humidity:
- φ_{hum}, the relative humidity of the output mass flow of the humidifier.

The equation 3.33 allows computing the partial pressure p_{sat} and it is used to determine the vapour partial pressure of the air cooler:

$$p_{v,cl} = \phi_{cl}\, p_{sat}(T_{cl}) \qquad 3.157$$

Because humid air is a mixture of dry air and vapour, then dry air partial pressure is the difference between the total pressure and vapour pressure:

$$p_{a,cl} = p_{cl} - p_{v,cl} \rightarrow \quad p_{a,cl} = p_{cl} - \phi_{cl}\, p_{sat}(T_{cl}) \qquad 3.158$$

The humidity ratio can then be calculated from:

$$\omega_{cl} = \frac{M_v}{M_a} \cdot \frac{p_{v,cl}}{p_{a,cl}} \qquad 3.159$$

where:

- M_v is the molar mass of water (kg/mol);
- M_a is the molar mass of dry air (kg/mol).

The molar mass of dry air is obtained by the following equation:

$$M_a = y_{O_2} \cdot M_{O_2} + (1 - y_{O_2}) \cdot M_{N_2} \qquad 3.160$$

where y_{O_2} is the oxygen concentration in the input air stream.

The mass flow rate of dry air $W_{a,cl}$ and vapour $W_{v,cl}$ from the cooler:

$$W_{a,cl} = \frac{1}{1+\omega_{cl}} W_{cl}\,; \qquad 3.161$$

$$W_{v,cl} = W_{cl} - W_{a,cl}\,. \qquad 3.162$$

The mass flow rate of dry air is the same for the inlet and outlet of the humidifier $W_{a,hm} = W_{a,cl}$

Obviously, the vapour flow rate increases by the amount of water injected:

$$W_{v,out} = W_{v,cl} + W_{v,inj} \qquad 3.163$$

where $W_{v,inj}$ is the vapour flow rate injected by the humidifier.

The mass flow rate $W_{v,out}$ is computed by the following equation:

$$W_{v,out} = \omega_{cl} W_{a,cl} \rightarrow \quad W_{v,out} = \frac{M_v}{M_a} \cdot \frac{p_{v,out}}{p_{a,cl}} \cdot W_{a,cl} \qquad 3.164$$

The vapour partial pressure in the humidifier is given by:

$$p_{v,out} = \phi_d \, p_{sat}(T_{cl}); \qquad 3.165$$

The vapour flow rate injected is obtained by equations 3.163, 3.164 and 3.165:

$$W_{v,inj} = W_{v,out} - W_{v,cl} \rightarrow W_{v,inj} = \frac{M_v}{M_a} \frac{\phi_d \, p_{sat}(T_{cl})}{p_{a,cl}} W_{a,cl} - W_{v,cl} \qquad 3.166$$

The total pressure of the air stream in the humidifier is given by:

$$p_{hm} = p_{a,cl} + p_{v,hm}.$$

The humidifier exit flow is governed by the mass continuity:

$$W_{hum,out} = W_{a,cl} + W_{v,out} = W_{a,cl} + W_{v,cl} + W_{v,inj}. \qquad 3.167$$

The mass flow rate in the output of the humidifier is the mass flow rate in the input of the cathode channel.

Chapter 4

Design, construction and experimental implementation of the emulator of the PEM-FC

This section describes the guidelines for analysis and design of a fuel cell PEM emulator by using a computer-controlled DC-DC power converter. The designed DC-DC converter, suitably driven, can in general accurately describe the current-voltage characteristics of several renewable systems. The goal of the PEM emulator is to reproduce the FC model described in chapter 3, taking into consideration the variation of the stack temperature, the partial pressures of the reactants and the load current. The operating principle of the PEM emulator is shown in figure 4.1. The first part of this system gives the output voltage of the PEM according to the several parameters that characterize the operating conditions of fuel cell system (temperature, pressure, etc). The reference voltage V_{FCref} is obtained by a software implementation in a Dspace board of the equations that represent the mathematical model of the PV system. The second part of emulator is formed by a hardware power electronic circuit and a controller block to drive the output voltage of the system. The hardware circuit is a classical DC-DC buck converter that gives the output voltage V_{FC} and the controller is implemented into the Dspace board to process the signal error V_{FCref}-V_{FC} and to give the correct value of the duty cycle δ to the DC-DC converter so that the voltage chopper V_{FC} will track the model fuel cell voltage reference V_{FCref}.

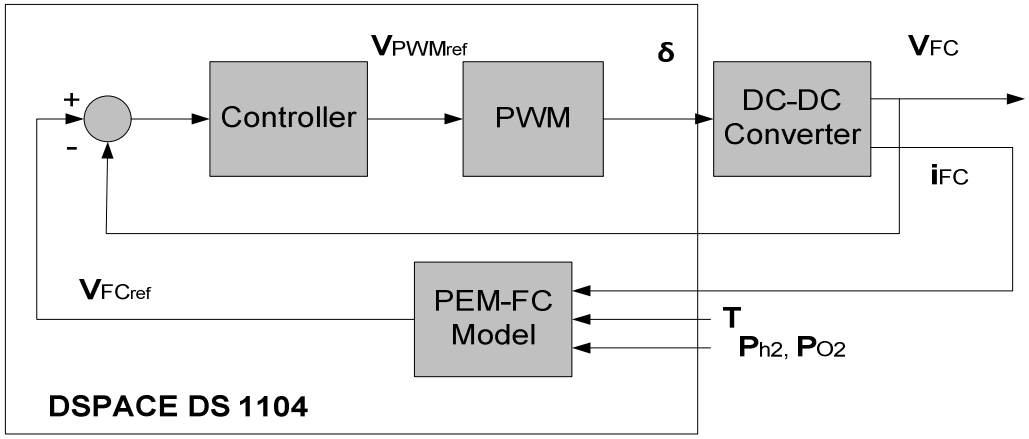

Fig. 4.1.Block diagram of fuel cell emulator.

The chapter 4 is organized as follows: the first section describes the DC-DC converter topology used, the hardware design of the power stage and the technological choices adopted to construct it; the second section reports the two converter control strategies adopted and the corresponding stability analysis; the third section presents the basic characteristics of the DSpace board, the implementation of control strategies and the generation of the PWM signal by using Simulink and the Control Desk tool; the last section shows and discusses the simulation and the experimental results.

4.1 DC-DC Converter Design

4.1.1 DC-DC Switch-mode converters

The DC-DC converters are widely used in regulated switch-mode dc power supplies and dc motor drive applications. The switch mode DC-DC converters are used to convert an unregulated dc input into a controlled dc output at a desired voltage level (Figure 4.2).

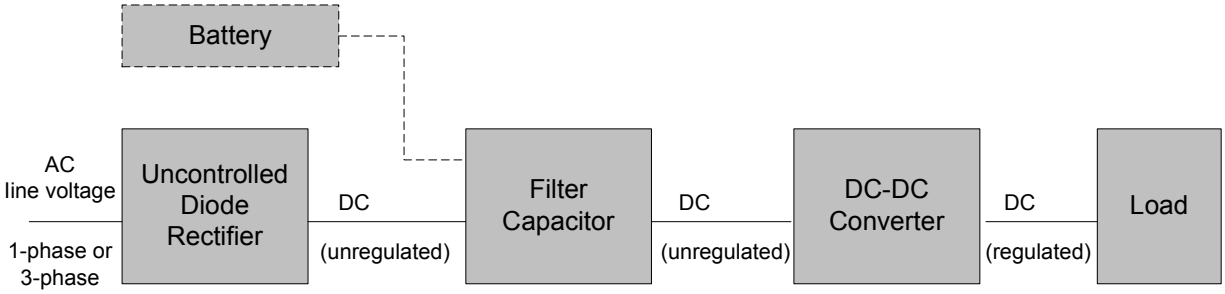

Fig.4.2. A DC-DC converter system.

In DC-DC converters the average dc output voltage must be controlled to equal a desired level, even though the input voltage and the output load may fluctuate. The DC-DC converters use one or more switches to transform dc from one level to another and the average output voltage is controlled by controlling the switch on and off duration (t_{on} and t_{off}). The switch-mode conversion concept is showed in figure 4.3, where the average value of the output depends on t_{on} and t_{off}. For controlling the output voltage two different methods can be used: the pulse-width modulation (PWM) and the variation in the switching

frequency. The PWM method uses a constant switching frequency and controls the average output voltage by tuning the on duration of the switch. In the other control method the on duration and the switching frequency are changed, but this solution is not used frequently because the variation in the switching frequency does not allow the ripple of input and the output waveforms of the converter to be easily filtered.

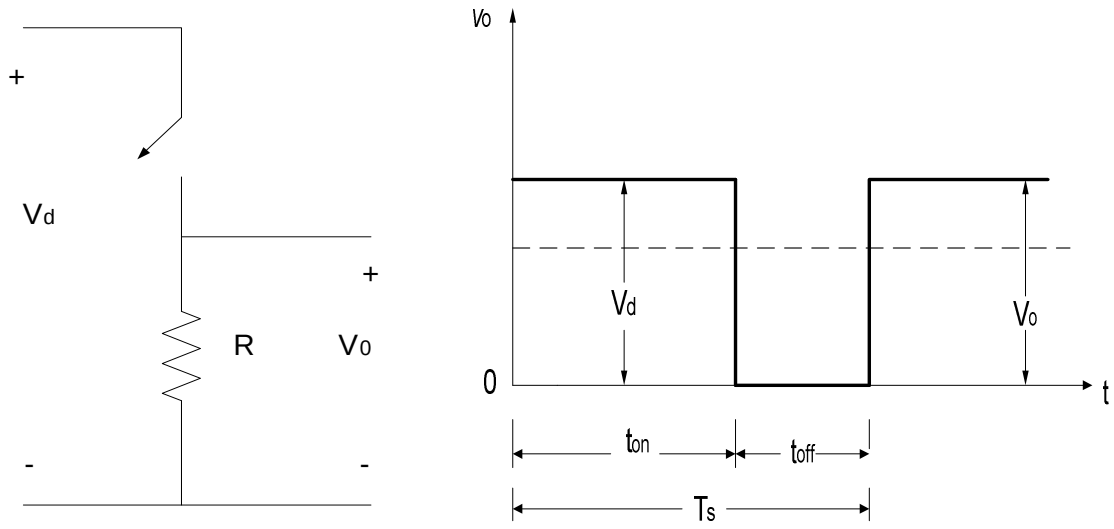

Fig. 4.3. Switch mode DC-DC conversion.

In the PWM switching with a constant switching frequency, the signal controlling the state of the switch (switch control signal) is generated by comparing a signal level control voltage $v_{control}$ with a periodic sawtooth waveform. The frequency of the sawooth determines the value of the switching frequency and this value is constant and is chosen between few kHz and few hundred kHz. In the figures 4.4a and 4.4b it is shown the PWM method: the switch control signal becomes high (switch on), when the difference between the actual output voltage and its desired value (amplified error signal) is greater than the sawtooth waveform. Otherwise, the switch is off. The switch duty ratio (or duty cycle) can be expressed as:

$$D = \frac{t_{on}}{T_S} = \frac{V_{control}}{V_{St}} \qquad 4.1$$

Where $v_{control}$ represents the amplified error signal ,V_{St} represents the peak of the waveform and $T_s = t_{on} + t_{off}$

The DC-DC converters can operate in the continuous current conduction mode, or in the discontinuous current conduction mode, which have significantly different characteristics. In practice, a converter may operate in both modes and therefore a converter and its control should be designed on the basis of both modes of operation.

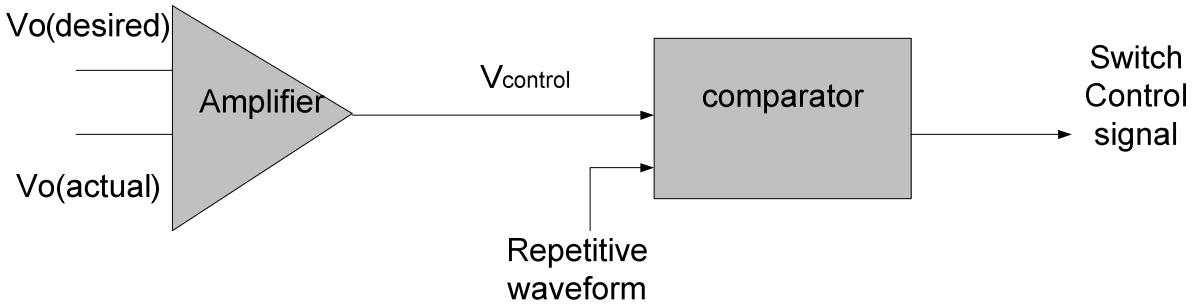

(a)

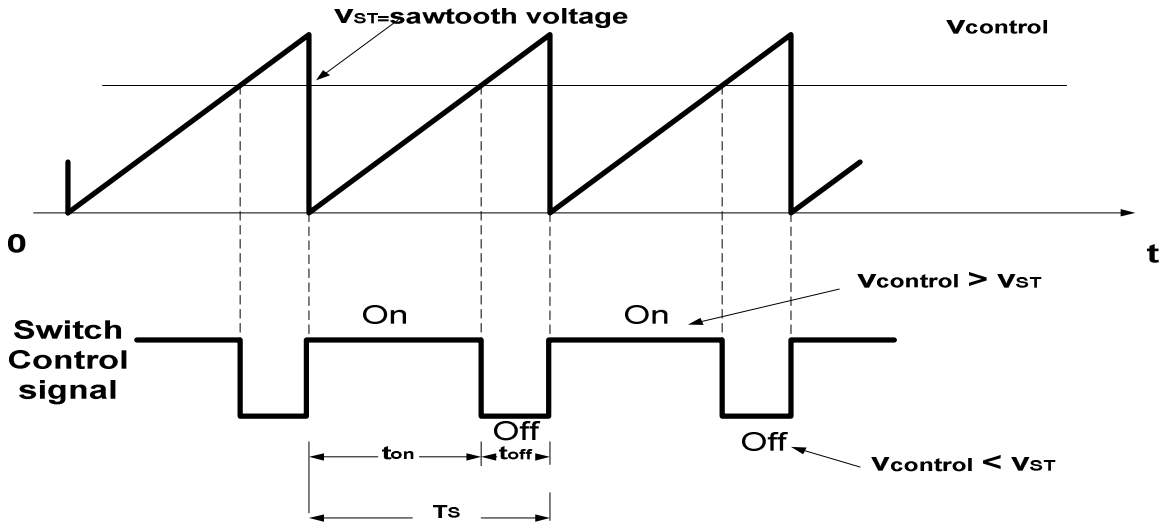

(b)

Fig.4.4. Pulse-width modulator: (a) block diagram; (b) comparator signals.

In this section the following DC-DC converters are considered the basic converter topologies:

- Step down (buck) converter;
- Step up (boost) converter.

The *step-down* (figure 4.5a) converter produces a lower average dc output voltage than the dc input voltage V_d. Its main application is in regulated dc power supplies and dc motor speed control. The output voltage of *step-up* converter (figure 4.5b) is always greater than the input voltage and its main application is in regulated dc power supplies and regenerative braking of dc motors. When the switch is on, the diode isolates the output voltage and the input supplies energy to the inductor. When the switch is off, the output stage receives energy from the inductor. In the steady-state analysis, the output filter capacitor is assumed to be very large to ensure a constant output voltage $v_o(t) = V_o$.

The converters will be analyzed in steady state and moreover, the switches are considered ideal and the losses in the inductive and the capacitive element are neglected [1],[2], [3].

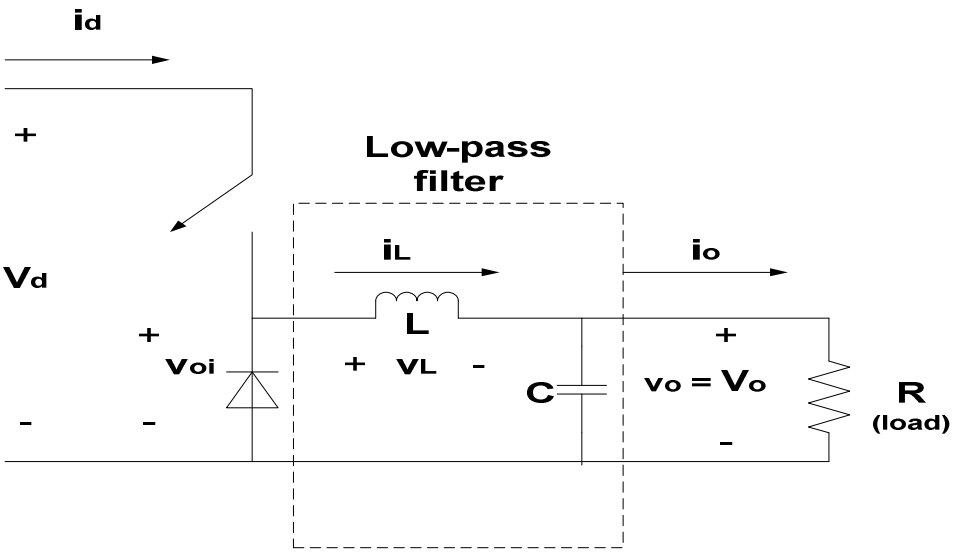

Fig. 4.5a. Step-down DC-DC converter

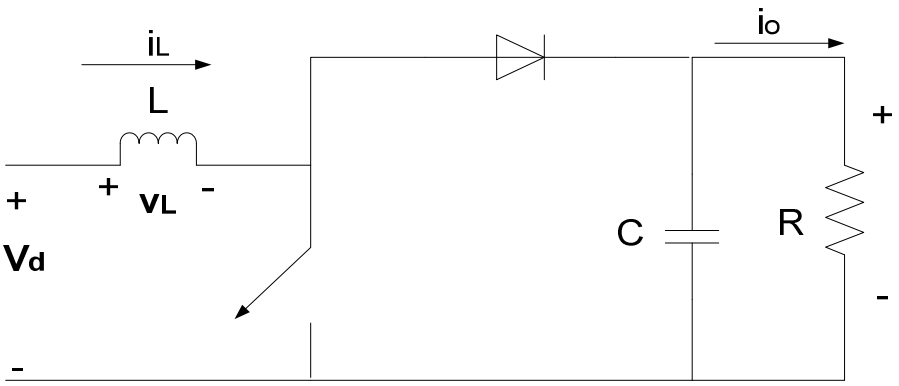

Fig.4.5b. Step-up DC-DC converter.

4.1.2 BUCK Converter

A switching DC-DC Buck converter has been chosen to reproduce the output voltage of the fuel cell. This topology has been chosen because it may be supplied by the rectified 380 V/ 50 Hz grid voltage and also, the high DC voltage levels are easily obtainable in laboratory.

The figure 4.5a represents a step-down converter with a resistive load and assumes a constant instantaneous input voltage V_d, while the instantaneous output voltage waveform is a function of the switch position (figure 4.6a). The average output voltage is obtained by the following equation:

$$V_o = \frac{1}{T_s}\int_o^{Ts} v_o(t)dt = \frac{1}{T_s}\left(\int_0^{t_{on}} V_d\,dt + \int_{t_{on}}^{T_s} 0dt\right) = \frac{t_{on}}{T_s}V_d = DV_d \qquad 4.3$$

By using the equation 4.1:

$$V_o = \frac{V_d}{V_{st}}v_{control} = kv_{control} \qquad 4.4$$

where $\frac{V_d}{V_{st}}$ = constant.

The average output voltage V_o changes linearly with the control voltage and the control of the output

voltage V_o can be obtained by varying the duty ratio $\frac{t_{on}}{T_S}$ of the switch.

In actual applications the load would be inductive, but even with a resistive load, there would always be an associated inductance. For this reason, the switch would have to absorb (or dissipate) the inductive energy and therefore it may be destroyed with resulting output voltage fluctuating between zero and V_d, which is not acceptable in most applications. The problem of stored inductive energy can be overcome by using a diode as shown in figure 4.5a, while the fluctuations can be reduced by using a low-pass filter, which is made by an inductor and a capacitor. The corner frequency f_c of the low pass filter is much lower than the switching frequency to erase the switching frequency ripple in the output voltage. The figure 4.6b shows the waveform of the input v_{oi} to the low-pass filter and it consists of a dc voltage V_o and the harmonics are present at the switching frequency f_c and its multiples. When the switch is on, the diode becomes reverse biased and the input supplies energy to the load. Otherwise when the switch is off, the inductor current passes through the diode and then it transfers some of its stored energy to the load. In the steady-state analysis, the filter capacitor at the output is very large to obtain a constant instantaneous output voltage $v_o(t) = V_o$ and the average inductor current is equal to the average output current I_o.

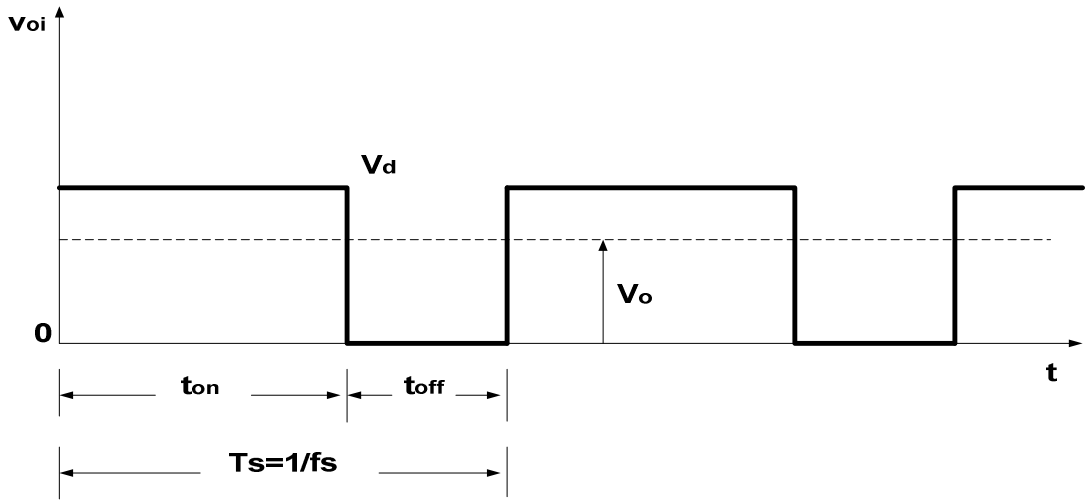

Fig. 4.6a. Instantaneous output voltage waveform is a function of the switch position.

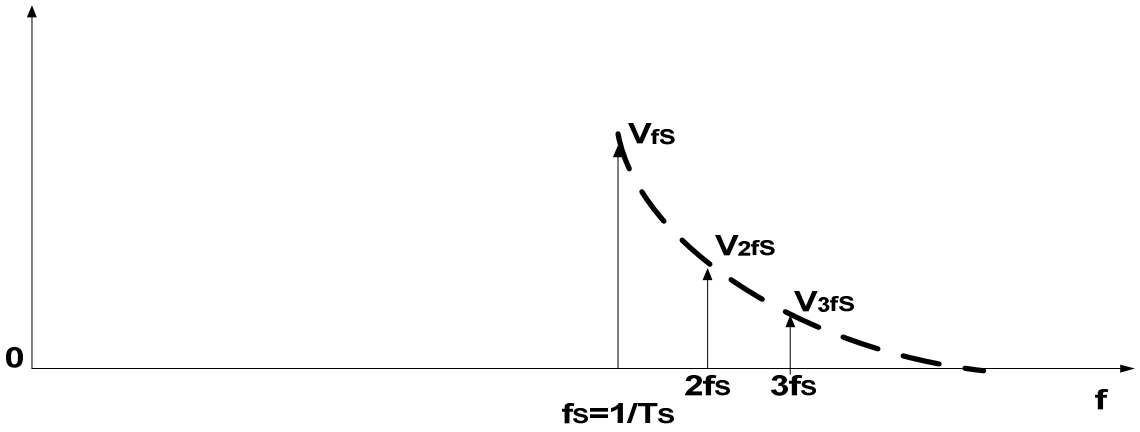

Fig. 4.6b. Frequency spectrum of v_{oi}.

4.1.2.1 Continuous-Conduction Mode

In the continuous-conduction mode the inductor current flows continuously ($i_L(t) \geq 0$) and it is shown in figure 4.7. When the switch is on during the time t_{on}, the switch supplies the inductor, the diode is reverse biased and then the voltage across the inductor is positive ($v_L = V_d - V_o$) . This voltage causes a linear increase in the inductor current i_L. When the switch is turned off, the inductor current continues to flow because of the inductive energy storage, the diode is forward biased and the inductor voltage $v_L = -V_o$. In the steady-state, the waveform must repeat from one time period to the next and the integral of the inductor voltage v_L over one time period ($T_s = t_{on} + t_{off}$) must be zero:

$$\int_0^{Ts} v_L dt = \int_0^{ton} v_l dt + \int_{ton}^{Ts} v_L dt = 0 \qquad 4.5$$

The equation 4.5 implies that the two areas A and B in the figure 4.7 must be equal and then:

$$(V_d - V_o)t_{on} = V_o(T_s - t_{on}) \qquad 4.6$$

$$\frac{V_o}{V_d} = \frac{t_{on}}{T_s} = D \qquad 4.7$$

The equation 4.7 shows that the output voltage varies linearly with the duty ratio of the switch for a given input voltage and it does not depend on any other circuit parameter.

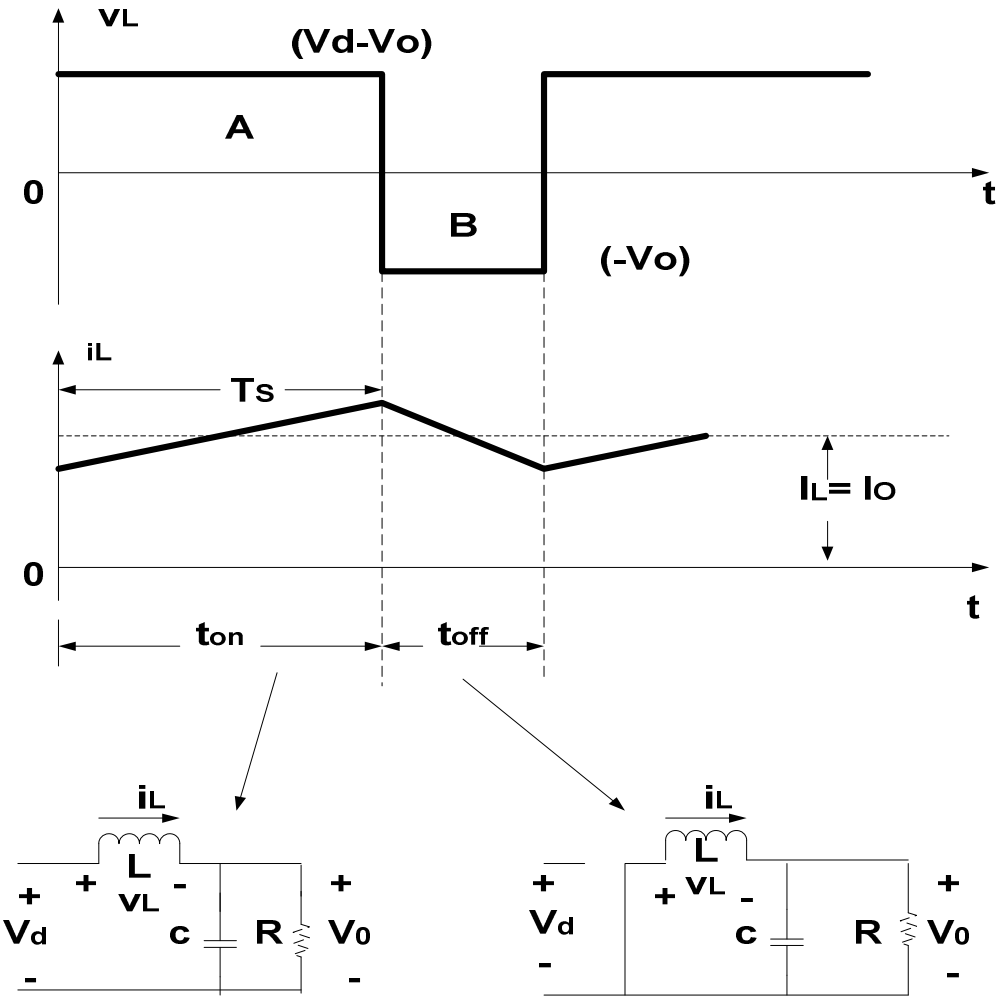

Fig. 4.7. Step-down converter circuit states.

4.1.2.2 Discontinuous/Continuous Conduction Mode

At the boundary between the continuous and the discontinuous mode, the inductor current i_L assumes the value zero at the end of the off period. The average inductor current at the boundary is:

$$I_{LB} = \frac{1}{2} i_{l,peak} = \frac{t_{on}}{2L}(V_d - V_o) = \frac{DT_s}{2L}(V_d - V_o) = I_{oB} \qquad 4.8$$

Therefore, if the average output current is less than I_{LB} for a given set of operating conditions (T_S, V_d, V_o, L, D), then i_L be discontinuous. The figure 4.8 shows the waveform for v_L and i_L.

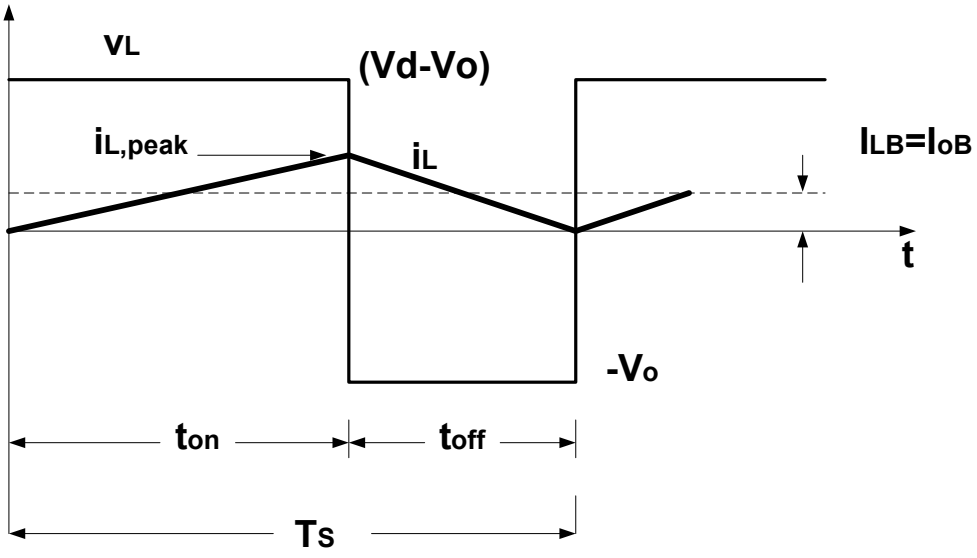

Fig. 4.8. v_L and i_L waveform at the boundary of continuous-discontinuous mode.

4.1.2.3 Discontinuous-Conduction Mode with V_d constant

When the voltage V_d is constant, then the output voltage V_o is controlled by tuning the converter duty ratio D. By using the equation 4.3 and the equation 4.8, the average inductor current is the following:

$$I_{LB} = \frac{T_s V_d}{2L} D(1-D) \qquad 4.9$$

It is possible to plot the current I_{LB} as a function of the duty ratio D, keeping V_d and the other parameters constant, by using the equation 4.9 (figure 4.9). The figure 4.9 shows that the output current required for a continuous-conduction mode is maximum at D=0.5:

$$I_{LB,\max} = \frac{T_s V_d}{8L} \qquad 4.10$$

From equations 4.9 and 4.10:

$$I_{LB} = 4 I_{LB,\max} D(1-D) \qquad 4.11$$

In the discontinuous mode the voltage ratio $\frac{V_o}{V_d}$ is equal to:

$$\frac{V_o}{V_d} = \frac{D^2}{D^2 + \frac{1}{4}\left(\frac{I_o}{I_{LB,\max}}\right)} \qquad 4.12$$

The figure 4.11 shows the voltage ratio $\frac{V_o}{V_d}$ as a function of $\frac{I_o}{I_{LB,max}}$ for various values of duty ratio and it is obtained buy using the equation 4.12.

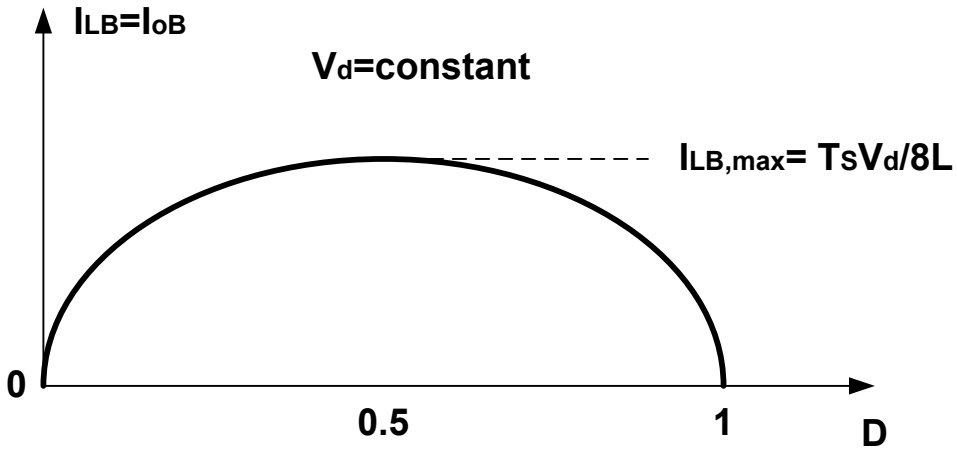

Fig.4.9. I_{LB} as a function of D.

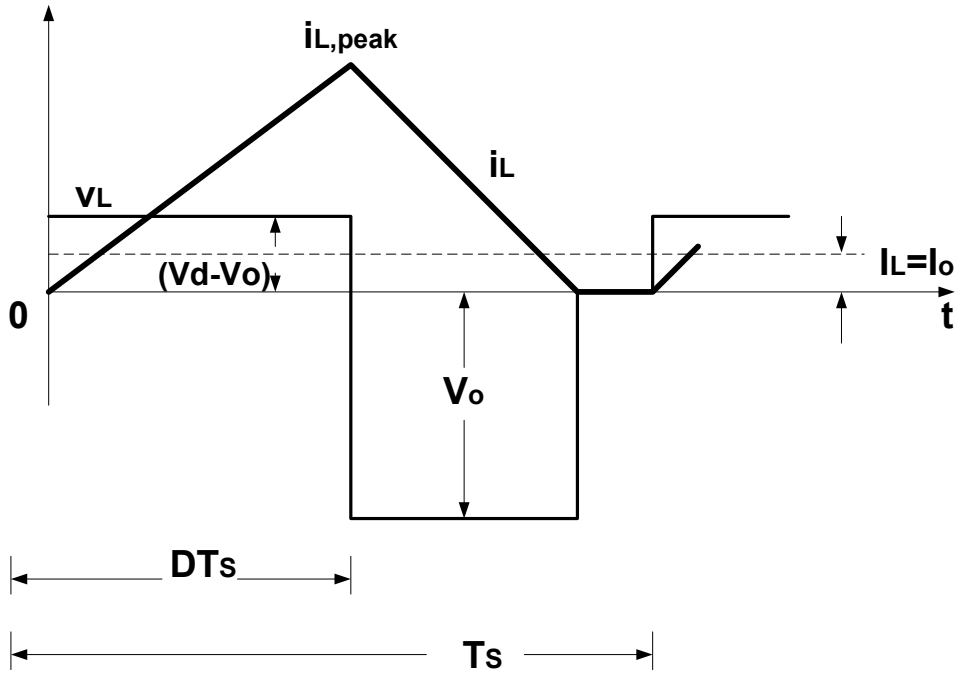

Fig. 4.10. Discontinuous conduction in step-down converter.

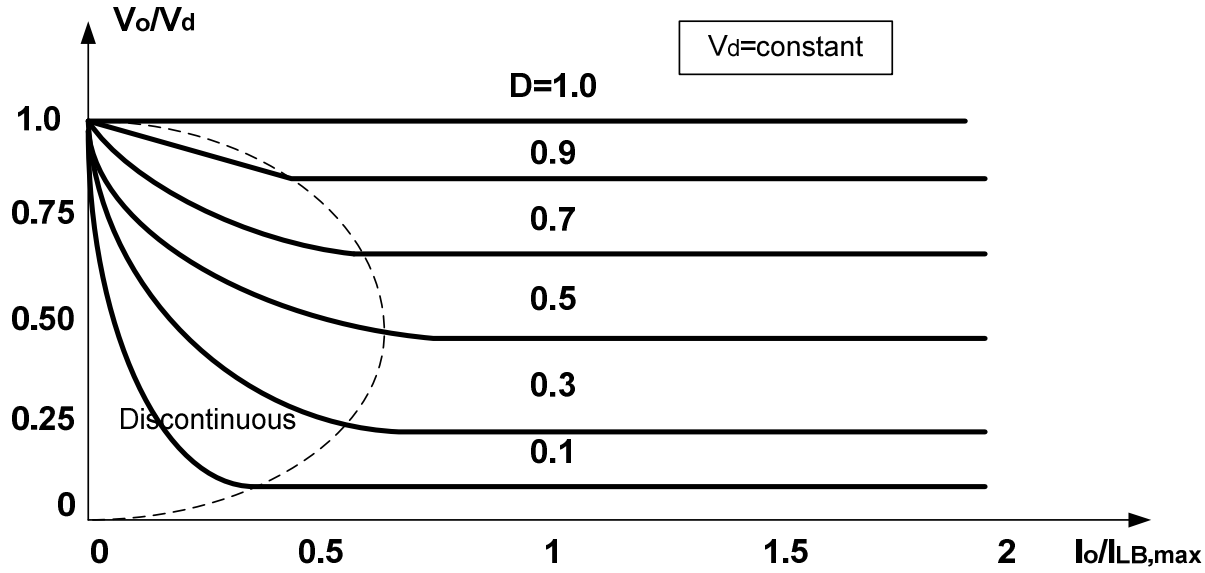

Fig. 4.11. Buck converter characteristics with V_d constant.

4.1.2.4 Output Voltage Ripple

The output capacitor is assumed to be large to yield v_o(t) = V_o and the ripple in the output voltage can be calculated by considering the waveforms of v_o, v_L and i_L (figure 4.12) for a continuous-conduction mode of operation. The area ΔQ in the figure 4.12 represents an additional charge, when the ripple component of i_L flows trough the capacitor and its average component flows trough the load resistor. Therefore, the peak-to-peak voltage ripple ΔV_o is:

$$\Delta V_o = \frac{\Delta Q}{C} = \frac{1}{C}\frac{1}{2}\frac{\Delta i_L}{2}\frac{T_s}{2} \qquad 4.13$$

During the interval t_{off}:

$$\Delta i_L = \frac{V_o}{L}(1-D)T_s \qquad 4.14$$

Using the equations 4.13 and 4.14 the voltage ripple ΔV_o is:

$$\Delta V_o = \frac{T_s}{8C}\frac{V_o}{L}(1-D)T_s \qquad 4.15$$

$$\frac{\Delta V_o}{V_o} = \frac{1}{8}\frac{T_s^2(1-D)}{LC} = \frac{\pi^2}{2}(1-D)(\frac{f_c}{f_s})^2 \qquad 4.16$$

Where $f_s = \frac{1}{T_s}$ is the switching frequency and $f_c = \frac{1}{2\pi\sqrt{LC}}$

The equation 4.15 shows that the voltage ripple can be minimized by using a cut-off frequency of the low-pass filter f_c such as $f_c \ll f_s$. The ripple is independent from the output load power when the converter operates in the continuous-conduction mode.

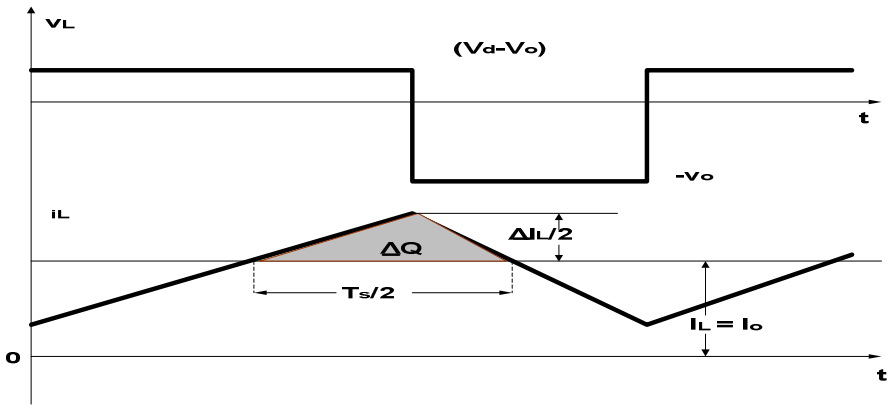

Fig. 4.12. Output voltage ripple in a step-down converter.

4.1.3 DC-DC Converter Filter Design

The DC-DC converter operation is with constant switching frequency and input DC voltage, while the regulation of output voltage is obtained by varying the converter duty cycle D. The value of input voltage is obtained from equation 4.17, which express the voltage at the output of a three phase rectifier supplied by a 380V/50Hz three phase voltage.

$$V_{dc} = \frac{1}{\pi/3}\int_{-\pi/6}^{\pi/6}\sqrt{2V_{LL}}\cos\omega d\omega = \frac{3}{\pi}\sqrt{2V_{LL}} = 1.35V_{ll} \qquad 4.17$$

The design of the converter output filter has been carried out on the basis of the following conditions:

1. continuous-current conduction operation of the converter for output currents higher than 62 mA;
2. ripple on the output voltage lower than 2%;
3. The switching frequency has been chosen f_s = 10KHz because it must be comparable to the obtained sampling frequency of DSP board and also, it must not be so little to cause acoustic noise.

The following design constraint is obtained by using the first condition in the equation 4.9:

$$L \geq \frac{\delta T_s}{2I_{LB}} V_{DC}(1-D) \qquad 4.18$$

where I_{LB} is the average inductor current at the boundary between continuous and discontinuous conduction. In order to prevent the buck converter from entering the discontinuous mode, it is required that the minimum output current it can provide (I_{LBmin}) be equal to the average maximum boundary current, which occurs at D=1/2 (Figure 4.9). The following component values have been chosen: I_{LBmin} = 62mA, V_{dc}= 50V, T_S= 1 10^{-4} s and $V_o ripple = 2\%$. This gives:

$$L \geq \frac{T_s}{8I_{LB\min}} V_{DC} = 10mH \qquad 4.19$$

The following design constraint on the capacitor C is obtained by using the equation 4.15:

$$C \geq \frac{1}{8}\frac{T_s^2(1-D)}{L}\left(\frac{V_o}{\Delta V_o}\right) \qquad 4.20$$

Since the greatest ripple occurs at δ=0 it is then required that:

$$C \geq \frac{1}{8}\frac{T_s^2}{L}\left(\frac{V_o}{\Delta V_o}\right) = 1\mu F \qquad 4.21$$

in figure 4.13 the scheme of the adopted DC-DC buck converter circuit is shown and in this scheme, the resistive components r_L and r_c represent the parasitic resistance of the output filter inductor and capacitor. These values have been measured by the RCL meter Fluke PM6304. On the basis of the design criteria in eq.s (4.19), (4.21) the LC filter components have been chosen with values available in the market, as shown in Tab.III.

Parameters	Value
L	10 [mH]
r_L	1.4 [Ω]
C	10 [μF]
r_c	2.06 [Ω]

Tab.III. Parameters of LC filter

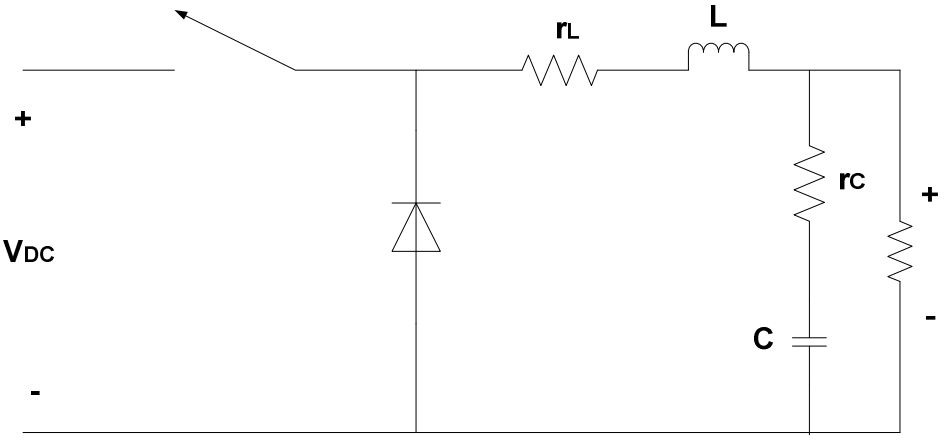

Fig. 4.13. Electrical scheme of a buck converter with parasitic resistances.

4.2 DC-DC Converter Control Design

A control strategy is needed in order to make the DC-DC converter able to describe the electrical behavior of the PEM fuel cell system with varying the electrical load, the temperature of the fuel cell, the pressure of oxygen, the pressure of hydrogen, etc. The schematic diagram of the converter control system is shown in the figure 4.14. The DC-DC buck converter has been driven by using two different control strategies, which are respectively based on a mathematical linearization of the step-down converter and on a space-state voltage methodology [1], [4].

In the following sections the two control techniques adopted are briefly described, as well as the stability of the system for different load conditions, the implementation of control strategies by Matlab/Simulink. Moreover experimental results are shown.

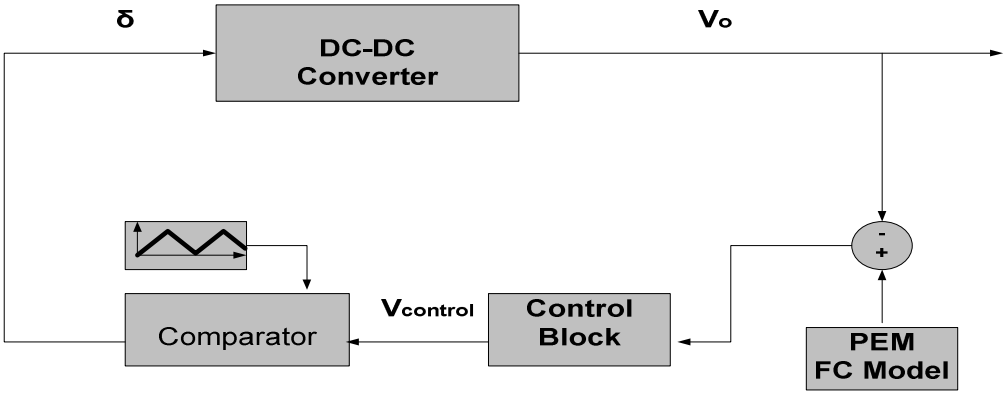

Figure 4.14: schematic representation of the DC-DC buck converter control.

4.2.1 Control Voltage based on the space state averaging technique

The space state averaging technique [1] allows the transfer function of the power stage of the buck converter to be obtained, which makes the frequency analysis possible. Therefore, the Nyquist stability criterion and the Bode plots can be used to determine the appropriate compensation in the feedback loop for the desired steady-state and transient responses. The space-state averaging technique permits to obtain a linear model of the power stage including the output filter for small ac signals, linearized around a steady-state dc operating point. Correspondingly, the PWM controller can be linearized around a steady state point. In the feedback control system (Figure 4.15), each block can be represented by a transfer function as shown in figure 4.16. The space state averaging technique is described in the Appendix B.

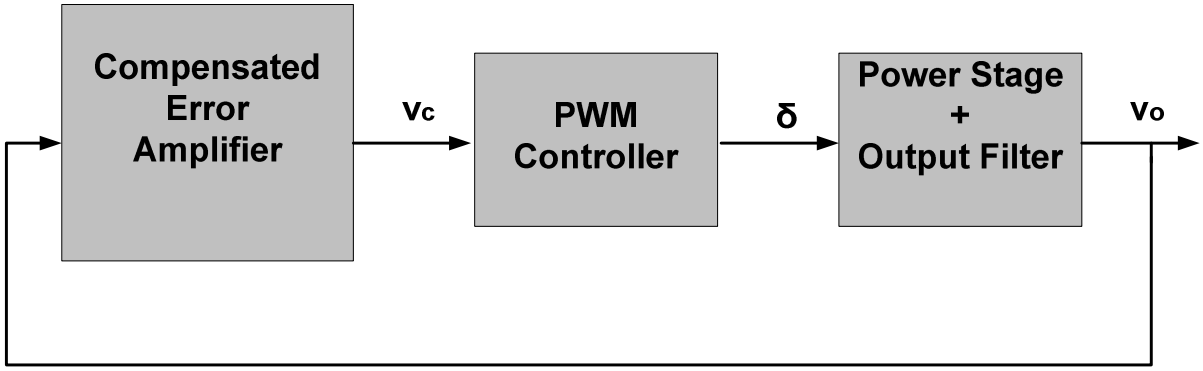

Fig. 4.15. Feedback control system.

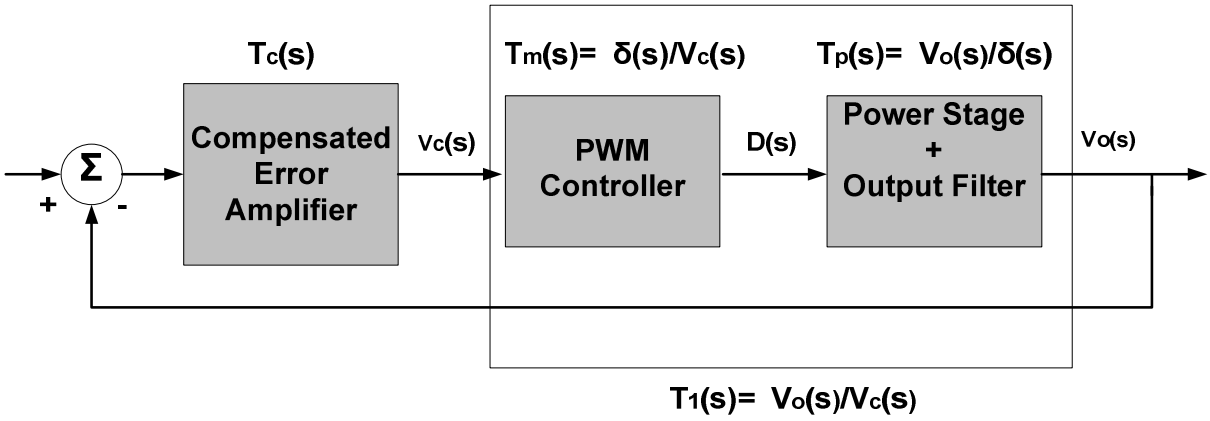

Fig. 4.16. Linearized feedback control system.

4.2.1.1 Compensation of the feedback system

The open-loop transfer function of the system shown in figure 4.15b is $T_{OL}(s) = T_1(s)T_c(s)$, where $T_1(s) = \frac{\tilde{v}_o(s)}{\tilde{v}_c(s)} = \frac{\tilde{v}_o(s)}{\tilde{\delta}(s)}\frac{\tilde{\delta}(s)}{\tilde{v}_c(s)} = T_p(s)\cdot T_m(s)$ and $T_c(s)$ represents the transfer function of compensated error amplifier. For a given transfer function $T_{OL}(s)$, the transfer function $T_c(s)$ must be chosen so that $T_{OL}(s)$ meets the performances expected of the power supply. Some of the desired characteristics are:

- The gain a low frequencies must be as high as possible to minimize the steady-state error in the power supply output;
- The crossover frequency is the frequency at which the gain of $T_{OL}(s)$ is equal to zero and it should be as high as possible but an order of magnitude below the switching frequency to allow the power supply to quickly respond to the transient (high bandwidth);
- The desirable range of the phase margin (PM) is 45°-60° to guarantee the stability of the system. This because the controlled system is a minimum-phase, so a phase margin above 45* is enough to attain a good relative stability.

A transfer function $T_c(s)$ with a couple of pole-zero and a pole at the origin is used to control the power stage. $T_c(s)$ is of the form:

$$T_c(s) = \frac{A}{s}\frac{(s+\omega_z)}{(s+\omega_p)} \qquad 4.22$$

where A is positive and $\omega_z < \omega_p$. The phase and the gain of $T_c(s)$ are shown in the Figures 4.17a and 4.17b.

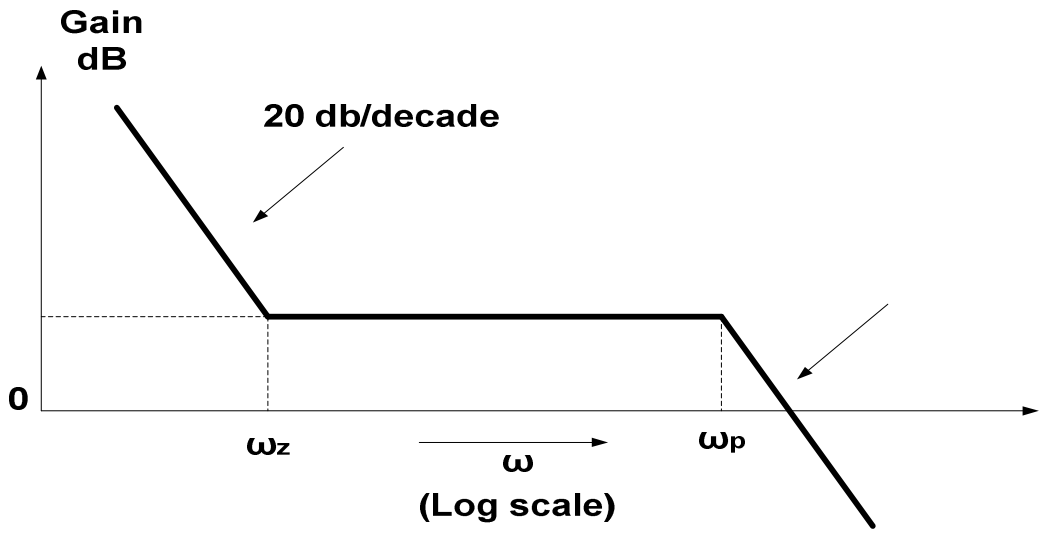

Fig. 4.17a. Gain of the Error Amplifier.

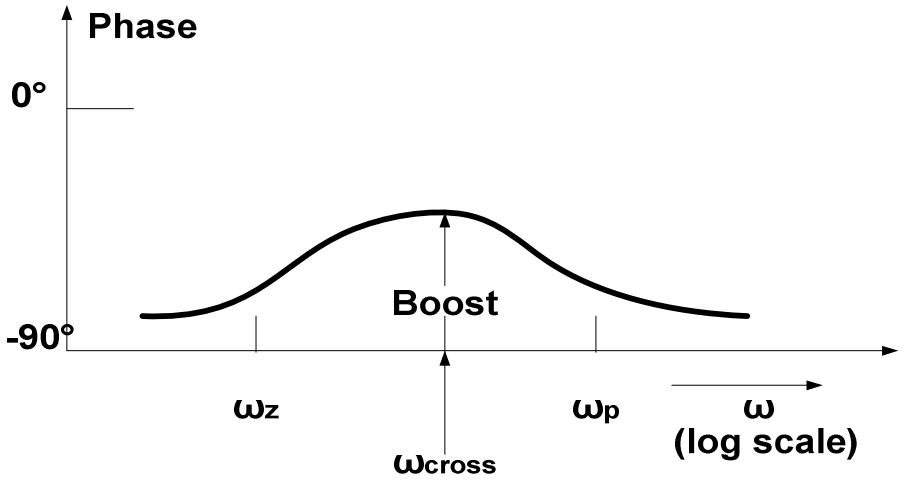

4.17b. Phase of the Error Amplifier.

The parameters of the transfer function $T_c(s)$ are determined by using the K-factor approach [55]:

$$\omega_z = \frac{\omega_{cross}}{K} \qquad \omega_p = K\omega_{cross} \tag{4.23}$$

$$K = \tan(45° + \frac{boost}{2}) \qquad 4.24$$

$$PM = \varphi_{OL} + 180° = 180° + \varphi_1 + \varphi_c \qquad 4.25$$

$$\varphi_1 = \varphi_p(s) + \varphi_m(s) \qquad 4.26$$

Where φ_c is the phase angle of $T_c(s)$ at the crossover frequency, φ_1 is the phase angle of $T_1(s)$, $\varphi_p(s)$ is the phase angle of the power stage $T_p(s)$ and $\varphi_m(s)$ is the phase angle of the modulator $T_m(s)$.

From the phase of the transfer function $T_c(s)$ (Figure 4.17b):

$$\varphi_c = -90° + boost \qquad 4.27$$

From equations 4.39 and 4.41:

$$boost = PM - \varphi_1 - 90° \qquad 4.28$$

Therefore, the boost is defined after choosing the phase margin where φ_1 is obtained from Figure 4.17b at the frequency chosen to be the crossover frequency. K can be calculated from equation 4.38.

The gain G_{OL} at the open loop system must be equal to 1 at the crossover frequency and this requires that ($T_{OL}(s) = T_1(s) \cdot T_c(s)$) G_c of the compensated error amplifier at ω_{cross} be:

$$G_c(at\,\omega_{cross}) = \frac{1}{G_1(at\,\omega_{cross})} \qquad 4.29$$

The design of the error amplifier is made by using PM=45°, $\omega_{cross} = 3.810^3 \text{rad/sec} < \omega_s$=6.28 10^4rad/sec → boost=81.48 → K=13.42. Then the following choice for the transfer function $T_c(s)$ of the compensator has been made:

$$T_c(s) = \frac{A}{s}\frac{(s+\omega_{zc})}{(s+\omega_{pc})} = \frac{2293}{s}\frac{(s+0.26\cdot10^3)}{(s+77.57\cdot10^3)} \qquad 4.30$$

In the Figure 4.18a are shown the Bode diagrams of the phase and the gain of $T_1(s)$ and in the Figure

4.18b the Bode diagrams of the phase and the gain of $T_c(s)$.

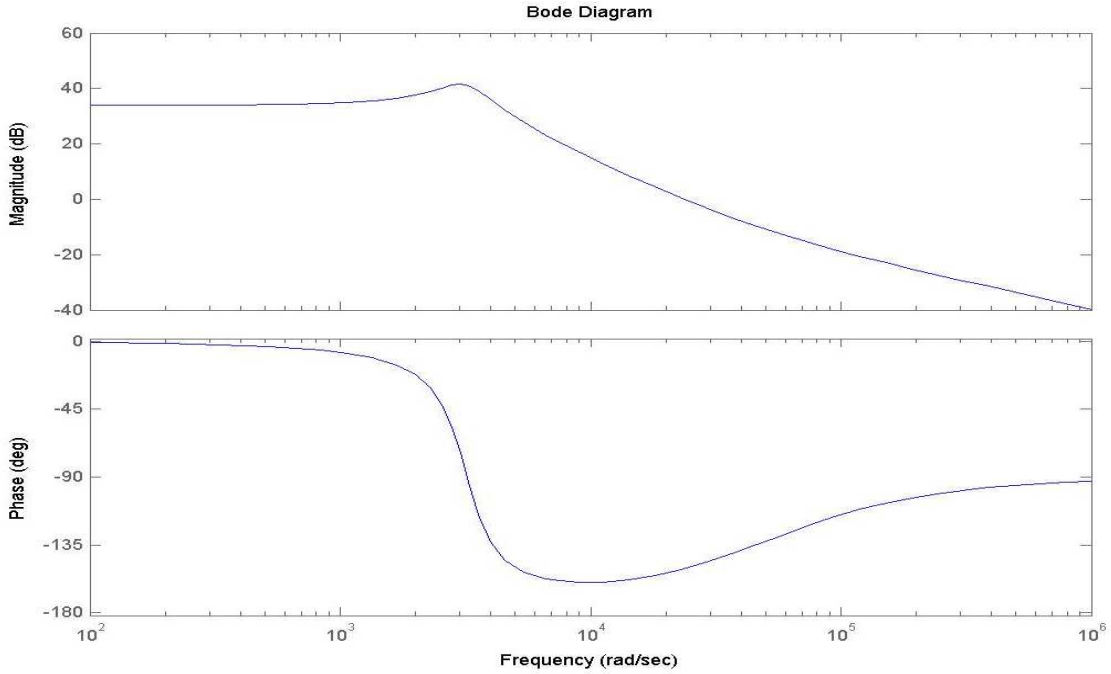

Fig. 4.18a. Bode diagrams of $T_1(s)$.

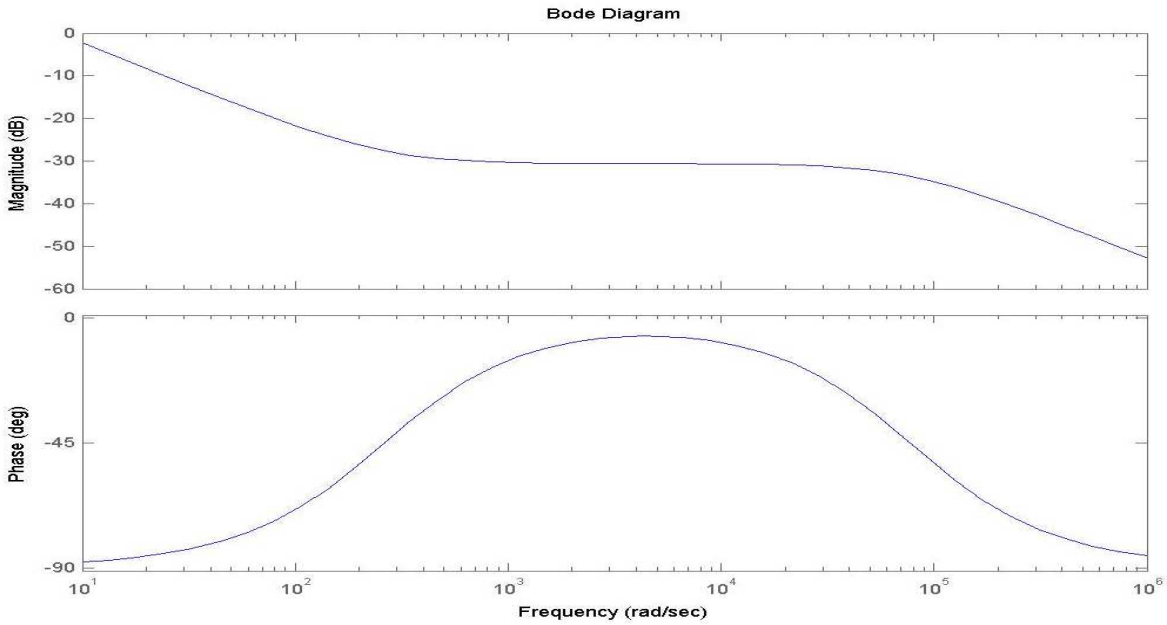

Fig. 4.18b. Bode diagrams of $T_c(s)$.

Some remarks should be made:

- The compensator which has been used, a lead compensator in cascade with an integrator, is essentially a PI, since the pole is at 7.7·103 > 6.28 ·103 which is the switching frequency.
- This controller has been employed since literature provides well defined design criteria ensuring high bandwidth and high stability margins.
- The uncontrolled system has a crossover frequency f_{ucross}=503 Hz. The PI-controlled has an open-loop crossover frequency f_{ccross}=605 Hz, while the closed-loop transfer function has a f_{cross}=496 Hz
- A PID cannot be used for amplification of noise at higher frequency

4.2.1.2 Stability Analysis

The stability of the system has been studied by the Nyquist diagram plotted for different load conditions, in order to establish the stability margins in the worst case.The worst case, in term of load condition, has been found with higher values of load resistance, R_L=130 Ω, corresponding to the boundary current I_{LBmin}, which also results in worst relative stability because of the reduction of the damping ratio ζ. This is a working condition in the activation zone. It should be considered that the implementation of the control law in a digital controller leads to an unavoidable time delay due to sampling and processing. This delay time, present in real system, can cause instability problems even in system theoretically designed as stable. For this reason, in the controller design, the delay-time introduced by the microprocessor board has been considered. This delay-time is one time sample of the control system (10^{-4} s in the application under hand), which can be approximated in the s-domain continuous domain by the following transfer function (1st order Padé approximation):

$$H_d(s) = \frac{(2 - 10^{-4} s)}{(2 + 10^{-4} s)} \qquad 4.31$$

Figure 4.19 shows the Nyquist plots of the system closed loop transfer function for two load limit conditions, respectively R_L=130 Ω and R_L=5 Ω, with and without the delay-time. This figure shows clearly that the system is always far from the stability limit, even taking into consideration the microprocessor delay time. This does not mean that the system is globally stable: it only means that for the practical range

of values of the resistive load, the system is stable.

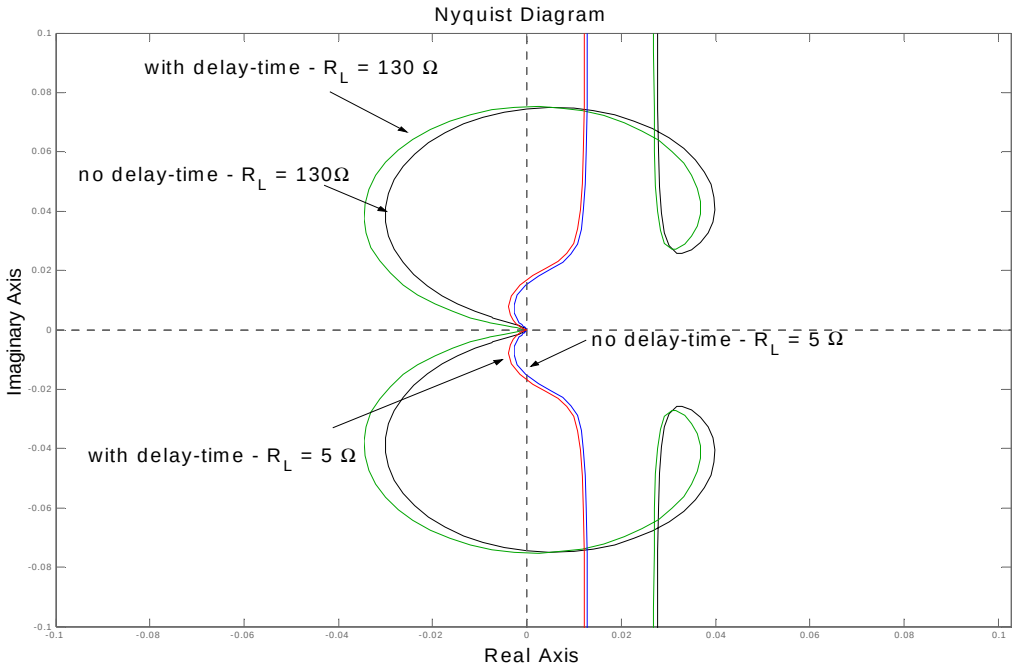

Fig. 4.19. Nyquist diagrams of the closed loop transfer function in the 3 different cases.

4.2.1.3 Numerical results

The control voltage, discussed in the previous section, has been tested in the Matlab/Simulink environment. The tests have been made considering three different values of the reference voltage V_{FCref} (15 V, 30V and 45V) and afterwards the output voltage and the duty ratio have been drawn. The experimental results obtained in numerical simulation (continuous domain) are shown in the figures 4.21a, 4.21b and 4.21c and it can be observed that, for each value of V_{FCref} the voltage chopper tracks the reference voltage in steady-state and that the output voltage ripple is very low. The figures 4.20a, 4.20b, 4.20c and 4.20d represent the Matlab/Simulink implementation of the closed-loop system constituted by the power stage and the voltage controller. The PWM controller shown in the figure 4.20b implements the following relation: the duty ratio δ(t) is equal to 1.0 if $v_c(t) \geq v_r(t)$ or zero if $v_c(t) < v_r$, where $v_r(t)$ is a sawtooth waveform that defines the switching frequency.

Figure 4.20c implements the LC filter by using the Laplace transformer and the figure 4.20d implements the load of the system.

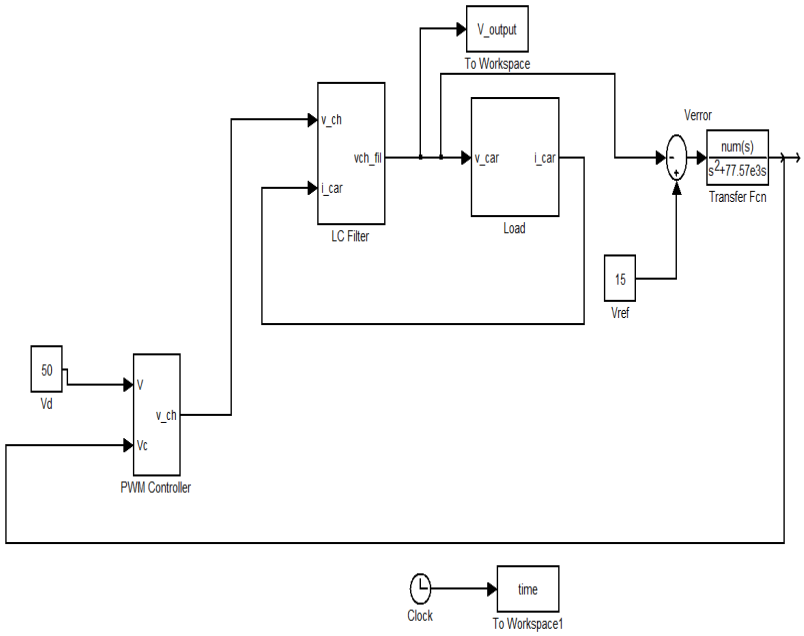

Fig. 4.20a. Matlab/Simulink implementation of the power stage and the controller.

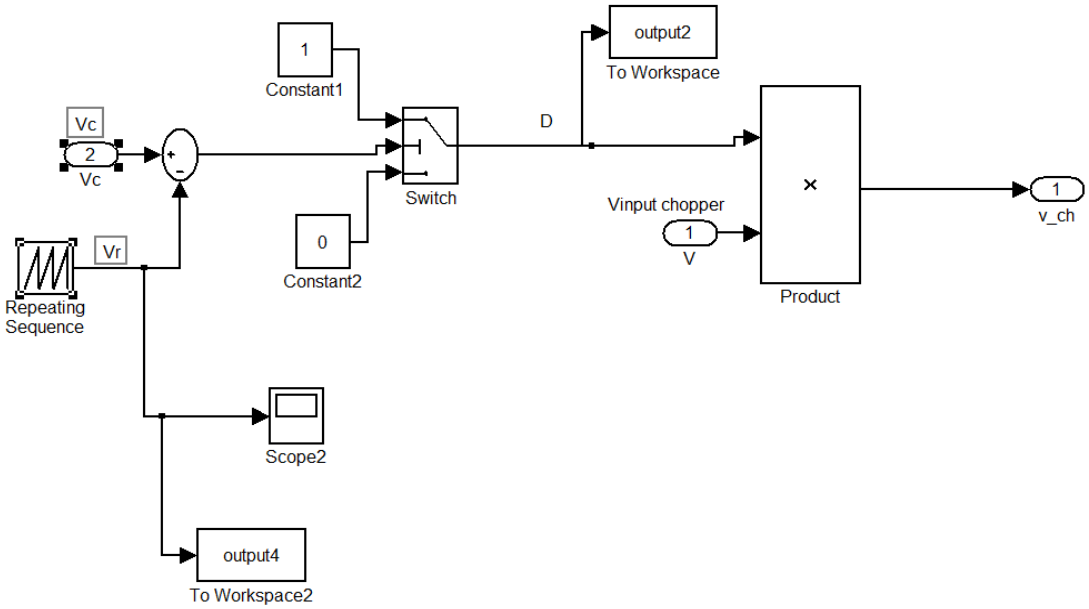

Fig. 4.20b. Matlab/Simulink implementation of the PWM Generator.

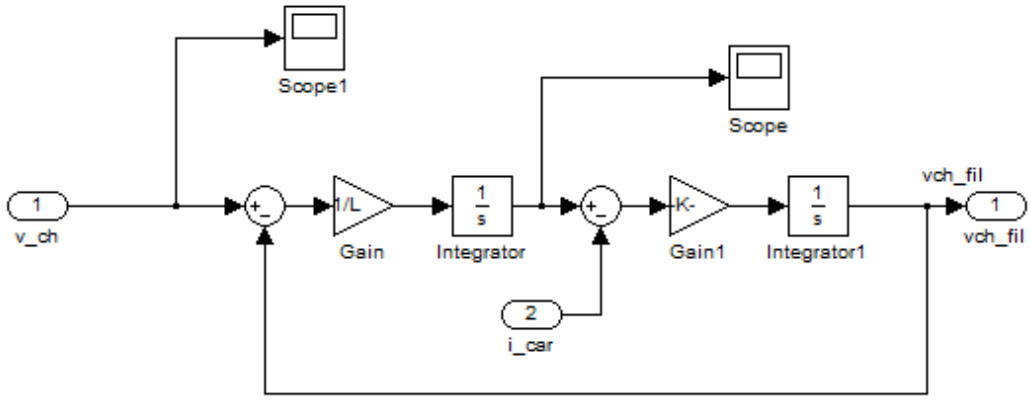

Fig. 4.20c. Matlab/Simulink implementation of the LC filter.

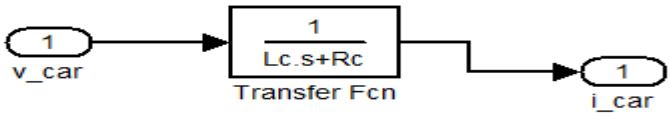

Fig. 4.20d. Matlab/Simulink implementation of the load.

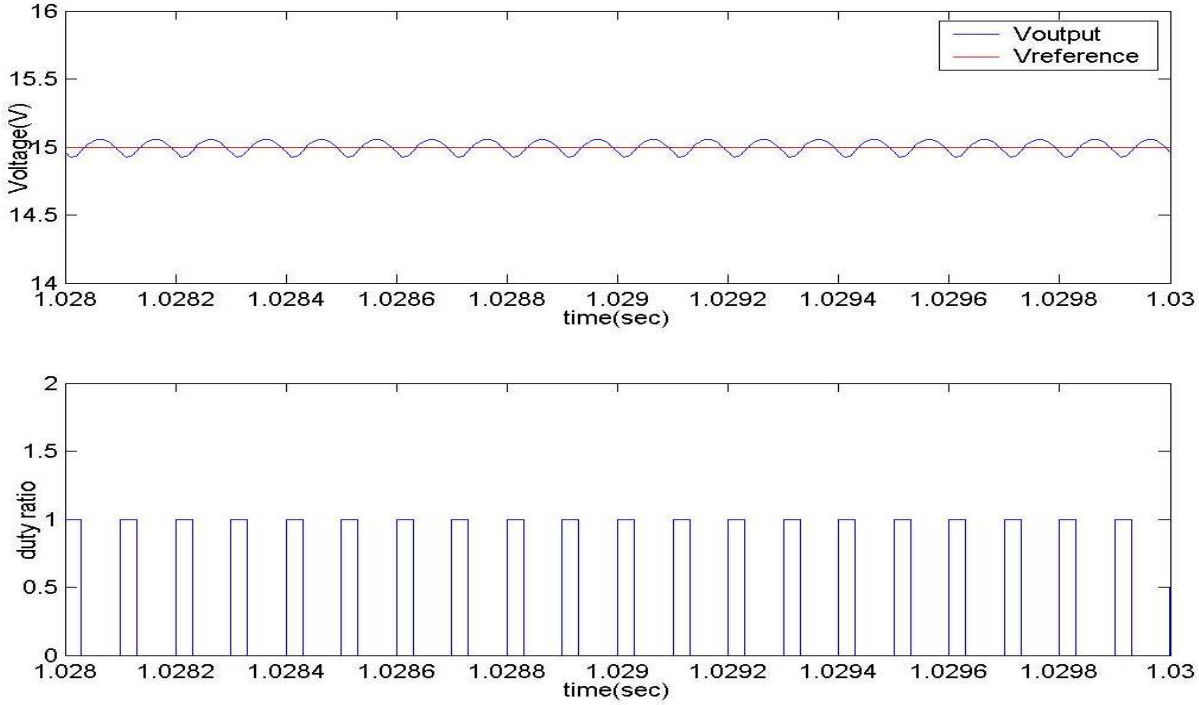

Fig. 4.21a. V_{output} and duty ratio with V_{ref}=15V.

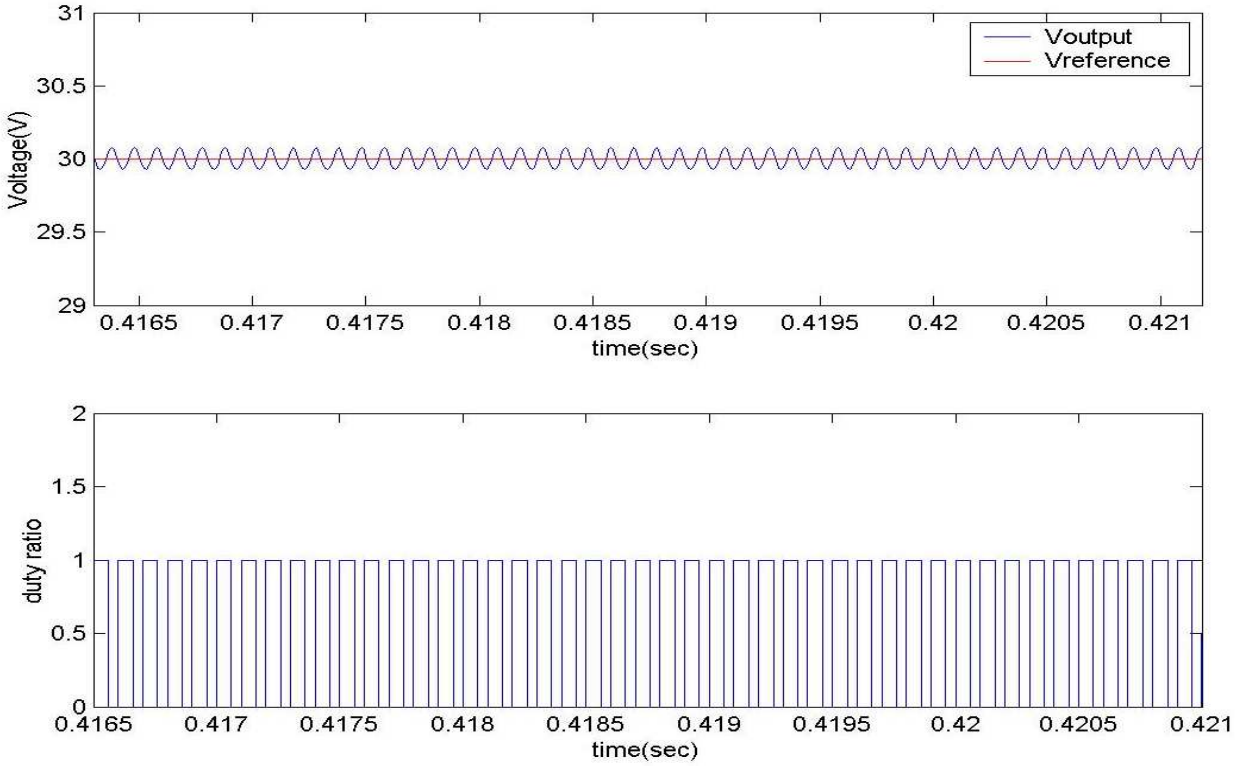

Fig. 4.21b. V_{output} and duty ratio with V_{ref}=30V.

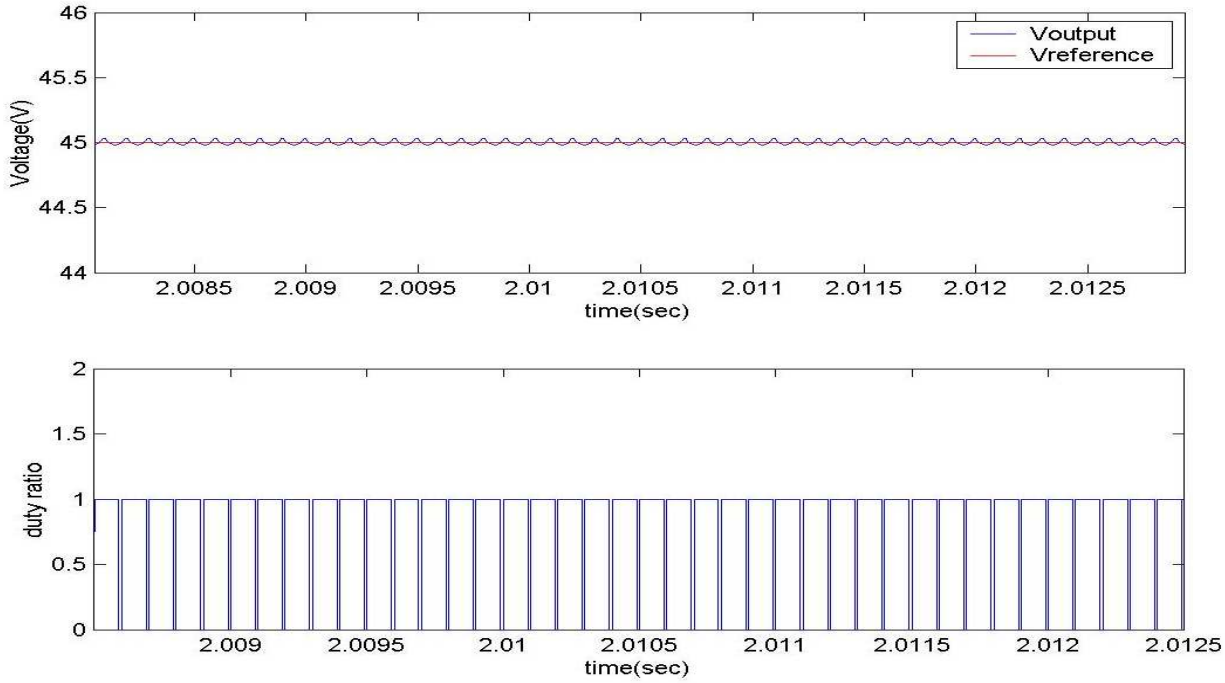

Fig. 4.21c. V_{output} and duty ratio with V_{ref}=45V.

4.2.2 Voltage Controller with State Variable Feedback

The voltage controller with state variable feedback of the DC-DC buck converter as proposed in [56] has been adopted here. In the following only the fundamentals of the methodology are provided. The large-signal averaged model of the buck converter in the continuous conduction mode, including the internal resistances of the inductor and the capacitor of the output filter, is described by the following set of equations in matrix form, where the load is considered in the general case as a real current generator i_{o1} with a parallel resistance R:

$$\begin{bmatrix} i_L \\ \dot{v}_c \end{bmatrix} = \begin{bmatrix} -1/L\left(r_L + Rr_C/R_{mC}\right) & -R/\left(LR_{mC}\right) \\ R/\left(R_{mC}C\right) & -R/\left(R_{mC}C\right) \end{bmatrix} \begin{bmatrix} i_L \\ v_c \end{bmatrix} + \begin{bmatrix} 1/L & r_C R/\left(LR_{mC}\right) \\ 0 & -R/\left(R_{mC}C\right) \end{bmatrix} \begin{bmatrix} w \\ i_{01} \end{bmatrix} \quad 4.32$$

where v_c is the output voltage, i_L the inductor current, $w=D\cdot v_{in}$ is a new control variable computed on the basis of the converter duty cycle D and the input voltage V_{DC}., L and C are the converter inductance and capacitance, and r_L and r_C are the corresponding parasitic resistances. Finally R_{mc} is defined as $R_{mc} = R + r_C$.
In the case under hand, the FCS has been loaded with a purely resistance load. As a consequence, the term

i_{01} = 0. If the non-linear feedback $w=D\cdot V_{DC}$ is adopted, the large-signal averaged model of the converter is linear. Thus the well-known methods of analysis and design of linear time invariant systems can be used.

Since in the proposed application of the buck converter an accurate output voltage control is needed, besides the existing state variables in (4.32) the integral of the output voltage error is introduced as a new state variable. It is noteworthy that, in general, the choice of state variables affects the performance of the system. For example, if the inductor current, the output voltage error and its integral are selected as state variables the result is the classical current mode control by a PI controller in the external voltage loop [56].

Here, as in [56], the following state variables have been adopted for feedback: the capacitor current, the output voltage and the integral of the output voltage error.

The choice of capacitor current instead of the inductance one can be justified by the following reasons [56]:

1) The output impedance of the DC-DC converter, when it is controlled in closed loop, is lower than that achievable with the inductance current;

2) Since the steady-state mean capacitor current is null a smaller volume, cheaper coil sensor can be used;

3) A higher robustness of the feedback gains versus output resistance variations can be achieved in comparison to that with the inductor current.

The following controller state-space equations can be then deduced [56]:

$$\begin{cases} \dot{i}_C = -\dfrac{1}{RC} i_C - \dfrac{1}{L} v_C + \dfrac{1}{L} w \\ \dot{v}_C = \dfrac{1}{C} i_C \\ \dot{x}_1 = v_C - v_{ref} \end{cases} \qquad 4.33$$

where v_{ref} is the reference voltage and $x_1 = \int \left(v_C - v_{ref} \right) dt$.

4.2.2.1 Pole Placement

On the basis of the well known pole placement approaches [57], the closed loop poles of the systems can be fixed on the basis of a proper choice of the feedback gains, which are g_1 (capacitor current), g_2 (capacitor voltage), g_3 (integral of the output voltage error) in the case considered here.

If the control input of the system is :

$$w = -g_1 i_C - g_2 v_C - g_3 x_1 \qquad 4.34$$

the following characteristic polynomial is obtained:

$$p(s) = s^3 + \left(\frac{g_1}{L} + \frac{1}{R_m C}\right)s^2 + \left(\frac{1+g_2}{LC}\right)s + \frac{g_3}{LC} \qquad 4.35$$

Finally, the feedback gains can be computed as beneath:

$$\begin{cases} g_1 = L\left(k_1 + k_2 + k_3 - \dfrac{1}{RC}\right) \\ g_2 = -1 + LC\left(k_1 k_2 + k_1 k_3 + k_2 k_3\right) \\ g_3 = LC\, k_1 k_2 k_3 \end{cases} \qquad 4.36$$

where $k_i = -p_i$ (i=1, 2, 3) and p_i are the desired poles of the system. Figure 4.22 shows the block diagram of the adopted state-space controller. In the experimental application, the chosen poles are one real $p_1 = -2\pi 500$, and the other two complex conjugate $p_{2,3} = -2\pi 500 \pm j\, 2\pi 500$, on the basis of a compromise between good dynamic performance and a proper distance from the switching frequency of the converter (f_c= 10 kHz). The bandwidth of the system should actually be at least 1/10 of the switching frequency of the converter.

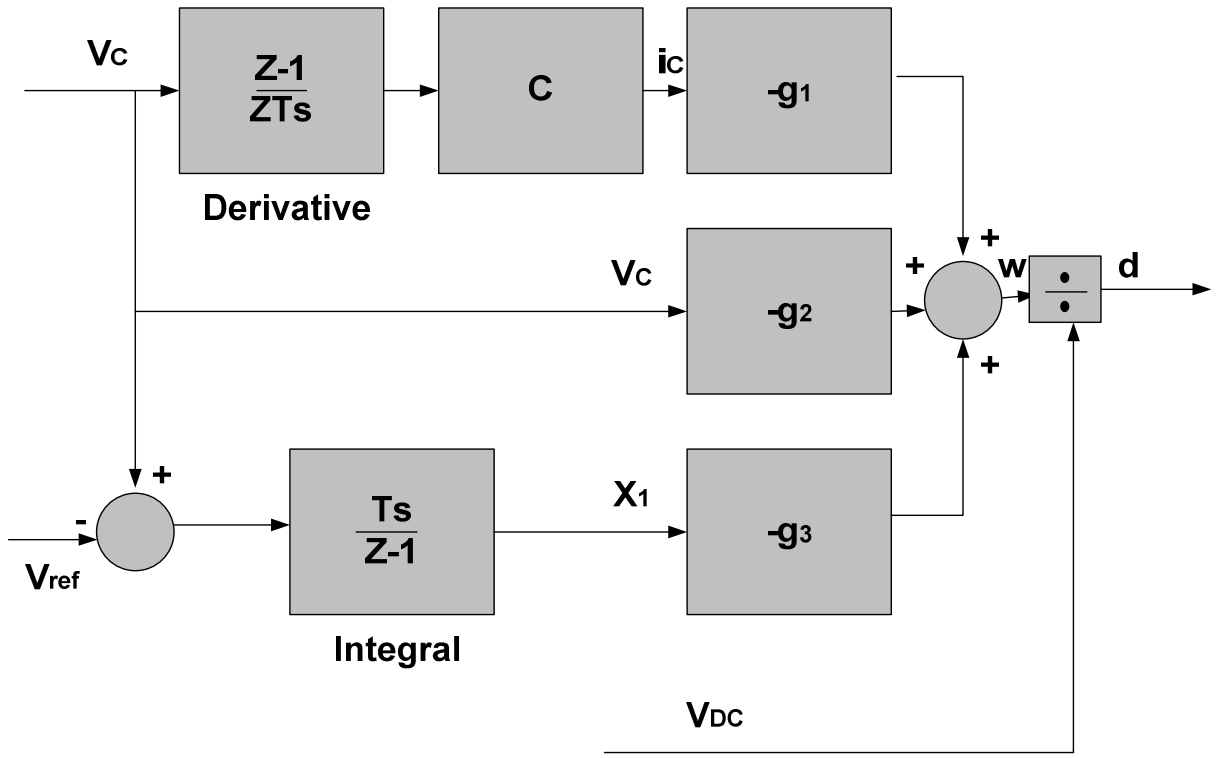

Fig. 4.22. Block diagram of the space-state controller.

4.2.2.2 Numerical results

The control voltage, discussed in the previous section, has been tested in the Matlab/Simulink environment. The tests have been made considering three different values of the reference voltage V_{FCref} (15 V, 30V and 45V) and afterwards the output voltage has been drawn. The experimental results obtained in numerical simulation (discrete domain) are shown in the figures 4.23a, 4.23b and 4.23c and it can be observed that, for each value of V_{FCref}, the voltage chopper tracks the reference voltage in steady-state and that the output voltage ripple is low. The figures 4.24a, 4.24b and 4.24c represent the Matlab/Simulink implementation of the voltage controller with state variable feedback system. Figure 4.23d shows the comparison between the V_{output} of the Buck converter when it is used a conventional control system (PI) and the voltage controller with state variable feedback, respectively. It is apparent that the rise time as well as the settling-time are definitely reduced when the state variable feedback controller is used, when an input reference V_{FCref} step from 30 to 45 V is given.

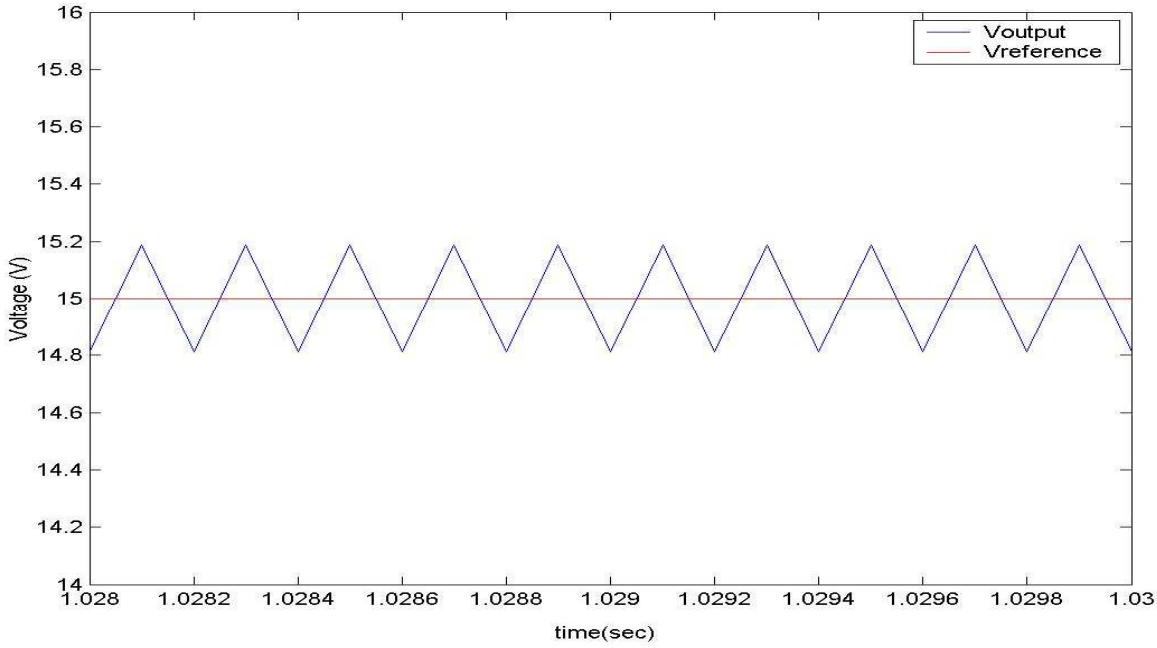

Fig. 4.23a. Voutput with Vref=15V.

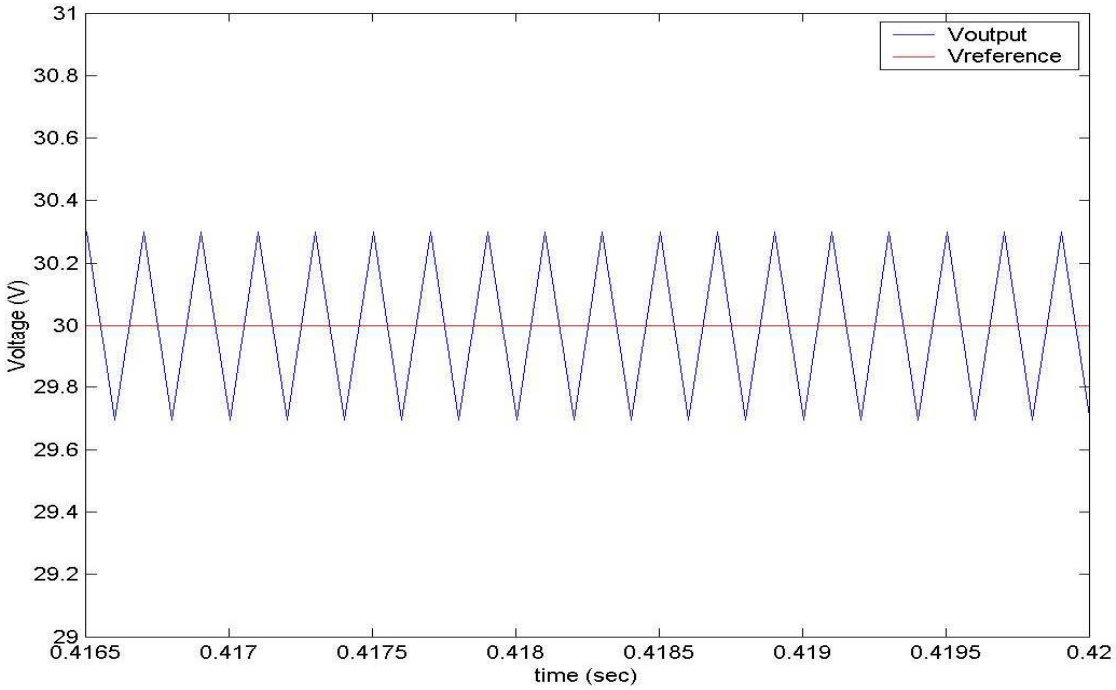

Fig. 4.23b. Voutput with Vref=30V.

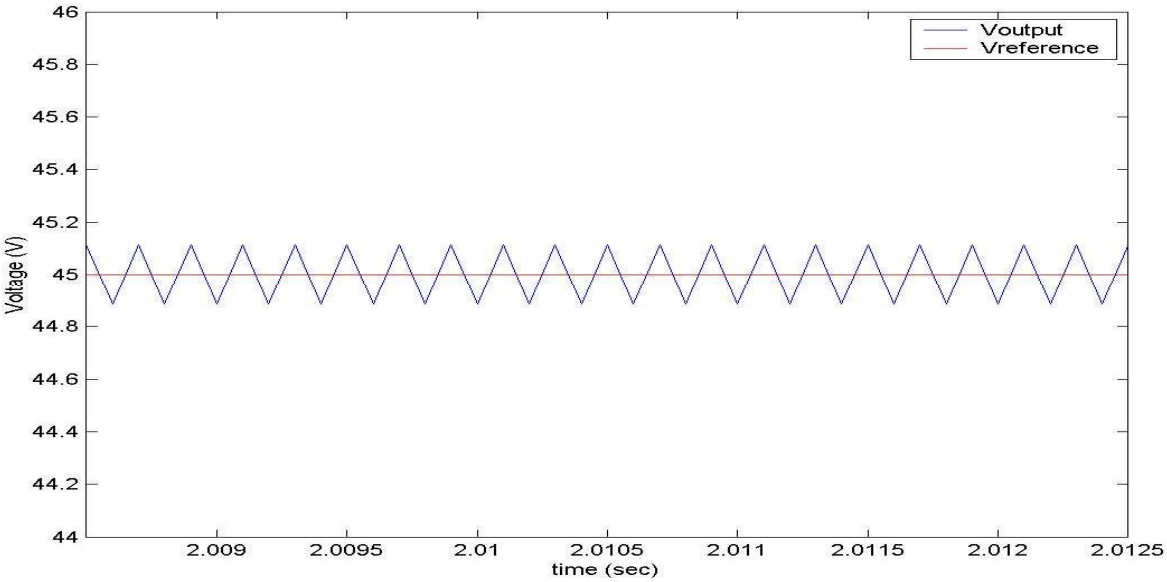

Fig. 4.23c. Voutput with Vref=45V.

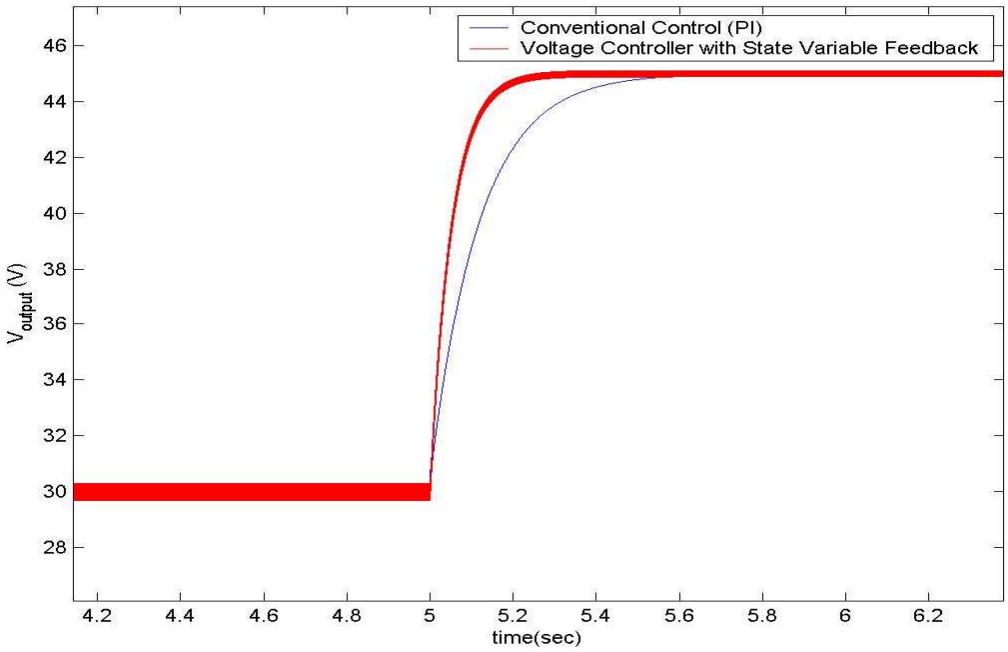

Fig. 4.23d. V_{output} **with conventional control system (PI) vs** V_{output} **with the voltage controller with state variable feedback when the input reference** V_{FCref} **step from 30 to 45 V is given.**

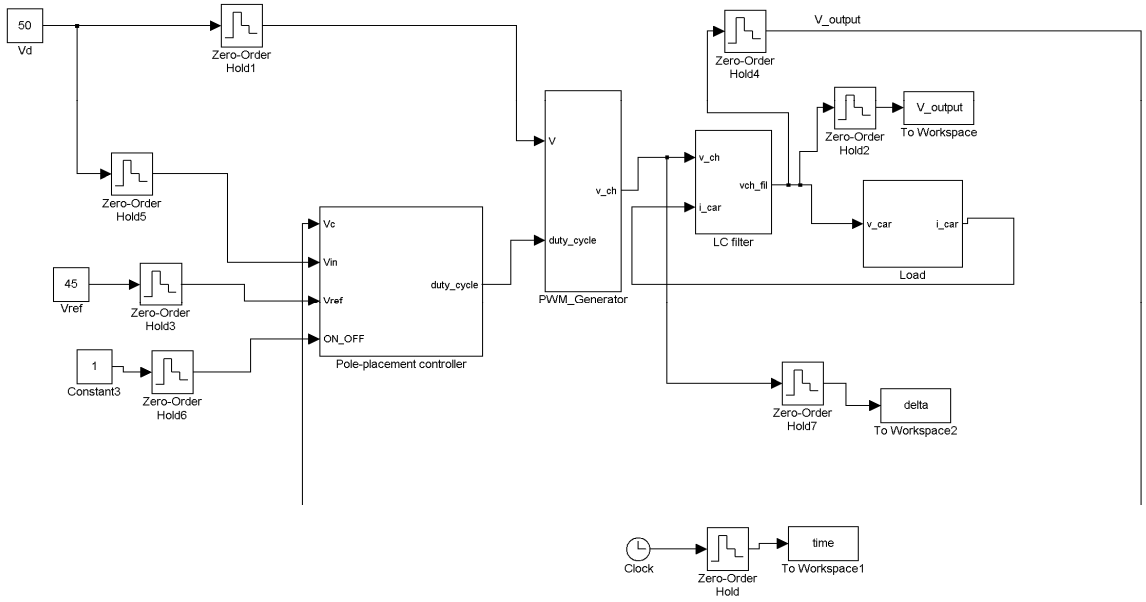

Fig. 4.24a. Matlab/Simulink implementation of the power stage with the Pole-Placement controller.

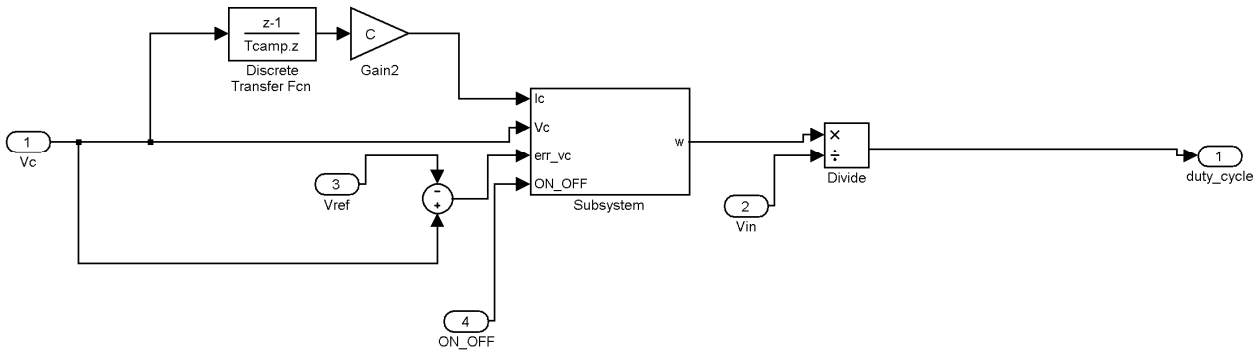

Fig. 4.24b. Matlab/Simulink implementation of the Pole-Placement controller (1).

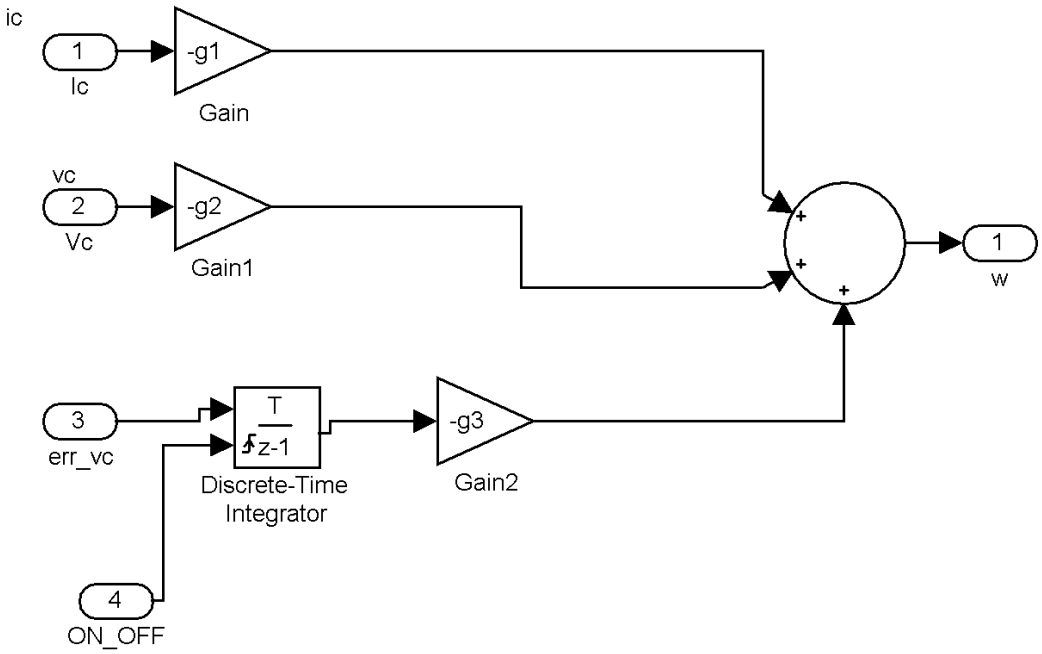

Fig. 4.24c. Matlab/Simulink implementation of the Pole-Placement controller (2).

4.3 Hardware Design of the PEM FC Emulator

The components of the fuel cell emulator and the experimental setup are described in this section. The prototype of FC emulator has been built in the framework of the scientific agreement between FCLab-SET-UTBM, Belfort – France and ISSIA-CNR, Palermo – Italy [6],[7]. The circuit designed is based upon simplified circuit showed in the Figure 4.25. The full schematic is detailed in Figure 4.26.

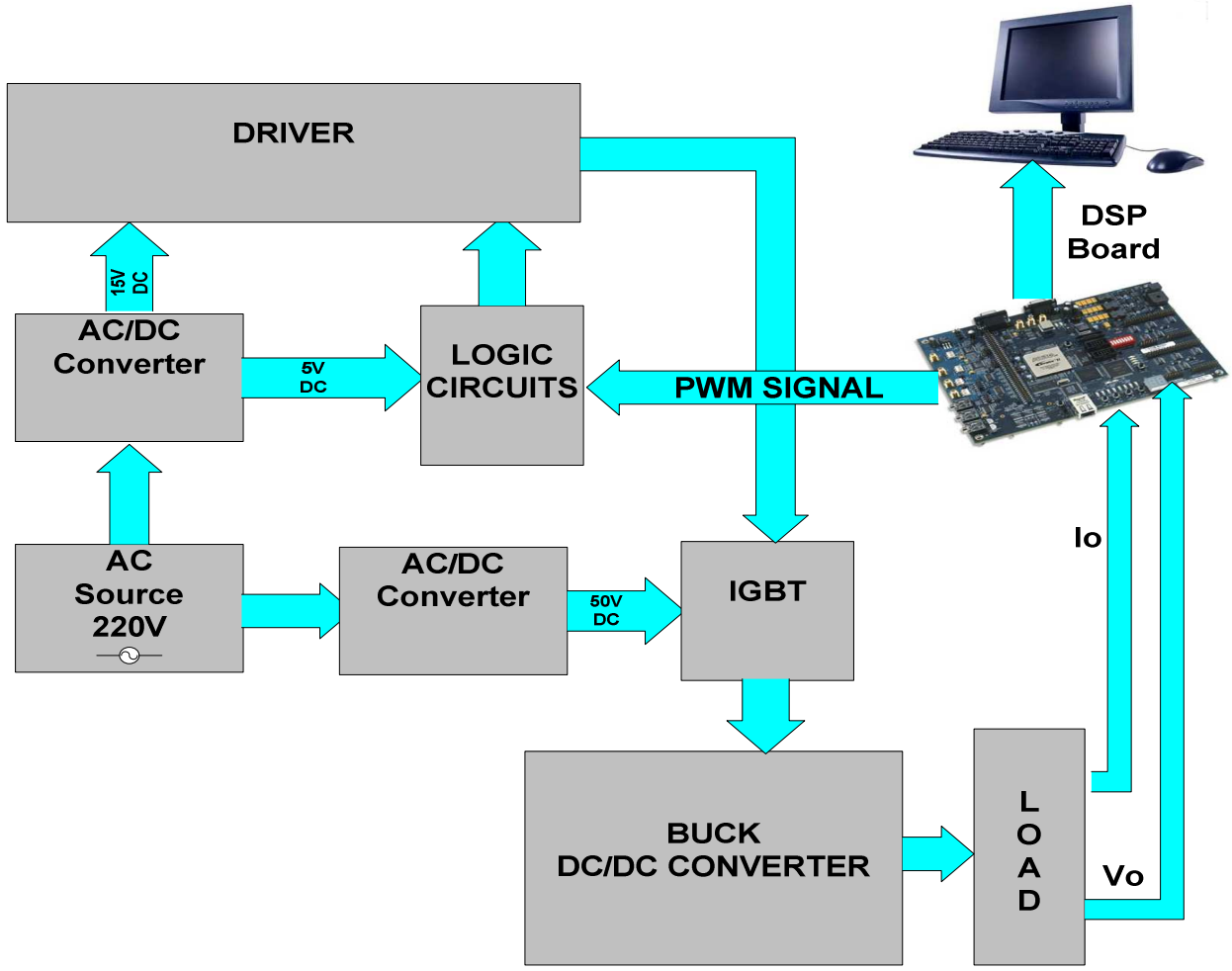

Fig. 4.25. Block diagram of the hardware system of the PEM FC Emulator.

The 220 AC input voltage (50Hz) supplies two AC/DC converters to obtain, respectively, the input voltage V_{dc}=50V of the DC-DC buck converter and the voltages of 5V and 15V used to supply the driver IR2101 and the logic circuits SN7400 and SN7406.

Figure 4.25 shows that the PWM signal at the output DSpace, is activated by a combined working of the two logic circuits SN7400 and SN7406. The inputs of the NAND SN7400 are the output of the switching and the PWM signal used to control the DC-DC buck converter. When the switching is in the on state, then an input of the N7400 is supplied with a voltage of 0V (0 logic level) and the PWM signal is transmitted in the output in the inverse configuration. This output supplies the NOT logic circuit N7406, which takes back the PWM signal in the original form and convert the TTL voltage levels to MOS levels. Therefore, the combined working of the two logic circuits allows to the PWM signal to assume the MOS levels needed to assure the correct working of the driver IR2101.

When the HIN input of the driver is equal to the TTL level 1 (5V), the power device IGBT works like a switching in the on state (switching closed) and then the input of the DC-DC buck is equal to V_{dc}=50V, whereas when the HIN input is equal to the TTL level 0 (0V), then the input of the buck is equal to 0V.

The voltage and the current output of the buck converter are acquired by the Analog/digital converter inputs of the Dspace 1103. These inputs work in the range -10V ÷ +10V and then a trimmer of 15KΩ and a resistance of 0.1Ω are used to obtain the electrical compatibility of the output signals of the buck converter with this voltage range. The trimmer gives a voltage value proportional to the output voltage of the buck converter (50V → 1V). The resistance of 0.1Ω gives a voltage value proportional to the output current of the buck converter (1A → 0.1V).

The output signals of the buck converter transmitted to the Dspace are used to control the buck. In fact, the voltage low control of the DC-DC converter and the mathematical model of the PEM FC are implemented into the memory of the Dspace board. The hardware is looped by the PWM signal, which is generated by the PWM output of the Dspace.

The components used to implement the hardware platform are the following:

- (220V,50Hz)→(50V) AC/DC converter
- (220V,50Hz)→ (5V, 15V) AC/DC converter

- Driver IR2101
- Logic circuit SN7400
- Logic circuit SN7406
- Power mesh IGBT STGP20NB60H
- LC filter with ultrafast diode MURB820
- Trimmer of 15KΩ
- Resistance of 0.1Ω
- DSpace Board 1103

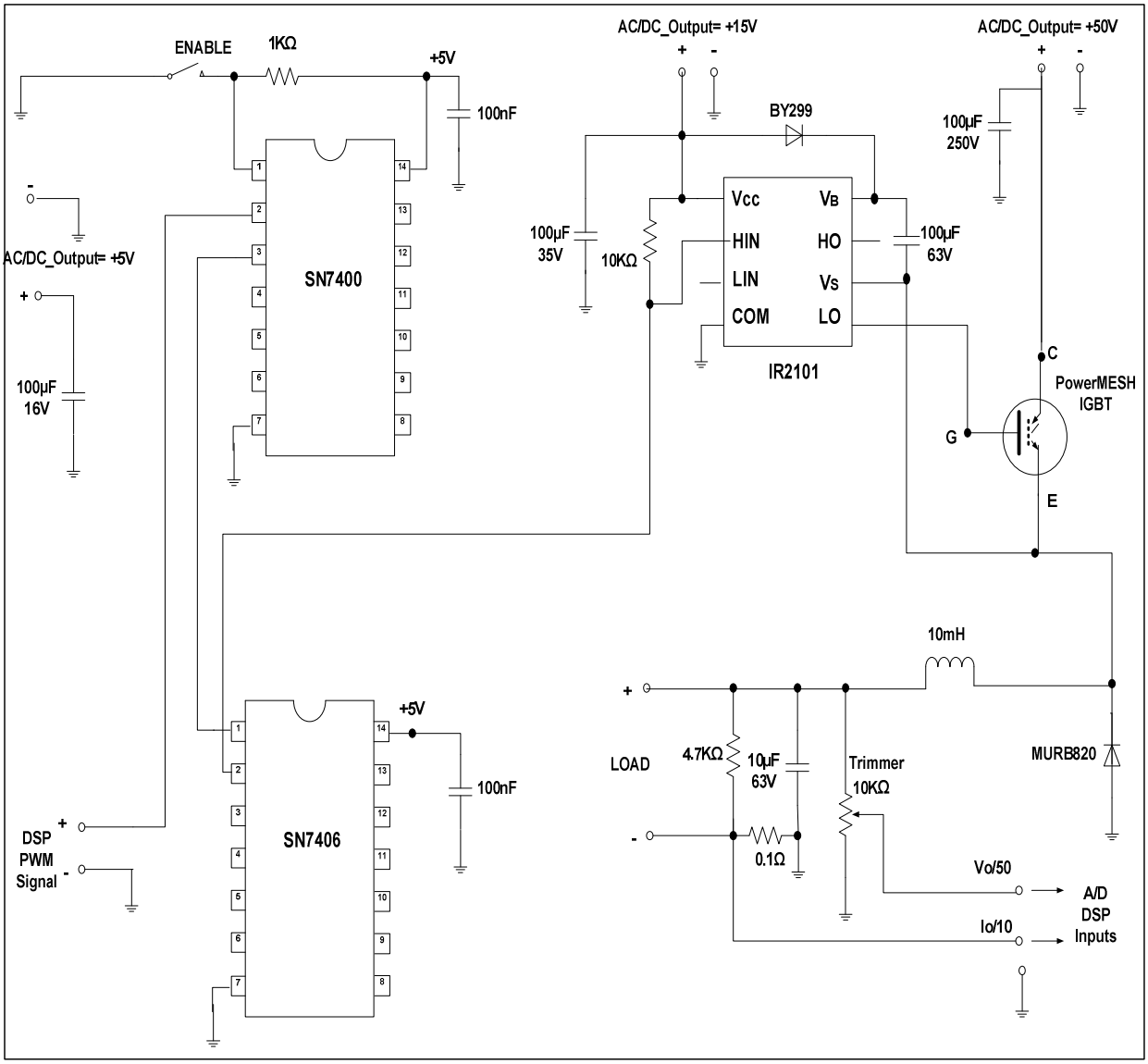

Fig. 4.26. Full schematic of the hardware system of the PEM FC Emulator.

4.3.1 Control Software Overview

The control of the DSP is composed of an initialization routine followed by periodic interrupts triggered by an internal trimmer. These interrupts occur once per switching cycle and set the reference for the phase shift modulator. This reference is then sent to the PWM modulator on the DSP so that it can be transmitted to the power stage of the emulator. A flow chart describing the operation of the interrupt is shown in Figure 4.27.

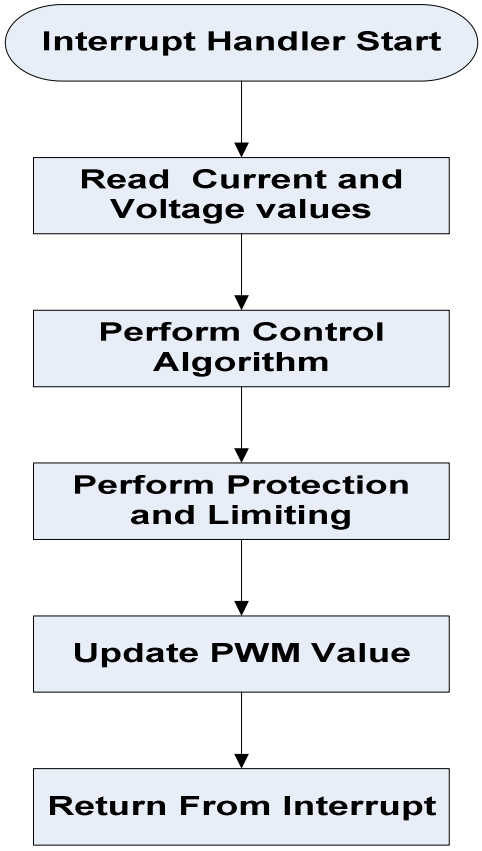

Fig. 4.27. Interrupt Handler Flow Chart.

The output voltage and current values are read from the analog to digital converter (ADC) on board DSP.

The output of the ADC is proportional to its input voltage so that an input of +10Volts gives a digital value of 0x7FFF (hexadecimal) and an input of 0.00 Volts gives a digital value of 0x0000. The first thing to at the time of the interrupt is to request the ADC to perform a conversion. This is done by writing the control register ADCTRL2. After the conversion is finished, indicated by testing ADCTRL2, the results are read into local memory locations and are shifted to maintain scaling.

All numbers in the DSP use an 8.8 format, where there are seven integer positions and eight fractional positions. The most significant bit represents the sign, allowing a maximum number of 127 and a minimum number of -128 with a resolution of 1/256.

The next step in the interrupt routine is the control algorithm execution. The control algorithm computes the new value of the duty cycle. A summary of the control algorithm is shown in Figure 4.28.

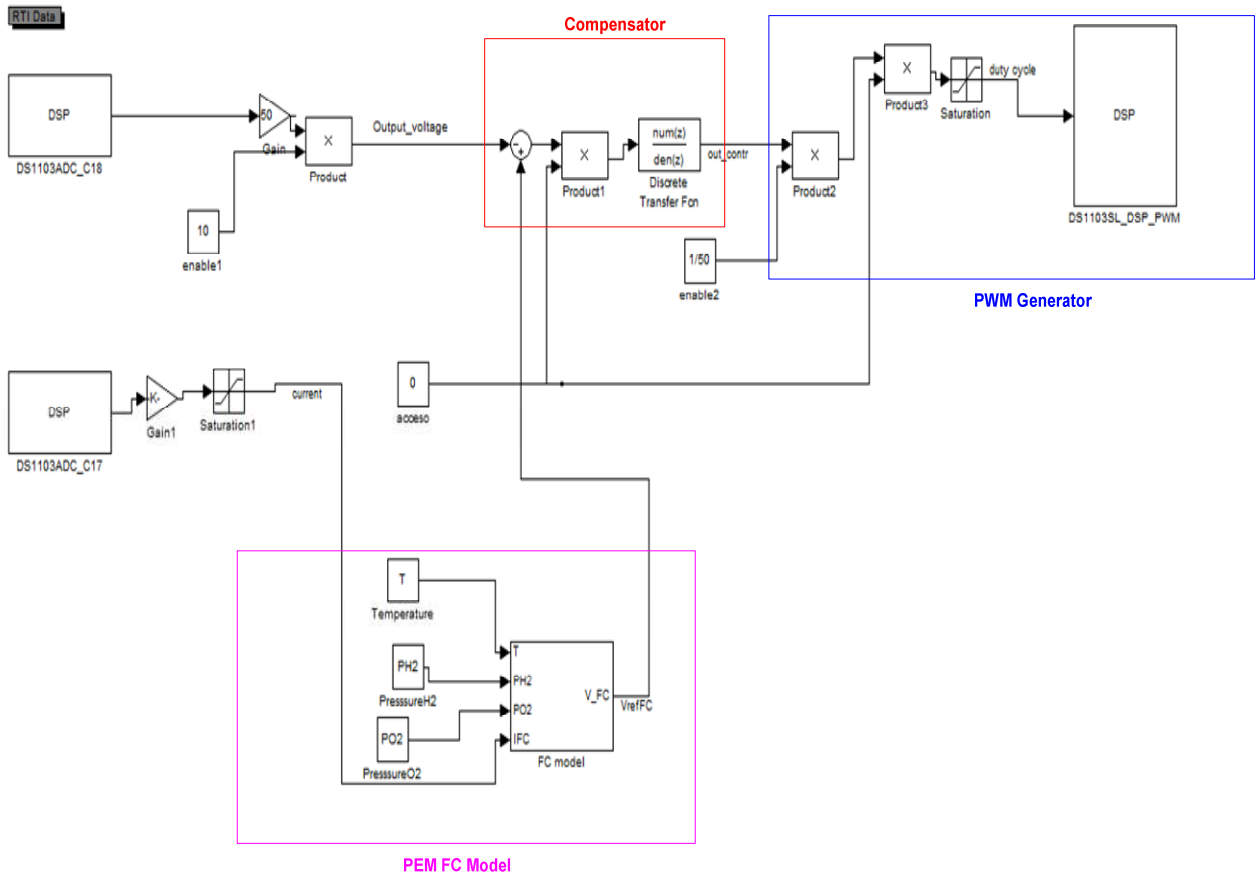

Fig. 4.28. Control Algorithm Description.

There are three primary components in the control algorithm. There is a compensator, where the controller allows the output to track the desired reference. The voltage output of the compensator is modified in the input of the PWM generator part to produce the desired voltage at the input to the PSPWM chip, which generates the corresponding duty cycle with a frequency of 10 KHz. The PEM FC Model produces the voltage reference that must be followed from the output voltage to emulate the PEM FC behavior. The result of the A/D conversion of the DS1103ADC_C18 channel is a digital number proportional to the output voltage of the Buck converter. This number is multiplied for a specific gain, to operate with the corresponding value of the analog input voltage. The same operation is made in the second A/D channel DS1103ADC_C17, which is used to convert an analog input voltage proportional to the output current of the buck converter. The simulation results of the control algorithm are obtained by working in the continuous domain. The control algorithm parameters must be converted to the discrete domain in order to be implemented in a DSP. This was done using the Matlab default conversion method Zero-Order Hold (ZOH).

The code files used and their description are shown in Appendix C (Table VII).

4.3.2 AC/DC Transformers

The DC input voltage V_d= 50 V of the step-down converter and the DC supplies of the driver IR201 and the logical circuits SN7400 and SN7406, are obtained by using two toroidal transformers. This solution is adopted to feed the emulator through its direct connection to the AC electrical network (220 V, 50Hz). The winding is made of flat copper layers, where each layer has a certain number of turns wound in a spiral pattern. Insulation between layers is made either of FR4 material or simple insulation paper. The core is usually ferrite and low profile compared to traditional transformers.

A basic schematic of the toroidal transformer that was used to obtain the input voltage V_d= 50 V is shown having one primary winding and two secondaries (Figure 4.29).

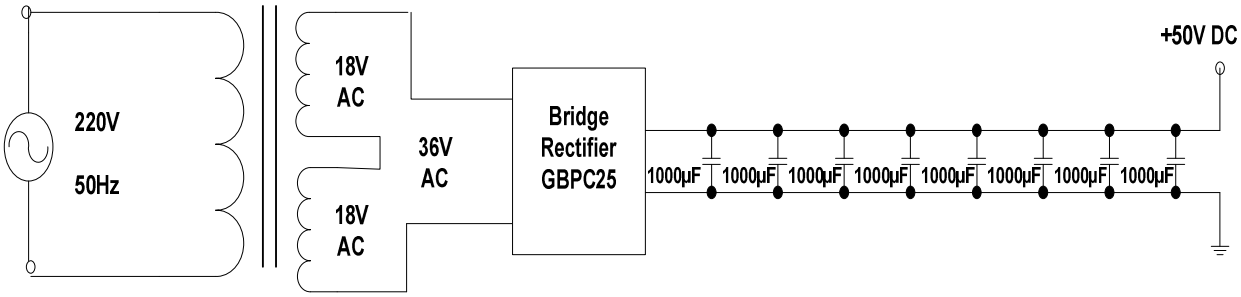

Fig.4.29. Basic schematic of the transformer (AC 220,50Hz)→DC 50V.

In each secondary winding there is an AC voltage of 18 V and a current of 6.3 A, while the bridge rectifier GBPC25 is supplied with an AC voltage of 36 V. the function of the parallel connection of the eight capacitors (1000 µF, 100V) is to lessen the variation in the rectified AC output waveform from the bridge. In other terms, the capacitors (called smoothing capacitors) provide a low impedance path to the AC component of the output, reducing the AC voltage and AC current trough the load.

The basic schematic of the toroidal transformer that was used to obtain the supplies of the driver and the logic circuits is shown in figure 4.30. In the secondary winding there is an AC voltage of 18 V and a current of 1.4 A, while the bridge rectifier W02G940C is supplied with an AC voltage of 18 V. An electrolytic capacitor (1000 µF, 25V) and a polyester capacitor (100 nF, 100V) are used like smoothing capacitors in the output of the rectifier. The voltage regulators LM7805 and LM7815 are used to obtain the DC voltage values 5 V and 15 V. in fact, the family LM78XX can assume the following output values: 5 V, 12 V and 15 V. The voltage regulator allows supporting fast load changes, big instantaneous overloads and also, it offers a protection to the electrical devices against the high frequency noise and voltage peaks. The other secondary wending is used to supply an air-cooling fan to dissipate the heat.

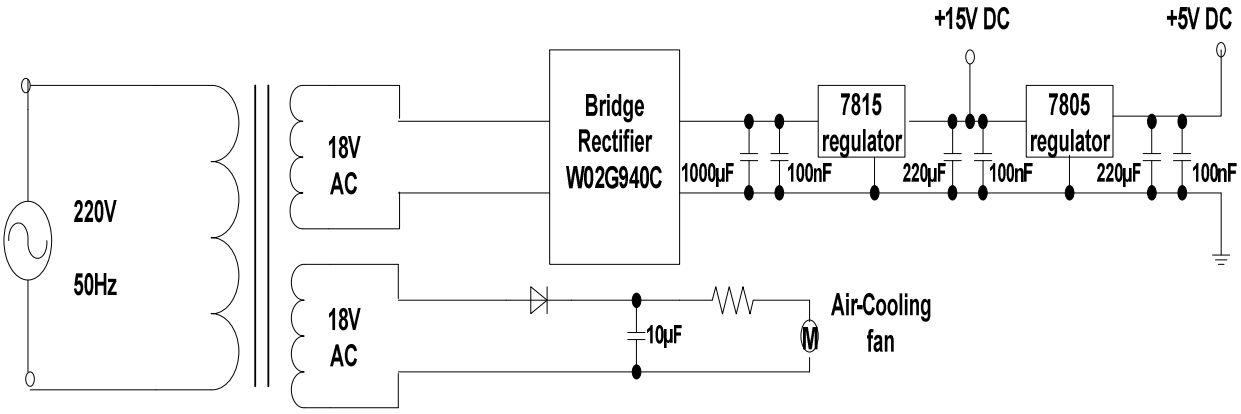

Fig.4.30. Basic schematic of the transformer (AC 220,50Hz)→DC 5V, 15V.

4.3.3 Driver IR201

The gate driver chosen to drive the IGBT power device is the IR201, a high and low side gate driver. The IR201 is a high voltage, high speed MOSFET and IGBT driver independent high and low side referenced output channels. The floating channel can be used to drive an N-channel power MOSFET or IGBT in the high side configuration which operates up to 600 volts. The logic input is compatible with standard CMOS or LSTTL output, down to 3.3V logic.

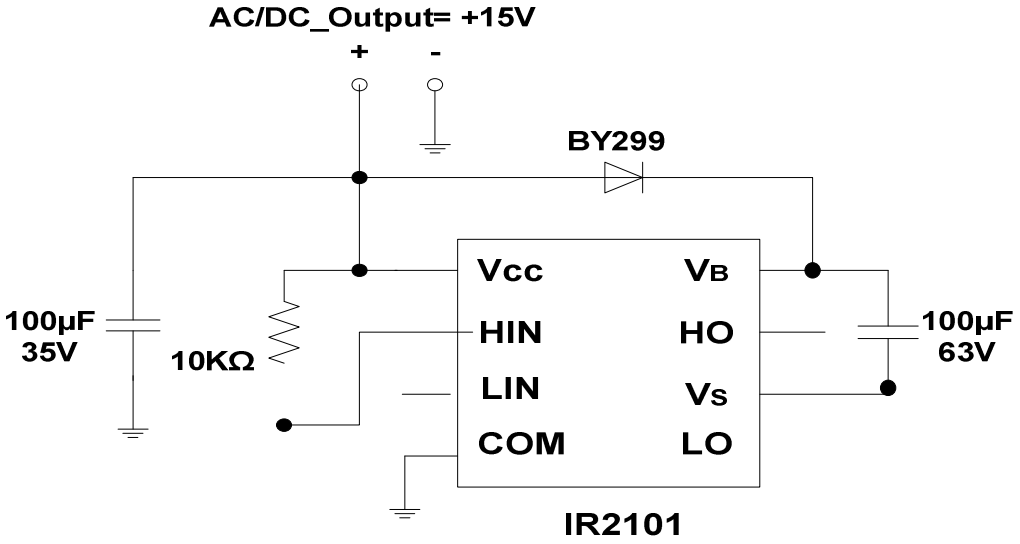

Fig. 4.31. Standard configuration of the Driver IR2101.

Fig. 4.32. Driver IR2101.

4.3.4 PowerMESH IGBT

The IGBT have been the preferred power device for these reasons:

- Low duty cycle
- Low frequency (20kHz)
- Narrow or small line or load variations
- High-voltage applications(>1000V)
- Operation at high junction temperature is allowed (>100°C)
- >5kW output power

In the emulator has been used the $PowerMESH^{TM}IGBT$ STGP20NB60H, which uses the latest high voltage technology based on a patented strip layout. The suffix “H” identifies a family optimized to achieve very low switching times for high frequency applications (<120KHz). This power device is characterized by high input impedance, low-on voltage drop, high current capability and very high frequency operation. The absolute maximum rating of V_{CES} is 600 V and $I_{C=}$ 20A, in according to the characteristics of the driver IR2101.

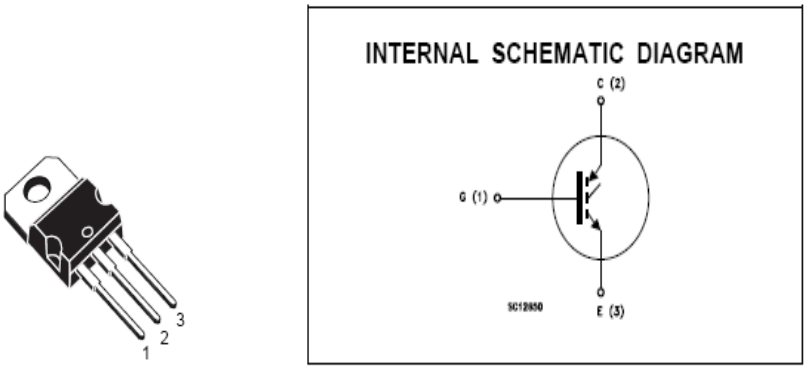

Fig.4.33. IGBT PowerMESH STGP20NB60H.

4.3.5 Logic circuits SN7400 and SN7406

The SN7406 is a TTL can work like a hexadecimal inverter buffer or like a driver feature high-voltage open collector outputs for interfacing with high-level circuits (such as MOS) or for driving high-current loads (such as lamps or relays) and also is characterized for use as inverter buffer for driving TTL inputs. The SN7406 have minimum breakdown voltage of 30 V and a maximum sink current of 40 mA.

The SN7400 is a positive-NAND gate used to enable the working of the emulator and to obtain a PWM signal compatible to the TTL voltage levels 0 V and 5 V.

4.3.6 LC Filter

The output filter inductor and capacitor values have been designed in section 4.1.3 and it is based on an output voltage ripple of 2% and a limit between continue and discontinue conduction. The Buck DC-DC converter has a rated power of 800 W, with DC link voltage V_{dc}= 50 V and a rate current i_{FCrate}= 16 A. LC filter permits to avoid the discontinuous conduction mode for almost all working conditions. The equivalent time constant of the close loop voltage is about 0.1 sec, while the time constant τ of the FC is variable quantity ranging from about 0.5 s to about 50 s. The FC time constant is thus in the worst case 5 times slower than that of the control voltage loop.

In the Buck converter ultrafast rectifier MURB820 has been used, which is specifically designed with optimized performance of forward voltage drop and ultra fast recovery time. Its extremely optimized stored charge and low recovery current minimize the switching losses and reduce over dissipation in the

switching element and snubbers.

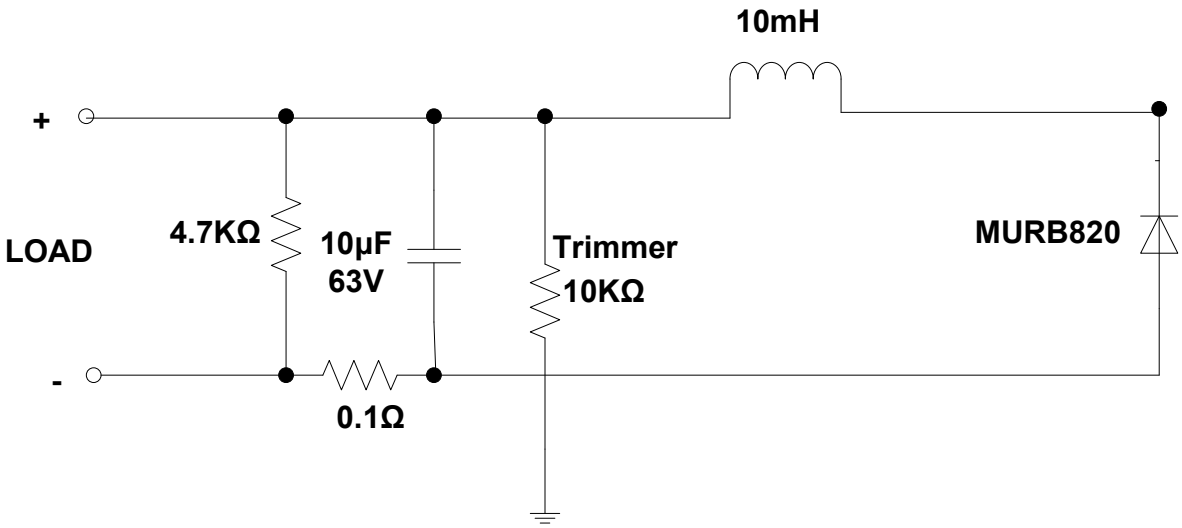

Fig.4.34. Buck DC-DC converter.

4.3.7 TRIMMER

The Analog/Digital converter channels in the dSPACE board work in the voltage range -10÷10 V. in the PEM FC emulator are used two A/D channels to input in the dSPACE, the output voltage and the output current of the Buck converter, used to implement the voltage control algorithm. The 10 KΩ Trimmer allows obtaining the voltage compatibility between the values of the Buck output voltage and the A/D channel. In fact, the trimmer is tuned to have 1 V in the output, when the input voltage assumes the maximum value of 50 V.

The analog/digital conversion of the Buck output current is obtained by the resistance of 0.1 Ω, because when the current value is 10 A, then the voltage drop in the resistance is 1 V.

In the Figure 4.34 is shown the picture of the PEM FC emulator and also, are indicated the several electric components.

In the Figures 4.35a and 4.35 b are shown the printed circuit boards (PCB) of the PEM FC emulator. They are made by using the FIDOCAD open source program, which is characterized by the ability to design and print the PCBs. In addition to two new special primitive (track pitch and electricity) has been introduced a

new print mode, the “PCB mode”, which allows printing circuit boards to their natural size.

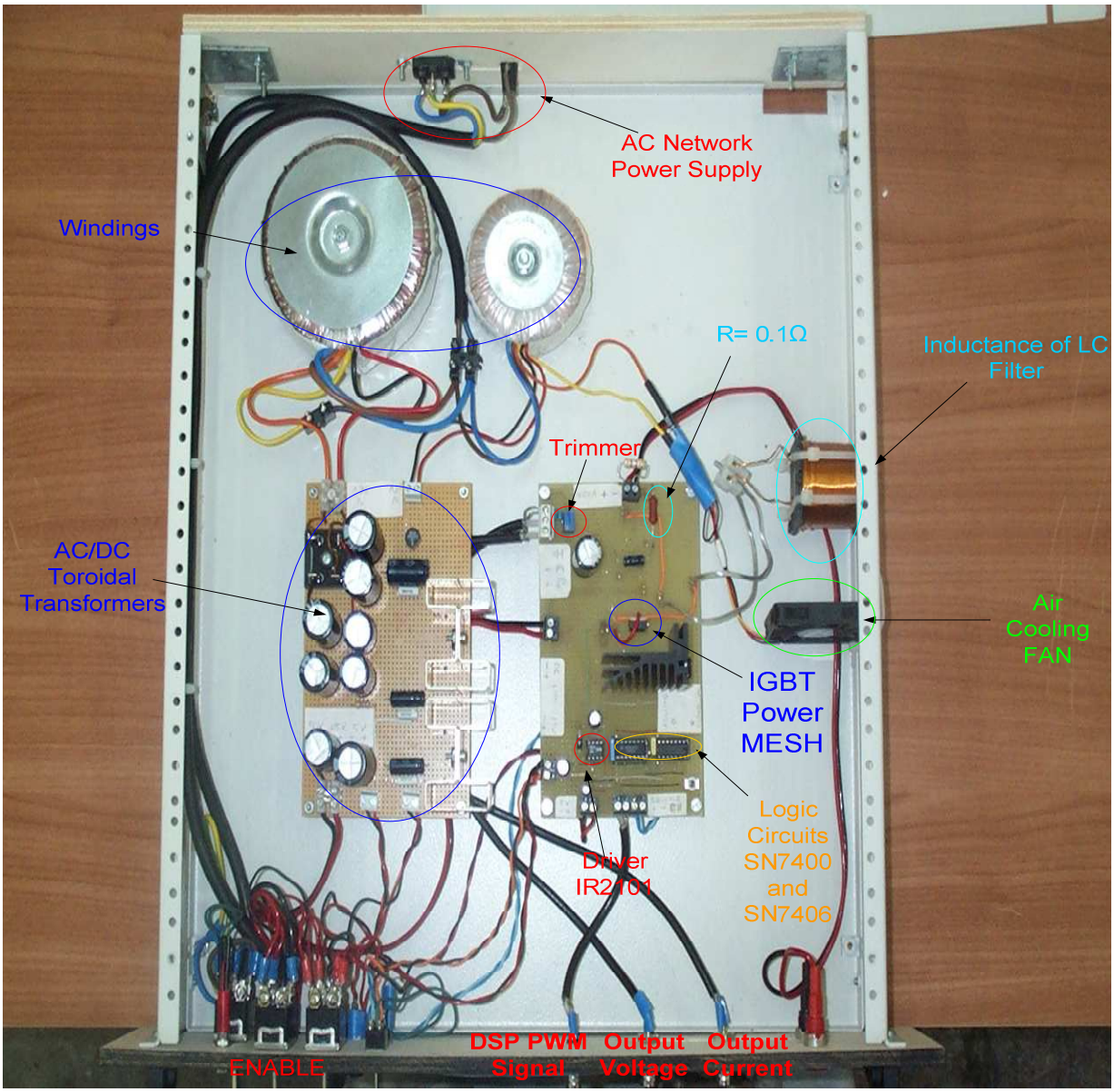

Fig. 4.35. PEM FC Emulator

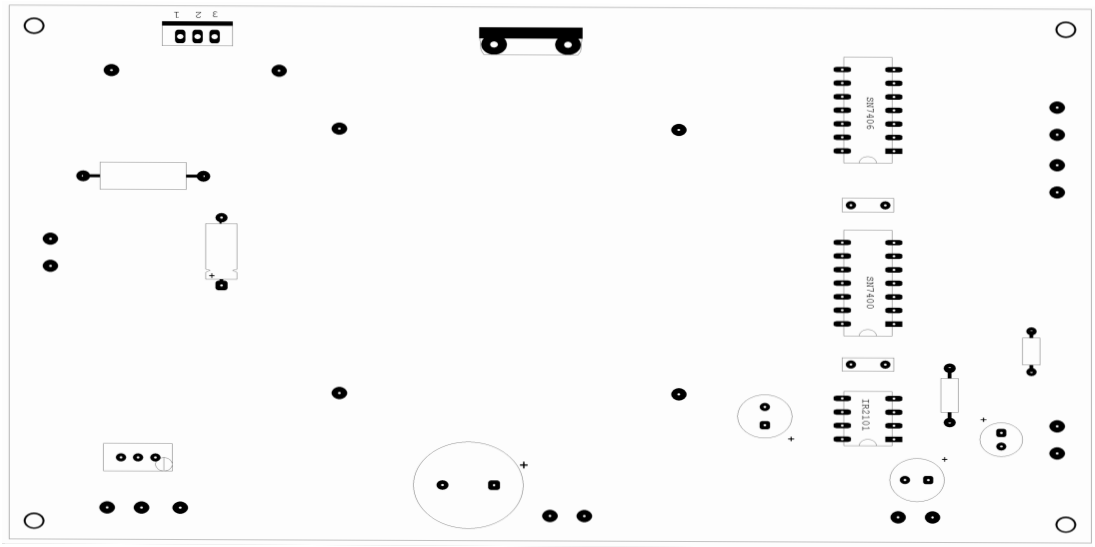

(a)

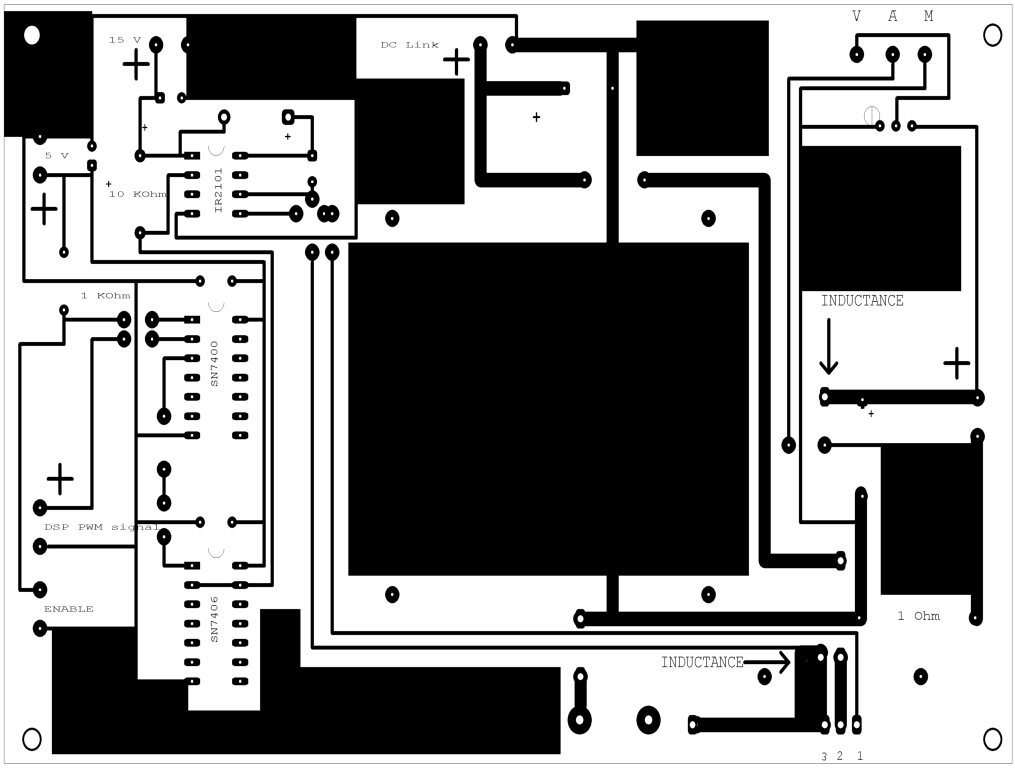

(b)

Fig. 4.36. Printer Circuit Board: (a) "Components Side"; (b) "Copper Side .

4.4 Testing

The adopted Test Set-Up is shown in the figure 4.36 and it is composed of:

- the PEM FC emulator;
- a three-phase resistive load bank (REO) that works in the range 10Ω – 300Ω and it has been used to change the current value;
- a potentiometer with the following features: R= 0Ω–100Ω, $I_{MAX} = 2.45$ A and P_{MAX} =600W;
- a multimeter Fluke 76;
- a digital oscilloscope Yokogawa DL1540 used to monitor the PWM waveform, the output voltage waveform and the output current waveform;
- a laboratory DC power supply that gives the voltage values 5V and 15V;
- a Host PC connected to the dSPACE board DS1103 ;
- a Sub-D connector used to interface the PEM FC emulator with the Host PC;
- the ControlDesk Software application.

The tests have been done considering two different mathematical models of the PEM FC emulator [6],[7],[8]. In the first type of tests, the PEM FC has been modeled with the equations that represent only the core of the fuel cell. These equations are a mathematical representation of the Nerst formula, of the Ohmic voltage drop, of the activation overpotential and of the concentration overpotential (chapter 3). In the model is also considered the dynamics of the fuel cell that is mainly governed by the so called “charge double layer” effect.

The second type of tests have been done by modeling the whole FCS complex system, which is composed from several auxiliaries components in order to work properly, like the hydrogen supply system for the anode, the air management system for the cathode, the cooling system and the humidifier system (chapter 3). The results of this second type of test are shown in the chapter 5 [8].

Fig. 4.37. Test Bench used to determine the experimental results .

4.4.1 Experimental Test-Setup on the PEM-FC emulator

The system emulates a FC with 41 stacks and two kinds of tests have been done: static and dynamic. As for the static test, the voltage versus current and the power versus current characteristics of the FC under different values of hydrogen pressure and environmental temperature have been drawn, and the comparison has been made among the ideal curve, that obtained in numerical simulation and the corresponding experimental one. These comparisons are given in Figure 4.38. The oxygen partial pressure has been always equal to the hydrogen one. In the Table IV shows the values of the FC emulator obtained by numerical simulation (Matlab/Simulink environment) and by experimental simulation. The values have been obtained by considering two values of hydrogen pressure p_{H_2} (1 atm and 6 atm) and two values of the stack temperature T_{st} (313 K and 383 K). By varying the load R, various current values in a reasonable range have been obtained to cover the the FC characteristics (0.1 A to 5 A). In particular, Figure 4.38 shows a polarization curve and the corresponding output power graph in three different working conditions: 1) P_{H2}=1 atm and T= 313 K, 2) P_{H2}=1 atm and T= 383 K, 3) P_{H2}=6 atm and T= 313 K. The average error is good for almost all values of the load current, with the exception of the concentration zone, where the nonlinearity is higher.

As for the transient tests, they have been made considering both a load current variation and a pressure variation. All the following figures refer to experimental tests. In the test of the load current variation, two challenging situations have been accounted for: one from the linear zone to the activation zone, and the other from the linear zone to the concentration zone. Figure 4.39, about the transition from the linear zone to the activation zone shows the plots of the output current, the output power, the output voltage and its voltage terms (Nernst, activation, concentration, ohmic). Figure 4.40 shows the same curves regarding the transition from the linear zone to the concentration zone. A similar test has been made with a constant load but with a step change of the partial pressure from 1 atm to 10 atm; the results are shown in Figure 4.41. Table III, a,b,c show the results of the output voltage for different values of load, pressure and temperature during transient tests.

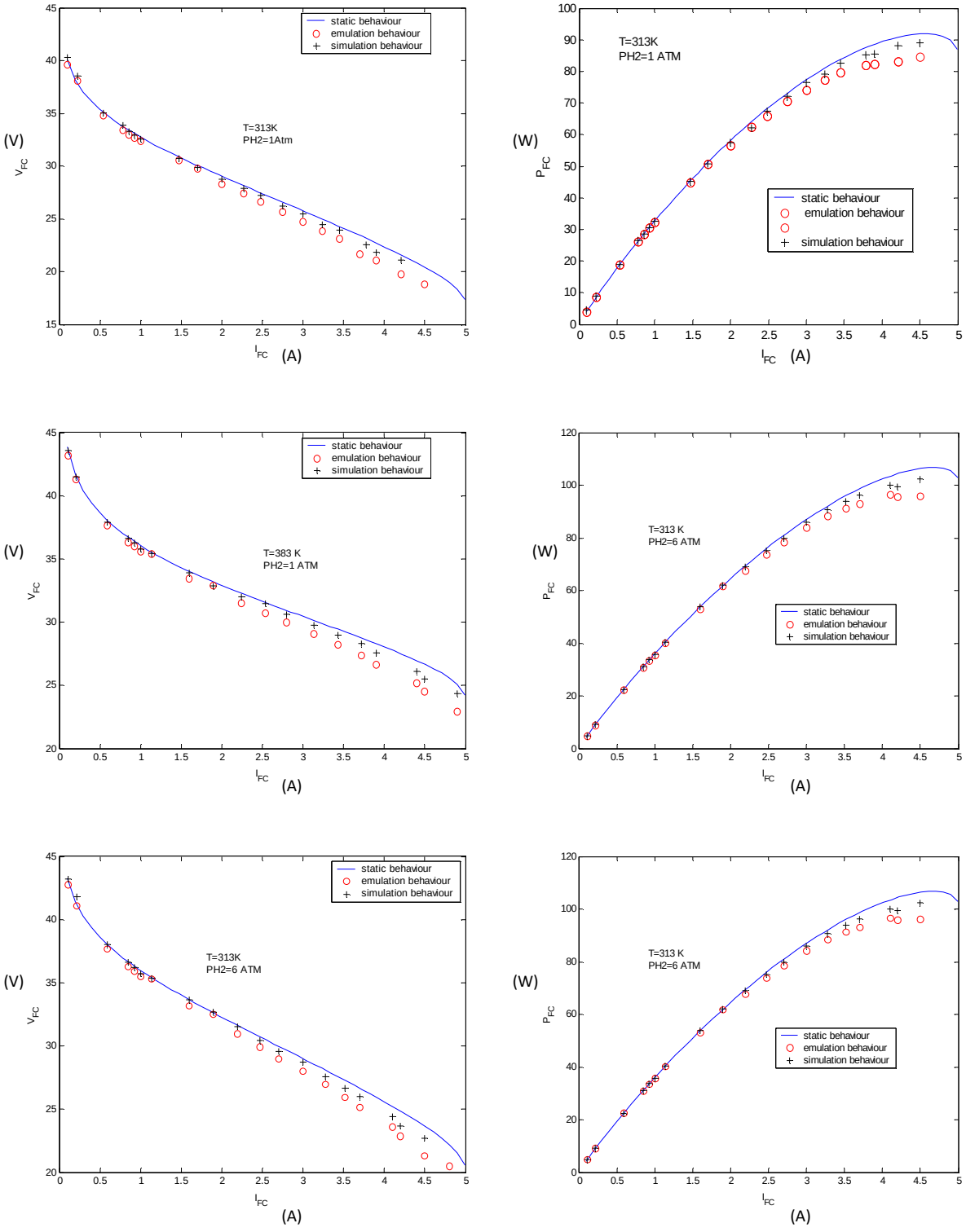

Fig 4.38. V-I e P-I curves obtained with the FC model, in simulation and experimentally for : 1) T=313K, PH2=1atm, 2) T=383K, PH2=1atm, 3) T=313K PH2=6atm.

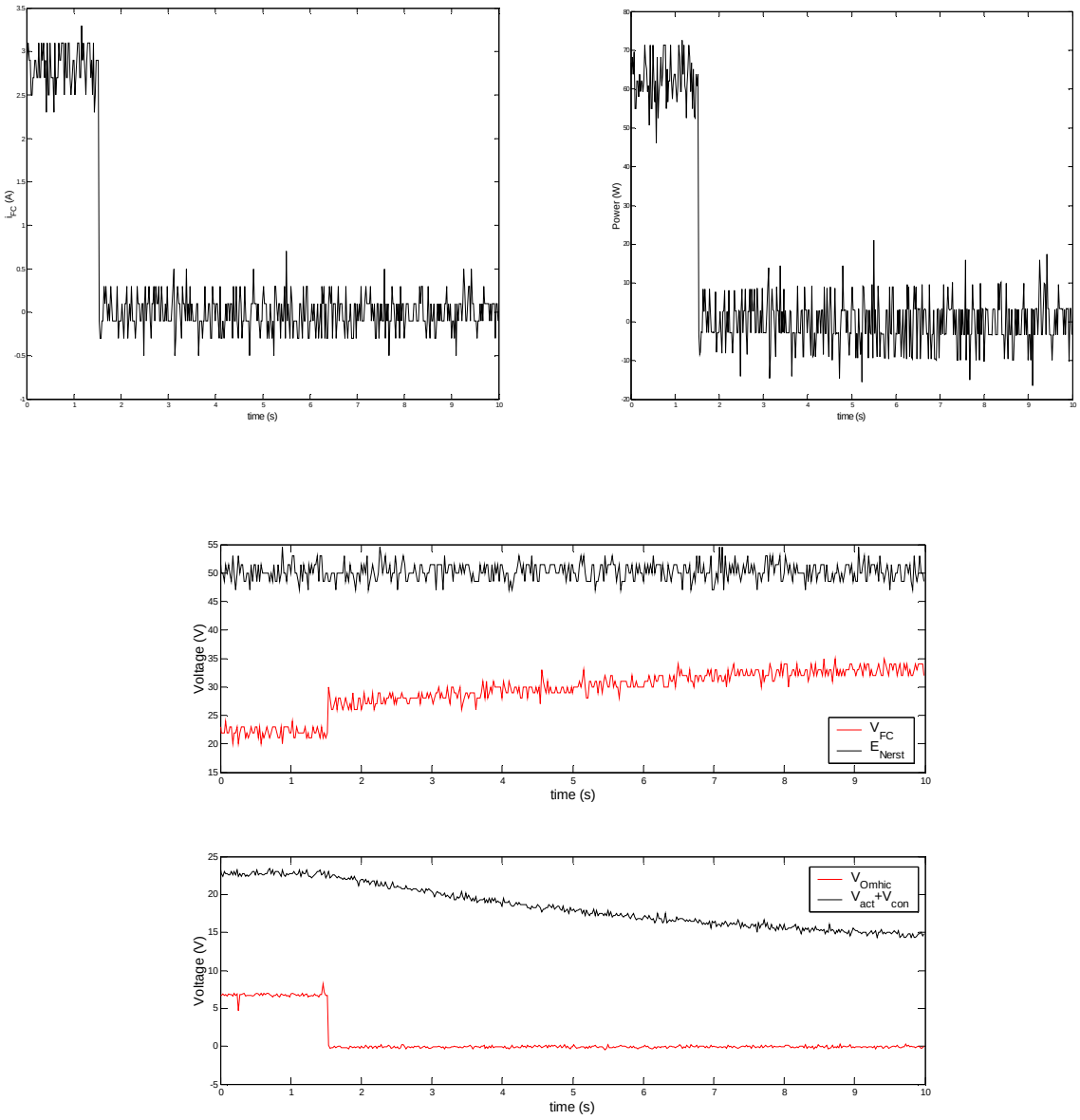

Fig.4.39. Transition from the linear zone to the activation zone. waveforms of the output current, the output power, the output voltage and the FC voltage drops (experiment).

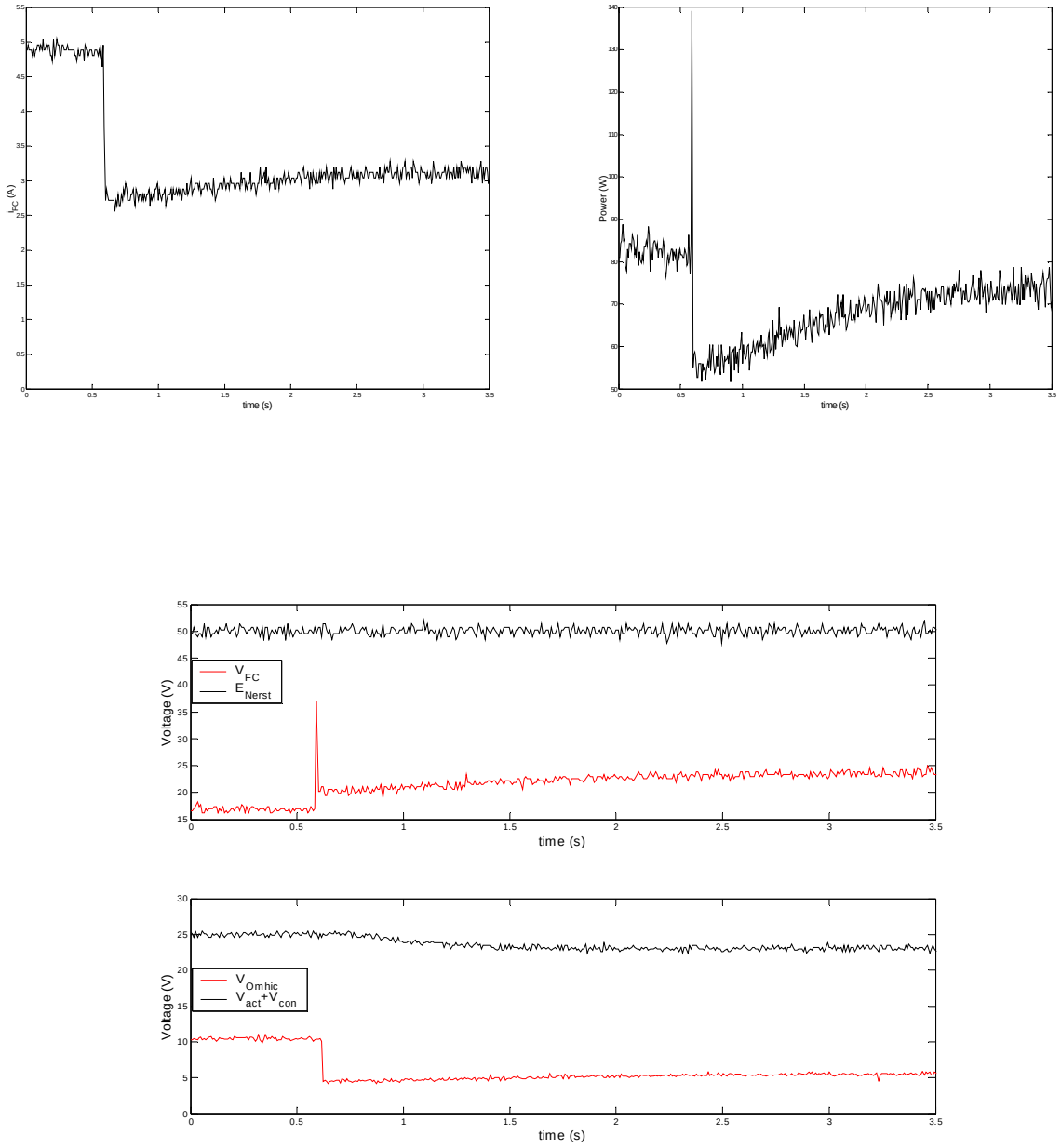

Fig. 4.40. Transition from the linear zone to the concentration zone. waveforms of the output current, the output power, the output voltage and the FC voltage drops (experiment).

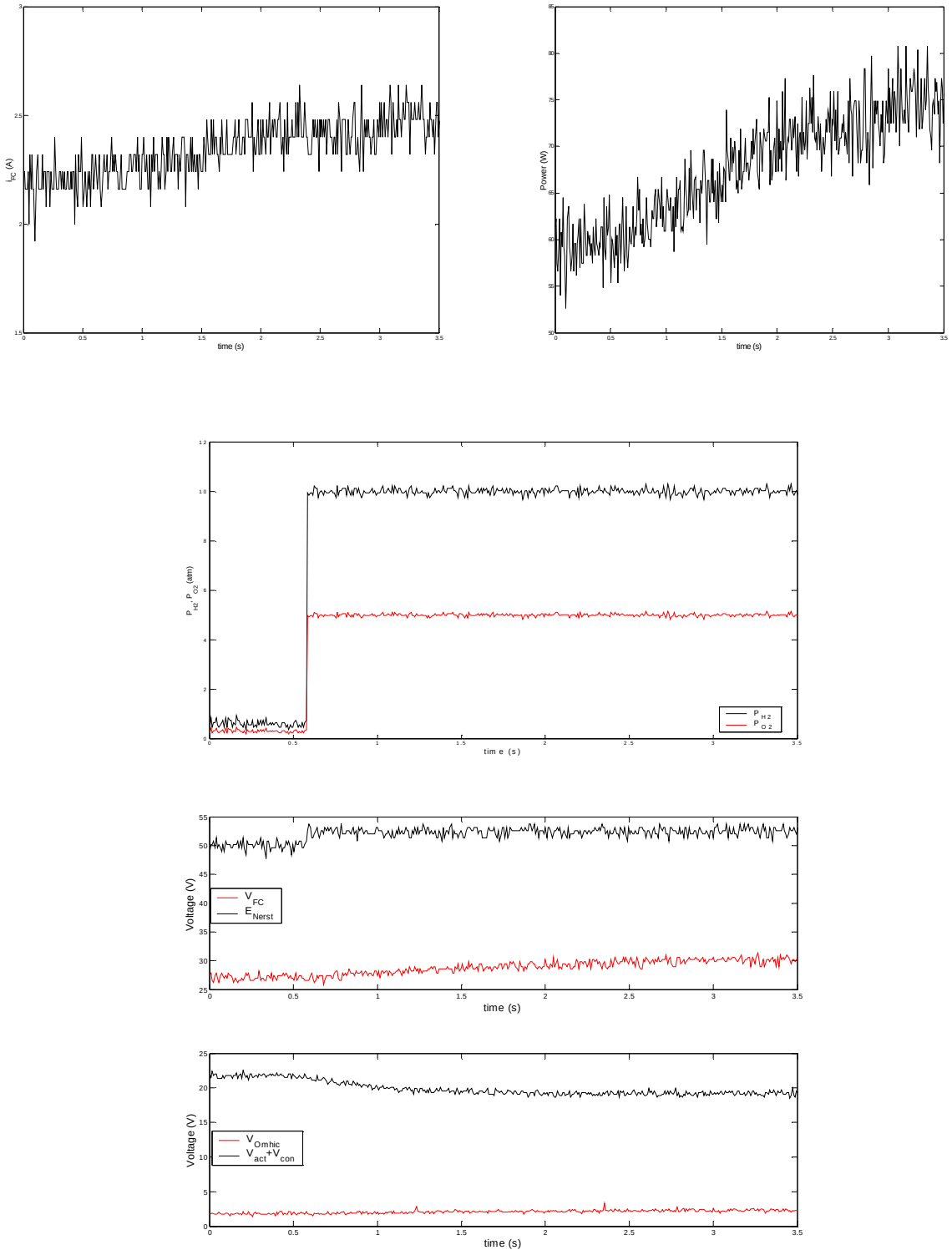

Fig. 4.41. Transition from PH2=1atm to PH2=10 atm: waveforms of PH2 and PO2, output current, outputpower, output voltage and fuel cell drops (experiment).

Tab. IV a. Transition from linear zone to activation zone.

	Linear Zone	Activation zone
Load (ohm)	9.6	384.7
I_FC (A)	2.75	0.1
V_FC (V)	26.2	39.65
T (K)	313	313
PH2 (atm)	1	1

Tab. IV b. Transition from concentration zone to linear zone.

	Concentration Zone	Linear Zone
Load (ohm)	3.7	7
I_FC (A)	4.7	3.45
V_FC (V)	18	23.92
T (K)	313	313
PH2 (atm)	1	1

Tab. VI c. Transition from 1 atm to 10 atm

Load (ohm)	12.5	12.5
I_FC (A)	2.1	2.3
V_FC (V)	27.88	30.6
T (K)	313	313
PH2 (atm)	1	10

p_{H_2} (atm)	StackTemperature (K)	Resistance (Ω)	Current (A)	$FC\ Voltage_{sim}$ (V)	$FC\ Voltage_{emu}$ (V)
1	313	384,7	0,11	40,31	39,65
1	383	384,7	0,11	43,55	43,2
6	313	384,7	0,11	43,22	42,7
1	313	190	0,23	38,52	38,1
1	383	190	0,21	41,5	41,3
6	313	190	0,22	41,8	41,1
1	313	64	0,54	35,06	34,85
1	383	64	0,59	37,89	37,7
6	313	64	0,59	38,02	37,9
1	313	43	0,78	33,88	33,4
1	383	43	0,85	36,64	36,3
6	313	43	0,85	36,65	36,32
1	313	38,7	0,86	33,32	33
1	383	38,7	0,93	36,26	36
6	313	38,7	0,93	36,22	35,9
1	313	35,2	0,94	32,94	32,7
1	383	35,2	1	35,81	35,6
6	313	35,2	1	35,73	35,5
1	313	31	1	32,57	32,4
1	383	31	1,14	35,4	35,4
6	313	31	1,14	35,37	35,3
1	313	21	1,47	30,73	30,6
1	383	21	1,6	33,9	33,5
6	313	21	1,6	33,64	33,17
1	313	17	1,7	29,87	29,8
1	383	17	1,9	32,84	32,9
6	313	17	1,9	32,67	32,5
1	313	14,4	2	28,74	28,3
1	383	14,4	2,24	32	31,54

6	313	14,4	2,19	31,5	30,9
1	313	12,4	2,27	27,88	27,45
1	383	12,4	2,54	31,46	30,76
6	313	12,4	2,47	30,41	29,9
1	313	11	2,48	27,22	26,61
1	383	11	2,8	30,6	30
6	313	11	2,7	29,59	29
1	313	9,6	2,75	26,2	25,67
1	383	9,6	3,13	29,77	29,12
6	313	9,6	3	28,71	28
1	313	8,5	3,1	25,45	24,74
1	383	8,5	3,43	28,96	28,24
6	313	8,5	3,28	27,6	26,95
1	313	7,6	3,24	24,45	23,86
1	383	7,6	3,72	28,28	27,41
6	313	7,6	3,52	26,64	25,94
1	313	7	3,45	23,92	23,12
1	383	7	3,9	27,58	26,66
6	313	7	3,7	25,99	25,13
1	313	6	3,78	22,55	21,7
1	383	6	4,4	26,13	25,22
6	313	6	4,10	24,41	23,55
1	313	5,6	3,9	21,8	21,07
1	383	5,6	4,5	25,55	24,52
6	313	5,6	4,2	23,68	22,8
1	313	5,1	4,21	21,1	19,77
1	383	5,1	4,9	24,37	22,98
6	313	5,1	4,5	22,71	21,31

Tab. V. Values of the FC emulator obtained by numerical simulation and by experimental simulation.

Chapter 5

Implementation of Advanced Approaches for the Control of the Air Supply System using the PEM-FC Emulator

To compete with existing internal combustion engines (ICE), fuel cell systems must operate at a similar level of performance. In particular the transient behaviour is one of the key requirements for the success of fuel cell vehicles, in terms of increased time response to load variations. Efficient fuel cell system power response depends on the air and the hydrogen supply, the flow and pressure regulation and the heat and water management. As the current is instantaneously drawn from the load source connected to the fuel cell stack, heat and water are generated, whereas the oxygen is consumed in the reaction with the hydrogen. During this transient, the fuel cell control system is required to maintain exact value of temperature, membrane hydration and partial pressure of the reactants across the membrane to avoid serious degradation of the stack voltage and thus efficiency reduction, as well as any damage across the membrane.

The mathematical model of the Fuel Cell System (FCS), described in chapter 3, shows the need for the FCS to have several auxiliary components: that is, the hydrogen supply system for the anode, the air management system for the cathode, the cooling system, the humidifier system as well as the Power Conditioner System (PCS) (see Fig.3.13). All of the components in these auxiliary subsystems should be analysed, designed and controlled to enhance the FCS performance, so that not only the FC stack output can be improved but also that the strong non linear interactions between the different auxiliaries can be managed.

The control of this complex system is a difficult task, because of the multiple interconnections among the different subsystems and the presence of nonlinearities, as well as numerous constraints to be enforced. The first problem is the control of the air supply system for a high-pressure direct hydrogen FCS. The aim is to control the compressor motor command to quickly and efficiently fill again the cathode oxygen consumed during system power generation [62]. The second problem is the control of the low pressure natural gas fuel processor system (FPS) which is achieved by a coordination of an air blower and a fuel valve in order to quickly fill the hydrogen consumed in the fuel cell anode while maintaining the desired temperature of the catalytic partial oxidation reactor. A control system should in any case ensure that the difference in pressure across the membrane be kept constant, to avoid damages or even rupture.

The idea proposed in this chapter, for the air management system, is the use of a static feedforward to optimise a conventional PI control of the FCS for oxygen starvation prevention by using the control scheme

suggested by M. Kavato [63]. The feedforward is necessary since it is a practical way for dealing with constraints, in particular those hard constraints of the compressor that supplies the air flow into the cathode. It is generally a high-speed centrifugal compressor, whose operation must be ensured within the surge and the choke limits to prevent any damage to itself. [64] [65]. This requirement is one of the reasons why a simple PI cannot be used “tout court” in a real FCS, and the utility of an emulator appears evident. A PI should be designed in a “trial-and-error’ fashion (if no “if-then” are used, which would make the control too computationally cumbersome) and this could have irreversible effects on the FC or on the FCS, which is not the case with an emulator. In any case the performance of the PI, in terms especially of recovery time of the oxygen excess ratio, may be suboptimal .

In order to improve the performance a static feed-forward controller can be added. This static controller implements the nonlinear relationship between the input motor voltage and the load current perturbation and the desired output. The computation of this feedforward controller is not a simple task since it demands that the above-mentioned constraints be enforced. The strategy adopted could be then to identify the forward model, satisfying the constraints, of the FCS by using a neural network, and then invert it. However inversion is not a problem easy to tackle in nonlinear systems, since multi-valued forward functions can occur. Therefore a novel neural network has been used, the recent neural network GMR (Generalized Mapping Regressor Mapping) (appendix A1) [75]. This neural network is suitable for approximating every function or relation (general mapping), also with every kind of discontinuity and, simultaneously, its inverse, if it exists, or the inverse relation with any different possible branch and also giving multi-values for an input. The thesis presents in the appendix A2 how the recall phase of the GMR should be used for being suitably applied to the FCS systems. Other kinds of NNs could be in general used, like the well known multilayer perceptron trained the back-propagation algorithm (BPN); it is to be noted however that the BPN can give unreliable or wrong results if the inverse function is multi-valued or presents any discontinuities. The control strategy proposed employs a classical PI control of the fuel cell paralleled by the inverse model of the fuel cell stack obtained by the GMR, acting as a feedforward controller (figure 5.1).

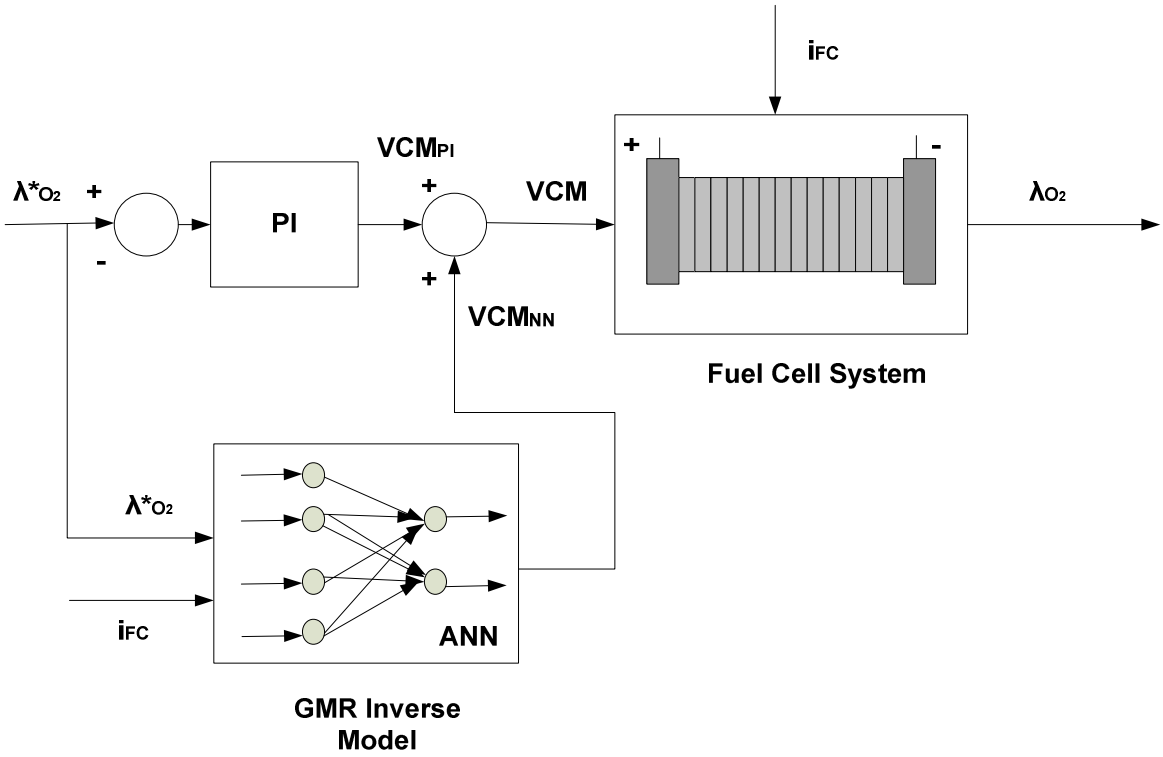

Figure 5.1. PI+GMR control scheme.

The chapter 5 is organized as follows: the first section briefly describes the PEM-FC control strategies proposed in the literature; the second section presents the control problem formulation; the third section describes the design of the PI controller and shows the results obtained by using this conventional kind of control; the last section describes the advanced control scheme adopted, and shows the results and the comparison between the two different strategies implemented.

5.1 State of the Art

The control strategies for PEM-FC proposed by A. Stefanopoulou et al. ([64],[65]) are based on the mathematical model described in [66]. In [64], the control of the air supply system acting only on the compressor motor input v_{cm} is proposed. The overall control design objective is to define the compressor motor input voltage to maintain the oxygen excess ratio λ_{O_2} at a constant value and achieve the desired FC system net power. Three different control schemes for the FCS are presented, shown in figures 5.2a, 5.2b and 5.2c. The scheme in figure 5.2a represents a static feedforward (sFF) control and is implemented with a look-up table. This determines a static function that correlates the steady-state value between the control input v_{cm} and the measured disturbance I_{st} (stack current). The static feedforward controller computes the compressor voltage command v^*_{cm}, which achieves an air flow that refills the oxygen flow consumed during a current command I_{st}. For specific ambient conditions of pressure, temperature and humidity, the required air flow can be calculated analytically by using an equation $W_{cp} = f_{cp}(I_{st})$ based on electrochemical and thermodynamic principles. The static feedforward controller sFF, used to cancel the effect of the current disturbance, is determined by using a nonlinear simulation of the FCS regulated at. λ_{O_2} =2 and satisfying the constraints of the compressor.

The control scheme shown in figure 5.2b is used when the analytic model of the FCS is available and allows a better transient response to be achieved. It uses a dynamic feedforward controller (dFF) that cancels the effect of I_{st} to the oxygen excess ratio λ_{O_2} over a wide range of frequencies. Also, a proportional integral feedback controller (PI) is designed to reduce sensitivity to modelling error, device aging and variation in ambient conditions. The PI feedback controller can give better results that the sole use of the sFF, and its design is simple, however, to avoid a reduction of the system robustness, the feedforward control action should be reduced. This can be achieved by using an observer instead of the PI. In any case the use of the dFF requires the design of a anticasual controller that must be therefore suitably modified to make it physically realizable, which increases the difficulty of design. Moreover its response to unknown disturbances and parameter variations can adversely affect its disturbance rejection capability, in spite of the fact that its dynamical response is better than the one obtainable with a sFF. This is the main reasons why in this thesis the GMR of fig. 5.1 has been used as a static feedforward.

In [66], to overcome this problem; another feedback controller is combined with the static feedforward controller as shown in figure 5.2c to form the sFF+obsFB controller whose order is similar to the order of the dFF+PI controller. In [64] is shown that an observer-based feedback that uses only the air flow measurement $y_1 = W_{cp}$ achieves higher closed-loop bandwidth than the simple PI feedback controller.

Significant improvement of the closed-loop bandwidth is achieved by measuring the stack voltage V_{st} as well as the supply manifold pressure p_{sm} and using this signal in the observer-based feedback controller. These multiple measurements allow better observability of the system states and, consequently, better regulation of the transient excess oxygen ratio λ_{O_2}. Although these control schemes give good results, they can maintain λ_{O_2} at an optimal value only at steady state, but not during transients.

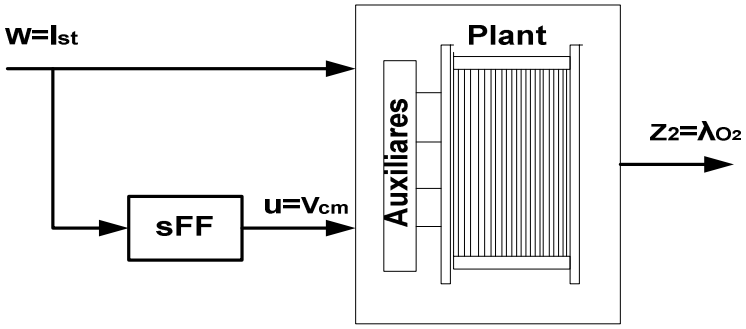

Figure 5.2a. Steady-state feedforward control implemented with a look-up table.

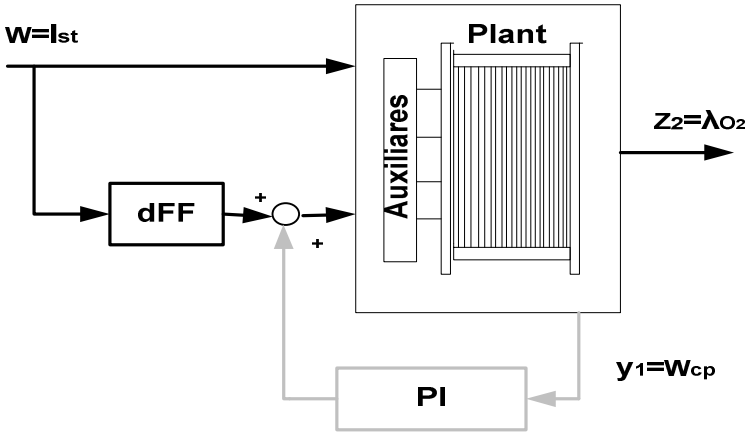

Figure 5.2b. Dynamic feedforward controller and a PI feedback controller for steady-state regulation.

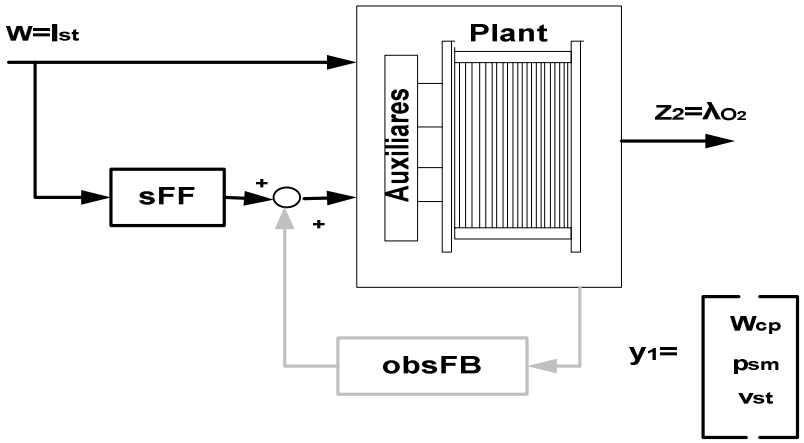

Figure 5.2c. Control configuration with observer-based feedback and a static feedforward controller.

P. Rodatz et al. developed a model controller of the PEM-FC that acts on both the compressor input and stack downstream valve and is designed using Linear Quadratic Gaussian (LQG) methodology [67]. This control strategy was implemented by using a stack of 100 PEM cells connected in series, that produces an electrical output capability of 6 kW under optimal conditions with regard to pressure, humidity, reactants flow and temperature. The air supply system (figure 5.3) consists of a compressor, a water injection device, a vessel which is filled with porous material, a water separator in front of the fuel cell (to avoid the penetration of liquid water into the fuel cell), the fuel cell itself, followed by another water separator (to collect water needed for the humidification) and finally the proportional control valve. With regard to the air supply of the fuel cell system, four states have been considered for as controlled variables: mass flow, return manifold oxygen pressure, inlet temperature and humidity, but only three actuators are available: compressor, pressure valve and humidification device. This results in difficulty of controlling all output variables.

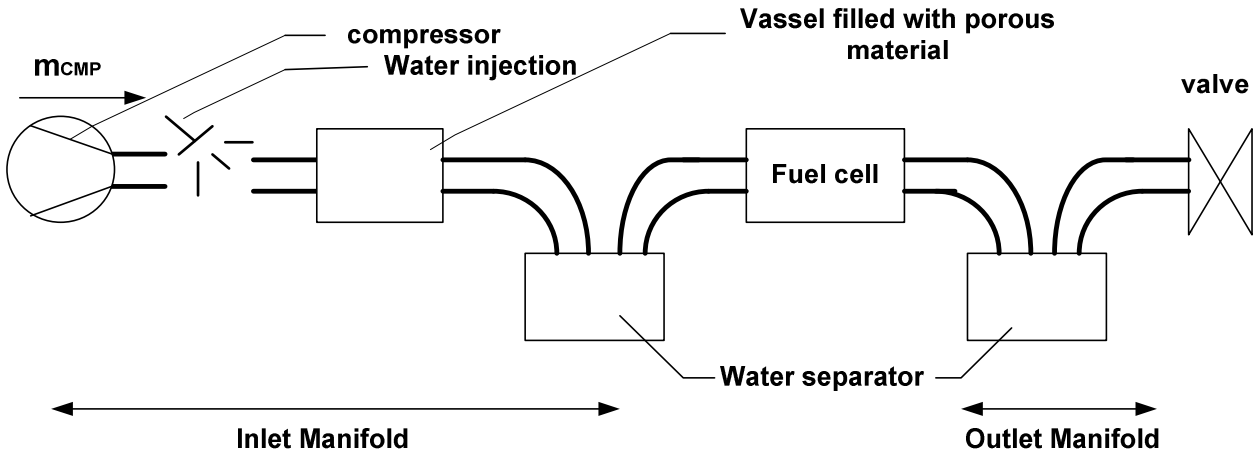

Figure 5.3. Basic scheme of air supply system of the testbench used in [6].

The Linear Quadratic Gaussian (LQG) approach allows obtaining a trade off between control input and error output signal energy. The PEM fuel cell system response to step changes in pressure and mass flow setpoint is investigated for a set of PI controllers and the LGQ controller. This strategy offers significant improvements compared with the behaviour of the closed-loop system obtained using a PI controller, because with the LGQ controller it is possible to decouple the mass flow from changes in pressure. This effect allows the mass flow to follow its setpoint, whereas the PI controllers cause large deviations. The negative overshoots in mass flow rate are considerably small with the LGQ controller and this is a very important goal because the negative overshoot in mass flow leads to insufficient air supply, which inhibits the electrochemical reaction.

P. Almeida and G. Simoes have developed a neural strategy to control the output voltage of a proton exchange membrane fuel cell PEM-FC [68]. The advantages of this control approach are demonstrated by using an emulator of the PEM FC, which implements the mathematical model of the core of the fuel cell, and by testing its voltage behaviour at different load conditions. The proposed control system uses a parametric CMAC (Cerebellar Model Articulation Controller) network (the P-CMAC) which acts by means of a Neural Optimal Control Architecture (NOC) (Figure 5.4). The P-CMAC network is a neural structure derived from Albus's CMAC algorithm and Tagagi-Sugeno-Kang parametric fuzzy inference systems. In the diagram of Figure 5.4 the system output is compared to a reference model chosen by the designer. The resulting error signal is then fed back to evaluate a cost criterion function, together with the back-propagated desired control signal from the direct model. The controller network is trained to minimize this criterion, approximating the overall operation to the operation of a conventional optimal controller. A dynamic model of a PEM-FC is adapted to run inside a control scheme. The dynamic model of the fuel cell, implemented by Simulink/Matlab, calculates the nonlinear characteristic V-I of the FC stack. The results show that the NOC work well and has operation advantages when compared to the design drawbacks and worse performance exhibited by a typical PID controller. A limitation of this work depends on the mathematical model of the PEM-FC implemented, because his model does not consider the equations that describe the different physical phenomena happening simultaneously in the fuel cell stack. Moreover the input signals are the partial pressure ratios of the cathode and the anode in the stoichiometry ratio, which is questionable, because such a difference between the anode and cathode can cause irreversible damages to the membrane.

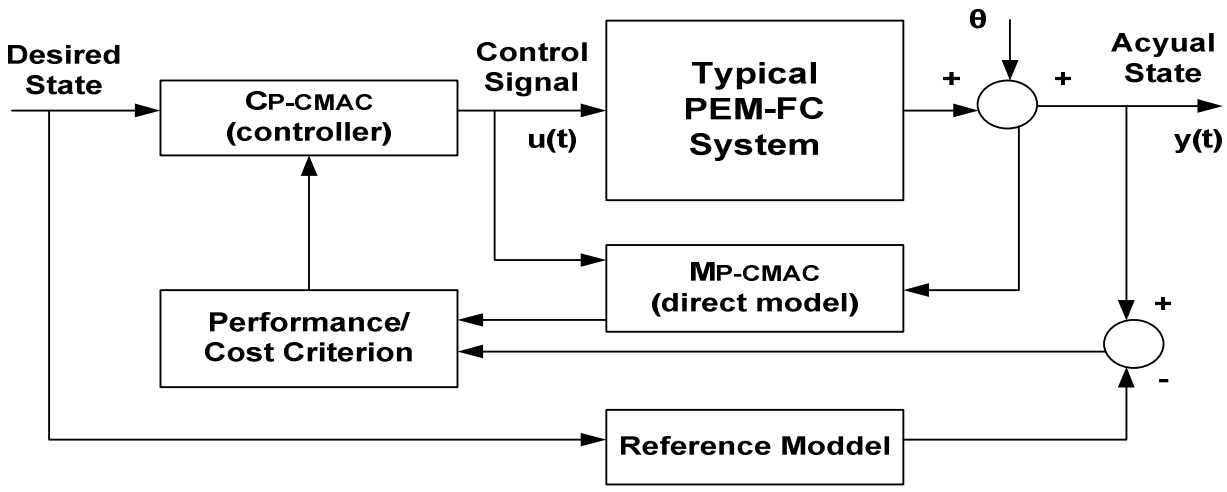

Figure 5.4. NOC Architecture Diagram Using P-CMAC Networks.

5.2 Control Problems

The principle of electricity generation from PEM-FC is straightforward when the correct material properties, cell structure and hydrogen are in place. The FC power response, however, is limited by air flow, pressure regulation, heat and water management [69]. Since current is instantaneously drawn from the load source connected to the FC, the FCS control is required to maintain optimal temperature, membrane hydration and partial pressure of the reactants across the membrane to avoid degradation of the FC voltage, which can reduce efficiency. These critical FCS parameters must be controlled over a wide range of currents by a series of actuators such as valves, pumps, compressor motors, expander vanes, fan motors, humidifiers and condensers. The auxiliary actuator system is shown in Figure 5.5 and is necessary for making fine adjustments to satisfy performance, safety and reliability requirements that are independent of age and operating conditions. In the following the FCS will be considered in the state representation and the state vector, the input vector, the output vector, the controlled output variables and the perturbation will be described.

The control problem attacked here is limited to the air management system. The overall FCS and the all-important variables are shown in Figure 5.5. The stack terminal voltage V_{st} is calculated based on the dynamically evolving load current and FC operating conditions such as hydrogen and oxygen partial pressure. The FC air flow needs to be controlled rapidly and efficiently to avoid oxygen starvation and extend the life of the stack [70], while minimizing parasitic losses of the compressor [71]. Oxygen starvation is a complicated phenomenon that occurs when the partial pressure of oxygen falls below a critical level at any location within the meander of the air stream in the cathode [72]. This phenomenon causes a rapid decrease in cell voltage, which in severe cases can cause a hot spot or even burn through the surface of the membrane. To prevent this catastrophic event, the stack diagnostic system must either remove the current from the stack or trigger a shut-down. Although the oxygen starvation is spatially varying, this phenomenon is believed to be avoidable by regulating the cathode excess oxygen ratio $\lambda_{O_2} = W_{O_2,in} / W_{O_2,react}$, where $W_{O_2,in}$ is the oxygen supplied to the cathode volume, and $W_{O_2,react}$ is the oxygen consumed in the reaction. This variable is a lumped variable and is regulated by controlling the compressor motor voltage v_{cm} during step changes current I_{st} drawn from the FCS. The control problem is not simple for two reasons:

1. the topology of actuators, disturbances and performance variables limits the disturbance rejection capabilities of any realizable controller; particularly, the variables manipulated by means of the actuating signal v_{cm} are upstream of where the disturbance I_{st} affects the performance variable λ_{O_2}.

2. traditionally used measurements for λ_{O_2} regulation are upstream of the performance variable due to difficulties in sensing within a vapour-saturated flow stream.

3. the various elements composing the FCS and in particular the air-management system can have constraints to be enforced. This is particularly true for the centrifugal compressor, whose control action should not drive its operating point beyond the surge or the choke limits, or else the compressor can be irreversibly damaged.

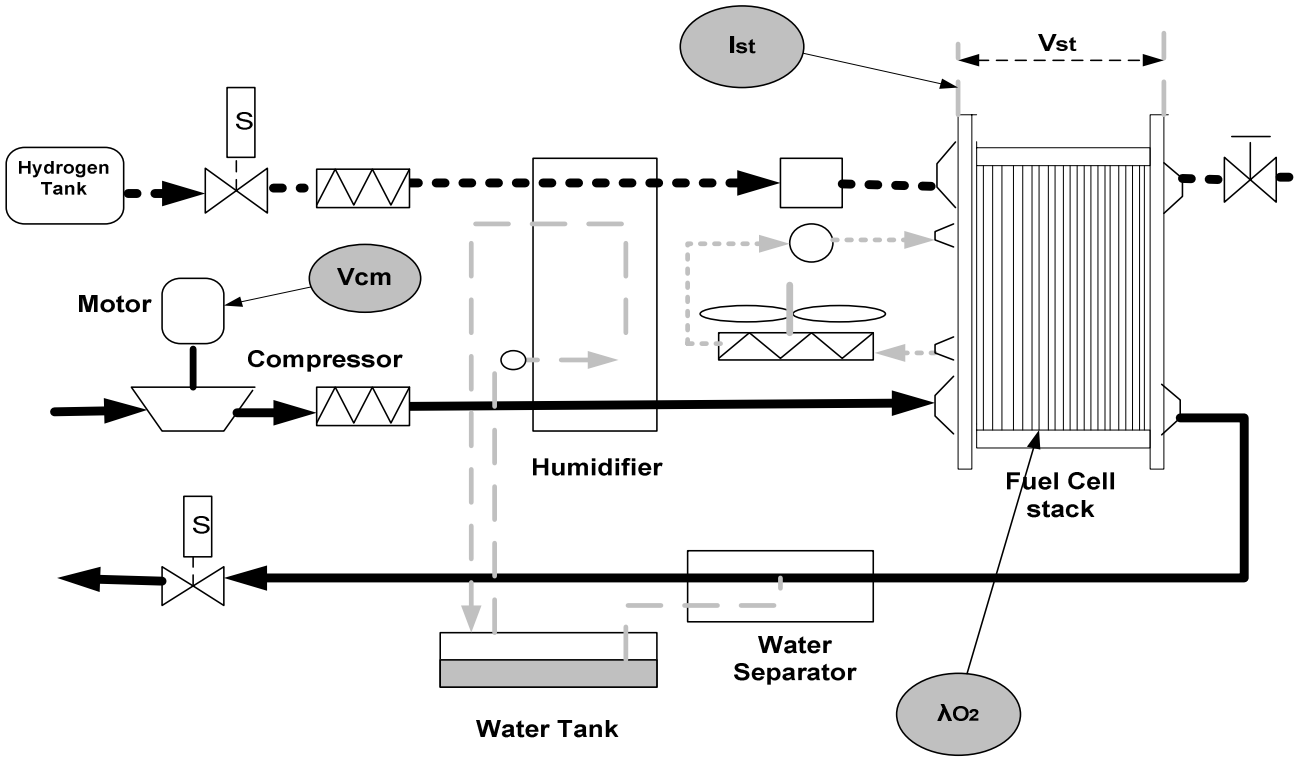

Figure 5.5. FCS (fuel cell system) with control subsystems. An FCS includes four sub-systems that manage the air, hydrogen, humidity and temperature. The figure also shows the control inputs and outputs of the air subsystems in the darkened circles.

5.2.1 State-Space Representation for the Management of the Air System

The nonlinear dynamic model of the FCS using electrochemical, thermodynamic and zero-dimensional fluid flow principles have been shown in detail in chapter 3. They will be however recalled in the following for easy reading.

The following assumptions are made for the FCS:

1. the compressed hydrogen is available and pure;
2. the control system ensures that the anode and cathode partial pressures are kept very close to one another;
3. the humidifier system is regulated to make the membrane hydrated perfectly;
4. the temperature is constant.

Assumption 1 means that the fuel is supplied continuously for the exact demanded amount and controlled by a valve. In general a high-pressure tank is used and this allows the hydrogen control system to react fast, so that the bandwidth of the closed-loop control system for the anode has a high bandwidth (it is practically considered instantaneous).

Assumption 2 is generally satisfied by a simple PI controller having as input the difference between the oxygen partial pressure and the hydrogen partial pressure. Proper adjustment of the PI parameters allow the control-loop to react quickly so as to quickly minimize this pressure difference across the FC membrane

Assumption 3 is just a simplification. Up to now a proper modelling of the humidification still lacks, so as a first approximation it is assumed that the membrane is always fully humified [43] [64]. Likewise the inlet reactant flows in the cathode and anode are assumed to be humidified in a consistent and a rapid way.

Assumption 4 claims that the average stack temperature T_{st} is well regulated for all phases of modelling, analysis and control design, so any fluctuations of the temperature is neglected.

With these assumptions, **the control problem is limited to the subsystem of air management**.

The overall FCS and the all-important variables are shown in figure 5.5, while fig. 5.6 shows the schematics of the of the air management systems (see chapter 3 or the list of symbols for the explanation of the variables):

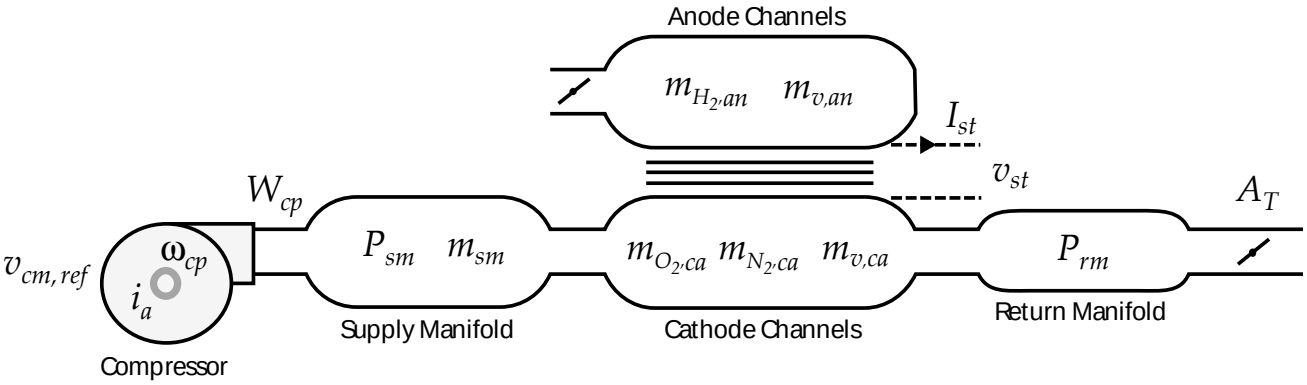

Figure 5.6. Schematics of the air management system.

The stack air supply system is composed of a centrifugal compressor, a supply manifold, cathode channels and a return manifold as shown in Fig. 5.6. The compressor supplies the air flow following the command to its motor. The supply manifold, cathode channels and return manifold all act as a gas storage volume. The end of the return manifold connects to atmosphere through an actuator valve.

The first state equation comes from the compressor dynamics governed by its inertia, as the following torque equation shows:

$$J_{cp}\frac{d\omega_{cp}}{dt} = \tau_{cm} - \tau_{cp} \qquad 5.1$$

where J_{cp} is the compressor inertia, ω_{cp} is the compressor speed, τ_{cm} and τ_{cp} are compressor motor torque and compressor load torque, respectively. The compressor speed, computed by integrating equation 5.1, together with the downstream pressure, i.e. supply manifold pressure, p_{sm}, influences different air flow rates through the compressor, W_{cp}. The relation between the compressor speed, downstream pressure and the compressor air flow rate is governed by the compressor flow map, as shown in Figure 5.7.

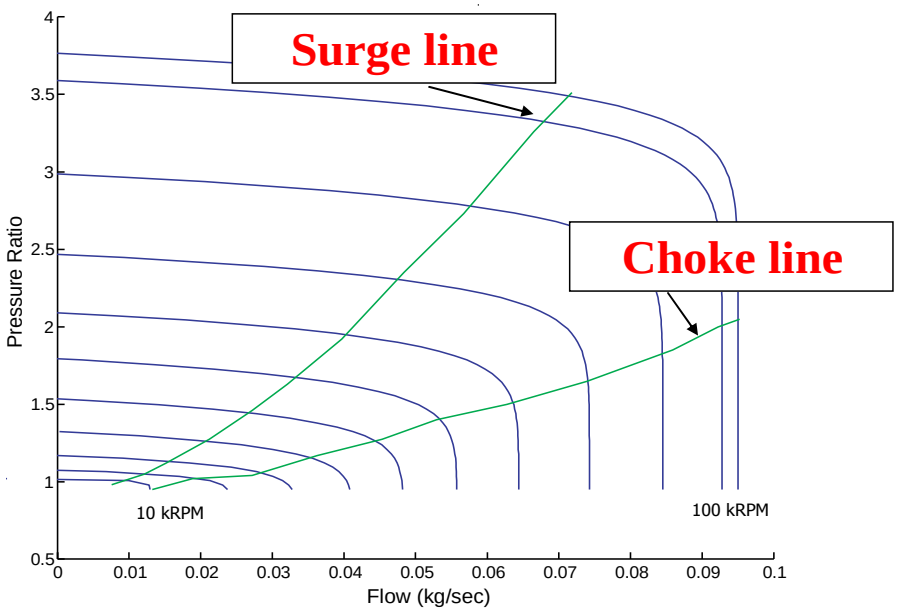

Figure 5.7. Compressor Flow Map.

The armature current of the DC motor driving the compressor should be also taken into consideration, this gives another state as suggested by the armature voltage equation:

$$\frac{di_a}{dt} = \frac{1}{L_a}\left(v_{cm} - R_a i_a - k_v \omega_{cp}\right) \qquad 5.2$$

Where v_{cm} is the armature voltage, i_a is the armature current, *Ra and* L_a are respectively the resistance and the inductance of the armature, k_v is the characteristic constants of the electrical motor. Note that a model of a DC motor is used here for sake of simplicity, but it should be remarked that, because of the high rotating speed required by the centrifugal compressor, an AC drive (particularly a brushless AC drive) should be employed.

The compressor air flow gets into the supply manifold and so influences the changes in the pressure inside the supply manifold through mass and energy conservation laws (see chapter 3 for the supply manifold model), which give two further state equations:

$$\frac{dm_{sm}}{dt} = W_{cp} - W_{sm,out}$$
$$\frac{dp_{sm}}{dt} = \frac{\gamma R_a}{V_{sm}}\left(W_{cp} T_{cp,out} - W_{sm,out} T_{sm}\right) \qquad 5.3$$

where $W_{sm,out}$ is the air flow out of the supply manifold into the stack cathode volume which is a function of the supply manifold pressure. V_{sm} is the supply manifold volume, R_a is the gas constant of air and γ is the ratio of the specific heat capacities, which is case of air is 1.4. The temperatures $T_{cp,out}$ and T_{sm} are the temperature of the air at compressor outlet and that of the air inside the supply manifold, respectively. They are calculated using thermodynamic principles and the ideal gas law. The change in supply manifold pressure affects the rate of air entering the stack cathode through the linear nozzle equation, where $k_{sm,ou}$ is the supply manifold nozzle constant.

$$W_{sm,out} = k_{sm,out}(p_{sm} - p_{ca}) \qquad 5.4$$

This air flow rate going into the cathode then affects the oxygen level in the cathode, and therefore affects the stack voltage, and the stack power output.

The dynamics of the oxygen level in the cathode is governed by the mass conservation law. There are three states in the cathode volume model, namely the oxygen mass $m_{O_2,ca}$, the nitrogen mass $m_{N_2,ca}$ and the vapor mass $m_{w,ca}$. Their state equations give other 3 state equations:

$$\begin{aligned}
\frac{dm_{O_2,ca}}{dt} &= W_{O_2,ca,in} - W_{O_2,ca,out} - W_{O_2,react} \\
\frac{dm_{N_2,ca}}{dt} &= W_{N_2,ca,in} - W_{N_2,ca,out} \\
\frac{dm_{w,ca}}{dt} &= W_{w,ca,in} - W_{w,ca,out} + W_{v,ca,gen} + W_{v,membr}
\end{aligned} \qquad 5.5$$

The oxygen partial pressure which affects the stack voltage can be calculated from these states using the ideal gas law.

However the term giving the liquid water mass leaving the stack is neglected, with respect to eq. 5.5: this means that the phenomena of “flooding” of the membrane are not considered and that the cathode gas is therefore vapour-saturated; which leads up to the corresponding partial pressure to be constant for constant temperature and equal to the saturated vapour pressure. This constancy is paid off in the linearization explained beneath with the fact that this variable is not observable.

As explained in chapter 3 the mass flow rates with subscript ‘in’ are calculated from $W_{sm,out}$ and the air thermodynamic properties. The amount of oxygen reacted or used in the reaction, $W_{O_2,react}$, is a function of stack current, I_{fc}, which is considered in this thesis as a disturbance input.

$$W_{O_2,react} = M_{O_2}\frac{nI_{fc}}{4F} \qquad 5.6$$

where F is Faraday's number.

The mass flows with subscript 'out' are functions of the states ($m_{O_2,ca}$, $m_{N_2,ca}$, $m_{w,ca}$) and the cathode outlet flow, which is a function of the pressure downstream, i.e. the return manifold pressure, p_{rm}. The function is the linear nozzle equation in the same form as equation 5.4, where $k_{ca,out}$ is the return manifold nozzle constant:

$$W_{ca,out} = k_{ca,out}(p_{ca} - p_{rm}) \qquad 5.7$$

The return manifold is an air storage volume similar to the supply manifold but the temperature changes can be neglected. The last state equation is then given by the dynamic of the return manifold pressure , given by:

$$\frac{dp_{rm}}{dt} = \frac{R_a T_{rm}}{V_{sm}}(W_{ca,out} - W_{rm,out}) \qquad 5.8$$

where the return manifold outlet flow, $W_{rm,out}$, is calculated by the nonlinear nozzle equations as explained written below since the pressure drop is large.

$$W_{rm,out} = \frac{C_{D,rm}A_T p_{rm}}{\sqrt{R_a T_{rm}}}\left(\frac{p_{atm}}{p_{rm}}\right)^{\frac{1}{\gamma}}\left\{\frac{2\gamma}{\gamma-1}\left[1-\left(\frac{p_{atm}}{p_{rm}}\right)^{\frac{\gamma-1}{\gamma}}\right]\right\}^{\frac{1}{2}} \quad for\ \frac{p_{atm}}{p_{rm}} > \left(\frac{2\gamma}{\gamma+1}\right)^{\frac{\gamma-1}{\gamma}}$$

$$W_{rm,out} = \frac{C_{D,rm}A_T p_{rm}}{\sqrt{R_a T_{rm}}}\gamma^{\frac{1}{2}}\left(\frac{2\gamma}{\gamma+1}\right)^{\frac{\gamma+1}{2(\gamma-1)}} \quad for\ \frac{p_{atm}}{p_{rm}} \le \left(\frac{2\gamma}{\gamma+1}\right)^{\frac{\gamma-1}{\gamma}} \qquad 5.9$$

where A_T is the valve opening area that can be adjusted using, for example, a solenoid valve

As shown in equations 5.5 and 5.6, the electrical current that is drawn from the stack will cause the oxygen partial pressure to drop inside the cathode volume, which reduces the stack efficiency and also increases the risk of oxygen starvation. To replenish the oxygen, the compressor has to increase the air flow to the supply manifold. However, the cathode oxygen cannot be replenished instantaneously since the dynamics of the compressor, the supply manifold and the cathode volume are affected. The return manifold valve opening can be used to alter the cathode oxygen transient response by closing it down or opening it up during transients. Depending on the speed and the coordination between the compressor command and the opening of the return manifold valve, the recovery speed of the oxygen partial pressure is modified.

In summary, the nonlinear model based on the state equations (5.1)-(5.9) involves 10 states (see Appendix E)

$$x_{NL} = [m_{O_2}, m_{H_2}, m_{N_2}, i_a, \omega_{cp}, p_{sm}, m_{sm}, m_{w,an}, m_{w,ca}, p_{rm}]^T \qquad 5.10$$

5.2.2 Input and Output Variables

For the air management system the targets are to supply enough air to ensure the reaction and to avoid the membrane to be depleted of oxygen. The first goal is governed by the current the FCS must supply to the electrical load, which is given by equation (5.6), and then it can be considered an external disturbance. As for the input fig. 5.5 shows that either the motor voltage vcm or the AT , the valve opening area of the return manifold valve, can be used as input variables. Since the variation of the return manifold pressure entailed by the use of this valve causes the compressor to move from its optimal efficiency conditions, in general only the motor voltage is used as control input [65]. In [74] it is demonstrated however that the use of both inputs can cause the air management system to have better performance with minimal loss of efficiency. In any case, for the problem at hand, only the motor voltage is considered for the high burden of computation that DSPACE could require if a control strategy with two inputs were used.

In summary then he following equations are provided:

$u = v_{cm}$ (actuating (control) signals) 5.11

$w = I_{st}$ (exogenous inputs) 5.12

where u is the actuating signal and w is the disturbance input, : v_{cm} is the motor voltage and finally I_{st} is the current drawn from the FCS.

As for the output variables, they should be divided into the vector z of the controlled variable, the choice of which depends on the control target, and the vector y. of measurable outputs.

As for the choice of the controlled variables, the following one is introduced, which takes into account both the amount of air flow necessary for the reaction and the air flow necessary to prevent the oxygen depletion. This parameter is the oxygen excess ratio written as follows, emphasizing its non-linear dependency on the state vector xNL defined above:

$$\lambda_{O_2} = \frac{W_{O_2,in}(x_{NL})}{W_{O_2,rct}(x_{NL}, I_{st})} \quad 5.13$$

where $W_{O_2,in}$ is the mass flow rate of oxygen gas entering the cathode and $W_{O_2,rct}$ is the rate of oxygen reacted. The oxygen excess ratio λ_{O_2} is then used as a lumped variable and is directly correlated with the FCS oxygen starvation.

However:

$$W_{O_2,in} = y_{O_2} \frac{1}{1+\Omega_{atm}} W_{sm} \qquad 5.14$$

where $W_{sm}(p_{ca}, p_{sm}, T_{st})$ is the mass flow rate of the supply manifold (given by the compressor or the blower), $y_{O_2} = \frac{x_{O_2} M_{O_2}}{M_{atm}}$ is the mass fraction of oxygen in the dry atmospheric air, $M_a^{atm} = x_{O_2} M_{O_2} + (1 - x_{O_2}) M_{N_2}$ is the molar mass of air and x_{O_2}=0.21 is the oxygen mole fraction in dry air. The atmospheric humidity ratio Ω_{atm} is given by:

$$\Omega_{atm} = \frac{M_v}{M_a} \frac{\phi_{atm} p_{sat}^{atm} / p_{atm}}{1 - \phi_{atm} p_{sat}^{atm} / p_{atm}} \qquad 5.15$$

where M_v and M_a are the molar masses of the vapour and the dry air, respectively.

The oxygen reaction rate $W_{O_2,rct}$ is calculated from the stack current I_{st} by using (5.6).

In equation 5.6 and then in equation 5.13 , the input I_{st} directly affects $W_{O_2,rct}$ and causes an instantaneous drop of λ_{O_2}. The actuator v_{cm} affects the oxygen excess ratio λ_{O_2} indirectly through the states x_{NL}. A high value of λ_{O_2}, and thus high oxygen partial pressure, improves the stack power P_{st} but also requires higher compressor P_{cm}. In fact, the air compressor is the main contributor of parasitic losses in the FCS (about 20% of the total output FCS power) [71].

Since the net power obtained from the FC stack system is given by:

$$P_{net} = P_{st}(x_{NL}, I_{st}) - P_{cm}(x_{NL}, v_{cm}) \qquad 5.15$$

above an optimum λ_{O_2} level, that depends on I_{st} [73], an increase of λ_{O_2} will cause a decrease in P_{net}. For simplification the fixed value $\lambda_{o_2}^{d}$ = 2 is assumed as a good value for preventing oxygen starvation without excessively reducing the output net power[66].

Thus, the overall control design objective is to control the compressor motor v_{cm} so as to maintain $\lambda_{O_2}^{d}$ = 2 and achieve the desired FCS net power $P_{net} = P_{net}^{ref}(I_{st})$ required by the electrical load.

The accessible output measurements include air flow rate W_{cp} through the compressor, supply manifold pressure p_{sm} and stack voltage v_{st}.

The measured output vector y and the controlled output vector z is then given by:

$$y = [W_{cp}\, p_{sm} v_{st}]^T = h_y(x_{NL}, u, w) \quad 5.16$$

$$z = [P_{net,} \lambda_{O_2}] = h_z(x_{NL}, u, w) \quad 5.17$$

It should be stressed that λ_{O_2} is not a measurable variable, but should be reconstructed by the equations above, as explained. From this standpoint the model of the FCS is then used as a nonlinear observer for this variable.

5.2.3 Linearization

The nonlinear FCS system can be linearized around an operating point. In the FCS this is defined by a value of the stack current I_{st} and a value of the compressor motor voltage v_{cm} and a value of λ_{O2} . The linear model is given by:

$$\delta \dot{x} = A\delta x + B_u \delta_u + B_w \delta_w \quad 5.18$$

$$\delta \dot{x} = C_z \delta x + D_{zu} \delta_u + D_{zw} \delta_w \; 5.23 \quad 5.19$$

$$\delta \dot{x} = C_y \delta x + D_{yu} \delta_u + D_{yw} \delta_w \quad 5.20$$

where $\delta(\cdot) = (\cdot) - (\cdot)^{\circ}$ represents deviation from a nominal value. The state x, measurements y, performance variable z, input u and disturbance are defined by:

$$x^T = [m_{O_2}, m_{H_2}, m_{N_2}, i_a, \omega_{cp}, p_{sm}, m_{sm}, m_{w,an}, p_{rm}] \quad 5.21$$

$$y^T = [W_{cp}, p_{sm}, v_{st}] \quad 5.22$$

$$z = \lambda_{O_2} \quad 5.23$$

$$u = v_{cm} \quad 5.24$$

$$w = I_{st} \quad 5.25$$

Note that the resulting linear model has eight states [66], whereas the nonlinear model has nine states. The mass $m_{w,ca}$ of water in the cathode is removed because it is unobservable after linearization. The reason is that with the available data of the membrane flow, the model outputs too water flow from the anode to the cathode, which results in fully humidified cathode gas (vapour saturated). Thus, for constant temperature, the vapour pressure is constant and equal to the saturated vapour pressure. The nonlinear model of [66] does not include the effects of liquid condensation, also know as "flooding", on the FCS voltage response.

The linearization of the nonlinear FCS system is used to design the classical control scheme based on PI (Proportional Integrative) for regulating the FCS (Figure 5.8).

5.2.4 Design of the λ_{O_2} PI Controller for a Case Study

The design of the PI controller has been done considering the linearized model of the system having as outputs the P_n: Net Power, the λ_{O_2}: oxygen excess ratio, the W_{cp} : compressor flow, the p_{sm} supply manifold pressure, and the V_s: stack voltage; and as inputs the i_{ST}: stack current, and the V_{CM}: compressor motor voltage. Then, the transfer function between λ_{O_2} and V_{CM} of this multi-input/multi-output system has been considered, after linearization.

All the data of the FCS are shown in appendix D and they refer to an FCS [66] with a Fuel Cell by Ballard of 80 kW employed on the electrical vehicle FORD P2000, with:

- Number of stacks = 381;
- Centrifugal Compressor by 'Allied Signal;
- Temperature = 80 °C;
- Rated current = 310 A.

Then, the transfer function between λ_{O_2} and v_{cm} of this multi-input/multi-output system has been considered, after linearization. Figure 5.8 shows the control scheme.

The linearization has been performed by means of a proper software tool in Matlab® environment. In particular, given the non-linear Simulink® model of the system, the Matlab® function *linmod* permits to obtain the state-space representation of the linearized system from which the transfer matrix can be easily deduced. In the case under hand, the above recalled transfer function is the term of the transfer matrix which correlates the input oxygen excess ratio to the output compressor motor voltage.

In order to use the classical PI control, the FCS linear model has been obtained by linearizing the nonlinear model around the operating point at the FCS at half rated values, characterized by the following values [66]:

I_{st} = 190 A

v_{cm} = 164 V

P_{net} = 40 kW

Tests have been performed to check the approximation error brought about using the linear model instead of the nonlinear one. These tests have shown an output error less than 3% for a current variation of 100A above and below the operating point.

The system presents 7 poles and 4 zeros as shown in Tab. VI. It can be remarked by inspection that Z_2 compensates P_6 and Z_4 almost compensates P_7. The PI controller has been then designed trying to achieve the highest bandwidth, guaranteeing a phase margin of 50° to achieve a good relative stability. The compressor constraints should be always enforced, however, which makes the design more complex . As a result, figure 5.9 shows the Bode diagram of the open-loop system (plant+controller) which exhibits a -3 dB bandwidth of 16 rad/s and a phase margin of 50°.

It should be remarked that the PI design has been repeated many a time in a trial-and-error fashion, in order to enforce the constraints of the compressor, thus the dynamical performance is sub-optimal. It is in this stage of design that the emulator is particularly useful, since any mistake in the design phase does not have irremediable effects on a real FCS when the experimental assessment of the control law is implemented.

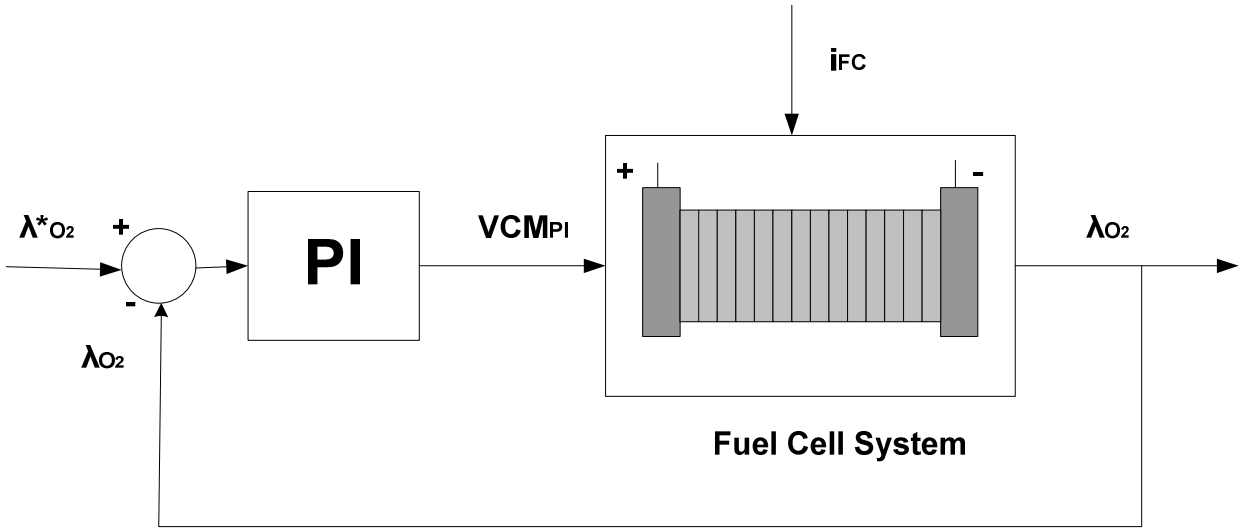

Figure 5.8. Block diagram of the classic PI control scheme.

Poles	Zeros
P_1= -93.9	Z_1=-68.1
P_2= -46.1	Z_2=-3.1
P_3= -10.5	Z_3=-2.3
$P_{4,5}$= - 4.85 ± 0.82 i	Z_4=-1.35
P_6=-3.1	
P_7=-1.4	

Tab. VI. Poles and zeros of the linearized system.

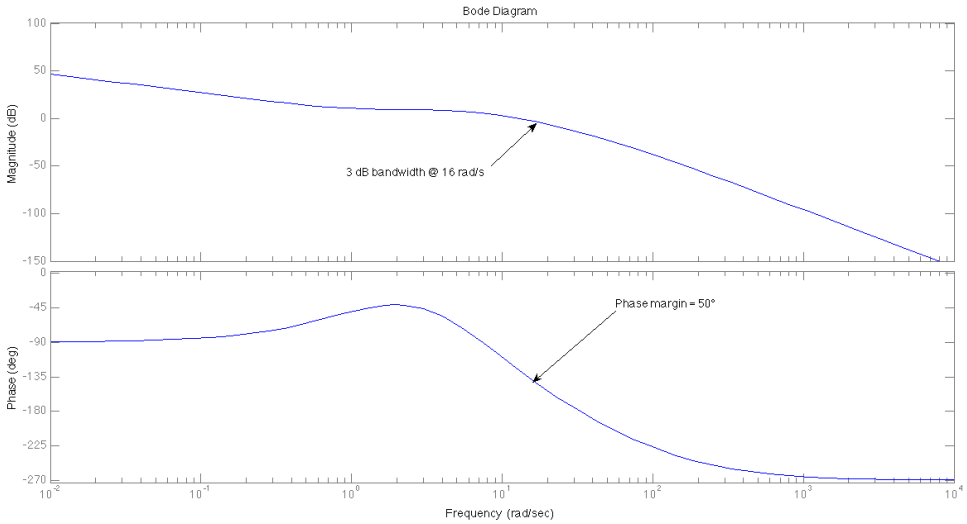

Fig. 5.9. Bode diagram of the open-loop system.

5.2.5 Experimental Results

Simulation and experimental results have been performed in Matlab®-Simulink® environment adopting the FCS emulator described in chapter 4 respectively. The entire model of the FCS system, including the FC stack and its auxiliaries, as well as the control system of the DC-DC converter has been implemented on the DSPACE DS1003 board. The voltage loop control of the DC-DC converter has been implemented at a sampling frequency of f_c=10 kHz, while the entire FCS model has been implemented at a sampling frequency of $f_{c2}=f_c/20$= 500 Hz. This has been done because of the complexity and computational requirement of the FCS model, maintaining at the same time the bandwidth of the DC-DC converter. This does not influence the FCS model behaviour, since the time constants of the FCS system are much higher than the sampling time of its model.

As a first test, the FCS working characteristics has been acquired, averaging the voltage versus current static characteristics obtained at a constant working temperature (353 K in this case) with the FCS auxiliaries (see Fig. 5.5) working as in a normal operating condition. Fig. 5.10 shows the experimental data of the PEM-FC characteristics taking into account the whole model and whose fitting is obtained with a cubic interpolation. On the same graph the stack characteristics of the same FC have been plotted for three different values of the cathode pressure (experimental data and their fitting). It can be observed that the stack characteristic presents a higher voltage for each current at increasing values of cathode pressures, as expected. Moreover, the FCS working characteristics match the experimental points of the different stack

characteristics, respectively from those at lower pressure to those at higher pressure for increasing values of current. Furthermore, when observing the FCS characteristics in Figure 5.10 (see square symbols), it can be remarked that the FCS actually operates as a quasi-ideal voltage generator in a wide current range, with an internal resistance close to zero. Figure 5.11 shows the corresponding static characteristic power versus current of the FCS, respectively the experimental data and their fitting. The power characteristic, since the voltage one is quasi-constant in the linear zone, is a straight line, which is typical of ideal voltage generators. Finally, Figure 5.12 shows the corresponding P_{H2} and P_{O2} static characteristics versus current, respectively the experimental data and their fitting. As expected the two partial pressures are quite superimposed and they increase at increasing currents, because of the increased pressure during operation.

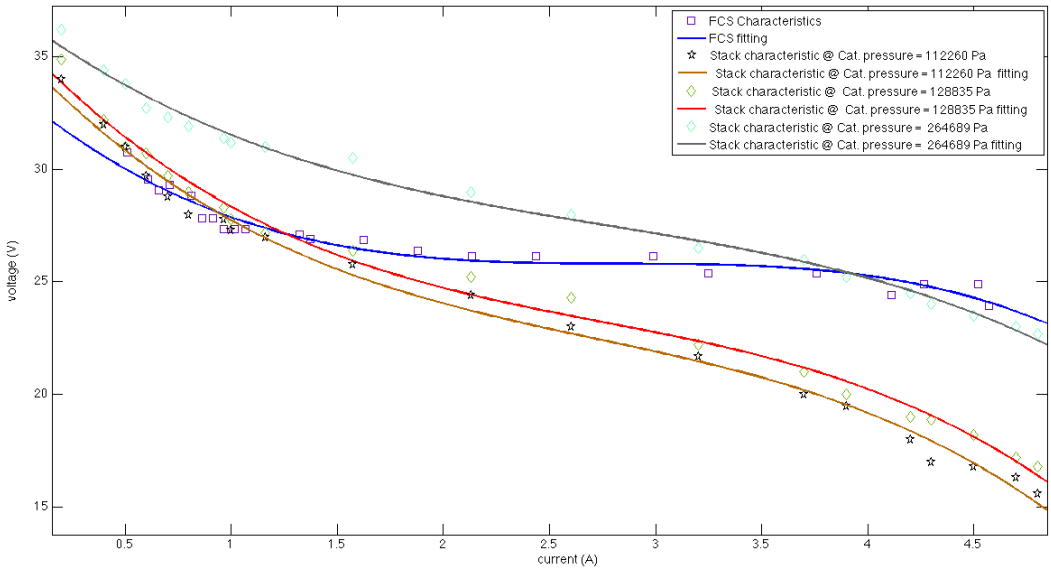

Fig. 5.10. Stack characteristics at different cathode pressures and FCS characteristics: experimental points and their fitting.

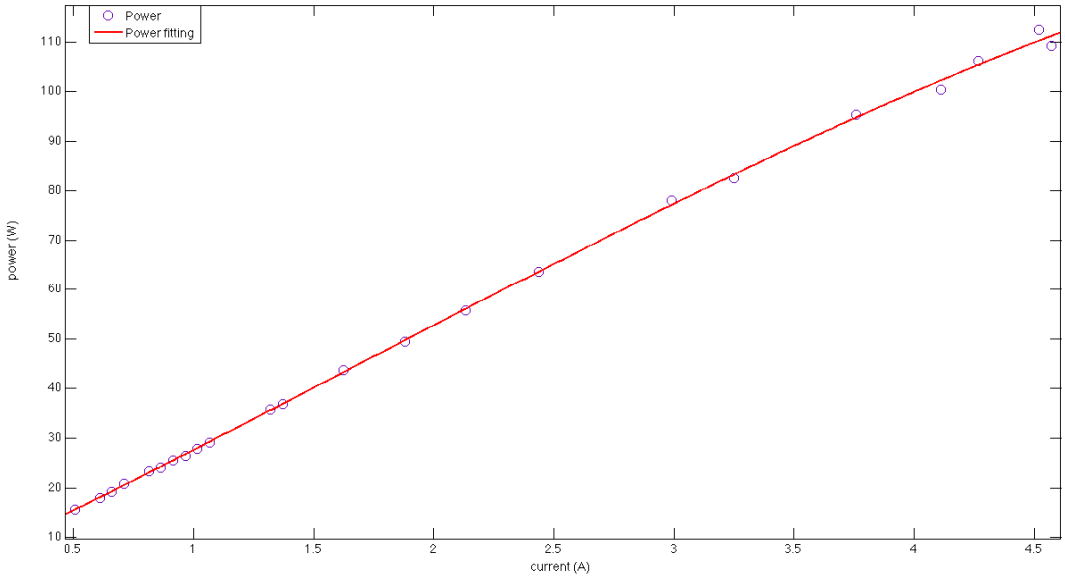

Fig. 5.11. Power FCS characteristics versus load current.

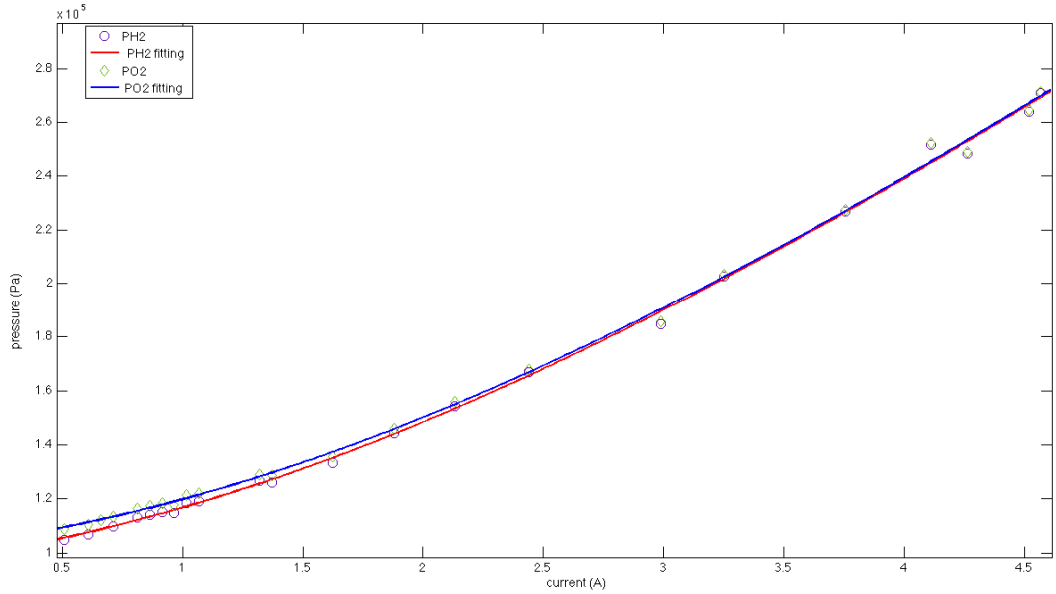

Fig. 5.12. P_{H2} and P_{O2} versus load current curves.

Afterwords, some transient tests have been performed. In particular two transients have been analysed, the first from the activation zone into the linear one, the second from the linear zone into the concentration one. They have been obtained respectively with step variations of the load resistance from 44 Ω (erogated power equal to 19 W) to 19.6 Ω (erogated power equal to 37 W) and from 8.7 Ω (erogated power equal to 78 W) to 5.5 Ω (erogated power equal to 112 W). Figure 5.13 shows the reference and measured voltage, the corresponding current and power during the first transient. The measured voltage quickly follows its reference, showing the good dynamic performance of the state controller. Moreover, the

transient occurs between two operating points belonging to the same FCS working characteristics in Fig. 5.12. In particular, the higher the load current, the lower the corresponding voltage and the higher the erogated power. Correspondingly, Figure 5.14 shows the supply voltage of the compressor motor and the oxygen excess ratio λ_{O2}. It can be observed that, at increasing currents, the compressor motor voltage increases to keep the oxygen excess ratio λ_{O2} equal to its reference value = 2: indeed the oxygen excess ratio λ_{O2}, after a fast transient, approaches its reference and after a slower transient (not visible at the scale of the graph) converges with zero steady-state error to its reference. Figure 5.15 shows the reference and measured voltage, the corresponding current and power during the second transient. Also in this case, the measured voltage quickly follows its reference. Like in the former test, the higher the load current, the lower the corresponding voltage and the higher the erogated power. Correspondingly, Figure 5.16 shows the supply voltage of the compressor motor and the oxygen excess ratio λ_{O2}. It can be observed that, at increasing currents, the compressor motor voltage increase to maintain theoxygen excess ratio λ_{O2} equal to its reference 2, and the oxygen excess ratio λ_{O2} quickly converges to its reference. It should be noted that, in this test, the response of the compressor motor and of the fluid is underdamped, with significant oscillations of both the motor voltage and the oxygen excess ratio λ_{O2}: indeed the at low loads the load torque produced by the compressor is very low leading up to a low DC motor torque driving only the the inertia.

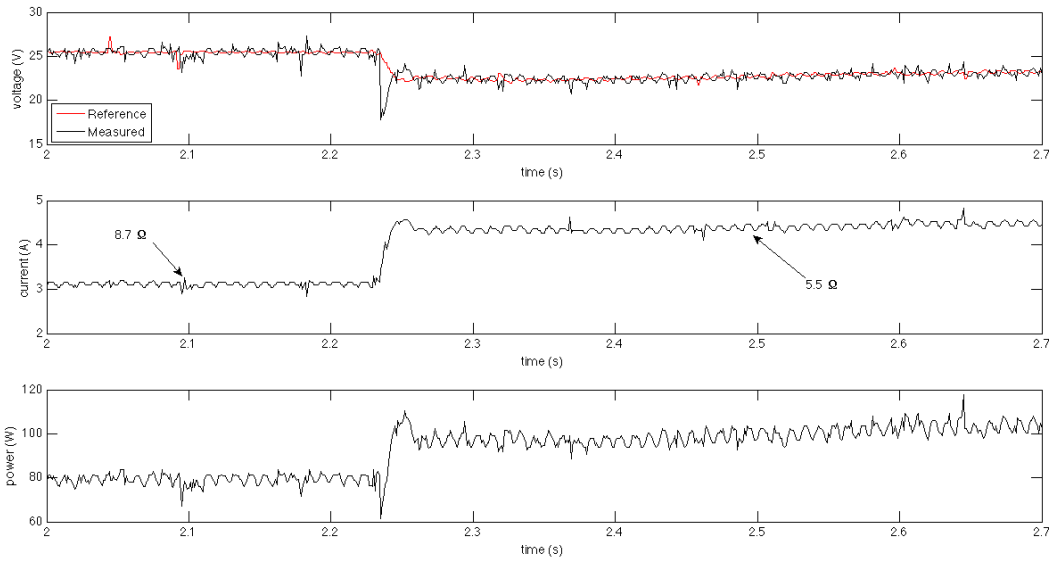

Fig. 5.13. Reference and measured voltage, current and power of the FCS during a load step from 8.7 Ω to 5.5 Ω.

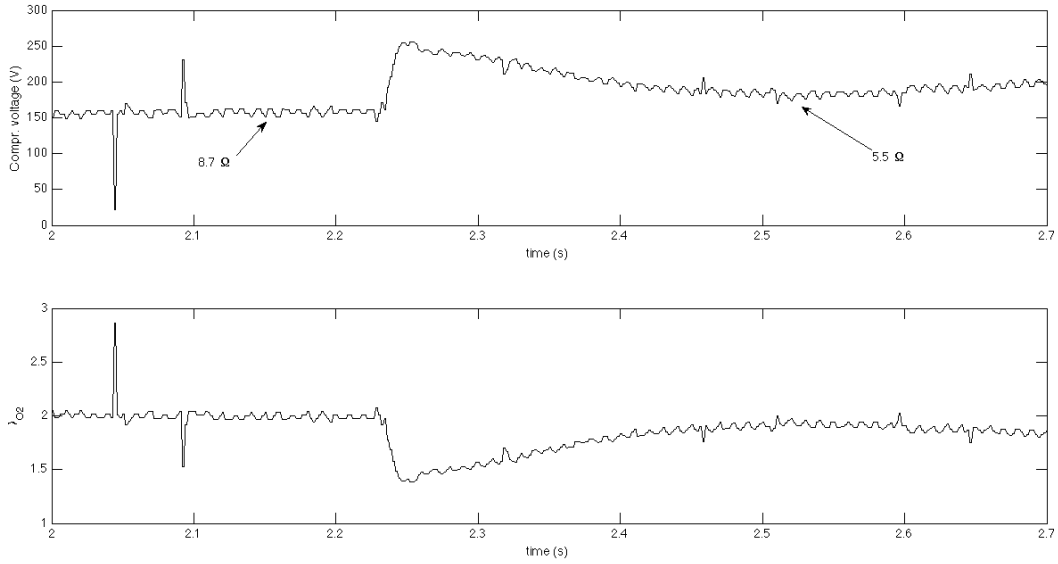

Fig. 5.14. Compressor voltage and λ_{O2} during a load step from 8.7 Ω to 5.5 Ω.

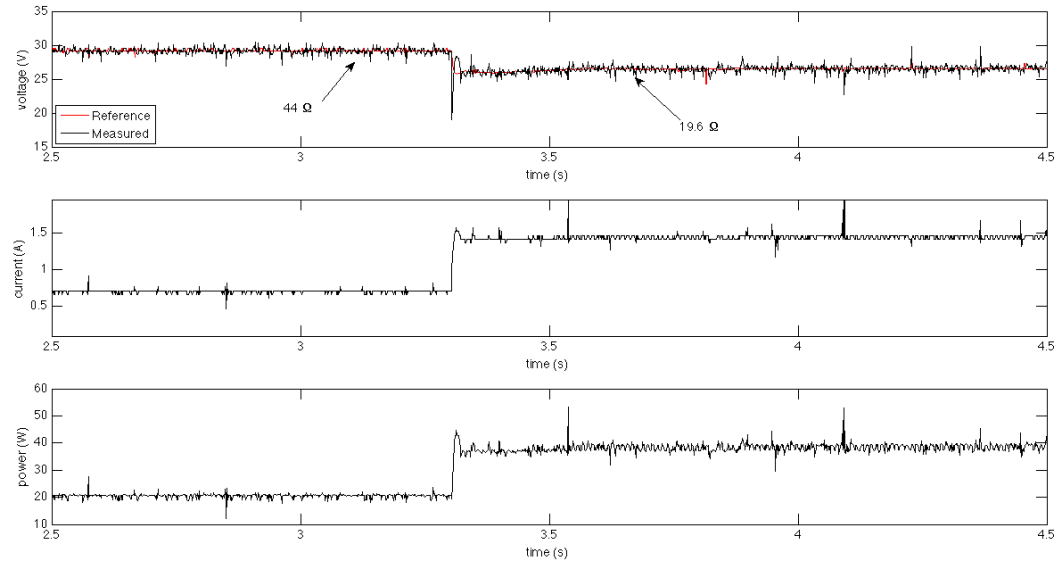

Fig. 5.15 Reference and measured voltage, current and power of the FCS during a load step from 44 Ω to 19.6 Ω.

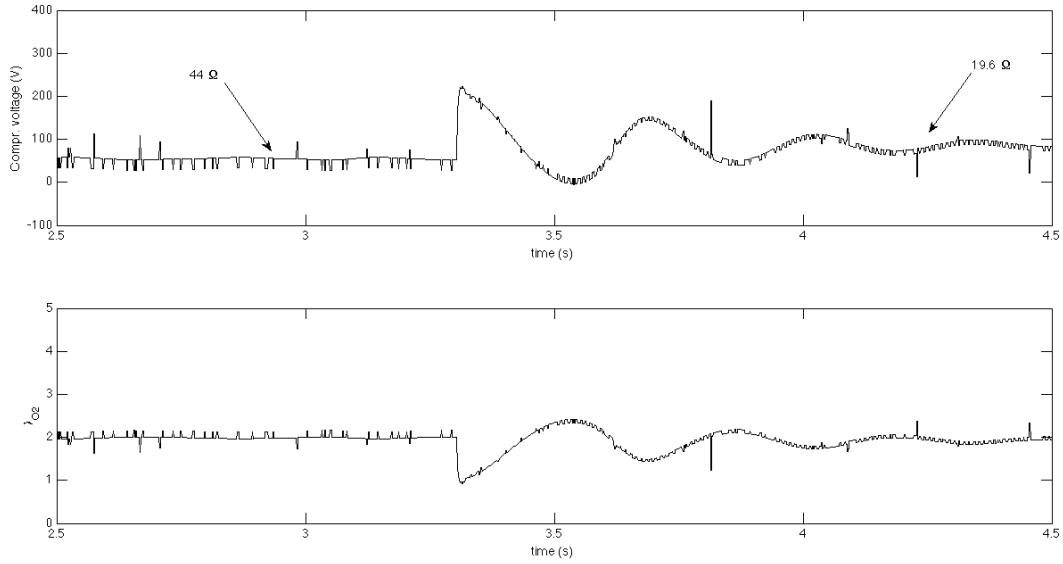

Fig. 5.16. Compressor voltage and λ_{O2} during a load step from 44 Ω to 19.6 Ω.

5.3 Neural Inverse Control of a PEM-FC System

The idea proposed here is to complement the PI designed above with a static feed-forward to improve the performance of the above PI controller., to optimise its dynamical performance.

The use of the PI in the previous section was justified by the fact that most industrial systems are controlled by PI, they are easy to tune and work relatively well even if the system is not known in detail. So it is the reference type of control for any system, even if nonlinear ones. However the performance of a system can be enhanced by paralleling the PID with a feed-forward controller, which can be also implemented by a neural network. The principle is described in Figure 5.17.

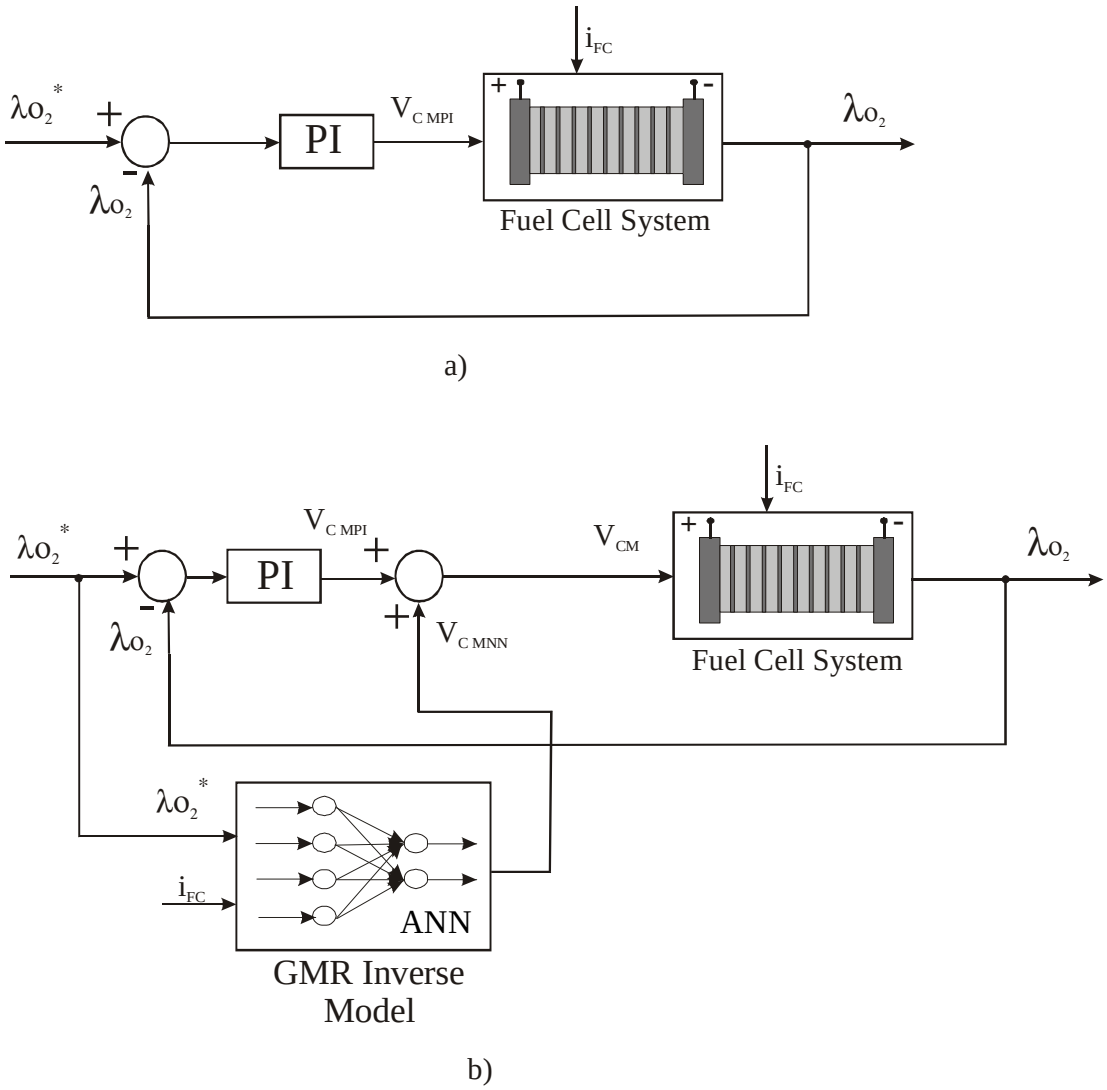

Fig. 5.17. Block diagram of the classic PI control scheme (a) and PI+GMR control scheme (b).

This figure shows the difference between the PI scheme and the one with a static feedforward, which essentially implements the inverse of the system to be controlled. Basically this approach can use either a dynamical or a static feedforward. The dynamical feedback is simply a neural network whose inputs are the reference and its future values and the commands of the real system in previous instants of time. The use of a dynamical one is marred by the fact the system to be controlled may have an unstable inverse, and it may be difficult to decide a priori whether or not the inverse system is really stable [76].

To avoid this problem a static feedforward can be used. The idea is just to use a Neural Network to implement the inverse of the system in steady state. Moreover any modelling error need not have a harmful impact on the control action, since the presence of a feedback controller can make up for any slight error of the feed-forward control signal.

As for the FCS regulation problem of λ_{O2}, where the reference is around the value 2 for long periods of time, the static feedforward is typically designed to provide the steady-state of the control signal [77]. As a matter of fact the strategy for FCS air_management is to make a number of experiments on the controlled system over a wide range of load currents trying to enforce the constraints and then use this collection of data to make the feed-forward controller implement the inverse of the system. A neural network can be used, specifically the GMR neural network (see appendix), which is naturally able to learn the inverse of multi-valued functions of several variables. The problem at-hand has in fact 2 input variables (compressor motor voltage and load current, and one output) and one output (λ_{O2}), which is equal to 2. This means that many input-pairs can have the same output, thus making the inversion difficult. The usual back-propagation multi-layer perceptron is not suited for this task, that is why the GMR should be used. The GMR network therefore receives the reference value of λ_{O_2}=2 and the value of the load current of the PEM-FC as inputs and gives compressor motor voltage, v_{cmNN} as output, which is then summed to the output of the PI controller v_{cmPI}. . In this way t the steady state accuracy of the control system is improved in all working regions. It should be remarked that the coefficient λ_{O_2} is not a measurable variable, but is inferred by the non-linear model of the FCS, which would then act as an observer of the real value. In the application at hand it is assumed that the fed-back λ_{O_2} coincides with the real value.

5.3.1 Brief Description of the GMR

In the lowing the fundamentals of the GMR are given to simplify the reading of the chapter. A complete description of the GMR and its PC interface are given in Appendix A1. The GMR is mainly an incremental self-organizing neural network and, unlike MLP, it can easily compute the inverse function even for multi-valued functions and in presence of discontinuities [75]. Its algorithm transforms the mapping problem $f : \boldsymbol{x} \rightarrow \boldsymbol{y}$ into a pattern recognition problem in the augmented space Z represented by vectors $\boldsymbol{z} = [\boldsymbol{x}^T \boldsymbol{y}^T]^T$, which are the inputs of GMR. In this space, the branches of the mapping become clusters which have to be identified. The weights of the first layer are continuous variables and represent the Z space, while those of the second layer are discrete (chains between neurons) and represent the branches mapping. The first layer weights are computed in the training phase by a multi-resolution quantization phase; the second layer weights are generally computed in the linking phase by a PCA technique or a geometrical technique [75].

1) Training phase (multiresolution vector quantization)

The training phase concerns the vector quantization of the *Z* space. This can be obtained by using different neural incremental approaches i.e. the number of neurons changes according to the mapping to be approximated: the *PLN* (Progressive Learning Network) competitive learning law [75] has been implemented, also called *EXIN SNN*, which is unsupervised and incremental. Training can be split into two sub-phases: coarse quantization and fine quantization. The coarse quantization is obtained by using the EXIN SNN algorithm and it produces neurons called *object neurons*. In the second subphase, the fine quantization, at first a preprocessing labels each neuron with the list of the input data which had the neuron as a winner. At the end, for each neuron a list of the inputs for which it has won is stored. This list represents the *domain* of the object neuron. Obviously the domains are mutually exclusive (no overlap) and their sum is the original training set (TS). Every list is considered as the TS for a subsequent secondary *EXIN SNN*. Hence, as many *EXIN SNN*'s as the object neurons are used in parallel in order to quantize each object domain. The secondary learning can have an a priori fixed number of epochs or a termination criterion. At the end, the neural network is composed of the neurons generated by the secondary learning phases (*pool of neurons*), labelled as belonging to a compact set defined by object neuron.

2) Linking and Merging

Linking and merging enable the cluster to be reconstructed under the assumption that the clusters represent the mapping branches. The principle is the *branch tracking*, that is the shape of the cluster is tracked by using links between neurons (it looks like exploiting the *inertia* of the clusters). Two approaches are possible, but in this paper only the PCA method has been used. [75].

3) Recall phase

In the recall phase, the input (called **x**) can be any collection of components of **z** and the input space is defined as X. Hence the output y is the vector composed of the other elements of **z** and the output space is defined as Y. All weight vectors are then projected onto X: this projection is easily accomplished by using only the elements of the weight vector whose position indices correspond to the position indices of the input elements in the augmented vector Z. An interpolation formula is then used to retrieve the results. See [75] for a complete description.

The training set for the GMR has been created by using the nonlinear model with two inputs (the stack current I_{fc} and the compressor motor voltage V_{CM}) and one output (λ_{O2}). For I_{fc} the following interval has been chosen:

$I_{fcstart}$=60 A

I_{fcstop}=300 A

And the corresponding inputs V_{CM} have been given the values of $V_{CMstart}$=100 V and V_{CMstop}=250 V corresponding both to the output value λ_{O2}=2. By dividing the input current and voltage intervals, so as to obtain 75 current values and 100 voltage values, 7000 points have been obtained, for each of which the corresponding value of λ_{O2} has been computed.

Figure 5.18 shows the 3D characteristic of the λ_{O2} vs. the I_{fc} stack current and the compressor motor voltage, V_{CM}, as well as the neurons generated by the PLN (Progressive Learning Network) in its learning phase. Remark that the values are given in a normalized way: both λ_{O2} and V_{CM} are the standard normalized variables (.i.e. with zero mean and variance equal to 1), while the I_{fc} has been linearly transformed into the interval [1, 75]. It can be observed that the neurons cover the 3D surface entirely, thus confirming the correct learning of the network.

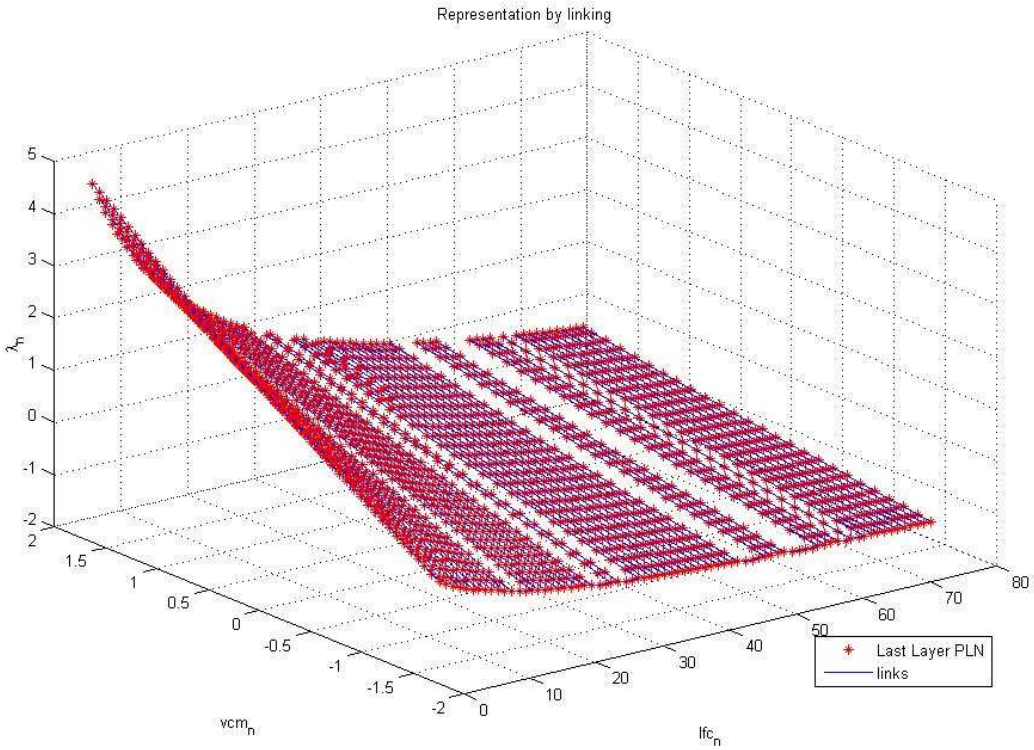

Fig. 5.18. GMR Polarization curve obtained by the GMR in 3D.

5.3.2 Results

A. Simulation

The tests presented in this section have been performed on the Matlab-Simulink® environment. A series of load currents steps ranging from 100 A to 300 A has been given. The input steps are not of the same amplitude (Figure 5.19). Figure 5.20 shows the corresponding inputs given by the PI and the PI+GMR control schemes, that is the applied compressor motor voltages. Figure 5.21 and 5.22 are the zooming of Figure 5.20 at t=25s and t=85s. Figure 5.23, 5.24, 5.25 show the regulation of the λ_{O_2} for the PI and PI+GMR control schemes. It is apparent from this figures that, when a positive load current step is demanded, the oxygen excess ratio λ_{O_2} drops because of the depletion of oxygen, which leads up to a reduction of the stack voltage (Figure 5.26).

Figure 5.21 and Figure 5.24 describe at t=25s how the PI control scheme reacts to the load current step by boosting the compressor motor voltage as well as the resulting regulation action on λ_{O_2}. Since the current step is small, and therefore the corresponding value of the GMR is not present in the training set, there is little difference between the linearised model and the nonlinear model of the FCS, and this causes the PI control scheme to act in the same way as the PI+GMR control scheme, so no difference appear. This is not however the case when a larger load current step is applied leading the GMR to react. In this case the action of the neural controller compensates for the nonlinearities and the contribution of the PI should be ideally close to zero, thus leading up to a quicker response. This is shown, for example, at t= 85 s when a strong step current is applied. Figure 5.22 shows the strong boost in the compressor motor voltage caused by the action of the neural controller with a resulting overshoot to react to the strong depletion of oxygen brought about by the load current step. The consequent regulation action results in a faster recovery time of the PI+GMR control scheme than the PI one. The PI+GMR control scheme quickly provides more oxygen to the membrane as a result of the rapid increase of the compressor air mass flow. It is noteworthy in Figure 5.23 and in its zooming in Figure 5.25, that the λ_{O_2} waveform has a beneficial overshoot, which permits the membrane to be quickly oxygenated, unlike the PI scheme, which finds it difficult to reject the disturbance, with a resulting high steady-state time and consequent detrimental effect on the FC stack because of oxygen starvation. The main reason of slow response is that PI needs to detect the oxygen drop from the output which lags the disturbance due to the plant dynamics.

This decrease of the time response of the system is also apparent in the reduction of the transient effect in the stack voltage in Figure 5.26, which is reflected in the stack power diagram (Figure 5.27).

A fast regulation of the stack voltage is an indirect measure of a good level of oxygen concentration in the fuel cell cathode.

The increase of the air mass flow is also reflected in an increase of the oxygen partial pressure in the supply manifold, as shown in Figure 5.28, where the PI+GMR scheme makes the increase in pressure be faster than the one obtained with the PI-scheme.

Figure 5.29 shows that for both schemes the compressor transient responses on the compressor map lie between the choke and the surge boundaries, which is the region of safe operation.

In the end, Figure 5.30 shows the output of the PI controller in the PI scheme and the outputs of the PI controller and the GMR controller in the PI+GMR control scheme, along with their sum, at t=85s. It can be seen that the PI controller in the PI-scheme acts for a longer time than the PI controller in the PI+GMR scheme This latter goes rapidly close to zero, helped in this by the control action of the GMR controller.

B. Experiments

Experimental results have been performed on the emulator prototype above described (Figure 4.1). The full nonlinear fuel cell system model, describing the voltage versus current relationship, its dynamics and the auxiliaries behaviour, the inner voltage loop of the DC-DC converter control (Figure 4.22) and the fuel cell λ_{O_2} control system, both in its PI and PI+GMR versions (Figures 5.17 a and 5.17 b), have been implemented on the DSP board.

Thus a hardware-in-the-loop FCS system has been implemented, where the hardware part is the buck-converter emulating the FC stack, and the software part is the whole FCS system and its control.

With this regard, different sampling frequencies for the different part of the system have been adopted to exploit at the best the computational power of the DSP board .

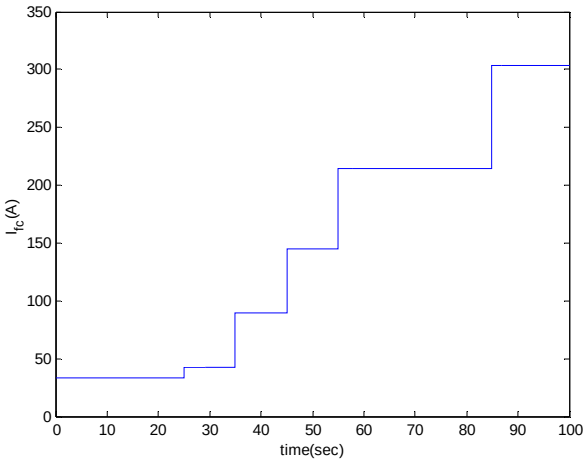

Fig. 5.19. Series of stack current steps.

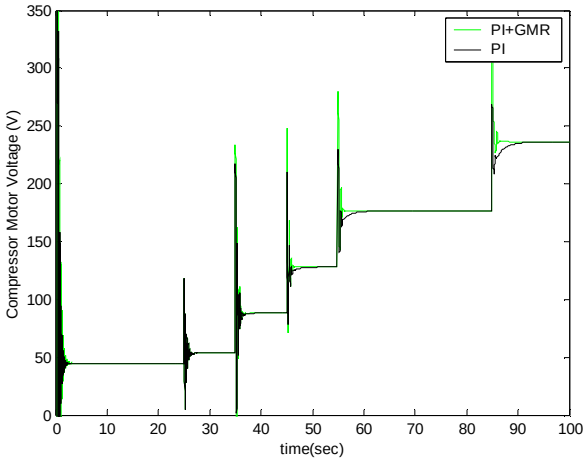

Fig. 5.20. Compressor motor voltages for the PI and PI+GMR control schemes.

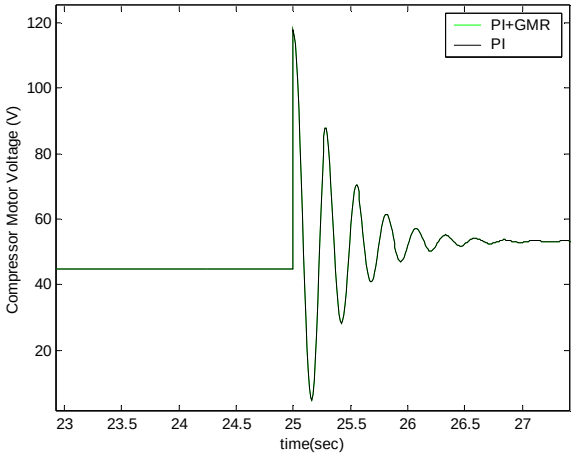

Fig.5.21. Zoom of Fig. 5.20 at t=25 seconds.

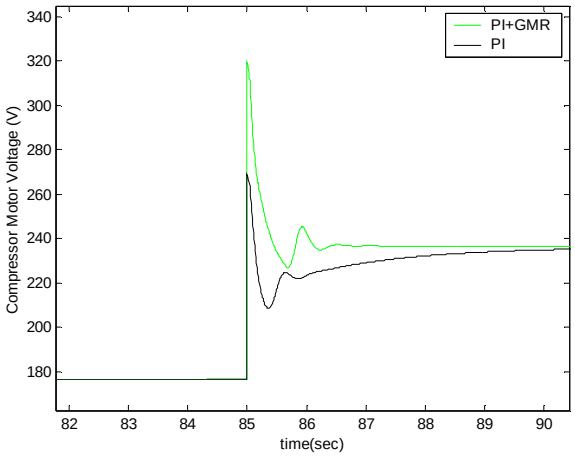

Fig. 5.22. Zoom of Fig. 5.20 at t=85 seconds.

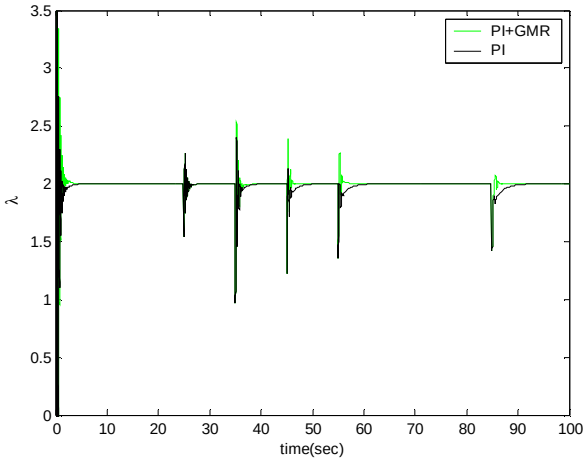

Fig. 5.23. Regulation of the λ_{O_2} for the PI and PI+GMR control schemes.

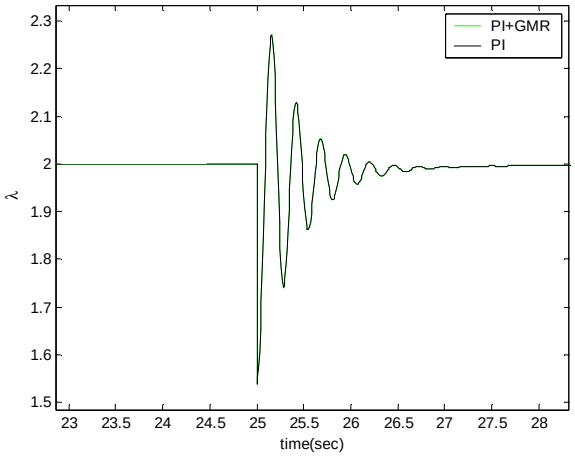

Fig. 5.24. Zoom of Fig. 5.23 at t=25 seconds.

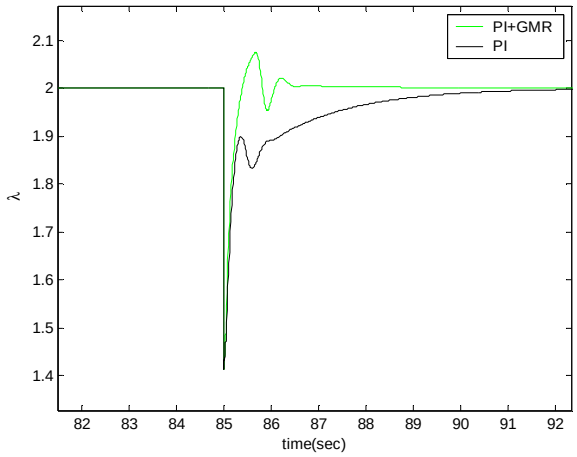

Fig. 5.25. Zoom of Fig. 5.23 at t=85 seconds.

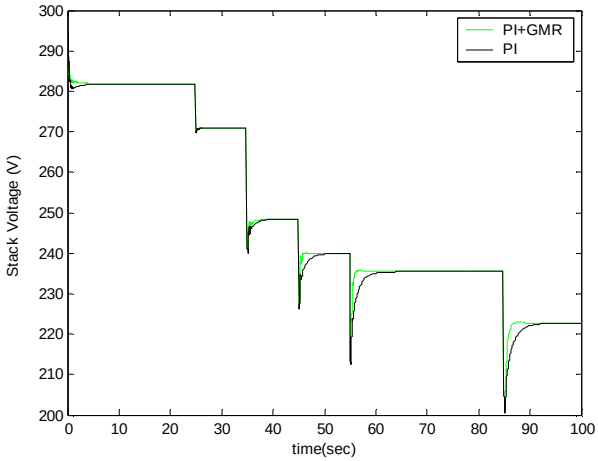

Fig. 5.26. Stack voltages for the PI and PI+GMR control schemes.

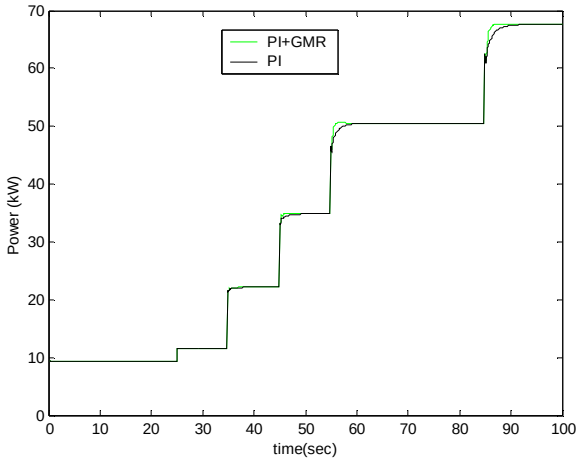

Fig. 5.27. Stack power for the PI and PI+GMR control schemes.

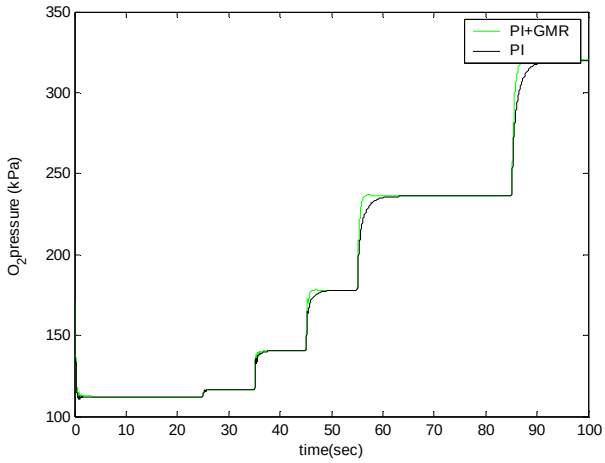

Fig. 5.28. Oxygen partial pressure for the PI and PI+GMR control schemes.

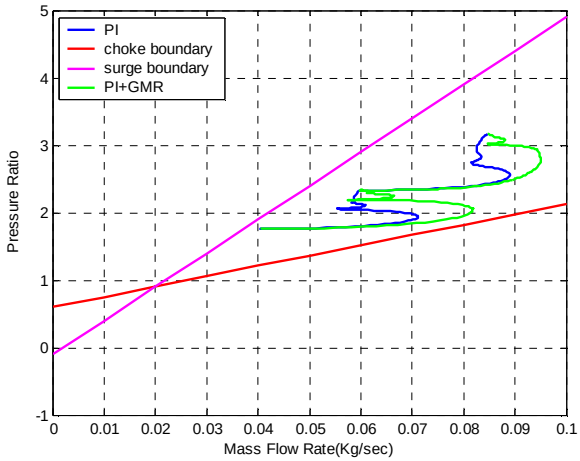

Fig. 5.29. Compressor transient response on compressor map for the PI and PI+GMR control schemes.

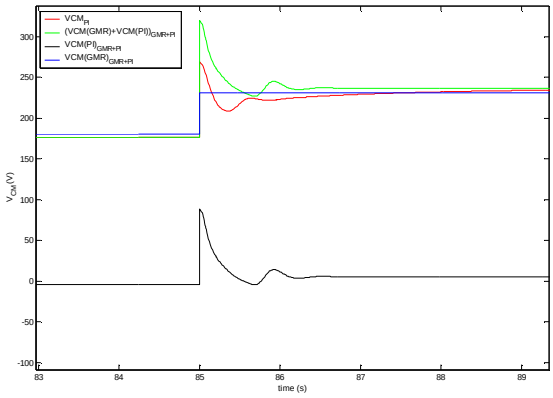

Fig. 5.30. Input control actions for the two control schemes.

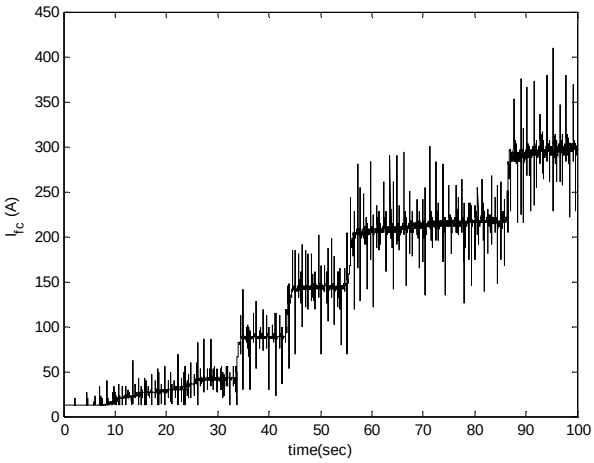

Fig. 5.31. Series of stack current steps (experiment).

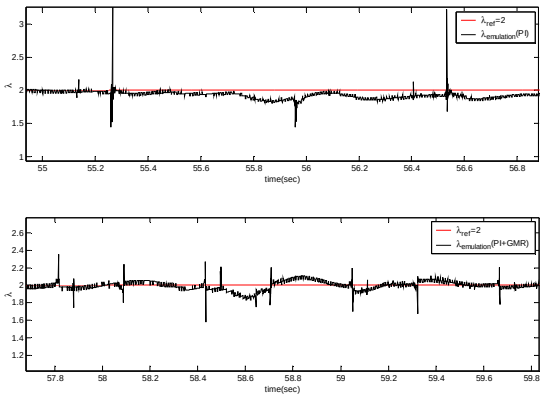

Fig. 5.32. Regulation of the λ_{O_2} for the PI and PI+GMR control schemes at 58 s (experiment).

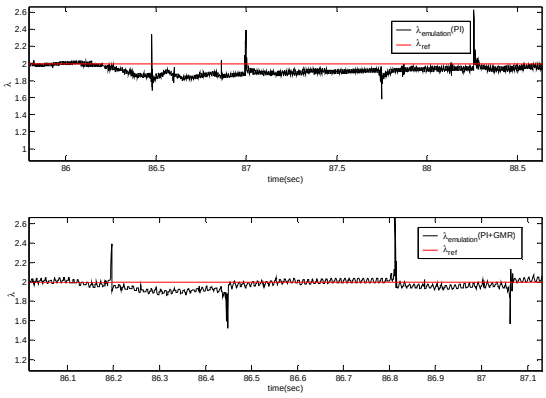

Fig. 5.33. Regulation of the λ_{O_2} for the PI and PI+GMR control schemes at 87 s (experiment).

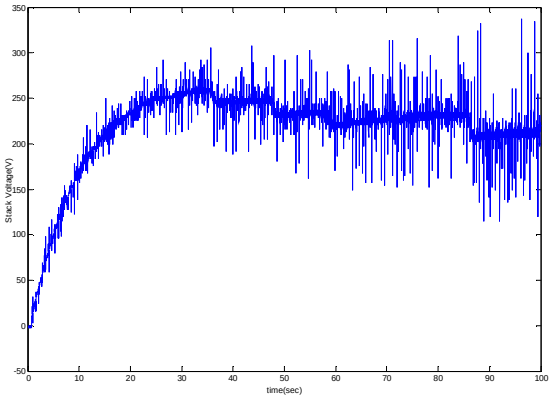

Fig.5.34. Stack voltages for the PI+GMR control scheme (experiment).

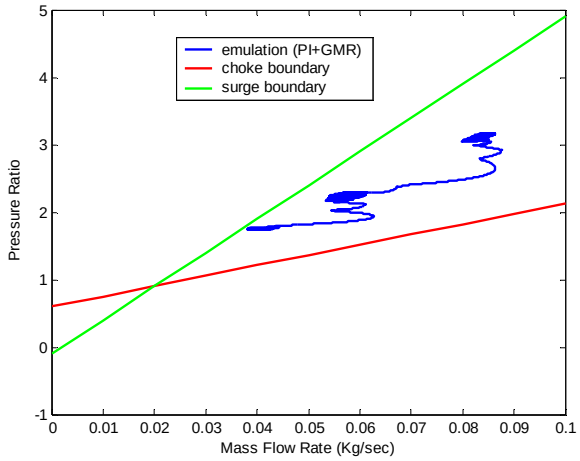

Fig. 5.35. Compressor transient response on compressor map for PI+GMR control scheme (experiment).

In particular, the DC-DC converter control, the FC system as well as the PI and PI+GMR controls run all at 10 kHz. A suitable virtual measurement system has been devise to monitor all the interesting variables of the system and to give the references to the controlled variables (λ_{O_2} in this case). Similar tests to those shown in simulation have been performed. Figure 5.31 shows a set of load current steps, obtained experimentally changing a resistive load. Figures 5.32 and 5.33 show the λ_{O_2} , respectively reference and actual, obtained with the PI and PI+GMR control schemes in two particular instants of this cycle. In both case the PI+GMR scheme outperforms the PI scheme, permitting a faster regulation of λ_{O_2} against the load current

variations. Also in this case, the PI+GMR control scheme makes than the compressor supply quickly more oxygen to the membrane as a result of the increase of the compressor air mass flow. Figure 5.34 shows the corresponding stack voltage waveform, which has a step-like waveform with decreasing values of the voltage at increasing load currents, as expected. Finally, Figure 5.35 shows that for the PI+GMR scheme the compressor transient responses on the compressor map lie between the choke and the surge boundaries, which is the region of safe operation. Experimental results thus confirm the simulation tests.

5.3.3 Conclusions

This chapter deals with the air management subsystem in fuel cell systems (FCS). It proposes to use a feedforward control action for improving a classical PI control of the FCS for preventing oxygen starvation. The application of a recent neural network, the GMR (Generalized Mapping Regressor Mapping) has been proposed to implement the feedforward controller, which is obtained with the inversion of the FCS model. This control system has been implemented both in numerical simulation and experimentally adopting a properly devised FCS in which the FC stack is realized by a buck-converter (emulator), that is by using a hardware-in-the-loop experimental rig. This control system has been implemented both in numerical simulation and experimentally adopting a properly devised FC emulator. Results have shown that the PI+GMR control system outperforms the classic PI regulator. The PI+GMR controller reacts faster giving strong boost in the compressor motor voltage, because of the action of the neural controller, being thus able to react to the strong depletion of oxygen brought about by the load current steps. The consequent regulation action results in a faster recovery time of the PI+GMR control scheme than the PI one. The PI+GMR control scheme makes than the compressor supply quickly more oxygen to the membrane as a result of the increase of the compressor air mass flow with a resulting lower tracking times and consequent reduced detrimental effects on the FC stack because of oxygen starvation.

The requirement of enforcing the constraints is one of the reasons why a simple PI cannot be used “tout court” in a real FCS, and the utility of an emulator appears evident. A PI should be designed in a “trial-and-error’ fashion (if no “if-then” are used, which would make the control too computationally cumbersome) and this could have irreversible effects on the FC or on the FCS, which is not the case with an emulator. In any case the performance of the PI, in terms especially of recovery time of the oxygen excess ratio, are suboptimal and even detrimental as for the starvation of the membrane. The use of the emulator not only has facilitated the implementation of a PI controller, but has also been suitable for using several other control laws, without any fear of damaging the real FCS.

Conclusions

This thesis has produced a prototype of an emulator for PEM-FC realised by constructing a suitable buck-converter. This work has been developed in the framework of the on-going activity research between the the FClab-SET-UTBM and the ISSIA-CNR about modelling and controlling Fuel Cell Systems for developing a complete PEM-FCS emulator, as explained in the introduction. With this regard the implementation of the stack-voltage emulator represents the first realization of this project. Moreover it gives the immediate possibility of developing an advanced experimental rig both for studying several control strategies and for analysing the connection with the output PCS.

Chapter 2 stresses the importance of developing an emulator and justifies its use by giving an insight into the state of the art. At present most emulators do not take into consideration the variations of the V-I characteristic as a result of the hydrogen or oxygen partial pressures or temperature, which makes their use questionable. With this regard chapter 3 presents a model not only of the FC stack but also of all the sub-systems of the FCS. These models have been then implemented on a dSPACE platform capable of managing also the emulator of the FC system. In this case a Hardware-in-the-Loop configuration has been constructed for giving realistic responses of the entire FCS. Particular attention has been paid on the modelling of the manifold (supply and return), which are a key element for simulating the dynamical response of the FCS in case of load current variations.

Chapter 4 deals with the problem of designing and implementing an emulator which responds quickly to any variation of the reference voltage, which has been solved by constructing a high-bandwidth buck-converter, controlled using a state-variable-feedback .A comparison with a traditional PI voltage control is shown and the advantages in terms of decreased rise time and settling time are shown. This chapter gives step-by-step guidelines for the construction of the emulator, from the general design down to the choice of the components and tuning of the controllers.

Chapter 5 deals with the control of the FCS with the emulator. In particular one case study has been treated, the management of the air-system. With this regard some assumptions have been made, i.e. a PI controller capable of keeping the pressure difference between anode and cathode as little as possible, perfect humidification of the membrane, constant temperature and quick supply of pure hydrogen. The control objective has been described, particularly the excess oxygen ratio has been considered for preventing oxygen starvation of the membrane.

The first type of control has been a classical PI, after proper linearization of the FC system around an operating point. Then different load steps have been given to test the response of the FCS with the emulator. Particular attention must be paid to the fact that any constraints of the FCS be enforced. For the air management system the surge and choke limits of the centrifugal compressor should be carefully enforced, or else the compressor breaks down. This requirement is one of the reasons why a simple PI

cannot be used “tout court” in a real FCS, and the utility of an emulator appears evident. A PI should be designed in a “trial-and-error’ fashion (if no “if-then” are used, which would make the control too computationally cumbersome) and this could have irreversible effects on the FC or on the FCS, which is not the case with an emulator. In any case the performance of the PI, in terms especially of the recovery time of the oxygen excess ratio, are suboptimal and even detrimental as for the starvation of the membrane.

In order to improve the recovery time of the oxygen excess ratio a static feed-forward controller has been added. This static controller implements the nonlinear relationship between the input motor voltage and the load current perturbation and the desired output oxygen excess ratio. The computation of this feedforward controller is not a simple task since it demands that the above-mentioned constraints be enforced. The strategy adopted has been then to identify the forward model, satisfying the constraints, of the FCS air-management system by using a neural network, and then invert it. However inversion is not a problem easy to tackle in nonlinear systems, since multi-valued forward functions can occur. Therefore a novel neural network has been used, the GMR, which is the only neural network capable of inverting a relationship accounting for any different branch and of giving multi-values for an input. The thesis presents in the appendix A2 how the recall phase of the GMR should be used for being suitably applied to the FCS systems and then the last part of chapter 5 applies it to enhance the performance of the previous PI. A strong improvement in terms of rise-time and settling time is shown in the results.

At present other control strategies are being developed by the author of this thesis. In particular in simulation the model predictive control (MPC) has already been developed and tested on the FCS described in this thesis and it gives good results for improving the dynamic performance of the excess oxygen ratio [86]; its experimentation on the emulator is in progress at present. Other works in progress are about the optimal computation of the excess oxygen ratio by connecting he output of the emulator to a real DC-DC converter whose output is connected with a DC-link supplying an electrical motor emulating itself the motor of a compressor, taking into consideration the scaling necessary for high-speed operation.

This work as well its follow-up, much of which in progress, lie in the framework of the research group of the UTBM-GESC-SET and the ISSIA-CNR, whose target is to manage to realise an emulator for a complete FCS, both for the electrical part, which is the topic of this thesis, and for the thermodynamical and fluodynamical parts. As a matter of fact the UTBM-GESC-SET focuses its research on transportation problems trying to envisage possible solutions. Therefore electrical vehicles, hybrid experimental rigs and FCS are placed in a same area inside the laboratory. The research activity is moreover connected with the French initiative “Vehicles of the Future”, in the framework of the “Competitive Pole”., whose goal is to propose high-technological solutions for novel types of vehicles. On the other hand the ISSIA-CNR and the UTBM-GESC-SET are involved in the research in renewable energy sources and energy management of multi-sources for Distributed Generation, with particular attention to the power conditioning and quality. With this respect the work of this thesis develops the possibility of testing the interface of a FCS with a real multi-source energy generation system, but has also given the possibility of emulating a PV (photo-voltaic) array

connected to a real load, topic which has been the object of one publication [87, published and submitted to journal for 1st revision].

APPENDIX A1

BRIEF DESCRIPTION OF THE GMR NEURAL NETWORK

The GMR (Generalized Mapping Regressor) is mainly an incremental self-organizing neural network and belongs to the family of self-supervised models. Its architecture is sketched in Figure A1.1. Its algorithm transforms the mapping problem **f: x** $\rightarrow$ **y** into a pattern recognition problem in the augmented space *Z* represented by vectors $\mathbf{z} = [\mathbf{x}^T\ \mathbf{y}^T]^T$, where T is the transpose operator, which are the inputs of the GMR. In this space, the mapping branches become clusters which have to be identified. The weights of the first layer are continuous and represent the Z space, while the others are discrete (chains between neurons) and represent the mapping branches. The first layer weights are computed (**training phase**) by a multi-resolution quantization phase, the second layer weights are computed (**linking phase**) by a PCA technique, unlike the original algorithm [78] which used geometrical criteria.

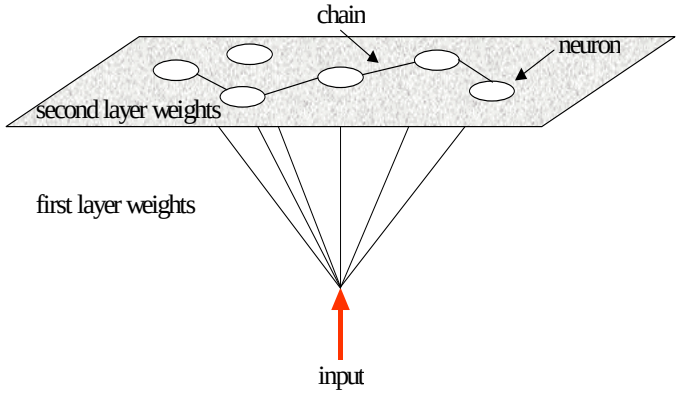

Fig. A1.1. Sketch of the THE GMR architecture.

This latest linking is *directional*, i.e. takes into account the shape of the branch. The productive pase, called **"the recall phase**" uses several interpolation techniques to give the output.

A. Training phase (multi-resolution vector quantization)

In respect of the GMR, learning means "vector quantization (VQ) of the Z space". To this aim, a lot of VQ techniques can be used. In this work, a simple incremental approach, called EXIN Segmentation Neural Network (EXIN SNN), has been chosen because the Z space is assumed low dimensional. The EXIN SNN [79] algorithm works as follows. At each epoch all data are fed to the network one by one. At the presentation of one datum, only two cases are possible: creation of a new neuron (i.e. a new weight vector attached to it) or weight adaptation. In the beginning the network contains no neurons. At the presentation of each datum, **x**(t), it is checked (novelty test) if there are weight vectors into a neighbourhood of the data, defined by the resolution scalar threshold ρ (also called vigilance threshold [80]).

If not, a new neuron is created, whose weight is given by the datum. If at least one neuron is found, the closest neuron adapts its weight **w**(t) according to :

$$\mathbf{w}(t+1) = \mathbf{w}(t) + \frac{1}{N+1}\left(\mathbf{x}(t) - \mathbf{w}(t)\right) \qquad \text{A1.1}$$

where *N* represents the number of changes of the weight vector until *t*-th time instant. This formula represents the Maximum Likelihood (ML) stochastic estimate of the mean of the normal distribution of the data represented by the neuron **w**(t), i.e. the data whose closest neuron is **w**(t) (these data represent the *domain* of the neuron). This corresponds to the adaptive *k*-means rule [81] As a consequence, the weight vector tends to the average of the data it represents, which implies the quantization of the space. It is easy to verify that N corresponds exactly to the conscience variable introduced by DeSieno [82].

The choice of ρ is very important: it can be constant or can change at each epoch; if it decreases, the resolution of the quantization increases and so does the number of neurons. It has been found out that the best solution, in terms of both computational cost and accuracy, is given by the following multi-resolution approach consisting of 2 phases:

l. *Coarse quantization*. The first epochs use a high value for ρ, say ρ_1. In general, the first epoch defines the number of neurons needed for VQ and the others adapt their weights in order to better approximate the input space. The neurons created in this phase are called *"object neurons"*, because they identify the basic components of the clusters. During this phase, data are labelled by their closest neuron and determine its domain (object domain).

2. *Fine quantization (divide-and-conquer)*. Each domain is considered as the training set (TS) for a subsequent (*secondary*) EXIN SNN. As many EXIN SNN's as the number of object domains are used in parallel to quantize each object domain. These intradomain learning technique needs a threshold ρ lower than ρ_1, say ρ_2 whose value is determined by the required resolution. Eventually, the neural network is composed of the neurons created by the secondary learning phases (*pool of neurons*), labelled as belonging to an object by the corresponding object neuron which however does not enter the pool and is only used for labelling purposes. These labelled neurons represent a discrete Voronoi tessellation of the input Z space.

Each phase can require either an a priori defined number of epochs or a stop criterion, which monitors the weight increments and stops if they fall under a certain threshold. However in general a small number of fixed epochs yields the best results. In this case, in the last epoch of fine quantization, each neuron also records the value of the distance from the farthest data in the domain. This is called the radius *r* of the domain. Obviously, the domains are mutually exclusive (no overlapping).

B. Linking and Merging

Linking and merging enable the cluster to be reconstructed under the assumption that the clusters represent the mapping branches. The principle is the *branch tracking*, that is the shape of the cluster is tracked by using links (it looks like exploiting the *inertia* of the clusters). Two approaches are therefore possible, the LD method and the PCA method, each with its pros and cons. After previous learning phase, the GMR architecture is composed of a pool of p neurons. To each neuron *i* ($i = 1, \ldots, p$) are associated a weight vector $\mathbf{w}_i$, the domain radius ρ_i and the label of the object to which it belongs.

1) LD method

The Linking Direction (LD) method is based on the requirement that a neuron should be connected to another neuron in the weight space, if it has the closest orientation to the line connecting the winning neuron (weight) with the input data. Hence, this linking carries a directional (orientation) information driven by the input data. The linking phase requires a complete presentation (production phase) of the TS (equivalent to one epoch) to the network. For each input $\mathbf{z}_i$ (one iteration), the following operations are performed, mainly to determine a neuron to be linked to the winning neuron (see Figure A1.2):

1. Compute all the Euclidean distances between the neuron weights and the input $\mathbf{z}_i$. Classify them according to the increasing distance and label the neurons according to their position (1 for the nearest). Hence, $\mathbf{w}_1$ represents the weight vector of the nearest neuron. Define $\mathbf{d}_j = \mathbf{s}_j - \mathbf{w}_1$ for $j = 1, \ldots, k$ where $\mathbf{s}_j = \mathbf{w}_j$ for $j > 1$, $\mathbf{s}_1 = \mathbf{z}_i$ (so $\mathbf{d}_1 = \mathbf{z}_1 - \mathbf{w}_1$) and k is given by the greatest index such that:

$$\left\| \mathbf{z}_i - \mathbf{w}_k \right\|_2 \leq \delta \left\| \mathbf{d}_1 \right\|_2 \qquad \text{A1.2}$$

   Being δ a predefined constant greater than 1 (δ -test). Hence, the $\mathbf{d}_j$'s represent, in the weight space, with regard to the winning neuron, the position vectors of the input and of the nonwinning neurons situated inside a hypersphere centered in the input $\mathbf{z}_i$ and of radius proportional to the distance from the input to the winning neuron. The δ-test (A1.2) eliminates neurons which are too far from the winning neuron (in the weight space) and are not therefore allowed to be linked to the winning neuron. As an alternative, it is possible to choose in advance the number k of candidates (k-test). Obviously, both parameters δ and k depend on the final resolution ρ of the fine quantization.

2. Compute, for $j = 2, \ldots, k$ (i.e. for all the neurons inside the hypersphere of radius $\delta \left\| \mathbf{d}_1 \right\|_2$ or for the k candidates the cosine of the angle of $\mathbf{d}_j$ with respect to $\mathbf{d}_1$)

$$\mathrm{p}_j = \frac{\mathbf{d}_1 \mathbf{d}_j}{\left\| \mathbf{d}_1 \right\|_2 \left\| \mathbf{d}_j \right\|_2} \qquad \text{A1.3}$$

   and the integer h such that:

$$\mathrm{p}_h = \begin{cases} \max_j \mathrm{p}_j & \text{if } \exists \mathrm{p}_j > 0 \text{ for at least one value of } j \\ \max_j \left| \mathrm{p}_j \right| & \text{otherwise} \end{cases} \qquad \text{A1.4}$$

   The neuron whose weight has index h, viz. $\mathbf{w}_h$, is connected to the winning neuron, if it is not already connected (in this case no linking is made). Eq. (A.4) means that the selected unit is the neuron j whose relative (to the winning neuron) weight vector, viz. $\mathbf{d}_j$, is the nearest to the straight line parallel to $\mathbf{d}_1$ (*linking direction*), among all neurons whose relative weights are situated in the half space bordered by the hyperplane containing the winning neuron weight vector and normal to the linking direction. If all neurons have relative weights outside this half space, the selected neuron must have the nearest relative weight among all neurons. In a nutshell, the criterion of choice for the neuron to be linked does not take into consideration the distance from the winning neuron or the input, but the angular distance from the linking direction, which *drives* the selection. This choice is justified by the fact that linking has a geometrical meaning which is lost if an Euclidean distance,

which ignores the orientation information, is used as a criterion. Only one connection is made at each input presentation (the winning neuron 1 is linked to the neuron *h*).

3. If $\mathbf{d}_1 = 0$ (i.e. winning neuron whose weight coincides with the input data), then neuron 1 is connected to neuron 2. This may happen in regions of the Z space which are under-represented by data in the TS.
4. (Merging) If neurons belonging to different objects are linked, the two objects are merged into a unique object and the associated neurons are relabelled.

Remark that only one parameter is needed (either δ or k) for this method.

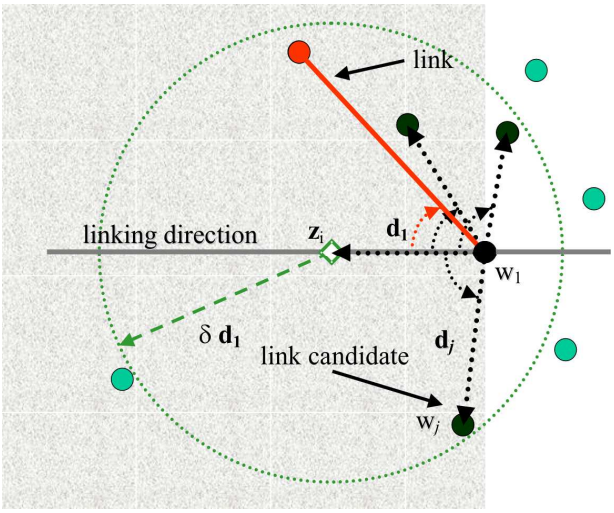

Fig. A1.2. Linking direction method.

2) PCA method

The Principal Component Analysis (PCA) method exploits the shape of the neuron domain for reconstructing the cluster. To this aim, the domain is represented by the unit vector (centred at the neuron weight) in the direction of the principal component of the domain data. This vector is here called Principal Direction (PD). Obviously, this approach is limited to the extent by which PD represents the shape of the domain and the accuracy is proportional to the ratio between the two greatest eigenvalues of the autocorrelation matrix of the domain data [79]. Figure A1.3a shows a 2D example of domain together with its radius and PD. Both direct and iterative techniques can be used for the PD setting. Here is proposed an iterative algorithm called PCA EXIN [2], which computes the PCA p of the domain data x's according to:

$$\mathbf{p}(t+1) = \mathbf{p}(t) + \Delta\mathbf{p}(t) = \mathbf{p}(t) + \frac{\alpha(t)\,\mathbf{p}^T(t)\,\mathbf{x}(t)}{\|\mathbf{p}(t)\|_2^2}\left[\mathbf{x}(t) - \frac{\alpha(t)\,\mathbf{p}^T(t)\,\mathbf{x}(t)}{\|\mathbf{p}(t)\|_2^2}\mathbf{p}(t)\right] \qquad \text{A1.5}$$

where x(t) are the domain data which are input in random order and α(t) is the learning rate, which has to satisfy some conditions: for example, the sequence α(t) = const t-γ with $0 < \gamma \leq 1$ can be used. Then the PD is given by $\mathbf{p}(t)/\|\mathbf{p}(t)\|_2$. There are simpler PCA learning laws (for a general analysis of PCA algorithms see [83, p. 229]), but the advantage of PCA EXIN derives from the fact that the minor component (MC) of the domain, that is the direction of noise and its extension, can be easily and very accurately computed by simply

reversing the sign of the increment $\Delta p(t)$ in eq. (A1.5): this is the MCA EXIN [7] rule and can be used, together with PD, if the TS is noisy: in this sense it can both reduce noise and help the neuron linking. If the domain of a neuron contains only two or fewer data, the neuron is tagged. This approach is reminiscent of LPCA [85], but differs from it because the partitioning of data is performed by a neural network and no global criteria are considered.

Linking is achieved by one complete presentation of the TS. For each data, the weights are sorted according to the Euclidean distance from the data (see Figure A1.3 b) and the winning (nearest) neuron is determined. This it is then linked to another neuron chosen in a subset of the neuron pool (candidate neurons). Two criteria can be implemented: the first (δ-test) considers only the neurons included in a hypersphere centred in the data and of radius a multiple (a priori defined by the scalar δ) of the distance between the input and the winner weight vector; the second (k-test) considers only the k nearest neighbours of the input. Then, for each candidate, the absolute value of the scalar product between its PD and the winner's PD is evaluated: the winner is linked to the candidate yielding the maximum scalar product (i.e., whose PD is closest in direction to the winner's PD). This approach is justified by the fact that clusters with similar shapes have to be connected. However, this linking approach is not flexible w.r.t. noise. Indeed, if two neurons were linked because they are close and in the same branch, but their PD's slightly differed because of noise, it would be possible that elsewhere another neuron has the same PD as the winning neuron and so it would be incorrectly linked. In this case it is important to define a threshold λ which has to be a fraction of the final resolution ρ in order to define the equivalent maxima (see Figure A1.3 b), i.e. neurons whose PD's differ from the winner PD only of $\pm \lambda$. Then the following geometrical criterion is used in order to decide the equivalent maximum which has to be linked to the winning neuron. For each equivalent maximum, compute the absolute scalar product between the winner PD's unit vector and the directed vector from the winner weight to the candidate weight. The neuron yielding the maximum of this quantity is linked (in Figure A1.3 b the winner is linked to the neuron #7). This criterion is justified by the fact that linking results in a branch tracking and this branch is in general smooth, so it has to be tracked in a small spatial window, as required by this geometrical approach. If the winning neuron has a tag (instead of the PC direction), the LD approach is used instead (with the same value of δ or k). After this linking phase, objects are merged in the same way as in the LD approach.

Remark that, for this method only 3 parameters are necessary for linking (either δ or k), one for equivalent maxima in case of high noise (λ) and one for the PD computation if an iterative algorithm is used (the learning rate α).

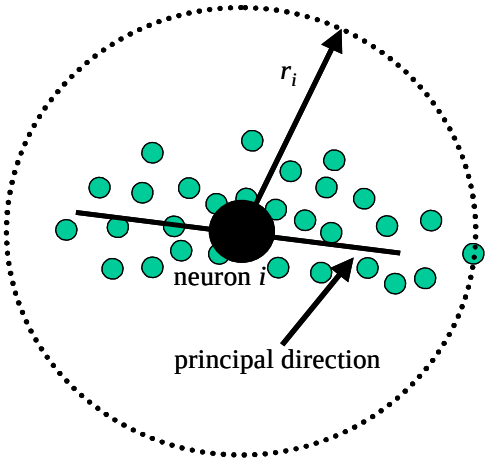

Fig. A1.3a. Neuron domain parameters.

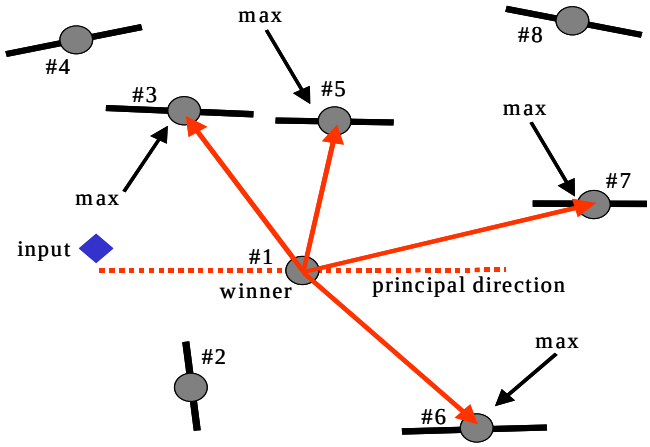

Fig. A1.3 b. Linking in presence of equivalent maxima.

C. Recall phase

In the recall phase, the input (from now on called x) can be any collection of components of z and the input space is defined as X. Hence the output y is the vector composed of the other elements of z and the output space is defined as Y. All weight vectors are also projected onto X. This projection is easily accomplished by using only the elements of the weight vector whose position indices correspond to the position indices of the input elements in the augmented vector Z. For example, if the first three elements of the vector z are taken as input, the projected weight vectors are composed of only the first three elements of the weight vectors. Unlike the original method shown in [84], in X space each neuron is replaced with a Gaussian which represents the neuron domain. Its parameters (mean, covariance) are given by the ML (maximum Likelihood) estimates (the sample mean and sample unbiased covariance). When an input vector x is fed to the GMR, the Gaussians are sorted out in decreasing order according to their value in x (the value of the Gaussian in x is here considered as a metric). Following this order, each Gaussian is labelled as level one if the hypersphere, centred in the mean and whose radius is the domain radius , contains the input (level one

test) and level two if it is not level one, but is directly linked to a level one Gaussian. This labelling is controlled by the following stop criterion: if the Gaussian is neither classified as level one nor as level two, then the labelling is stopped. All level one Gaussians and level two neurons which are connected each other (even not directly) are considered as belonging to the same mapping branch. Then, for each Gaussian k the complement of the weight of the corresponding domain is defined as $\mathbf{t}_k$. The outputs are associated to the level one Gaussians. For each of these Gaussians, say the p_i, the interpolation phase considers the two Gaussians (either level one or level two) directly linked to it. Call them p_{i-1} and p_{i+1}. The associated output y_i is given by the following kernel interpolation formula:

$$\mathbf{y}_i = \frac{\mathbf{t}_{i-1} p_{i-1}(x) + \mathbf{t}_i p_i(x) + \mathbf{t}_{i+1} p_{i+1}(x)}{p_{i-1}(x) + p_i(x) + p_{i+1}(x)} \qquad \text{A1.6}$$

If one of the two Gaussians does not exist or is neither level one nor level two, its value is set to zero. If the i-th Gaussian has no links, the interpolation is given by:

$$\mathbf{y}_i = \mathbf{t}_i p_i(x) \qquad \text{A1.7}$$

No interpolation is required if the value of the i-th Gaussian in x is nearly one (w.r.t. the training resolution). In the end, as a consequence of the interpolation, each level one Gaussian yields an output y. Two different outputs belong to the same branch if they correspond to Gaussians belonging to the same branch. All level one Gaussians and the branches or portions of branches containing only level one Gaussians constitute a discretization of the equilevel hypersurfaces. It is possible to have disjoint equilevel hypersurfaces (branches) for the same object, e.g. the equilevel curves of a saddle in the 3D space for certain section orientations.

APPENDIX A2

Implementation of GMR-Recall in Matlab/Simulink Environment for the PEM-FCS

As explained in chapter 5, the training set for the GMR has been created by using the nonlinear model with two inputs (the stack current I_{fc} and the compressor motor voltage V_{CM}) and one output (λ_{O2}). For I_{fc} the following interval has been chosen:

$I_{fcstart}$=60 A
I_{fcstop}=300 A

And the corresponding inputs V_{CM} have been given the values of $V_{CMstart}$=100 V and V_{CMstop}=250 V corresponding both to the output value λ_{O2}=2 . By dividing the input current and voltage intervals, so as to obtain 75 current values and 100 voltage values, 7000 points have been obtained, for each of which the corresponding value of λ_{O2} has been computed.

Fig. A2.1 shows the 3D characteristic of the λ_{O2} vs. the I_{fc} stack current and the compressor motor voltage, V_{CM}, as well as the neurons generated by the PLN (Progressive Learning Network) in its learning phase. Remark that the values are given in a normalized way: both λ_{O2} and V_{CM} are the standard normalized variables (.i.e. with zero mean and variance equal to 1), while the I_{fc} has been linearly transformed into the interval [1, 75].

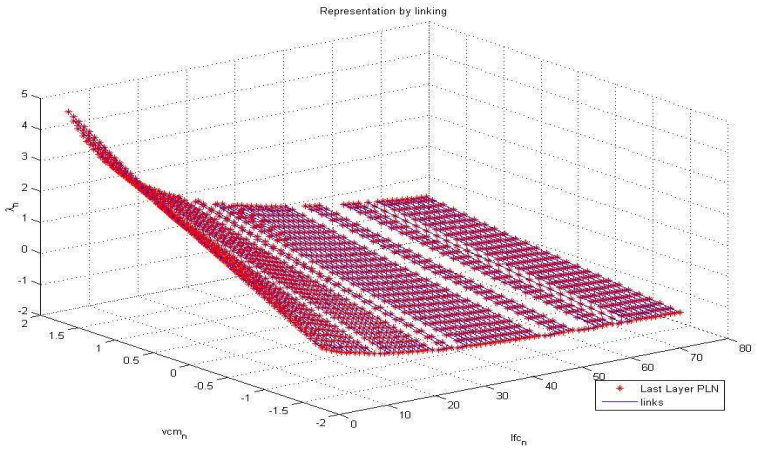

Fig. A2.1. GMR Polarization curve obtained by the GMR in 3D.

To allow the GMR identify the different curves λ_{O_2} vs V_{cm} ($I_{fc} = const$), *the Coarse quantization,* implemented in the file EXIN SNN (see Appendix A1), has been modified. By this change, the number of object neurons created during the first epoch is equal to the number of current values I_{fc} used in the training set (TS). Therefore at the end of the first learning phase, each curve of TS λ_{O_2} vs V_{cm} has been represented by a different object domain (OD). The *Fine quantization* has not been changed and at the end of this phase, GMR has identified a pool of 50 neurons for each domain. Therefore, the result of the training phase is a structure of objects 75 X 50x 50, where the first component represents the current I_{fc}, the second component the compressor voltage V_{cm} and the third component the oxygen excess ratio λ_{O_2}. Although the model of the PEM-FC system (**f: x → y, x=[** $I_{fc} V_{cm}$ **]** and **y=** λ_{O_2}) has been identified, the implementation of the PEM-FC control scheme discussed in chapter 5 requires the use of the inverse model of the system. GMR allows the model to be inverted, because it works in the augmented space Z represented by vectors **z = [x^T y^T]^T**. Therefore, in the inverse model the inputs are the oxygen excess ratio λ_{O_2} and the current I_{fc} and the output is the compressor voltage V_{cm}. The Recall phase must give the value of V_{cm} that corresponds to the two inputs I_{fc} and λ_{O_2}.

A. Recall Algorithm

Because the curves λ_{O_2} vs V_{cm} can be considered straight lines (Fig. A2.1), the recall phase has been developed by using an algorithm of linear interpolation. This approach allows an easier implementation of the Recall in the Matlab/Simulink environment.

The values of V_{cm} are obtained by the following equation:

$$V_{cm} = \frac{(V_{cm1a} \cdot W_{1a} + V_{cm1b} W_{1b} + V_{cm2a} \cdot W_{2a})}{(W_{1a} + W_{1b} + W_{2a})} \qquad \text{A2.1}$$

where:

- V_{cm1a}, V_{cm1b}, V_{cm2a} are the values of the compressor voltage used in the interpolation;
- W_{1a}, W_{1b}, W_{2a} are the weights of V_{cm1a}, V_{cm1b}, V_{cm2a}, respectively.

To implement the equation A2.1 in matlab/Simulink environment, the structure of neurons given by GMR is used to compute the vector I_{ref} with 75 values and the 75-by-50 matrixes $\lambda_{O_2\,ref}$ and Vcm_{ref} . I_{ref} is a row vector of the current values I_{fc} that identify the several λ_{O_2} vs V_{cm} curves of PEM-FC system, Vcm_{ref} and $\lambda_{O_2\,ref}$ are matrixes, where the elements of i-th row represent respectively, the values of compressor voltage and the oxygen excess ratio belong to the λ_{O_2} vs V_{cm} curve identified by the current value I_{fc} = I_{ref} (i) (Figure A2.2).

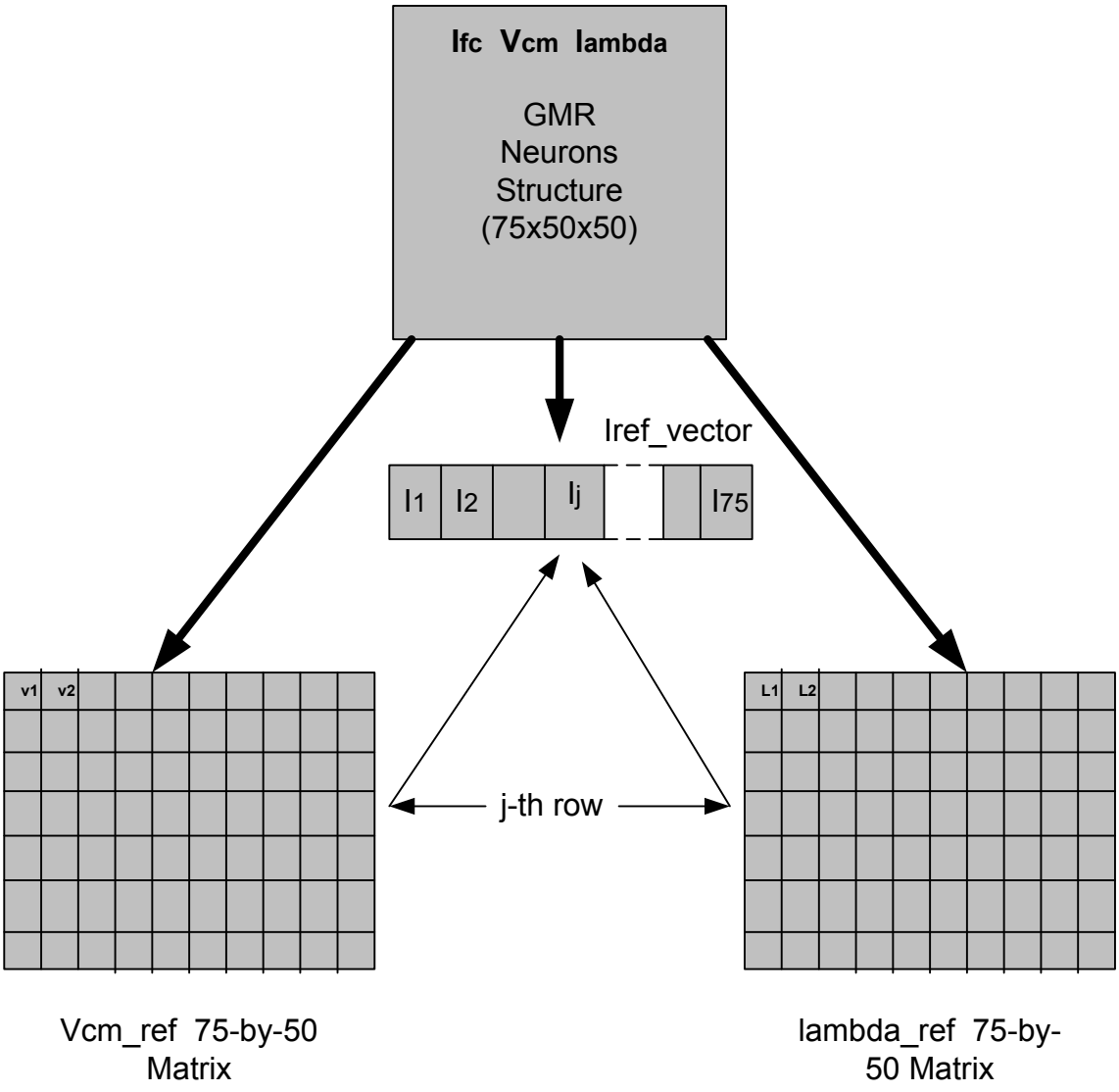

Fig. A2.2. Computation of the matrix I_{ref} , Vcm_{ref} and $\lambda_{O_2\,ref}$ by the GMR Neurons structure.

B. Computing of $V_{cm\,\mathrm{Re}call}$

The values of $V_{cm\,\mathrm{Re}call} = f(V_{cm1a}, V_{cm1b}, V_{cm2a}, W_{1a}, W_{1b}, W_{2a})$ depends on the reference input values I_{fc}^{*} and $\lambda_{O_2}^{*}$ as shown in figure A2.3.

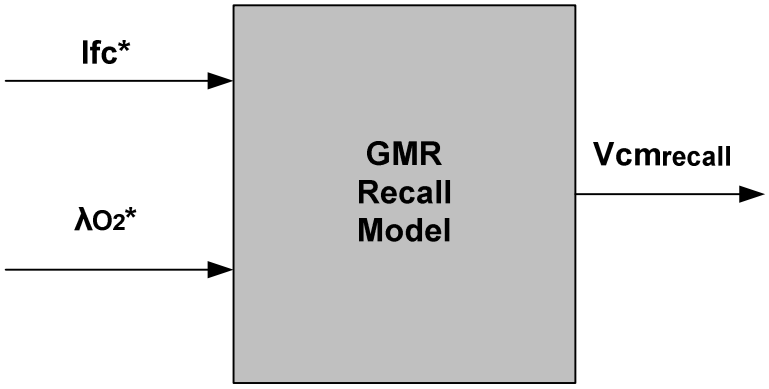

Fig. A2.3. Recall Model.

The steps of the Recall algorithm are the following:

- Identification of the two values I_{fc1} and of I_{fc2} of the vector I_{ref}, that are closer to I_{fc}^{*} by a comparison between all elements of vector I_{ref} and I_{fc}^{*};
- Identification of the rows i-th and j-th of matrix $\lambda_{O_2\,ref}$ by using the index of position of I_{fc1} and I_{fc2} in the vector I_{ref}, respectively;
- Identification of the two values $\lambda_{O_2 1a}$ and $\lambda_{O_2 1b}$ of the row i-th of matrix $\lambda_{O_2\,ref}$ that are closer to $\lambda_{O_2}^{*}$;
- Saving the column indexes k and w of $\lambda_{O_2 1a}$ and $\lambda_{O_2 1b}$ in the vector $\lambda_{O_2\,ref}$, respectively;
- Identification of the values $\lambda_{O_2 2a}$ of the row j-th of matrix $\lambda_{O_2\,ref}$ that is closer to $\lambda_{O_2\,ref}$;
- Saving the column index r of $\lambda_{O_2 2a}$ in the vector $\lambda_{O_2\,ref}$;
- Computing of weights:

$$W_{1a} = \frac{1}{\sqrt{(I_{fc}^{*} - I_{fc1})^2 + (\lambda_{O_2}^{*} - \lambda_{O_2 1a})^2}} \qquad \text{A2.2}$$

$$W_{1b} = \frac{1}{\sqrt{(I_{fc}^{*} - I_{fc1})^2 + (\lambda_{O_2}^{*} - \lambda_{O_2 1b})^2}} \qquad \text{A2.3}$$

$$W_{2a} = \frac{1}{\sqrt{(I_{fc}^{*} - I_{fc2})^2 + (\lambda_{O_2}^{*} - \lambda_{O_2 2a})^2}} \qquad \text{A2.4}$$

- Identification of the two values V_{cm1a} and V_{cm1b} of the row i-th and column k-th and w-th of matrix V_{cmref}, respectively;

- Identification of value V_{cm2a} of the row i-th and column r-th of matrix V_{cmref};
- Computing of $V_{cmrecall}$ by the equation A2.1.

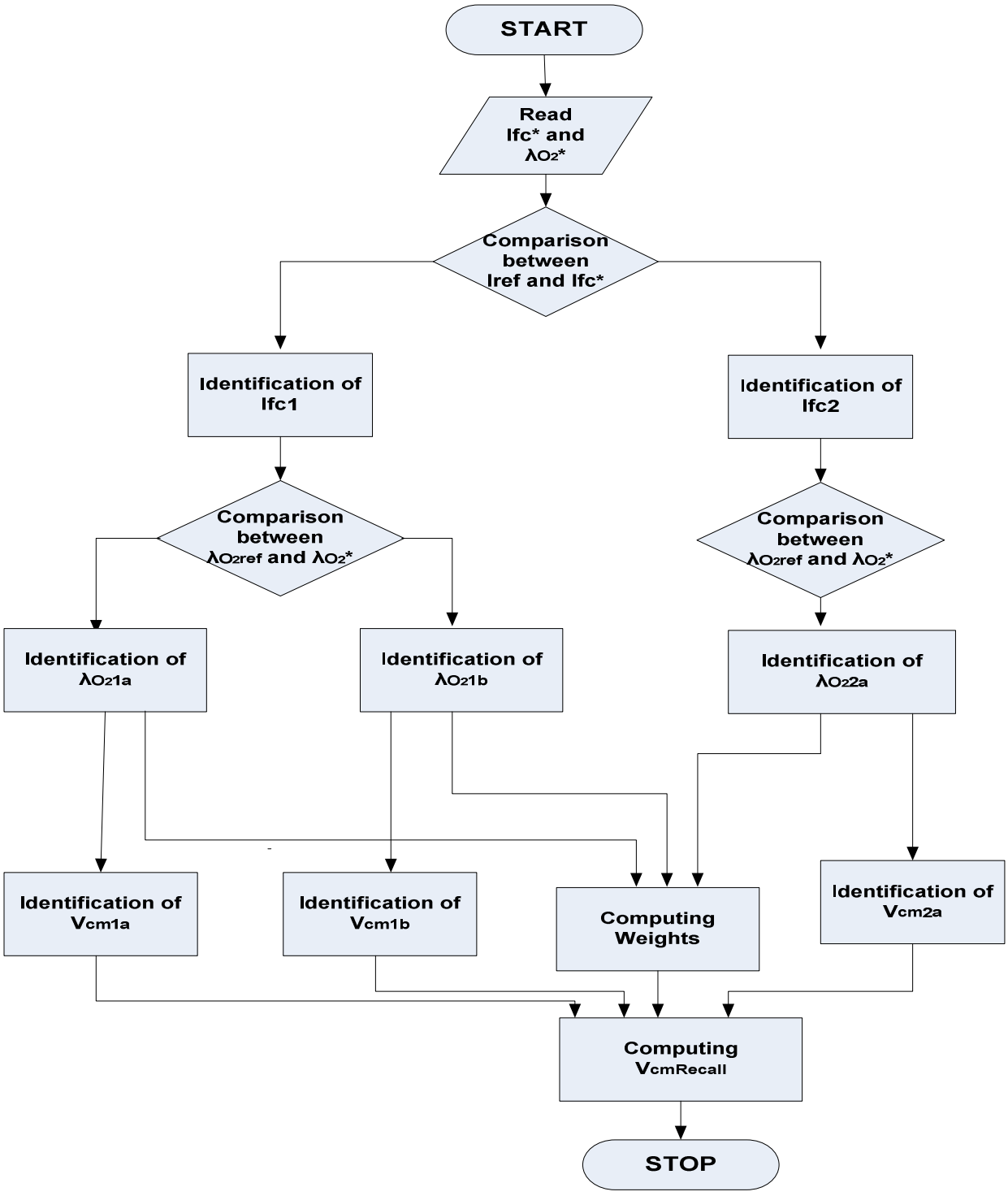

Fig. A2.4. Block Diagram of the Recall Algorithm.

C. Implementation of Recall Method in matlab/Simulink Environment

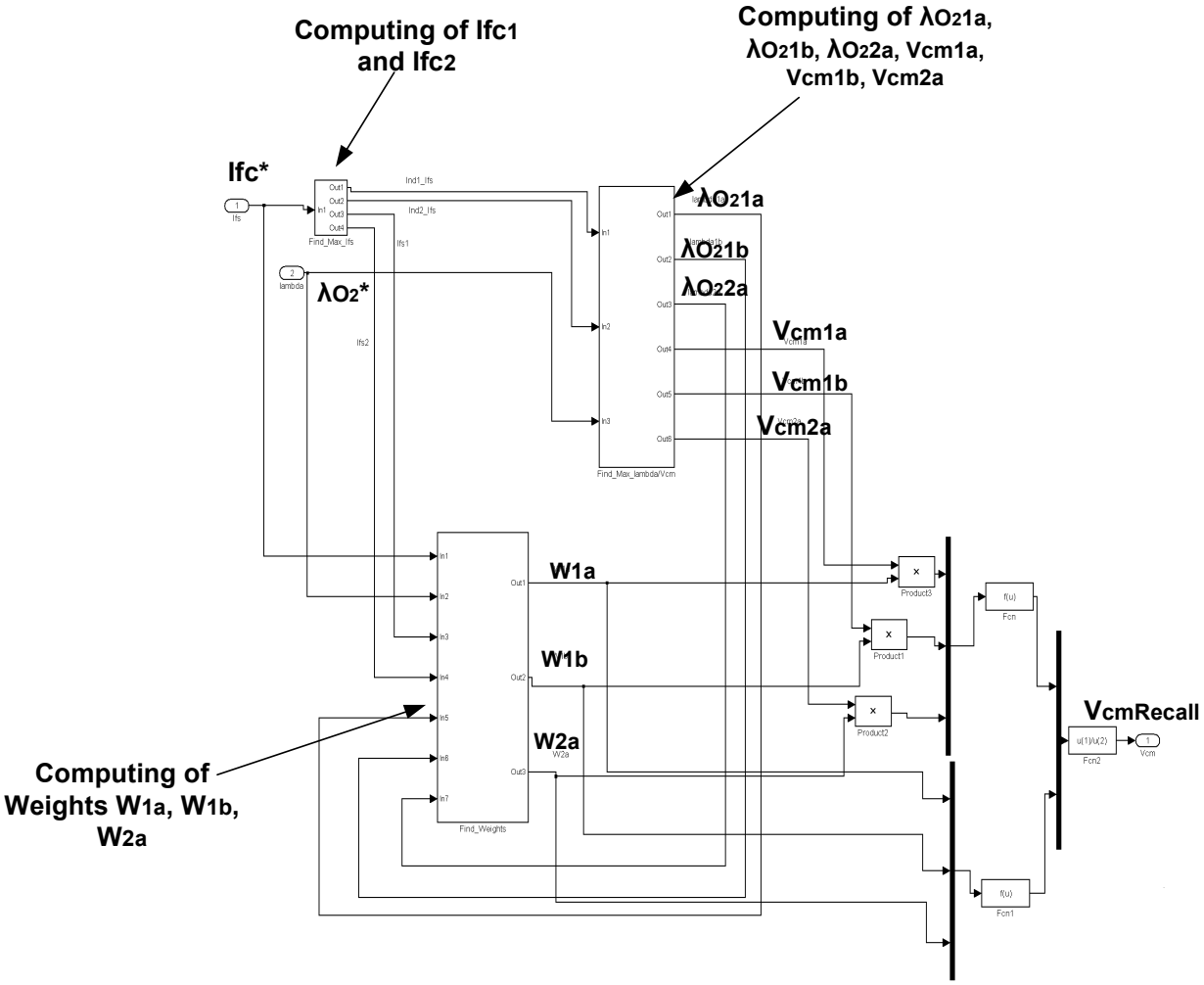

Fig. A2.5. Matlab/Simulink Block Model of Recall.

1. *Computing of* I_{fc1} *and*

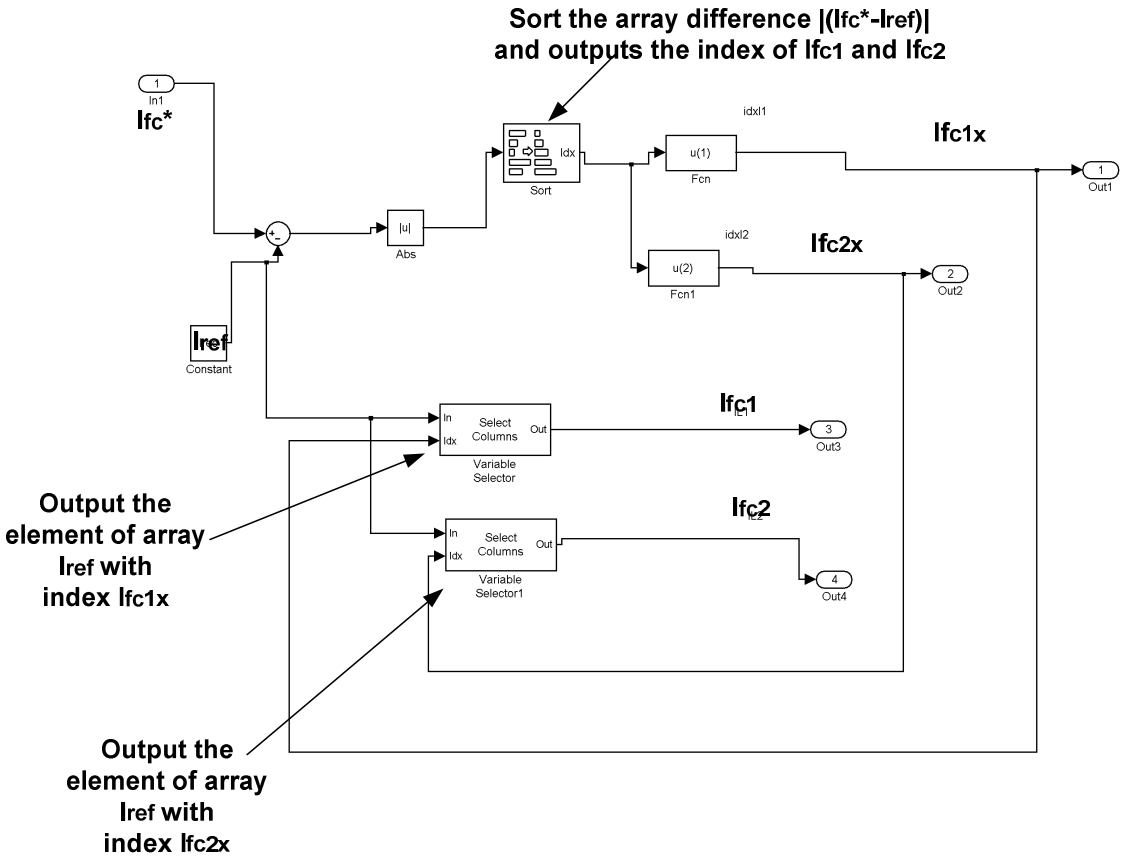

Fig. A2.6. Matlab/Simulink Model used to compute Ifc1 and Ifc2 .

2. *Computing of $\lambda_{O_2 1a}$, $\lambda_{O_2 1b}$ and*

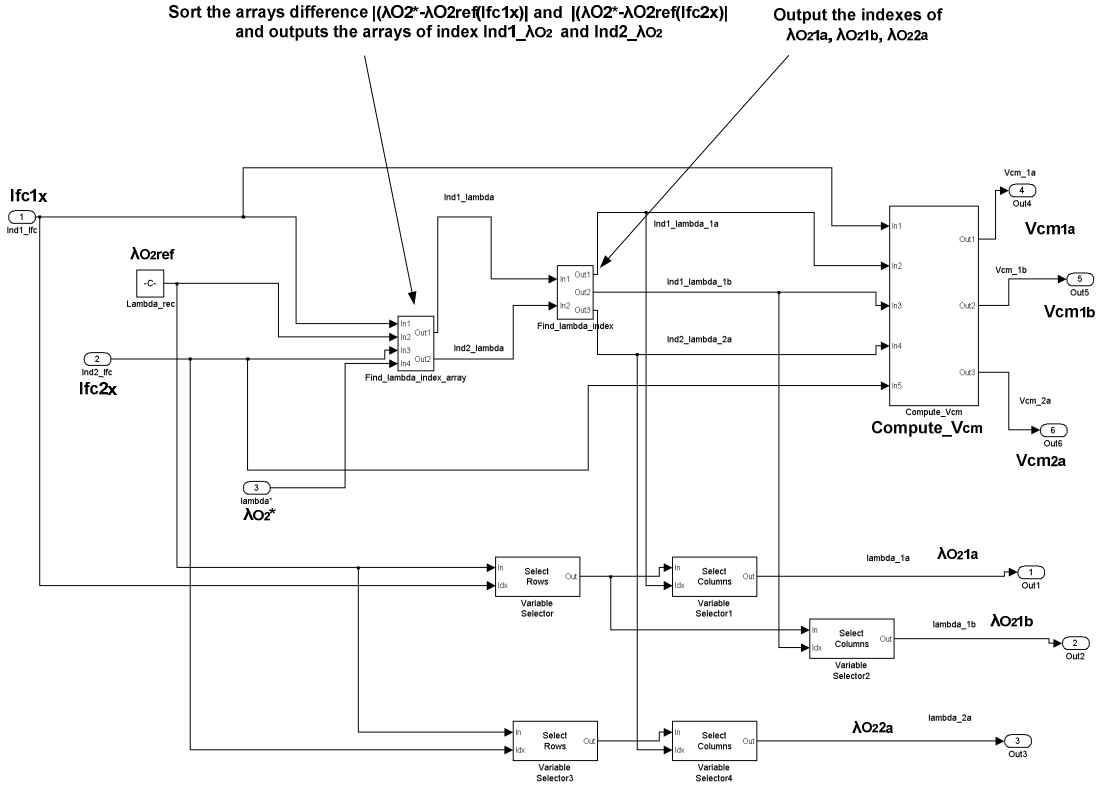

Fig. A2.7. Matlab/Simulink Model used to compute $\lambda_{O_2 1a}$, $\lambda_{O_2 1b}$ and $\lambda_{O_2 2a}$.

3. Computing of V_{cm1a}, V_{cm1b} and V_{cm2a}

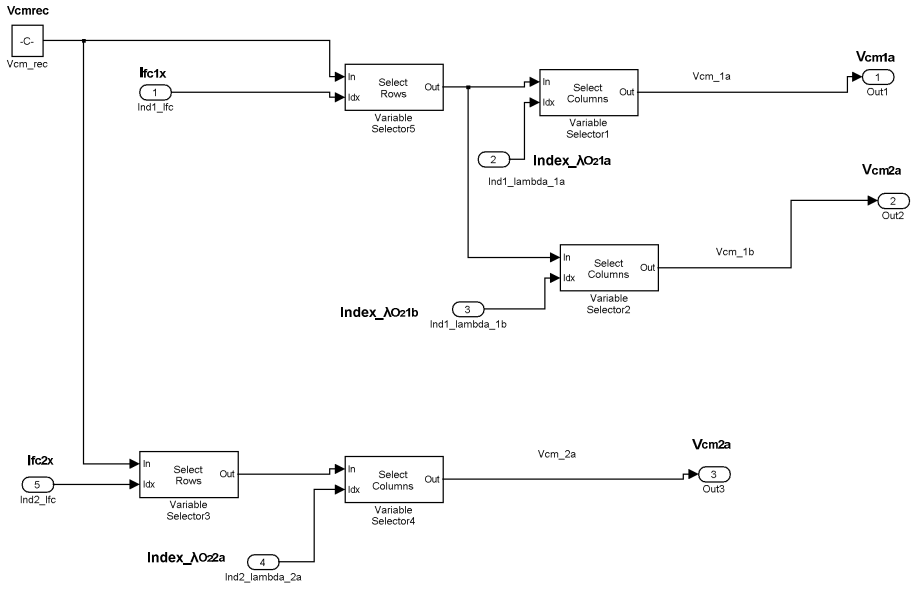

Fig. A2.8. Matlab/Simulink Model used to compute V_{cm1a}, V_{cm1b} and V_{cm2a}

.

4. Computing of W_{1a}, W_{1b} and W_{2a}

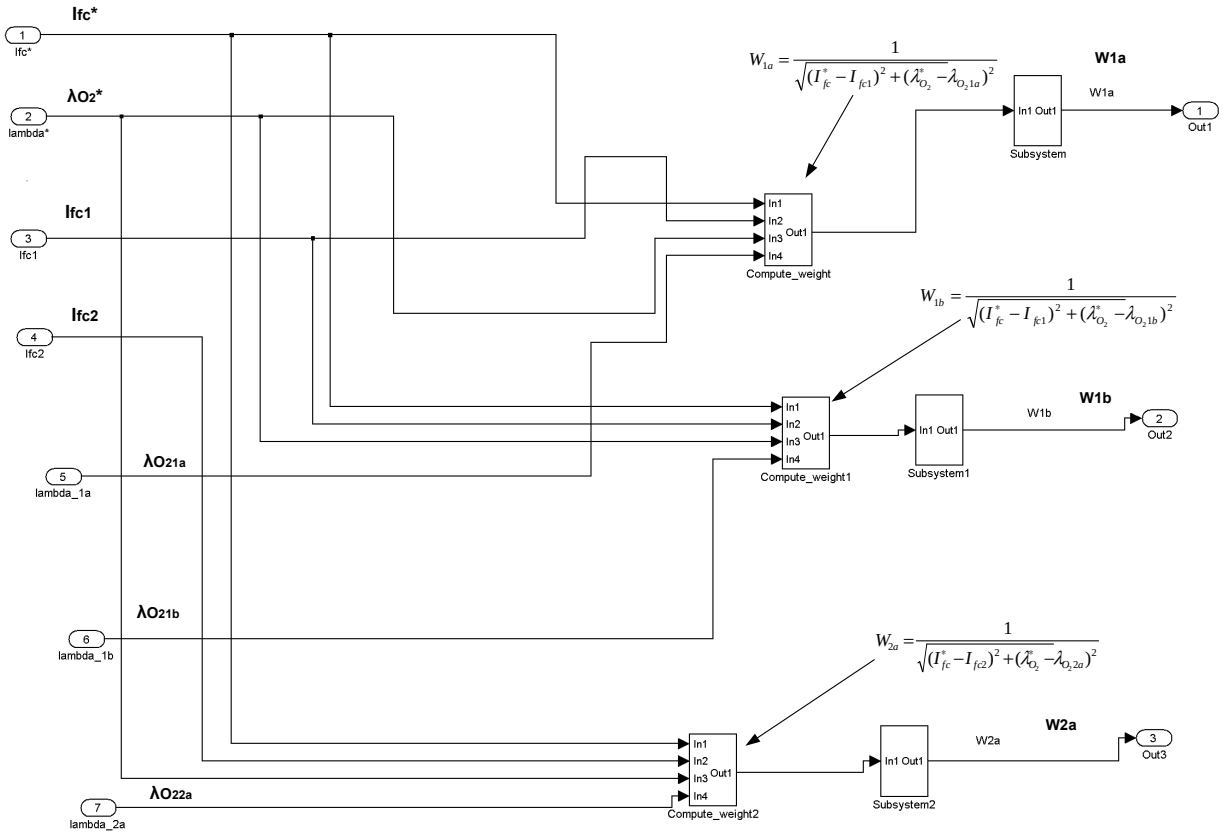

Fig. A2.9. Matlab/Simulink Model used to compute W_{1a}, W_{1b} and W_{2a}

APPENDIX B

The State-Space Averaging Technique

The state-space averaging technique [1] allows a small signal transfer function $\frac{\tilde{v}_0(s)}{\tilde{\delta}(s)}$ to be obtained where $\tilde{v}_0(s)$ and $\tilde{\delta}(s)$ are small perturbations in the output voltage v_0 and the switch duty ratio δ, respectively, around their steady-state dc operating values V_0 and D. The linearization of the of the power stage of the dc-dc converter, operating in a continuous-conduction mode, is obtained by the following steps:

1. State-variable description for each circuit state. The two electrical circuits that correspond to the on state and the off state of the switch are considered. During each circuit state, the linear circuit is described by a state-variable x consisting of the inductor current and the capacitor voltage. Therefore, during each circuit state, the following equations can be written:

$$\dot{x} = A_1 x + B_1 v_d \quad \text{during } \delta T_s \qquad \text{B.1}$$

$$\dot{x} = A_2 x + B_2 v_d \quad \text{during } (1-\delta) T_s \qquad \text{B.2}$$

$$v_o = C_1^T x \quad \text{during } \delta T_s \qquad \text{B.3}$$

$$v_o = C_2^T x \quad \text{during } (1-\delta) T_s \qquad \text{B.4}$$

Where A_1 and A_2 are state matrix, B_1 and B_2 are vectors and C_1 and C_2 are vectors.

2. Averaging the state-variable description using the duty ratio. The average description of the circuit over a switching period is obtained by a time average of the two states. The results of this operation is represented from the following equations:

$$\dot{x} = [A_1\delta + A_2(1-\delta)]x + [B_1 v_d + B_2(1-\delta)]v_d \qquad \text{B.5}$$

$$v_o = \left[C_1^T \delta + C_2^T (1-\delta)\right]x \qquad \text{B.6}$$

3. Introducing small ac perturbations and separations into ac and dc components. Small ac perturbations are introduced in the dc steady-state quantities:

$$x = X + \tilde{x} \quad \text{B.7}$$

$$v_o = V_o + \tilde{v}_o \quad \text{B.8}$$

$$\delta = \Delta + \tilde{\delta} \quad \text{B.9}$$

$$v_d = V_d + \tilde{v}_d \quad \text{B.10}$$

The perturbation $\tilde{v}_d(s)$ in the input voltage is assumed to be zero to simplify the analysis.

4. Transformation of the ac equations into s-domain for the transfer function. The Laplace transformation is used in the previous equations to obtain the transfer function of the power stage and the output filter.

.

The result of the space state averaging technique is the following transfer function in the s-domain:

$$T_p(s) = \frac{\tilde{v}_o(s)}{\tilde{\delta}(s)} = V_d \frac{1 + sr_C C}{LC\left\{s^2 + s\left[\frac{1}{CR} + (r_C + r_L)/L\right] + 1/LC\right\}} \quad \text{B.11}$$

where $\omega_0 = \frac{1}{\sqrt{LC}}$, $\zeta = \frac{\frac{1}{CR} + (r_C + r_L)/L}{2\omega_0}$

The transfer function of the power stage and the output filter can be therefore written:

$$T_p(s) = \frac{\tilde{v}_o(s)}{\tilde{\delta}(s)} = V_d \frac{\omega_0^2}{\omega_z} \frac{s + \omega_z}{s^2 + 2\zeta\omega_0 s + \omega_0^2} \quad \text{B.12}$$

Where the zero depends on the equivalent series resistance of the output capacitor at the frequency $\omega_z = \frac{1}{r_C C}$.

In the PWM modulator, the control voltage v_c is compared with a repetitive waveform $v_r(t)$, which defines the switching frequency f_s and it consists of a dc component and a small ac perturbation component:

$$v_c(t) = V_c + \tilde{v}_c(t) \quad \text{B.13}$$

Where $\tilde{v}_c(t)$ is in a range between zero and V_r and the ac perturbation in the control voltage can be written in the following way [1]:

$$\tilde{v}_c(t) = a\sin(\omega t - \varphi) \qquad \text{B.14}$$

The duty ratio δ(t) is equal to 1.0 if $v_c(t) \geq v_r(t)$ or zero if $v_c(t) < v_r(t)$ as is shown in Figure B.1. The duty ratio can be expressed in terms of the Fourier series:

$$\delta(t) = \frac{V_c}{V_r} + \frac{a}{\mathrm{V_r}}\sin(\omega t - \varphi) \quad \text{+ other high frequency components} \qquad \text{B.15}$$

the high frequency components of δ(t) are eliminated by the low pass filter of the converter and therefore,

$$\delta(t) = \Delta + \tilde{\delta}(t) \rightarrow \Delta = \frac{V_c}{V_r}$$

from which

$$T_m(s) = \frac{\tilde{d}(s)}{\tilde{v}_c(s)} = \frac{1}{V_r} \qquad \text{B.16}$$

in the design of the emulator $V_r = V_d$ is assumed and therefore:

$$T_m(s) = \frac{\tilde{d}(s)}{\tilde{v}_c(s)} = \frac{1}{V_d}$$

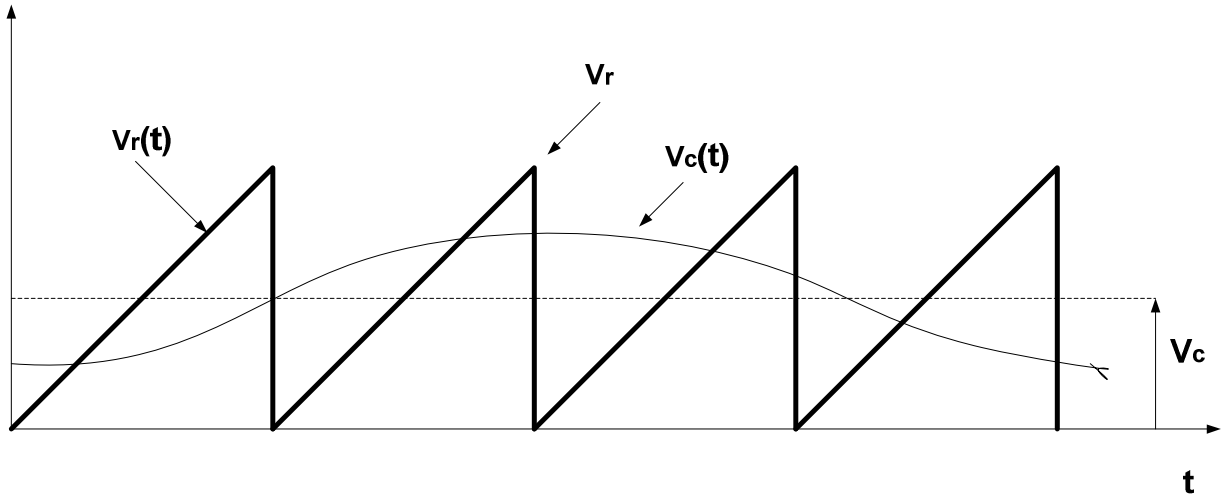

Fig. B.1. Pulse-width modulator.

APPENDIX C

DSpace Board

The DSP1103 PPC Controller Board is specifically designed for development of high-speed multivariable digital controllers and real-time simulations in various fields. It is a complete real-time control based on the Motorola PowerPC 604e processor. For advanced I/O purposes, the board includes a slave-DSP subsystem based on the *Texas Instruments* TMS320F240 DSP microcontroller. The DS1103 PPC Controller Board is a standard PC/AT card that can be plugged into a PC using the ISA bus as a backplane. The card can also be inserted in a dSPACE expansion box communicating with the host PC via an ISA-bus extension or Ethernet. In Figure C.1 is shown the block diagram of a dSPACE board.

A. DSP Board features

The dSPACE offers all tools useful for implementing, experimenting and testing control systems. These tools are the following:

- **Real-time interface** (RTI and RTI-MP), the interface between Simulink and the dSPACE hardware. Real-time interface can be used to build real-time code and to download and execute this code on dSPACE hardware.
- **ControlDesk Standard**, offering a variety of virtual instruments to build and configure virtual instruments panels via Instrumentation, providing functions to perform parameter studies via Parameter Editor and functions to automate ControlDesk's features via Automation.
- **ControlDesk Multiprocessor Extension**, is an extension for dSPACE multiprocessor systems.
- **ControlDesk Test Automation,** is the extension of ControlDesk Standard for advanced test automation features.
- **MLIB/MTRACE,** is the MATLAB-dSPACE interface libraries. The functions of these libraries allow direct access to dSPACE real-time hardware from MATLAB workspace.

The testing and experimenting of a system by the dSPACE board can be obtained in this way: At the start, the application is tested in the Simulink/Matlab environment to verify its correct working. In the next step, the icons available in the dSPACE board library are chosen and used in the Simulink platform to work with the hardware components of the dSPACE board. In fact, each icon represents a hardware part of the microcontroller, as, for example, the PWM generator, the Analog/Digital converter, etc.
The RTI interface builds and downloads the real time code on dSPACE board and produces an executable file SDF (System Description file) for the ControlDesk software. This tool allows observing the variables of a

running real-time application by a creation of a layout with an instrument such as a plotter and a connection of the instruments to the variables to be observed.

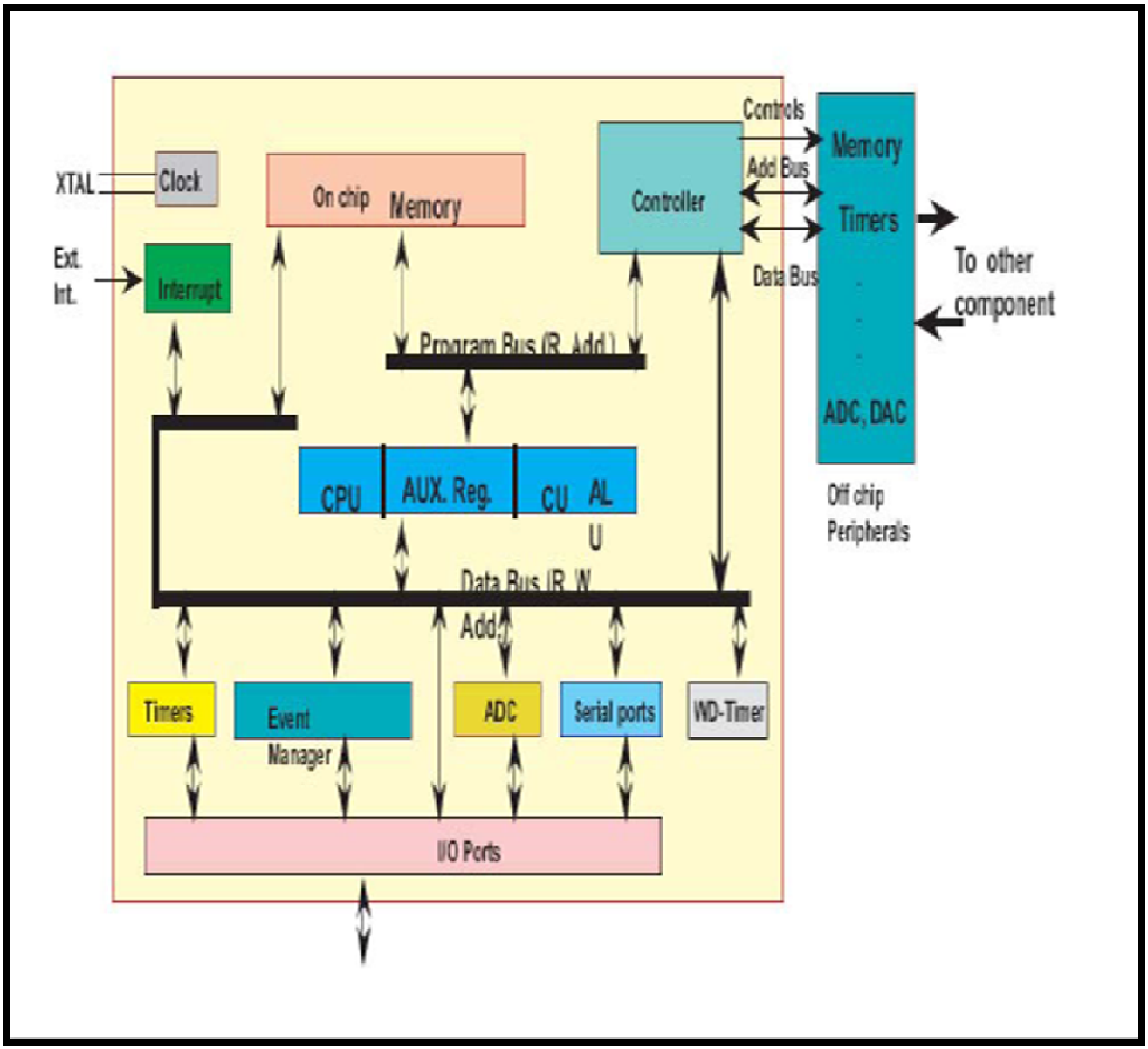

Fig. C.1. Block diagram of dSPACE board.

The hardware characteristics of the dSPACE board DS1103 are the following:

- Single-board system with comprehensive I/O
- CAN interface and serial interface
- Interfaces for connecting incremental encoders
- High I/O speed and accuracy
- PWM-synchronous or externally triggered I/O strobe
- 32 MB application memory
- PLL-driven UART for accurate baud rate selection

The unparalleled number of I/O interfaces makes the DS1103 a versatile controller board for numerous applications. It provides a great selection of interfaces, including 50 bit-I/O channels, 36 A/D channels and 8 D/A channels. For additional I/O tasks, a DSP controller unit built around Texas Instruments TM320F240 DSP is used as a subsystem. The access to the board hardware is obtained by the analog connector P1 (100 pin connector), the digital connector P2 (100 pin connector) and the incremental Encoder/Digital connector P3 (100 pin connector). In addition, this DSP family includes an integrated development environment that speeds development time and debugging. The DSP code was written in standard ANSI C and assembly. Figure C.2 shows the connector panel CP1103 that provides easy-to use connections between the DS1103 PPC controller board and devices to be connected to it. The connector panel CP1103 contains BNC connectors, Slave ADC connector, Digital I/O connector, Slave I/O connector, Incremental sensor connectors, CAN connector and UART RS232 connector.

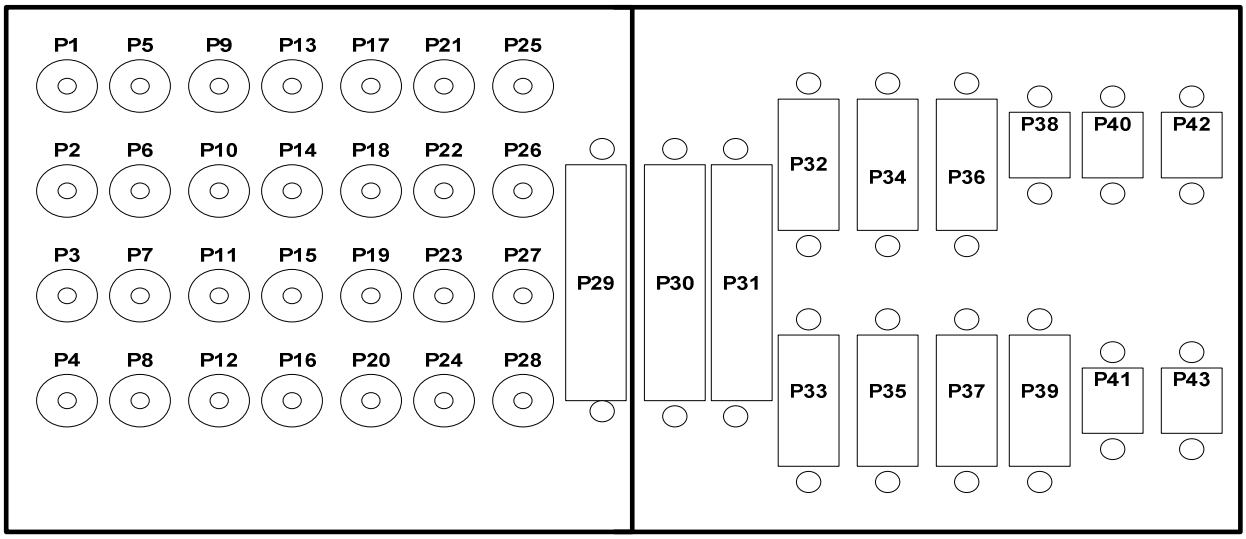

Fig. C.2. Connector Pinouts CP1103.

B. DSP Benefits

It is a common misconception that the DSP is just responsible for the control algorithm. There are many aspects of controlling a converter from tracking control to possibly online self-diagnostic that can be implemented in a DSP. Using a DSP has many benefits that make it attractive for use in control systems. Among these are the tracking and the flexibility of control, quick parameter adjustment and real-time simulation.

- *Tracking control*. The DSP should implement a controller that allows the output to track the desired reference.
- *Flexibility of Control.* When using analog circuits to perform control, the control algorithm is fixed and it is not easily modified. Using a DSP allows the designer to change the control code very quickly. It is often helpful to implement simple, slow control algorithms to verify the hardware is functioning correctly before moving to higher performance or complex control algorithm. If hardware were used to do it, this would mean separate hardware designs and implementations for each algorithm. With the use of the software, modifying the control algorithm means changing several lines of code, which will take only several minutes.
- *Parameter adjustment.* When the control algorithm is fixed, it is easy to modify the values of references and constants in the control code by directly modifying memory locations. This can be performed while the system is operational, allowing for quick adjustments to be made. If the control algorithm were implemented in analog hardware, this would not be as easy to do.
- *Backtracking.* The use of software allows for easy backtracking in the even that a control algorithm is not working. If the control were implemented in analog circuits, the physical modifications would need to be reversed, which may also introduce additional errors in the process.

In the next page is shown the procedure used from the dSPACE system to download the application on the microcontroller and to interface the board with the external world.

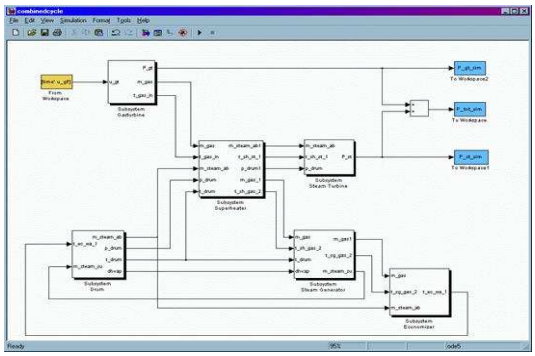

Simulink/Matlab model

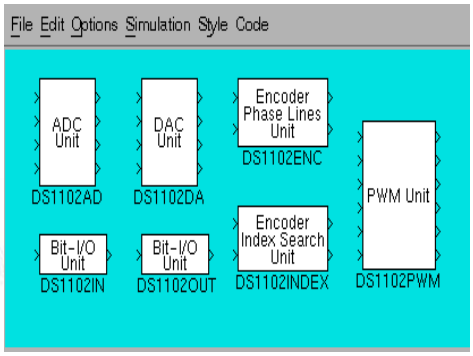

Matlab interface libraries

RTI

dSPACE connectors

dSpace Board DS1103

ControlDESK Tool

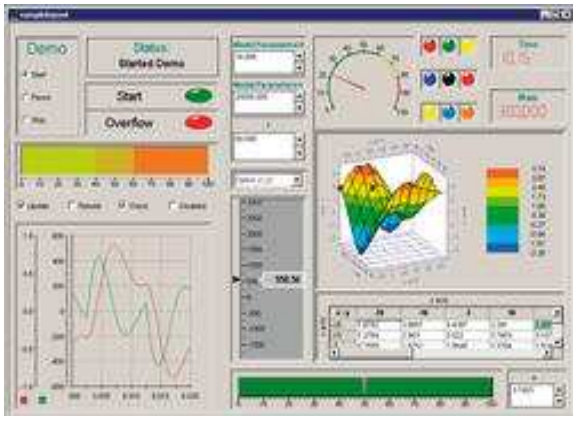

Fig.C.3. Dspace Environment.

File Name	Type	Description
adc.c	C Code File	Controls the Analog to Digital Converter
Adc.h	C Header File	
Cvectors.asm	Assembly File	
F2407.h	C Header File	
fir.c	C Code File	Implementation of a Finite Impulse Response Filter
Fir.h	C Header File	
init.c	C Code File	Controls Initialization of the DSP
Init.h	C Header File	
inv_main.c	C Code File	
io.c	C Code File	Control the I/O interface
Io.h	C Header File	
main.c	C Code File	Main initialization and interrupt routine
Matrixmult.asm	Assembly File	
MmfraG.asm	Assembly File	
pwm.c	C Code File	Control the PWM modulator
Pwm.h	C Header File	
qmath.c	C Code File	1.15 Format Signed number management
Qmath.h	C Header File	
spi.c	C Code File	Contains code for using the serial peripheral interface
Spi.h	C Header File	
ss.asm	Assembly File	
ss.c	C Code File	Contains code for state space implementation
ss.h C	Header File	
Ssasm.asm	Assembly File	
std.c	C Code File	
Std.h	C Header File	

TABLE VII. DSP Code File Description.

APPENDIX D

Parameters of the Fuel Cell Stack Emulated

This appendix shows the values of these system parameters that have been used to obtain the experimental results discussed in the chapter 4 and in the chapter 5 [66].

A. Parameters of the centrifugal compressor model

The parameters for modelling the compressor system are:

- compressor diameter d_c = 0,2286 m;
- atmospheric air density d_a = 1,23 $\left(\frac{kg}{m^3}\right)$;
- compressor efficiency η_{cp} =0,9;
- electrical motor efficiency η_{cm} = 0,98;
- specific heat at constant pressure= 1005 $\left(\frac{J}{kg \cdot K}\right)$;
- compressor inertia $J_{cp} = 5 \cdot 10^{-5}\left(kg \cdot m^2\right)$
- electrical motor constant k_t = 0,0153 $\frac{V}{rad \cdot s}$;
- electrical motor constant k_v =0,0153$\frac{Nm}{A}$;
- DC motor ohmic resistance R_{cm} = 0,82 Ω;
- specific heats ratio γ = 1,4.

B. *Parameters of the supply manifold model*

The parameters for modelling the supply manifold system are:

- dry air constant R_a = 286,9 $\left(\frac{J}{K \cdot mol}\right)$;
- specific heats ratio γ = 1,4;
- supply manifold volume $V_{sm} = 0{,}02\ m^3$.

C. *Parameters of the return manifold model*

The parameters for modelling the return manifold system:

- dry air constant R_a = 286,9 $\left(\frac{J}{K \cdot mol}\right)$;
- specific heats ratio γ = 1,4;
- nozzle opening area = $0{,}02\ m^2$;
- nozze discharge coefficient $C_{D,rm}$ = 0,0124;
- dry air constant R_a = 286,9 $\left(\frac{J}{K \cdot mol}\right)$;
- return manifold volume $V_{rm} = 0{,}005\ m^3$;
- critical pressure ratio $\left(\frac{2}{\gamma+1}\right)^{\frac{\gamma}{\gamma-1}}$ =0,105.

D. *Parameters of the air cooler model and the humidifier model*

The parameters for modelling the air cooler system and the humidifier system are:

- dry air constant R_a = 286,9 $\left(\frac{J}{K \cdot mol}\right)$;
- desired relative humidity of the output mass flow of the humidifier system φ_{des} =0,2;
- oxygen molar mass $M_{O_2} = 32 \cdot 10^{-3} \frac{kg}{mol}$;
- nitrose molar mass $M_{N_2} = 28 \cdot 10^{-3} \frac{kg}{mol}$;
- vapor molar mass $M_v = 18{,}02 \cdot 10^{-3} \frac{kg}{mol}$

E. *Parameters of the cathode model*

The parameters that allow modelling the cathode channel are the following:

- dry air constant R_a = 286,9 $\left(\frac{J}{K \cdot mol}\right)$;
- vapor constant R_v = 461,5 $\left(\frac{J}{K \cdot mol}\right)$;
- nitrogen constant R_{N_2} = 296,8 $\left(\frac{J}{K \cdot mol}\right)$;
- oxygen constant R_{O_2} = 259,8 $\left(\frac{J}{K \cdot mol}\right)$;
- cathodic volume $V_{ca} = 0{,}01\ m^3$;
- oxygen molar mass $M_{O_2} = 32 \cdot 10^{-3} \frac{kg}{mol}$;
- nitrogen molar mass $M_{N_2} = 28 \cdot 10^{-3} \frac{kg}{mol}$;
- vapour molar mass $M_v = 18{,}02 \cdot 10^{-3} \frac{kg}{mol}$
- orifice constant $k_{ca} = 0{,}2177 \cdot 10^{-5} \frac{kg}{s \cdot Pa}$
- oxygen concentration of the inlet air $y_{O_2,in}$ = 0,21;

F. *Parameters of the anode model*

The parameters for modelling the anode channel are:

- Vapor constant R_v =461,5 $\left(\frac{J}{K \cdot mol}\right)$;
- Hydrogen constant R_{H_2} =4124,3 $\left(\frac{J}{K \cdot mol}\right)$
- Anodic volume $V_{an} = 0{,}005\ m^3$;
- hydrogen molar mass $M_{H_2} = 2{,}016 \cdot 10^{-3} \frac{kg}{mol}$;

- vapor molar mass $M_v = 18{,}02 \cdot 10^{-3} \frac{kg}{mol}$;
- relative humidity of the input mass flow $\varphi_{an,in}$ = 0,4;
- orefice constant $k_1 = 2{,}1 \frac{kg}{s \cdot kPa}$;
- orefice constant k_2 =0,94;

G. *Parameters of the membrane hydration model*

The parameters for modelling the membrane hydration system are:

- membrane dry density $\rho_{m,dry} = 0{,}002 \frac{kg}{cm^3}$;
- membrane dry equivalent weight =1,1 $\frac{kg}{mol}$;
- membrane thickness t_m =0,01275 cm;
- vapor molar mass $M_v = 18{,}02 \cdot 10^{-3} \frac{kg}{mol}$;
- fuel cell active area $A_{fc} = 280\ cm^2$;

H. *Parameters of the stack voltage model*

The parameters for modelling the stack voltage model are:

- Membrane thickness t_m = 0,01275 cm;
- fuel cell active area $A_{fc} = 280\ cm^2$;
- max current density $i_{\max} = 2{,}2 \frac{mA}{cm^2}$;
- constant b_2 =350;
- constant b_{11} =0,005139;
- constant c_1 = 10;
- constant c_3 = 2.

In all models the values of the universal constant of gas, of the number of cells in the stack and of the Faraday number are:

- universal constant of gas $\overline{R}$ = 8,3145 $\left(\frac{J}{K \cdot mol}\right)$;
- Faraday constant F = 96485 C;
- number of cells in the stack n =381;

APPENDIX E

Input-state-output representation of the FCS

$$x = [m_{O_2}, m_{H_2}, m_{N_2}, \omega_{cp}, p_{sm}, m_{sm}, m_{w,an}, m_{w,ca}, p_{rm}, i_a]^T$$

$$d\frac{m_{O_{2,ca}}}{dt} = W_{O_{2,ca,in}} - W_{O_{2,ca,out}} - W_{O_{2,reagenti}}$$

$$d\frac{m_{N_{2,ca}}}{dt} = W_{N_{2,ca,in}} - W_{N_{2,ca,out}}$$

$$d\frac{m_{w,ca}}{dt} = W_{v,ca,in} - W_{v,ca,out} + W_{v,ca,gen} + W_{v,membrana} - W_{l,ca,out}$$

$$d\frac{m_{H_{2,an}}}{dt} = W_{H_{2,an,in}} - W_{H_{2,an,out}} - W_{H_{2,reacted}}$$

$$d\frac{m_{w,an}}{dt} = W_{v,an,in} - W_{v,an,out} + W_{v,menbrane} - W_{l,an,out}$$

$$J_{cp}\frac{d\omega_{cp}}{dt} = \tau_{cm} - \tau_{cp}$$

$$\frac{di_a}{dt} = \frac{1}{L_a}\left(v_{cm} - R_a i_a - k_v \omega_{cp}\right)$$

$$\frac{dm_{sm}}{dt} = W_{cp} - W_{sm,out}$$

$$\frac{dp_{sm}}{dt} = \frac{\gamma R_a}{V_{sm}}(W_{cp}T_{cp,out} - W_{sm,out}T_{sm})$$

$$\frac{dp_{rm}}{dt} = \frac{R_a T_{rm}}{V_{sm}}(W_{ca,out} - W_{rm,out})$$

$$\frac{dm_{rm}}{dt} = W_{ca} - W_{rm,out}$$

$W_{O_2,ca,in} = f_1(m_{O_2,ca}, m_{N_2,ca}, m_{v,ca,} p_{sm}, I_{st})$ by equations 3.48, 3.49, 3.50, 3.51, 3.59, 3.61 and 3.73

$W_{O_2,ca,out} = f_2(m_{O_2,ca}, m_{N_2,ca}, m_{v,ca,} p_{sm}, p_{rm})$ by equations 3.64, 3.65, 3.66, 3.68, 3.73, 3.74 and 3.76

$W_{N_2,ca,in} = f_3(m_{O_2,ca}, m_{N_2,ca}, m_{v,ca,} p_{sm}, I_{st})$ by equations 3.48, 3.49, 3.50, 3.51, 3.59, 3.61 and 3.73

$W_{N_2,ca,out} = f_4(m_{O_2,ca}, m_{N_2,ca}, m_{v,ca,} p_{sm}, p_{rm})$ by equations 3.64, 3.65, 3.66, 3.68, 3.73, 3.74 and 3.76

$W_{v,ca,in} = f_5(m_{O_2,ca}, m_{N_2,ca}, m_{v,ca,} p_{sm}, I_{st})$ by equations 3.48, 3.49, 3.50, 3.51, 3.59, 3.61 and 3.73

$W_{v\ ,ca,out} = f_6(m_{O_2,ca}, m_{N_2,ca}, m_{v,ca,} p_{sm}, p_{rm})$ by equations 3.64, 3.65, 3.66, 3.68, 3.73, 3.74 and 3.76

$W_{O_2,ca,reacted} = f_7(I_{st})$ by equation 3.42

$W_{v,ca,generated} = f_8(I_{st})$ by equation 3.43

$W_{v,membrane} = f_9(I_{st}, m_{v,ca}, m_{v,an})$ by equations 3.99, 3.101, 3.102, 3.103, 3.104, 3.105, 3.106, 3.107, 3.108, 3.109, 3.110

$W_{H_2,an,in} = f_{10}(m_{H_2,an}, m_{v,an,} p_{sm},)$ by equations 3.85, 3.86, 3.87, 3.89, 3.94, 3.95 and 3.96

$W_{H_2,an,out} = f_{11}(m_{H\ _2,an}, m_{v,an,} p_{rm})$ by equations 3.90, 3.91 3.94, 3.95

$W_{v,an,in} = f_{12}(m_{H_2,an}, m_{v,an,} p_{sm},)$ by equations 3.85, 3.86, 3.87, 3.88, 3.89, 3.94, 3.95, 3.96

$W_{v,an,out} = f_{13}(m_{H\ _2,an}, m_{v,an,} p_{rm})$ by equations 3.90, 3.91, 3.92, 3.94, 3.95

$W_{H_2,an,reacted} = f_{14}(I_{st})$ by equation 3.80

$W_{sm,out} = f_{15}(m_{O_2,ca}, m_{N_2,ca}, m_{v,ca,} p_{sm})$ by equations 3.147, 3.48, 3,49, 3.50

$W_{rm,out} = f_{16}(p_{rm})$ by equations 3.148

$\tau_{cm} = f_{17}(i_a)$ by equation 3.12

$\tau_{cp} = f_{18}(\omega_{cp})$ by equation 3.129

$W_{cp} = f_{19}(\omega_{cp})$

BIBLIOGRAPHY

[1] Larminie, James (May 2003). *Fuel Cell Systems Explained, Second Edition*. SAE International.

[2] Appleby, A. John. *Fuel Cell Handbook*. New York: Van Reinhold Co., 1989.

[3] Shuo-Jen Lee, Ching-Han Huang, Jian-Jang Lai and Yu-Pang Chen. *Corrosion-resistant component for PEM fuel cells.* Journal of Power Sources, Volume 131, Issues 1-2, 14 May 2004, Pages 162-168.

[4] "DOE Fundamentals, Handbook, Thermodynamics, Heat, Transfer and Fluid Flow ". Department of Energy of USA.

[5] Rayment Chris and Sherwin Scott, "*Introduction to fuel cell technology"*. Department of Aerospace and Mechanical Engineering. University of Notre Dame. Notre Dame, USA. 2 May 2003.

[6] Turner John A. "*Sustainable Hydrogen Production*". National Renewable Energy Laboratory, Golden, USA, 13 August 2004.

[7] Allen, R.M. and Bennetto, H.P. 1993. "Microbial fuel cells—Electricity production from carbohydrates". Appl. Biochem. Biotechnol., 39/40, pp. 27–40.

[8] "*Hydrogen Energy and Fuel Cell – A vision of our future*". Final Report of the High Level Group. European Commission- Community Research. 2003.

[9] K. Rajashekara, "Propulsion System Strategies for Fuel Cell Vehicles". SAE Paper 2000- 01- 0369. March 2000.

[10] Sandhu S.S., Saif Y.A. and Fellner J.P.. "*A reformer performance model for fuel cell applications*". Department of Chemical engineering and Materials Engineering, University of Dayton, Dayton, USA. Journal of Power Sources, 13 August 2004.

[11] Padro C., Putsche V., "*Survey of Economics of Hydrogen Technologies"*, National Renewable Energy Laboratory Study, 1999.

[12] Steinfeld G., Sanderson R.," *Landfill Gas Cleanup for Carbonate Fuel Cell Power Generation"*. Final Report. Energy Research Corporation, Danbury, Connecticut, USA. February 1998.

[13] Farrel E.A., Keith D.W., Corbett J.J., "*A strategy for introducing hydrogen into transportation"*. Energy and Resources Group, University of California, Berkley, USA. Energy Policy, volume 31, issue 13, October 2003.

[14] Cleghorn S.J., Ren X., Springer T.E., Wilson M.S., Zawodzinski T.A., Gottesfeld S. "*PEM Fuel Cells for transportation and Stationary Power Generation Applications*". Los Alamos National Lab., NM, USA, 1996.

[15] "*Course Manual of Hydrogen Fuel Cell Engines and Related Technologies".* Produced by College of the Desert and SunLine Transit agency with funding from the U.S.A. Federal Transit Administration.

[16] Dr. Chunto Tso, Director and Shih-Yun Chang, Assistant Research Fellow. "*A Viable Niche Market—Fuel Cells scooters in Taiwan.* Reaserch Division I, Taiwan Institute of Economic Research (TIER).

[17] "*Application of Fuel Cell to Fork Lift Trucks"*- article from the September /October 2005 issue of Industrial- Utility Vehicle Magazine.

[18] Miller A.R., Fuelcell Propulsion Institute; Barnes D.L., Veichle Projects LLC. Presented at Fuel Cell 2002, *"European Fuel Cell Forum",* July 2002.

[19] Oman H. "*Fuel-cell powered airplane propulsion".* Aerospace and Electronic System Magazine, IEEE, Volume 19, Issue 1, Jan 2004.

[20] "*Electric boat features hydrogen fuel cell".* Article in PC control, January 2005. Reports on the Hydroxy3000 catamaran using a fuel cell as the main source of energy.

[21] "*Hydrogen Fuel Cell Bus Evaluation for California Transit Agencies".* DOE's Hydrogen, Fuel Cells and Infrastructure Technologies Program webpage providing links to hydrogen fuel cell bus studies and reports.

[22] "*Beyond Batteries*: *Portable Hydrogen* Fuel Cells". Carol Potera, Environmental Health Perspectives, Volume 115, Number 1, January 2007.

[23] Mark Dixon B. Sc, C. Eng, M.I. Chem. E, "*Training emulators*"

[24] Jaakko Ollila, "A medium power PV-array emulator with a robust control strategy", IEEE transaction , 1995.

[25] P.H Chou, C. Park, J. Park, K. Pham and J. Liu "B#:a battery emulator and power profiling instrument", Proc. International Symposium on Low Power Electronics and Design, Seoul, Korea, pp. 288-293, August 2003.

[26] Q. Zeng, P. Song, and L. Chang, "*A photovoltaic emulator based on DC chopper*", IEEE Canadian Conference on Electrical and Computer Engineering, Winnipeg, Manitoba, Canada, vol.1, pp. 257-261, May 2002.

[27] K. Khouzam, C. Ly, C. K. Koh, P. Y. Ng, "*Simulation and real-time modeling of space photovoltaic systems*", IEEE transaction, 1994.

[28] C. Y. Thean, J. Junbo, A.W.K. Eric, " An Embedded Microchip System Design for Programmable Solar Panel Emulator", IEEE transaction, 2005.

[29] S. H. Lloyd, G. A. Smith, D. G. Infield, "*Design and Construction of a modular electronic Photo-Voltaic Emulator*", Power Electronics and Variable Speed Drives, Conference Publication, IEEE 2000.

[30] Elgar Electronics Corporation, "*Solar array emulators*", available on line at http://www.elgar.com/products/Elgar/sas.htm.

[31] Agilent Technologies Inc., "*Solar Array Emulators*", available on line at http://we.home.agilent.com/upload/cmc_upload_All/SAS_datasheet_May04.pdf.

[32] Spectra –Nova Technologies Inc., "*Solar array output emulators*", available on line at http://www.spectra.nova.com/atesters.html.

[33] D. J. Hall and R. G. Colclaser, "Transient modeling and simulation of a tubular solid oxide fuel cell", IEEE transaction on Energy Conversion, vol. 14, pp. 749-753, September 1999.

[34] D. J. Hall, "*Transient modeling and simulation of a solid oxide fuel cell*", Ph. D. dissertation, University of Pittsburgh, PA, 1997.

[35] L. A. Click, R. E. Williford, J. W. Stevenson, C. F. Windisch Jr. and S. P. Simner, "*Experimentally-calibrated, spreadsheet-based SOFC unit-cell performance model*", *Fuel Cell Seminar*, Palm Springs, CA, 2002.

[36] S. Yerramala, A. Davari and A. Feliachi, "*Dynamic Modeling and analysis of polymer electrolyte fuel cell*", IEEE Power Engineering Society Summer Meeting, Edmonton, Alberta, Canada, vol.1, pp. 82-86, July 2002.

[37] P. Acharya, P. Enjeti and I. J. Pitel, "An advanced fuel cell simulator", in Proceedings of IEEE Applied Power Electronics Conference and Exposition, 2004, pp.1554-1558.

[38] T. W. Lee, B. K. Lee, S. J. Jang, S. H. Kim and C. Y. Won, " *Development of a 3kW Fuel Cell Generation System with An Active Fuel Cell Emulator: Topology, Control and Design*". Power Electronics Specialists Conference, 2004. PESC 04. 2004 IEEE 35th Annual.

[39] T. W. Lee, B. K. Lee, S. J. Jang, S. H. Kim and C. Y. Won, "*A 3kW Fuel Cell Generation System using the Fuel Cell Simulator*". IEEE-ISIE 2004: proceedings of the 2004 IEEE International Symposium on Industrial Electronics, Ajaccio, France, May 4-7, 2004.

[40] A. Gebregergis and P. Pillay, "*The Development of Solid Oxide Fuel Cell (SOFC) Emulator*". Power Electronics Specialists Conference, 2007. PESC 2007. IEEE Volume. Issue, 17-21 June 2007 Page(s):1232-1238.

[41] M. Ordonez, M. T. Iqbal and J. E. Quaicoe, "*A Novel Fuel Cell Emulator*". Power Electronics Specialists Conference, 2005. PESC apos; 05. IEEE 36th Volume, issue, 2005 Page(s):178-184.

[42] Springer, Zawodzinski, Gottesfeld. *Polymer electrolyte fuel cell model*. *Journal of* Electrochemical *Society*,138, 2334-2342.

[43] Jay T. Pukrushpan, Anna G. Stefanopoulou, Huel Peng, *Control of fuel cell power systems,* Springer 2005.

[44] Larminie J. and Dicks A. (2000). *Fuel Cell Systems Explained*. Wiley, West Sussex, England.

[45] A. Cangel and M. Boles, "*Thermodynamics: An Engineering Aprroach*", McGraw-Hill.

[46] T. Nguyen, R. White, "A water and heat management model for proton-exchange- membrane fuel cells". *Journal of Electrochemical Society,* 140(8), 2178-2186.

[47] S.Dutta, S. Shimpalee and J. Van Zee, "Numerical prediction of mass-exchange between cathode and anode channels an a PEM fuel cell". International Journal of Heat and Mass Transfer, 44, 2029-2042.

[48] T. Springer, T. Zawodzinski and S. Gottesfeld, "*Polymer electrolyte fuel cell model". Journal of Electrochemical Society*, 138(8), 2334-2342.

[49] P. Moral, I. Kolmanovsky, "Turbocharger modelling for automotive control applications". SAE Paper 1999-01-0908.

[50] J. Cunningham, M. Hoffman, R. Moore and D. Friedman, "Requirements for a flexible and realistic air supply model for incorporation into a fuel cell vehicle (FCV) system simulation. SAE Paper 1999- 01-2912.

[51] M. Boyce, "*Gas Turbine Engineering Handbook*". Gulf, Houston, TX.

[52] J. Gravdahl and O. Egeland, "*Compressor Surge and Rotating Stall.* Springer, London.

[53] J. Heywood, "*Internal Combustion Engine Fundamentals*". McGraw-ill, New York.

[54] P. Rodatz, "Dynamics of the polymer electrolyte fuel cell: Experiments and model-based analysis". PH.D. thesis, Swiss Federal Institute of Technology, Zurich.

[55] Mohan, Undeland and Robbins, "Power Electronics Converters, Applications and Design", Wiley Press.

[56] R. W. Erickson and D. Maksimovic, "*Fundamentals of Power Electronics (Second Edition*)". University of Colorado, Boulder, Colorado (USA).

[57] I. A. Presssman, "*Switching Power Supply Design*", McGraw-Hill Press.

[58] G. Ioannidis, A. Kandianis and N. S. Manias, "*Novel Control Design for the Buck converter*". EEE proceedings. Electric Power applications. ISSN 1350-2352.

[59] K. Ogata, *Modern control engineering*, Prentice-Hall, Engineering.

[60] M. Cirrincione, M. C. Di Piazza, G. Marsala, M. Pucci, G. Vitale, "*Real Time Simulation of Renewable Sources by Model-Based Control of DC-DC Converters*", ISIE 2008 IEEE International Symposium on Industrial Electronics, Cambridge, UK.

[61] G. Marsala, M. Pucci , G. Vitale, M. Cirrincione, A. Miraoui, "*A Prototype of a Fuel Cell PEM Emulator Based on a Buck Converter* " submitted to Applied Energy ICAE 09.

[62] Shuo-Jen Lee, Ching-Han Huang, Jian-Jang Lai and Yu-Pang Chen. *Corrosion-resistant component for PEM fuel cells.* Journal of Power Sources, Volume 131, Issues 1-2, 14 May 2004, Pages 162-168.

[63] M. Kavato, "Feedback-error-learning neural network for supervised learning". In R. Eckmiller (ed.), *Advanced Neural Computers*, pp.365-372, Amsterdam-North Holland, 1990.

[64] J.T. Pukrushpan, A.G. Stefanopoulou and H. Peng, "Control of Fuel Cell Breathing, " *IEEE Control System Magazines,* Vol.24, No.2, pp. 30-46, April 2004.

[65] A. Vahidi, A. Stefanopoulou, and H. Peng, " Model Predictive Control for Starvation Prevention in a Hybrid Fuel Cell System", in Proc.Amer.Contr. Conf., 2004, pp.834-839.

[66] J. Pukrushpan, A. Stefanopoulou, and H. Peng., *Control of Fuel Cell Power Systems: Principles, Modeling, Analysis, and Feedback Design.* London, U.K.: Springer-Verlag, 2004.

[67] P. Rodatz, Dynamics of the Polymer Electrolyte Fuel Cell: Experiments and Model-Based Analysis, PhD Thesis, Ecole Polytechnique Federale de Lausanne, 2006.

[68] P.E.M. Almeida and M. G. Simoes, "Neural Optimal Control of PEM Fuel Cells with Parametric CMAC Networks", IEEE Trans. Ind., Appl., vol. 41, No. 1, JAN./FEB.2005.

[69] J.A. Adams, W. C. Yang, K. A. Oglesby and K. D. Osborne, "*The development of Ford's P2000 fuel cell vehicle*", SAE Paper 2000-01-1061.

[70] S. Varigonda, J. T. Pukrushpan and A. G. Stefanopoulou, " Challenges in fuel cell power plant control: The role of system level dynamic models", in Proc. AlChESpring Meeting, 2003.

[71] D. D. Boettner, G. Paganelli, Y. G. Guezennec, G. Rizzoni and M. J. Moran, "On-board reforming effects on the performance of proton exchange membrane (PEM) fuel cell vehicles", J. Energy Resources Technol., Transaction of the ASME, vol. 124, no. 3, pp. 191-196, 2002.

[72] T. E. Springer, R. Rockward, T. A. Zawodzinski and S. Gottesfeld, "*Model for polymer electrolyte fuel cell operation on reformate feed*", *J. Electrochem. Soc.* Vol. 148, no. 1, pp. A11-A23, 2001.

[73] J. T. Pukrushpan, H. Peng and A. G. Stefanopoulou, "Simulation and analysis of transient fuel cell system performance based on a dynamic reactant flow model", in Proc. ASME Int. Mechanical Engineering Congress & Exposition, 2002, pp. 1-12.

[74] G. Marsala, M. Cirrincione, G. Cirrincione, A. Miraoui, M. Pucci, G. Vitale, "*A Neural Inverse Control of the PEM-FC Voltage by the Generalized Mapping Regressor (GMR)"*, IEEE IAS 08 (43° Industry Applications Society Annual Meeting), , Edmonton, Canada.

[75] G. Cirrincione, M. Cirrincione, G. Marsala, M. Pucci, "*Computation of the Inverse Jacobian Matrix of a Robot Manipulator by the GMR Neural Network*" submitted to IEEE Transactions on Mechatronics.

[76] M. Norgaard, O. Ravn, N. K. Poulsen and L. K. Hansen, " *Neural Networks for Modelling and Control of Dynamics Systems*".

[77] G. F. Franklin, J. D. Powell, M. L. Workman (1998), " *Digital Control of Dynamic Systems".* Addison-Wesley, Reading, MA, 3rd edition.

[78] G.Cirrincione, M.Cirrincione and S. Van Huffel "Mapping Approximation by the THE GMR Neural Network ", 4th World Multiconference on Circuits, Systems, Communications & Computers (CSCC 2000), Athens (Greece), July 2000.

[79] G. Cirrincione, A Neural Approach to the Structure from Motion Problem, PhD thesis, LIS INPG Grenoble, December 1998.

[80] Carpenter, G.A. and Grossberg, S. (2003). Adaptive resonance theory. In M.A. Arbib (Ed.), The Handbook of Brain Theory and Neural Networks, Second Edition, Cambridge, MA:MIT Press, 87-90.

[81] C. Darken, J. Moody (1990). Fast adaptive k-means clustering: some empirical results. Proceedings of the International Joint Conference on Neural Networks (IJCNN'90), vol. 2, p. 233-238.

[82] D. DeSieno, Adding a Conscience to Competitive Learning, IEEE International Conference on Neural Networks, Vol. 1, pp. 117-124, San Diego, 1988.

[83] F. Luo, R. Unbehauen, Applied Neural Networks for Signal Processing, Cambridge University Press, 1997.

[84] G. Cirrincione, M. Cirrincione, J. Hérault, and S.Van Huffel, The MCA EXIN neuron for the minor component analysis: Fundamentals and comparisons, IEEE Trans. Neural Networks, vol. 12, pp. 160–187, Jan. 2001.

[85] P. Meinicke, H. Ritter, Local PCA Learning with Resolution-Dependent Mixtures of Gaussians, IEE ICANN 1999, Vol. 1, pp. 497-502, 1999.

[86] G. Marsala, A. Accetta, J. Pukrushpan, M. Pucci, M. Cirrincione, A. Miraoui, “Model Predictive Control Based Air Management of a PEM Fuel Cell System”.IEEE Energy Conversion.

[87] M. Cirrincione, M. C. Di Piazza, G. Marsala, M. Pucci, G. Vitale, “Real Time Simulation of Renewable Sources by Model-Based Control of DC/DC Converters”, ISIE 2008 IEEE International Symposium on Industrial Electronics, Cambridge, UK.

[88] Dimitri Torregrossa. “Modellizzazione di un sistema con pile a combustibile di tipo PEM: analisi teorica e caratterizzazione sperimentale. Master’s tesi”. Università degli Studi di Palermo, Palermo, 2007.